# MITIGATION OF LATERAL MISALIGNMENT PROBLEM IN WIRELESS POWER TRANSFER APPLICATIONS

Thesis Report Submitted to

Indian Institute of Technology Ropar

in partial fulfilment of the requirements for the
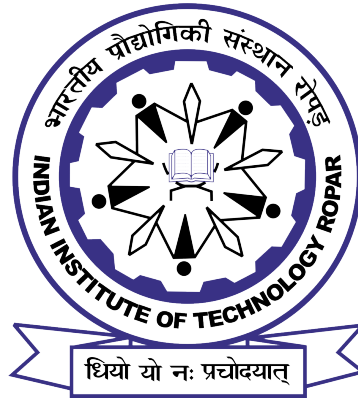
Degree of

## DOCTOR OF PHILOSOPHY

By

**Madduluri Ananth Bharadwaj**
**(Reg.No 2018eez0023)**

Under the guidance of

**Dr. Ashwani Sharma**
&
**Prof. C. C. Reddy**

Department of Electrical Engineering

Indian Institute of Technology Ropar

Rupnagar-14001, Punjab, India

2022-2023

April-2023

*Dedicated to my Parents, Wife, and Supervisors.*

# Declaration of Originality

I hereby declare that the work which is being presented in the thesis entitled **Mitigation of Lateral Misalignment Problem in Wireless Power Transfer Applications** has been solely authored by me. It presents the result of my own independent investigation/research conducted during the time period from January, 2019 of joining the Ph.D. program to April, 2023 of Ph.D. Thesis submission is under the supervision of Dr. Ashwani Sharma, Assistant Professor, Indian Institute of Technology, Ropar and Prof. C. C. Reddy, Professor, Indian Institute of Technology Ropar. To the best of my knowledge, it is an original work, both in terms of research content and narrative, and has not been submitted or accepted elsewhere, in part or in full, for the award of any degree, diploma, fellowship, associateship, or similar title of any university or institution. Further, due credit has been attributed to the relevant state-of-the-art and collaborations (if any) with appropriate citations and acknowledgments, in line with established ethical norms and practices. I also declare that any idea/data/fact/source stated in my thesis has not been fabricated/ falsified/ misrepresented. All the principles of academic honesty and integrity have been followed. I fully understand that if the thesis is found to be unoriginal, fabricated, or plagiarized, the Institute reserves the right to withdraw the thesis from its archive and revoke the associated Degree conferred. Additionally, the Institute also reserves the right to appraise all concerned sections of society of the matter for their information and necessary action (if any). If accepted, I hereby consent for my thesis to be available online in the Institute's Open Access repository, inter-library loan, and the title & abstract to be made available to outside organizations.

Signature

Name: Madduluri Ananth Bharadwaj
Entry Number: 2018eez0023
Program: Doctor of Philosophy (Ph.D.)
Department: Electrical Engineering
Indian Institute of Technology Ropar
Rupnagar, Punjab 140001

Date: 20-04-2023

# Acknowledgement

Firstly, I want to thank **Lord Shiva** for his blessings and unconditional support, which enabled me to withstand and move forward in all conditions of my life. I sincerely thank my supervisor **Dr. Ashwani Sharma** for showering immense knowledge and pullout the hidden research thirst within me. Moreover, the emotional support provided by him during unfavorable conditions of my initial research is unforgetful, and I am forever indebted for the same. I extend my sincere thanks to my co-supervisor **Prof. C. C. Reddy**, for providing constant advice in taking appropriate actions in writing research papers and tackling some challenging comments provided by potential reviewers. Also, I am grateful for being a part of the vibrant and highly motivated Antenna and Microwave Research (AMR) team.

I also thank doctoral committee members **Dr. Satyam Agarwal**, **Dr. A. V. Ravi Teja**, and **Dr. Himanshu Paliwal** for their insightful comments and suggestions in ehancing the quality of research work. Further I am greateful for **Director**, **Deans**, **HoD's** and **faculties** of Indian Institute of Technology Ropar for providing valuable resources for performing seamless research.

Moreover, my colleague cum dear friend **Vivek Kumar Srivastava** made the journey towards my Ph.D. degree more memorable as our discussions on research work resulted in fruitful outcomes. I am thankful for the efforts put by **Sagar Jain** for thoroughly reviewing my thesis and providing valuable suggestions. I want to thank my **Father (M. V. S Babaji Rao)** and **Mother (M. Jyothi)**, for being my role models and provide an unconditional love and support at all the times of my life. Their upbringing helped me in becoming a better person and made me capable of handling any kind of challenges in life. Last but not the least, I want to specially thank my dear **wife (Kavya)** for sharing abundant love and happiness. She also helped me by investing her time in reviewing, editing and improving my technical writing skills in my research papers and thesis.

**DEPARTMENT OF ELECTRICAL ENGINEERING**
**INDIAN INSTITUTE OF TECHNOLOGY ROPAR**
RUPNAGAR-140001, INDIA

# Certificate

This is to certify that the thesis entitled **Mitigation of Lateral Misalignment Problem in Wireless Power Transfer Applications**, submitted by **Madduluri Ananth Bharadwaj (2018EEZ0023)** for the award of the degree of **Doctor of Philosophy** of Indian Institute of Technology Ropar, is a record of bonafide research work carried out under our guidance and supervision. To the best of our knowledge and belief, the work presented in this thesis is original and has not been submitted, either in part or full, for the award of any other degree, diploma, fellowship, associateship or similar title of any university or institution.

In our opinion, the thesis has reached the standard fulfilling the requirements of the regulations relating to the Degree.

Signature

**Supervisor: Dr. Ashwani Sharma**
Department: Electrical Engineering
Indian Institute of Technology Ropar
Rupnagar, Punjab 140001
Date: 20-04-2023

Signature

**Co-supervisor:Prof. C. C. Reddy**
Department: Electrical Engineering
Indian Institute of Technology Ropar
Rupnagar, Punjab 140001
Date: 20-04-2023

# Lay Summary

This thesis aims to address the issue of lateral misalignment in near-field resonant wireless power transfer (WPT) systems. The scholar used a novel field forming technique using minimum mean square error (MMSE) algorithm to design several transmitter and receiver coils. As a valuable contribution to the research community, the scholar proposed six novel designs to overcome lateral misalignment in WPT systems. These new designs outperformed those proposed in literature studies.

# Abstract

Wireless power transfer (WPT) has been around for over a century originating with Nikola Tesla's pioneering ideas; however, it has recently drawn more attention due to its broad applicability in various current scenarios. Having the features like high flexibility, convenience, safety, and aesthetics, the WPT is widely used in many applications such as biomedical implants, mobile phones, and electric vehicles. The performance of the WPT system is greatly affected by misalignment between the transmitter (Tx) and the receiver (Rx) coils. In practice, perfect alignment is usually not ensured. Therefore, mitigation of the misalignment problem is currently a primary research direction. Among various such limitations, the lateral misalignment problem is most common in the WPT applications such as smartphones, drones, and electric vehicle charging stations, where the Tx and the Rx coils are co-planar but displaced. Hence, the primary objective of this thesis is to propose a solution to mitigate the lateral misalignment problem by employing the field forming technique. Additionally, a novel performance parameter called the Uniformity Factor (UF) is introduced to assess the potential misalignment tolerance of the proposed designs.

The thesis is split up into seven chapters. Chapter 1 discusses the basics of the near-field WPT system, describing various potential research problems involved in the WPT system, and later identifies the most challenging issue, which is targeted in this thesis. Further, the already available solutions in the literary works are investigated intensively in Chapter 1. Simultaneously, Chapter 2 deals with a mathematical background of field-forming technique and circuit analysis of distinct compensation topologies, and design procedure of Tx coil antenna to maximize efficiency under a perfectly aligned Rx coil antenna. Whereas the Chapter 3 deals with novel S-parameter-based efficiency equations for series-series, series-parallel, parallel-series, and parallel-parallel compensation topologies. Also, Chapter 4 focuses on addressing lateral misalignment problems by targeting to induce uniform voltage at the Rx coil using single port Tx coil antennas. The best Tx coil antenna design using single port is found to be Design-1C (n=3) with UF in regards to induced voltage is 45.41%. On the contrary, Chapter 5 aims to mitigate the lateral misalignment problem by minimizing flux leakage using switchable circuits and detection coils using multi-port Tx coil antennas. The Design-2B multi-port Tx coil antenna achieves UF of 75.5% in induced voltage with power transfer efficiency of 80% which stands out among all the designs mentioned in this thesis. Furthermore, the investigation of Rx coil antenna is intensively done by performing parametric optimization of various parameters of Rx coil to encapsulate all the magnetic-field components to induce a uniform voltage in Chapter 6. Finally, the thesis work is summarized and concluded in Chapter 7.

**Keywords**:Wireless Power Transfer (WPT); Magnetic Resonance Coupling (MRC); Magnetic Field Forming; Detection Coils; Vector Network Analyzer (VNA); Compensation Topologies.

# List of Publications

**Journal**

Article 1:

**A. Bharadwaj**, A. Sharma and C. C. Reddy, "Analytical Framework of S-parameter Based Efficiency for Secondary-Parallel Compensation WPT system to Authenticate Data Using VNA," in **IEEE Transactions on Instrumentation and Measurement**, doi: 10.1109/TIM.2023.3240224.

Article 2:

**A. Bharadwaj**, A. Sharma and C. R. Chandupatla, "A Switched Modular Multi-Coil Array Transmitter Pad With Coil Rectenna Sensors to Improve Lateral Misalignment Tolerance in Wireless Power Charging of Drone Systems," in **IEEE Transactions on Intelligent Transportation Systems**, 2022, doi: 10.1109/TITS.2022.3220793.

Article 3:

**A. Bharadwaj**, V. K. Srivastava, A. Sharma and C. C. Reddy, "A Tilted-Orthogonal Receiver Coil Antenna to Improve Misalignment Tolerance in WPT Systems," in **IEEE Transactions on Antennas and Propagation**, vol. 70, no. 12, pp. 11434-11441, Dec. 2022, doi: 10.1109/TAP.2022.3209207.

Article 4:

**A. Bharadwaj**, A. Sharma and C. C. Reddy, "An Unconventional Measurement Technique to Estimate Power Transfer Efficiency in Series–Series Resonant WPT System Using S-Parameters," in **IEEE Transactions on Instrumentation and Measurement**, vol. 71, pp. 1-9, 2022, Art no. 8004009, doi: 10.1109/TIM.2022.3181291.

Article 5:

**A. Bharadwaj**, A. Sharma and C. C. Reddy, "A Multi-Turn Coil Antenna With Nonuniform Clustered Turns Optimized Using Q-Assisted MMSE Procedure to Enhance Misalignment Tolerance in WPT Systems," in **IEEE Transactions on Antennas and Propagation**, vol. 70, no. 7, pp. 5302-5311, July 2022, doi: 10.1109/TAP.2022.3146433.

Article 6:

**A. Bharadwaj**, V. K. Srivastava, A. Sharma and C. C. Reddy, "A Switchable Multicoil Antenna With Booster Coil to Improve Coverage in WPT Systems," in **IEEE Transactions on Antennas and Propagation**, vol. 70, no. 4, pp. 2490-2498, April 2022, doi: 10.1109/TAP.2021.3137379.

Article 7:

A. Sharma, **A. Bharadwaj** and V. K. Srivastava, "An Analytical Framework to Design Planar Transmitting Array Antennas to Mitigate Lateral Misalignment in Wireless Power Transfer Systems," in **IEEE Transactions on Antennas and Propagation**, vol. 69, no. 9, pp. 5559-5569, Sept. 2021, doi: 10.1109/TAP.2021.3069518.

## Conference Proceeding

Article 1:

**A. Bharadwaj**, V. K. Srivastava, C. C. Reddy, and A. Sharma, "Design Methodology of Near-Field Transmitter Coil Antenna for Maximizing Efficiency of the WPT System," **accepted in 17th European Conference on Antennas and Propagation**, Florence, Italy, 2023.

Article 2:

**A. Bharadwaj**, V. K. Srivastava, A. Sharma and C. C. Reddy, "A Novel Trapezoidal Multi-Coil Antenna for Wireless Charging of Electric Vehicles," **2020 IEEE 15th International Conference on Industrial and Information Systems (ICIIS)**, RUPNAGAR, India, 2020, pp. 13-17, doi: 10.1109/ICIIS51140.2020.9342635.

Article 3:

**A. Bharadwaj**, Ashutosh Rai, Narsa Reddy Tummuru, C. C. Reddy and A. Sharma, "A Coil-Based Constant-Output-Current (C-O-C) and Constant-Output-Voltage (C-O-V) Resonant-WPT System under Lateral Misalignment of Rx Coil," **submitted in 11th National Power Electronics Conference (NPEC)**, Guwahati, India, 2023

## Patent

Patent 1:

**A. Bharadwaj**, A. Sharma and C. C. Reddy, "TITLE: Switched Modular Multi-Coil Array Antenna Arrangement for Wireless Charging Transmitter Pad." (**Patent filed with Indian patent office on 16-09-2021: Application No. 202111041922**)

Patent 2:

**A. Bharadwaj**, V. K. Srivastava, A. Sharma and C. C. Reddy, "TITLE: Dual-Mode Antenna with Non-Uniform Coil Array for Wireless Power Transmission and Method Thereof." (**Patent filed with Indian patent office on 25-03-2021: Application No. 202111013157**)

## Awards

Award 1:

Best paper award for the article titled "A Novel Trapezoidal Multi-Coil Antenna for Wireless Charging of Electric Vehicles" published in 2020 ICIIS conference.

Award 2:

Second Runner up in poster presentation titled "A Wireless Power Charging System to Enhance Lateral Misalignment Tolerance in Electric Vehicles." at 1st EE-RSF Research Day.

# Acronyms

**2-D**       Two Dimensional

**3-D**       Three Dimensional

**AC**       Alternating Current

**CC**       Constant Current

**CoV**       Coefficient of Variation

**CV**       Constant Voltage

**DC**       Direct Current

**DDQ**       Double D Quadrature

**DNG**       Double Negative

**DPS**       Double Positive

**eGaN**       enhancement mode Gallium Nitride

**EMI**       Electromagnetic Interference

**EMC**       Electromagnetic Compatability

**ENG**       Epsilon Negative

**EP**       Evolutionary Process

**EVs**       Electric Vehicles

**FET**       Field Effect Transistor

**HFSS**       High Frequency Structure Simulator

**MMSE**       Minimum Mean Square Error

**MNG**       Mu Negative

**MRC**       Magnetic Resonance Coupling

**MSE**       Minimum Square Error

**NUDT**       Non Uniformly Distributed Turns

**P-P**       Parallel-Parallel

**P-S**       Parallel-Series

**PTE**       Power Transfer Efficiency

| | |
|---|---|
| **Rx** | Receiver |
| **SiC** | Silicon Carbide |
| **SO** | Sub-Objective |
| **S-S** | Series-Series |
| **S-P** | Series Parallel |
| **Tx** | Transmitter |
| **UDT** | Uniform Distributed Turns |
| **UF** | Uniform Factor |
| **VNA** | Vector Network Analyzer |
| **WBG** | Wide Band Gap |
| **WPT** | Wireless Power Transfer |
| **ZVDS** | Zero Voltage Derivative Switching |
| **ZVS** | Zero Voltage Switching |

# Contents

# List of Figures

# List of Tables

# Chapter 1

# Introduction of WPT system

## 1.1 Introduction

The concept of Wireless Power Transfer (WPT) involves transmitting electrical energy from a transmitter (Tx) to a receiver (Rx) through the air utilizing electromagnetic waves. This technology can be divided into three primary categories, far-field radiative, near-field radiative, and near-field reactive systems, as demonstrated in Figure. 1.1. Far-field
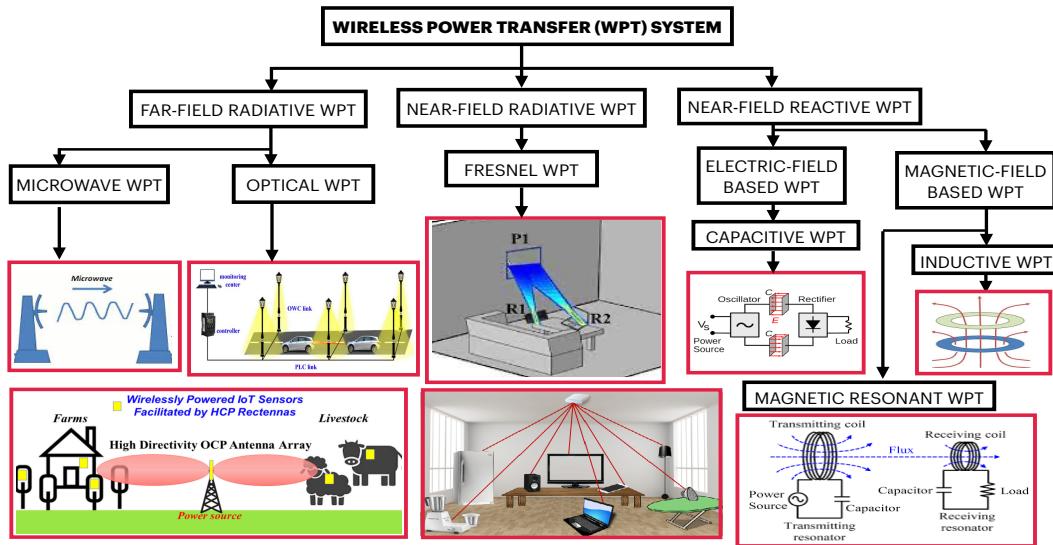


Figure 1.1: Classification of various types in WPT systems.

radiative WPT involves the transfer of energy over extensive distances through the use of electromagnetic waves such as microwaves and laser beams. However, this technology remains in its nascent stages due to the potential dangers posed by high-power microwaves and laser beams to living beings. On the other hand, near-field WPT can be subdivided into two categories: radiative and reactive. The radiative region in the near-field, also Known as the Fresnel region, entails transmission of low-power microwaves through antennas and is suitable for powering micro sensor nodes, low-power home appliances, and biomedical devices. Meanwhile, the reactive region, comprising electric field based WPT and magnetic field baased WPT, manages to power medium to high-power applications. Capacitive WPT relies on the electric field coupling between Tx and Rx metal plates, yet raises safety concerns as the human body can be polarized under the influence of electric fields. Furthermore, the presence of nearby stray metal objects can significantly

1

reduce the electric-field coupling between Tx-Rx coil metal plates, resulting in decreased power transfer efficiency (PTE). On the other hand, magnetic field WPT functions based on Faraday's law of electromagnetic induction, in which the Tx-Rx coils are subdivided into Inductive and Magnetic resonant WPT systems. The significant advantages of using an Inductive WPT system is it provides features such as high flexibility, convenience, aesthetics, safety, and spatial freedom, which are not possible using conventional plugin charging. Moreover, the magnetic fields originated from Inductive WPT have minimal impact on living beings, considering life on Earth is composed of non-magnetic components. However, inductive WPT experiences reduces coupling as the transfer distance increases from short to medium distances, due to significant magnetic flux leakage due to lack of resonance between Tx-Rx coils.

Researchers at MIT have developed a Magnetic Resonance Coupling (MRC) based WPT system to address this issue, which enhances the coupling between Tx-Rx coils. In the MRC technique, the reactance of the Tx-Rx coils is compensated using an external capacitor network at a single-tone operating frequency. The MRC technique [1] has proven to be the most efficient and reliable mode of contactless power transmission, making it the focal point of research work in this thesis due to its capability of transferring efficient power over medium transfer distances. The block diagram of the MRC based WPT system is displayed in Figure. 1.2 , which highlights that the system comprises of high-frequency
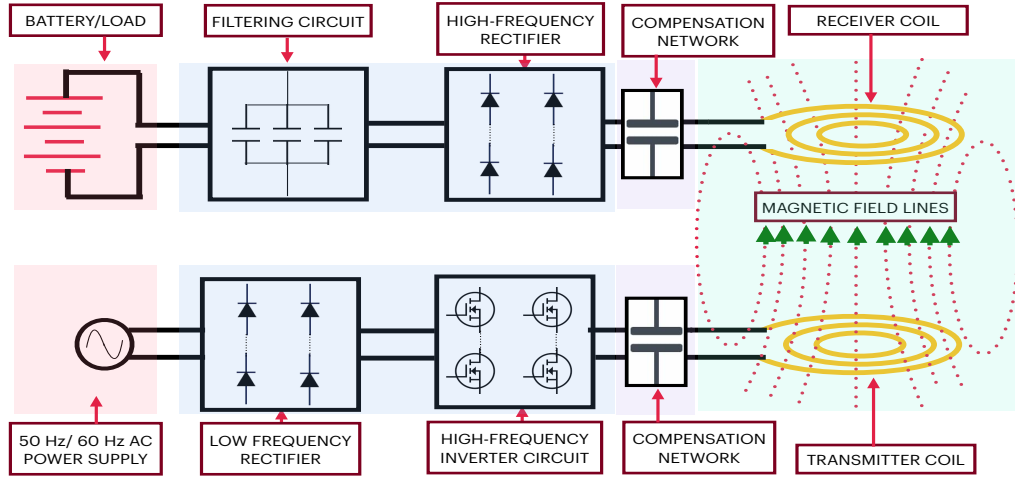


Figure 1.2: Block diagram of MRC based WPT system.

inverters to excite the resonant Tx coil, and at Rx side, the fast-recovery diodes are employed in the rectifier unit design to convert high-frequency induced voltage/current into Direct Current (DC) voltage/current. Filtering capacitors are utilized to eliminate ripples in the rectified DC voltage/current, ensuring that the battery/load is powered with pure DC power. The various commercial applications of MRC-based WPT systems such as electric drones, electric vehicles, smart phones, and biomedical implants are demonstrated in Figure. 1.3.

Despite the advancements of the MRC based WPT system, the coupling and link efficiency
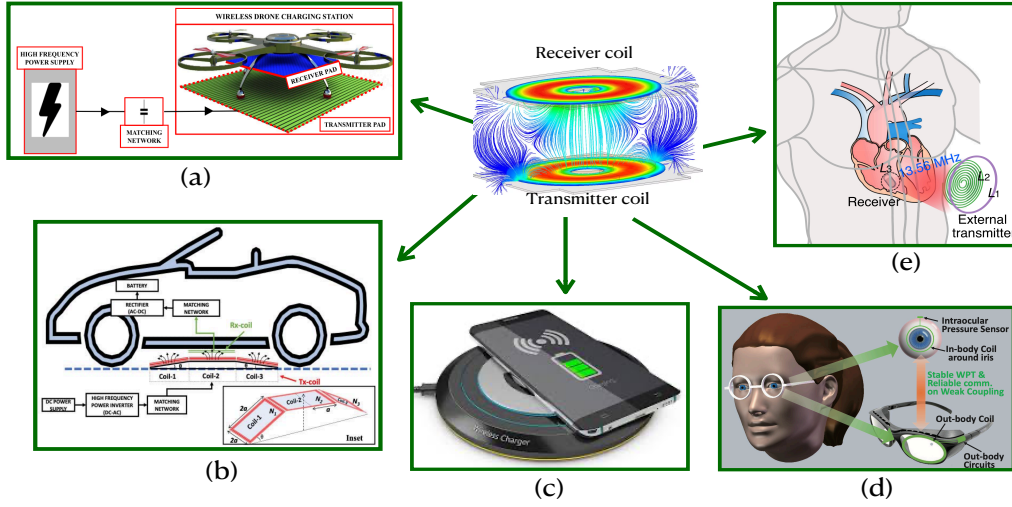
Figure 1.3: Applications of MRC based WPT system as (a) electric drones, (b) electric vehicles, (c) smart phones, (d) intraocular pressure sensor, and (e) biomedical implants.

between the Tx and Rx coils are significantly impeded due to misalignment between them. Ideally, the Rx coil should be coplanar and coaxially aligned with the charging platform (Tx). However, various misalignment issues, as depicted in Figure. 1.4, frequently arise due to human motor limitations. Of all the misalignment problems illustrated in Figure. 1.4, lateral misalignment is a common occurrence in a range of applications such as electric vehicles, mobile devices, and electric drones. The lateral misalignment happens due to a relative position variation between the Tx-Rx coils at a certain fixed transfer distance Thus, the study in this thesis aims to address the mitigation of this limitation.

## 1.2    Literature Survey of Near-Field Resonant WPT System

The literary assessment has been arranged in a systematic manner to address the potential research hurdles that may arise in the near-field MRC-based WPT systems, as depicted in Figure. 1.5. Through a thorough examination of the available literature, it is established that the primary difficulties can be categorically divided into four main domains: 1) high-frequency power electronic converters, 2) compensation topologies, 3) electromagnetic interference/compatibility (EMI/EMC), and 4) Tx-Rx coil design.

### 1.2.1    High-frequency power electronic converters

The requirement for a alternating current (AC) at high-frequencies to produce an electromagnetic field of equivalent frequency within the Tx coil arises from the utilization of high-frequency inverters. Subsequently, the high-frequency induced voltage produced within the secondary coil is rectified to DC. The DC signals with ripples are purified using filtering network and linked to the battery. It is imperative to design highly efficient power electronic converters to ensure that the aforementioned conversion procedure is achieved
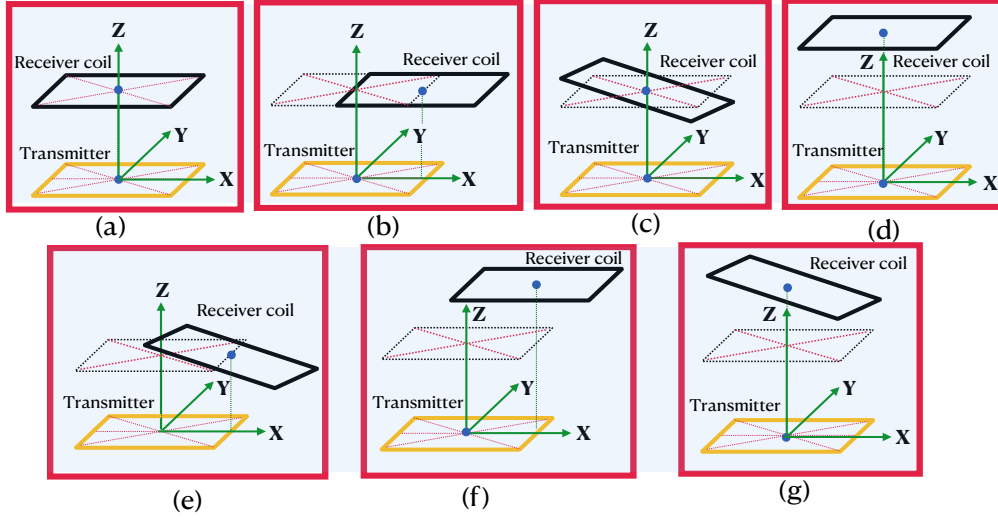
Figure 1.4: (a) Perfect alignment of Tx-Rx coils, distinct misalignment challenges such as (b) lateral misalignment, (c) angular misalignment, (d) longitudinal misalignment, (e) lateral and angular misalignment, (f) lateral and longitudinal misalignment, and (g) angular and longitudinal misalignment in resonant WPT system.
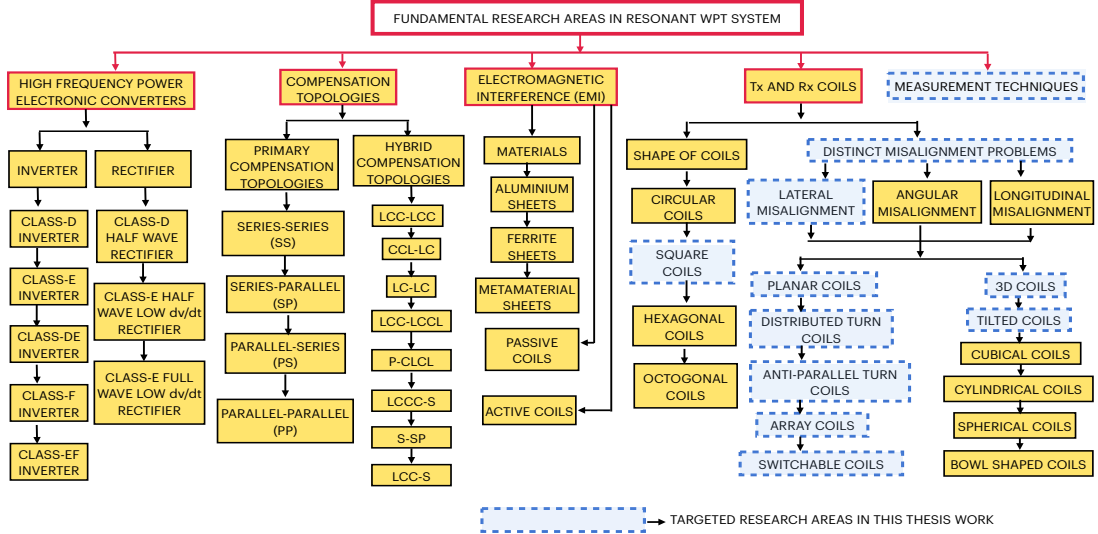


Figure 1.5: Various research areas in resonant WPT system.

with minimal losses, thereby augmenting the overall system efficiency.

### High-frequency inverters

The prime objective of a power electronic inverter in a WPT system is to function in two distinct modes of operation, namely, constant current (CC) and constant voltage (CV) modes, in order to enhance the durability, safety, and life cycle of the battery located at the load end. However, the equivalent resistance of the battery exhibits non-linear

variations during the charging process, and these variations can also occur as a result of misalignment-induced coupling problems. These factors pose a challenge for WPT systems to provide constant and load-independent output voltages/currents, and also to achieve high PTE, which is widely recognized as an important goal in WPT systems. The PTE of WPT systems is reduced by switching and conduction losses from high-frequency devices. To tackle these challenges, a DC-DC converter is sometimes added between the DC power supply and the high-frequency inverter to regulate the desired output voltages/currents by adjusting the duty cycle of high-frequency switching devices [2]. However, this solution incurs additional power losses and cost due to the DC-DC converter, and may not be feasible in practice. Half-bridge and full-bridge inverters combined with variable inductors provide a degree of freedom to control the output of DC signals of the WPT system [3]. However, the full-bridge inverters proposed in [3] can only operate at frequencies up to 10s of kHz, resulting in larger inverter sizes and increased losses, reducing overall system efficiency. To reduce the size of inverters, it is advisable to operate the switches at very high frequencies, typically in the MHz range. Therefore to miniaturize inverters a wide band gap (WBG) devices, such as Silicon Carbide (SiC) MOSFETs and enhancement-mode Gallium Nitride (eGaN) field effect transistors (FETs) are used in designing high-frequency inverters at MHz range. Moreover, the technology using WBG have made it easier to design high-frequency inverters with much higher breakdown voltages [4]. Among the WBG devices, eGaN FETs are ideal candidates for use in high-frequency inverters, as they have lower ON-resistance performance at high temperatures, lower input capacitances, and lower inductance in their packages compared to SiC MOSFETs.

The various types of inverter configurations using WBG devices are illustrated in Figure. 1.5 encompass class-D [4, 5], class-E [6, 7, 8], class-DE [9], class-F [10] and class-EF topologies [11, 12, 13]. The class-D inverters are renowned for their exceptional high-frequency performance, typically in the MHz range, and for providing output responses that are independent of load variations. The class-D resonant inverter is either a half-bridge or full-bridge configuration, which employs at least two MOSFETS to transform DC power into high-frequency AC power [4, 5]. Furthermore, the class-D topology operates under lower voltage and current stress on the switches, although it requires a more complex gate driver circuit to switch the devices. The bootstrap used for this purpose presents one of the major design challenges when implementing class-D inverters at multi-MHz switching frequencies. The total harmonic distortion of the output voltage of this topology is higher compared to other classes of inverters.

On the other hand, the class-E inverter, invented by Natha O Sokal and Alad D Sokal in 1975 [6], has been extensively researched and its analysis is well documented in literature. Generally, the class-E inverter provides a compact and efficient solution for high-frequency WPT systems and has less complexity in the design of gate driver circuits with only one switching device. Additionally, the voltage ringing across the switching device, which is almost half the sinusoidal waveform with finite derivatives on both the ON and OFF transitions, results in low total harmonic distortion, which is crucial for

electromagnetic compatibility [7]. Theoretically, class-E inverters exhibit 100% power efficiency by achieving zero-voltage switching (ZVS) and zero voltage derivative switching (ZVDS). However, the high voltage and current stresses on the switching devices and sensitivity to output filter design are major drawbacks of the class-E inverter. Furthermore, the class-E inverter's resonant operating point is dependent on variations in the load and coupling between the Tx-Rx coils.

By connecting two shunt capacitors in parallel with the transistors of the class-D inverter [9], the advantages of class-D and class-E inverters are combined in the class-DE inverter. The class-DE inverter benefits from low transistor voltage stress and ZVS operation. Class-F and the recently popularized dual inverse class $F^{-1}$ [10] have been developed primarily to increase the saturated performance of class-AB and class-B designs, resulting in higher attainable operating frequencies than those of class-E amplifiers. However, the performance limitations due to tuning requirements and a lack of simple circuit implementation for nearly ideal switching make class-F a poor choice at higher frequencies.

Finally, it has been established that by incorporating a series LC network, tuned to the second harmonic of the switching frequency and connecting it in parallel with the switch in the class-E inverter, the voltage stress across the switch can be reduced to 2-2.5 times the input voltage. This technique, which involves the addition of a resonant network in parallel with the switch, is commonly employed in class-$F^{-1}$ inverter circuits and rectifiers. As a result, the class-E topology that incorporates this LC network is referred to as the class-EF2 topology [11, 12, 13]. The reduction in voltage stress in the class-EF2 topology allows for the circuit to be designed with a higher operating DC voltage, which minimizes the fluctuations in the switch's non-linear output capacitance. Additionally, the class-EF2 topology offers an improved electromagnetic interference (EMI) performance as it eliminates the second harmonic component from the switches drain voltage and the output load current. In contrast, the class-E inverter is characterized by a strong second-harmonic component, which can make it challenging to comply with EMI regulations.

### Rectifiers

Wireless power receivers derive energy from the secondary coil of a WPT system, facilitating the transformation of AC into DC. Traditional rectifiers employ a two-stage structure, whereby the rectifier first converts the AC signal into an unregulated DC signal, which is then regulated through a DC-DC converter. However, the utilization of a two-stage rectification process incurs losses due to additional switching components and reduces the overall efficiency of the system [14]. As an alternative, single-stage receivers, which unify the functions of the rectifier and regulator into a single entity, have been proposed to enhance rectification efficiency [15]. This is achieved through a reduction in the number of switching devices compared to the two-stage rectification process. Additionally, single-stage rectifiers can typically be implemented through two means: a

reconfigurable rectifier approach [16], or through the modulation of the conduction time of power transistors to regulate the output voltage [17]. Nevertheless, the aforementioned methods present limitations in their ability to convert high-frequency AC signals, typically within the MHz range, into DC.

The rectifiers previously employed in similar works were all based on conventional half-wave and full-wave configurations. Although they are capable of performing AC-DC rectification, their utilization can negatively impact the overall performance and efficiency, as most resonant inverters, such as class-D and class-E, operate at resonance. Given that the outputs of class-D and class-E resonant inverters are sinusoidal, the input current of traditional rectifiers is not. This mismatch can cause the primary coil driver to operate under suboptimal switching conditions, necessitating the use of class-D rectifiers [18]. These rectifiers can convert sinusoidal voltage or current into DC voltage or current. The primary advantage of class-D rectifiers lies in the fact that the input voltage or current is a square wave, leading to enhanced power factor and total harmonic distortion factor, making it compatible with class-D and class-E inverters. Despite the advantages of class-D rectifiers, they necessitate the use of a minimum of two diodes, which results in increased switching losses. In contrast, class-E rectifiers [19] only require a single diode, leading to lower losses and ultimately improving rectification efficiency.

### 1.2.2 Compensation topologies of resonant WPT system

The four principal compensation topologies, namely series-series (S-S), series-parallel (S-P), parallel-series (P-S), and parallel-parallel (P-P), play a crucial role in optimizing the performance of resonant WPT systems in terms of PTE under varying optimal load conditions [20]. The resonant capacitors in the S-S compensation topology are unaffected by mutual coupling and load resistance, making it well-suited for applications such as dynamic wireless charging systems, which are susceptible to changes in mutual inductance and load resistances. In contrast, the compensation capacitors in the S-P topology are dependent on mutual inductance, which limits its suitability for applications prone to misalignment. Additionally, the S-P topology requires significantly less secondary inductance, making it an appropriate choice for biomedical applications. Meanwhile, capacitors in both the P-S and P-P topologies are influenced by both mutual inductance and load resistance, rendering them less suitable for many applications. However, P-S and P-P topologies find practical use in low-power and loosely coupled applications [20].

Furthermore, the utilization of hybrid compensation configurations, including primary series/secondary series-parallel (S-SP) [21], double-sided inductance-capacitance-capacitance (LCC-LCC), LCC-series (LCC-S), LCC-parallel (LCC-P), double-sided capacitance-inductance-capacitance (CLC-CLC) [20, 22], and higher-order compensation capacitors such as L-CCCS [23] and P-CLCL [24] networks, offer increased versatility in maintaining a consistent current output amidst varying load conditions. However, the inclusion of extra inductance and capacitance in these hybrid networks leads to higher losses due to stray resistance, and their cost is generally more

expensive than that of primary compensation topologies.

### 1.2.3   Electromagnetic interference in resonant WPT systems

The phenomenon of EMI refers to the unanticipated interaction between magnetic flux lines that occur outside the Rx coil region and foreign objects or living entities. This interaction results in flux leakage, which negatively influences the resonant WPT's performance parameters. Hence, it is imperative to mitigate the issue of flux leakage through the implementation of various shielding strategies, as demonstrated in Figure. 1.5. The optimal placement of aluminum plates behind the Tx-Rx coils can result in an enhancement of the total magnetic field intensity within the Rx coil [25]. This occurs because the eddy currents induced in the aluminum sheets augment the magnetic induction process. However, despite the increase in output power, the system's PTE experiences a reduction due to eddy current losses.

Ferrimagnetic materials, such as ferrites, are being considered as a viable alternative for shielding in WPT systems due to their ability to guide and confine magnetic flux [26]. Characterized by their elevated relative permeability and minimal loss tangent, these materials have gained consideration as a potential means of improving system performance. Nevertheless, ferrite structures are not without their drawbacks. Their inherent brittleness poses difficulties with regards to encapsulating the coils and attaching them to metal surfaces. Furthermore, the relatively rigid mechanical properties of ferrite structures pose challenges in terms of mass production. Additionally, ferrite materials are susceptible to eddy current losses at elevated frequencies, such as those in the MHz range or higher, as well as hysteresis losses.

As an alternative, one may incorporate more sophisticated materials, such as metamaterials [27], into the WPT system to boost its overall performance by mitigating the issue of leakage flux. Metamaterials are artificially constructed materials possessing uncommon and exotic properties not found in naturally occurring materials, thereby transcending the limitations associated with conventional materials. Permittivity and permeability are two parameters that reflect the electromagnetic properties of materials, and accordingly, materials can be divided into four categories based on the polarities of these parameters. When both permittivity and permeability are simultaneously positive ($\epsilon > 0, \mu > 0$), the materials are designated as double-positive (DPS) materials and are commonly known as conventional materials. On the other hand, materials with negative permittivity and positive permeability ($\epsilon < 0, \mu > 0$) are classified as epsilon-negative (ENG) materials, while materials with positive permittivity and negative permeability ($\epsilon > 0, \mu < 0$) are referred to as mu-negative (MNG) materials. Materials that are configured to have both parameters be negative ($\epsilon < 0, \mu < 0$) are known as double-negative (DNG) materials. The ENG, MNG, and DNG slabs are typically considered metamaterials and are initially classified based on the unit cell position, such as 1-D [28], 2-D [29], and 3-D [30], and can also be categorized based on their relative position with respect to the Tx-Rx coils, such as middle [31], front [32], back [33], and sideways [34]. The primary

challenge in utilizing metamaterials lies in their practical implementation, and the size of metamaterials increases significantly as the operating frequency decreases. As a result, the use of metamaterials becomes infeasible in applications where the operating frequency falls within the kHz range.

An economical method for EMI shielding is the utilization of passive coils, which rely on a resonant reactive current loop mechanism to produce a magnetic field that cancels out the original magnetic field, thereby reducing EMI. This approach is cost-effective as it does not require any external power source to generate the cancelling magnetic field, as it is derived from the original magnetic field noise [35]. In contrast, the active shielding technique has been proposed as a means of reducing magnetic leakage between the Tx and Rx coils. This involves the use of an active shield, comprised of an additional active coil, which generates a magnetic field that is opposite to the incident field, thus reducing the total magnetic field in a designated area. However, the active coils must be controlled by an external voltage source, which results in increased cost, complexity, and energy losses [36].

### 1.2.4   Measurement techniques for WPT systems

The measurement setup for determining the most significant performance parameters of WPT systems, such as PTE, can be broadly classified into two distinct techniques, each comprising various measurement methods/setups. The first measurement technique is built on circuitry laws and is further subdivided into passive and active measurement methods. In the passive measurement method, circuit parameters such as resistance and self-inductance are directly measured using either an impedance analyzer [37] or an LCR meter [38]. The mutual inductance of Tx-Rx coils is measured indirectly by the differential cumulative method [38, 39]. The PTE is then computed by replacing the measured values of the circuit parameters in the circuit-based efficiency formula [1]. In this method, the power supply is designed by the user, allowing them to control the value of source resistance [1, 40], while the load resistance [41] is chosen based on the user-defined application. However, the passive measurement technique has limitations, such as complexity in measuring mutual inductance value with low accuracy.

In the active measurement method, the circuit-based efficiency is obtained by determining the ratio of output power and input power aided with a dedicated power source [1]. However, a prime challenge in this method is using a high-frequency GaN-based inverter at high power levels to estimate the performance of Tx-Rx coils by designing a dedicated power source. Consequently, the system cost is escalated for a laboratory-level realization [42]. Alternatively, the signal generator-spectrum analyzer duo is adopted to measure PTE [42]. However, the source resistance value of the signal generator is $50\Omega$, which reduces the PTE value in comparison to a realistic power source in which the source resistance ranges from 0 to $0.1\Omega$ [1].

In the second measurement technique, the S-parameter-based efficiency is measured by acquiring the magnitude of S-parameters by calibrating the input port and output

port to 50Ω [43]. Based on the matching network at the load side, the conventional S-parameter-based efficiency is categorized as transducer gain [44] and power gain [43]. The S-parameters are effortlessly measured using a vector network analyzer (VNA) even at high frequencies considering the circuit is electrically small. Moreover, the instrument is independent of undesired harmonics, and the data is highly reproducible and less susceptible to external noises. Nevertheless, the most prominent challenge observed in this technique is implausible VNA measurement to extract S-parameters at source resistance equivalent to near zero condition while no power is exchanged between Tx-Rx coils. Withal, most of the energy is consumed by VNA instruments due to high internal resistance. Therefore, the measured value of efficiency attained from the two methods significantly differs; (Circuit-based efficiency > S-parameter-based efficiency) for identical Tx-Rx coil designs. This disparity in S-parameter-based efficiency has inspired scholar to devise a novel VNA-based measurement technique to produce results equivalent to circuit-based efficiency in this thesis work. The proposed technique is further adopted in our laboratory for measurement of PTE between Tx-Rx coils. Overall, the development of this new VNA-based measurement technique in this thesis represents an important advancement in the field of near-field WPT.

### 1.2.5 Literary compositions of the Tx-Rx coils of a resonant WPT system

The geometrical configuration of Tx-Rx coils play a crucial role in the WPT system and present a wealth of opportunities for optimizing its performance parameters. Two of the most widely used coil shapes are circular [45] and square [46]. Wherein, circular coils are preferred in applications that are more susceptible to angular misalignment, while square coils are utilized when lateral misalignment is a greater concern. Moreover, some researchers are exploring other shapes such as hexagonal [47] and octagonal [48] as alternative options.

To attain a superior link efficiency, the Tx-Rx coils must be precisely aligned. However, this misalignment is inescapable due to the limitations of human dexterity. Generally, three different misalignment scenarios between Tx-Rx coils may occur: (i) Lateral misalignment [49], wherein the coils are situated in parallel planes, but the Rx coil is offset horizontally; (ii) Angular misalignment [50], arising from the rotation of the Rx coil from its intended angle; and (iii) Longitudinal misalignment [51], whereby the Rx coil is misaligned from its intended transfer distance. These misalignments are aldready visually shown in Figure. 1.4. Of all the misalignment issues, lateral misalignment is an ineluctable challenge in a plethora of wireless charging scenarios, such as electric vehicles (EVs), mobile devices, and electric drones, among others. Thus, this thesis primarily focuses on addressing the significant problem of lateral misalignment.

**Why lateral misalignment problem needs to be addressed?**

When the Rx coil is laterally displaced, the magnetic field lines between the Tx and Rx coils become less interlinked, leading to a decrease in the mutual inductance ($M$) between them. This reduction in $M$ can directly affect both the PTE and the load power. Thus, the PTE of a resonant WPT system is dependent on the magnetic field distribution generated by the Tx pad in the Rx region, which in turn is determined by the current distribution of the Tx coil and the physical characteristics of the Tx pad. To address the issue of lateral misalignment, it is essential to optimize the design parameters of the Tx coil, such as its position, number of turns, inter-turn spacing, and conductive track width. Figure 1.6 depicts the impact of lateral misalignment on the magnetic flux at the misaligned region of the Rx coil.
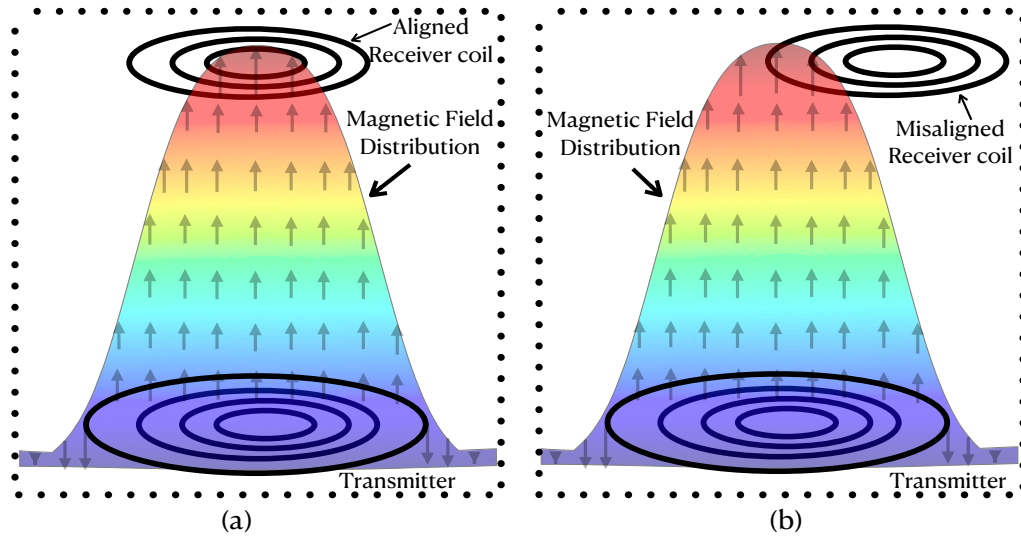
Figure 1.6: The effect of lateral misalignment under magnetic-field distribution at the Rx coil region.

**Literature Survey of Various Solutions Adopted in Past to Mitigate Lateral Misalignment**

The earliest method for addressing the issue of lateral misalignment is through the implementation of sensing coils to detect the displacement of the Rx-coil, which is then corrected through an electro-mechanical mechanism [52, 53, 54]. However, as detailed in [52], this technique necessitates an additional communication channel and a two-dimensional mechanical positioner to process the Rx coil data, thereby compromising the durability, reliability, and cost-effectiveness of the solution.

A more optimal approach to mitigate lateral misalignment issues is through the optimization of Tx coils using a field-forming strategy. Tx pads are generally classified into two categories, namely polarized and non-polarized coil structures. Polarized coil structures, such as double D (DD) [55], extended DD [56], double D quadrature

(DDQ) [57], and solenoid [58], are characterized by the presence of two opposing poles, north and south, within the pads. However, these designs have a low tolerance for misalignment due to the highly asymmetric distribution of the magnetic field, and the inclusion of ferrite sheets to increase coupling results in increased cost and weight of the WPT system. As a result, their use is limited to large EVs and similar applications. On the other hand, non-polarized pads, such as circular, rectangular, and hexagonal coils, have a single pole and distribute flux in all directions, with one pole located at the center of the coil and the other located outside the coil structure. Non-polarized pads, particularly unipolar designs, are favored for low-cost applications.

The optimization of Tx coil antenna geometric parameters is a crucial aspect of this approach. The shape of the coil element, selected from various forms such as square, circular, hexagonal, Taichi, etc. [1, 59, 60, 61], plays a pivotal role in mitigating misalignment. For instance, square coils have been found to be less sensitive to lateral misalignment compared to circular coils of similar size [62]. Subsequently, other geometric parameters are determined, such as the number of turns, trace width, and gap between turns. Advanced coil structures, including Uniformly Distributed Turns (UDT) [63, 64], Non-Uniformly Distributed Turns (NUDT) [65, 66], and opposite current distribution coil turns [1, 67, 68], have been developed through exploration of unconventional antenna geometries, including multi-coil, multi-turn, and coil array configurations with single and multiple turns.

The utilization of the field-forming technique to customize various coil designs has been documented in the literature as a means to rectify issues associated with lateral misalignment. A single-port Tx coil antenna capable of producing a uniform magnetic field within the Rx plane is widely recognized as a potential solution to mitigate these misalignment issues. Consequently, the aim of attaining a uniform magnetic field distribution within the Rx plane is a widely acknowledged objective [1, 69, 70, 71, 72, 73, 74, 75, 76, 77, 78]. In general, greater uniformity in the magnetic field distribution leads to a wider Rx area in which misalignment is reduced. For example, the issue of offset misalignment was addressed at various longitudinal displacements in [69] and vertical tilt was implemented to a rectangular coil in [70] to achieve a uniform magnetic field. However, this approach renders the coils unsuitable for applications where a planar design is preferred. An optimization algorithm based on the coefficient of variation (CoV) was utilized in [71] to attain a flat magnetic field distribution. However, the power transfer range in this application was limited to 1mm. A NUDT rectangular Tx coil structure was proposed in [72] based on $M$ per mm$^2$ area, where the achieved uniformity in $M$ resulted in a uniform magnetic field. Conversely, various optimization algorithms were utilized to form a uniform magnetic field in designs such as a two-coil Tx [73], a multi-coil anti-parallel current distributing coil structure [74], and a NUDT coil [75]. A planar multiple anti-parallel square coil design was proposed in [1] to attain magnetic field uniformity and its performance was compared against a conventional coil with all turns concentrated at the periphery. It is observed that the above single-port Tx coil

antennas constitute with large flux leakage, therefore to address this issue multi-port Tx coil antennas are evolved [60, 79]. Here, a switching mechanism was incorporated to mitigate lateral misalignment through the achievement of a quasi-uniform magnetic field distribution. However, this design is only suitable for applications where the Rx area is relatively small compared to the Tx area and the inclusion of a switching circuit results in a complex and unreliable system.

The newly introduced performance parameter, Uniform Factor (UF), is used to assess the degree of improvement in misalignment tolerance achieved by a particular design. UF is defined as the ratio of the misalignment tolerance range to the maximum dimensional area of the Tx charging pad, where the misalignment tolerance range refers to the total area of the Rx plane distributions, such as magnetic field $(H_x)$ or $(H_y)$ or $H_z$, induced voltage $(V)$, output power $(P_{R_R})$, or efficiency $(\eta)$, that are flat with maximum $\pm 10\%$ (for magnetic field) or $\pm 1\%$ (for $V$, $M$, $P_{R_R}$, and $\eta$) ripple fluctuations. Each performance parameter has its own UF, namely $\text{UF}(H_{x \text{ or } y \text{ or } z})$, $\text{UF}(M)$, $\text{UF}(V)$, $\text{UF}(P_{R_R})$, and $\text{UF}(\eta)$.

### Why near-field Tx-Rx coils can also be called as antennas?

The use of the term "antenna" in the context of near-field coils may initially seem confusing. However, this ambiguity can be clarified by considering the concept of a well-known Hertzian dipole antenna, which has an electrical length of $\frac{\lambda}{50}$. This electrical length is comparable to the dimensions of near-field coils. The current distribution is uniform in the case of a Hertzian dipole antenna. However, this type of antenna has limited practical applications due to its low radiation efficiency and higher generation of reactive fields. Fabricating Hertzian dipole antennas can also be relatively challenging. Interestingly, the disadvantages of the Hertzian dipole antenna can be transformed into advantages by identifying suitable applications that require low radiation efficiency and high reactive fields. Near-field wireless transmission-reception (Tx-Rx) coils, which have electrical lengths in the range of $\frac{\lambda}{50}$, exhibit these desired characteristics. Near-field wireless charging technology development since 2007 has provided a practical application for these coils. Moreover, fabricating near-field coils is relatively straightforward due to the low operating frequencies involved. In conclusion, considering the similar characteristics between Hertzian dipole antennas and near-field coils, the term "antenna" is appropriate when referring to Tx-Rx coils.

### The most successful literary designs

- The planar multiple anti-parallel Tx coil antenna [1] achieves the highest misalignment tolerance among various single port Tx coil antennas, with a $\text{UF}(H_z)$ of 51.84%, producing a uniform magnetic field.

- For multi-port Tx coil antennas, the design presented in [79] is found to be superior in mitigating lateral misalignment problems, with a $\text{UF}(V)$ of 31.36%.

- It is worth noting that the design in [79] also aims to reduce the flux leakage in the misaligned Rx coil region by incorporating switching circuits to achieve its superior performance.

Although the above mentioned literary designs have able to improve misalignment tolerance, the achieved UF values are surprisingly low and have a wide scope for improvement. This is mainly because prior literary designs lack comprehensive analytical optimization resulting from the magnetic field formation methodology. Thus, the author was motivated to develop a new and innovative field forming technique using Minimum Mean Square Error (MMSE) algorithm that aims to create Tx-Rx coil antennas that are insensitive to lateral misalignment.

Additionally, the validation of the measurement setup with analytical equations using S-parameters is limited to series-series compensation topology. Furthermore, as intensively discussed in subsection 1.2.4 regarding the disparity in S-parameter based efficiency made the author realize to develop a novel S-parameter based efficiency to forecast similar efficiency using realistic power sources.

## 1.3    Thesis Objective

To address the above challenges, the thesis objective has been divided broadly into two main categories: sub-objective A (SO-A) and sub-objective B (SO-B) as shown in Figure. 1.7. The main focus of Sub-objective A is to create a new measurement setup using S-parameters obtained from VNA. Here are the brief details of SO-A :

**SO-A**: A new measurement technique is being developed using S-parameters obtained from a VNA for the four primary compensation topologies, including S-S, S-P, P-S, and P-P, which are comparable to the responses achieved by stimulating Tx coils using practical power electronic converters. Additinally, the newly advanced measurement technique is employed in guaging the performance of designs evolved in SO-B.

Furthermore, SO-B involves the author contribution in a sequential evolutionary process (EP) aimed for designing Tx-Rx coil antennas using the field-forming technique, as outlined below:

**SO-B:**

**EP-1**: Exploring 3D Tx coil antennas to create a uniform magnetic field to address the issues of lateral misalignment.

**EP-2**: Studying singular planar distributed turn coil antennas to achieve maximum uniformity in the magnetic field distribution in the Rx region, thereby addressing the lateral misalignment issue without compromising the Q-factor.

**EP-3**: Creating an analytical framework to achieve an optimal magnetic field distribution with the objective of inducing uniform voltage despite the lateral misalignment of the Rx coil antenna

(a)



(b)
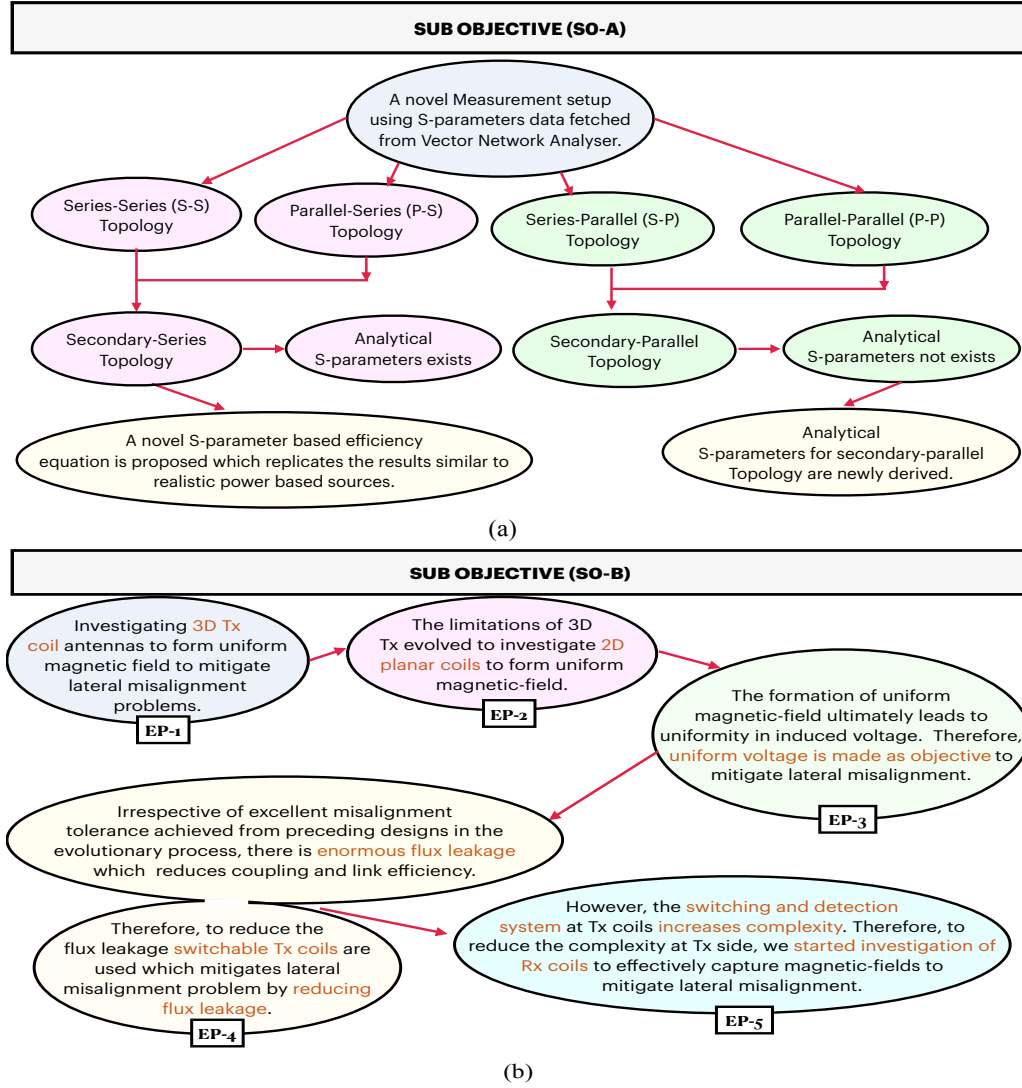
Figure 1.7: Visual representation of the tasks performed in (a) sub-objective A and (b) sub-objective B.

**EP-4**: Leveraging the potential to incorporate switching circuits integrated with multiple coils to improve lateral misalignment tolerance while reducing the posibilities of undesired flux leakage.

**EP-5**: Evaluating a 3D Rx coil antenna to capture the vertical and horizontal magnetic-field components present in the Rx coil region with the aim of inducing uniform voltage despite lateral misalignment.

The accomplishments of the sub-objectives mentioned earlier are summarized in Table 1.1.

Table 1.1: Targets achieved through this thesis work.

| Sub-Objective A (SO-A) | | | |
|---|---|---|---|
| Outcomes | S-parameters newly derived | New Measurement, setup using VNA, | Potential to generate realistic responses |
| Series-Series | - | ✓ | ✓ |
| Parallel-Series | - | ✓ | ✓ |
| Series-Parallel | ✓ | × | × |
| Parallel-Parallel | ✓ | × | × |
| **Sub-Objective B (SO-B)** | | | |
| Outcomes | lateral misalignment | 3D or Planar | Flux-control | Detection-unit |
| Design-1A (EP-1) | ✓ | 3D Tx coil | × | N.R |
| Design-1B (EP-2) | ✓ | Planar Tx coil | × | N.R |
| Design-1C (EP-3) | ✓ | Planar Tx coil | × | N.R |
| Design-2A (EP-4) | ✓ | Planar Tx coil | ✓ | ✓ |
| Design-2B (EP-4) | ✓ | Planar Tx coil | ✓ | ✓ |
| Design-3    (EP-5) | ✓ | 3D Rx coil | ✓ | N.R |

**Note:**
✓ denotes targets achieved, × denotes targets not achieved, − denotes targets already achieved in Literature works, N.R denotes Not Required

## 1.4  Thesis Outline

- **Chapter 1**: This chapter covers the fundamentals of the near-field wireless power transfer system, outlines various research challenges associated with the system, and then pinpoint the most challenging issue and aims to focus on it. Subsequently, existing solutions in the literature are thoroughly scrutinized.

- **Chapter 2**: This chapter explores the fundamental mathematics that underpin the field-forming technique and offers a thorough circuit analysis of several compensation topologies along with their respective block diagrams. Additionally, the thesis work's design process is briefly outlined by replicating the results of a conventional literature Tx coil antenna. Finally, a design methodology is presented for selecting optimal Tx coil parameters to achieve maximum efficiency when the Rx coil antenna is perfectly aligned.

- **Chapter 3**: In this chapter, we present a new S-parameter-based efficiency equation for compensation topologies, such as series-series, series-parallel, parallel-series, and parallel-parallel, which enables us to conduct experiments using VNA. The proposed equation accomplishes the objectives outlined in SO-A and provides a more accurate measurement of efficiency compared to traditional methods. Moreover, the newly developed measurement technique is employed to determine realistic efficiency values in the designs that are presented in subsequent chapters.

- **Chapter 4**: In this chapter, the author focus on resolving the challenge of lateral

misalignment in WPT system aiming to produce a uniform voltage at the misaligned receiving coil by utilizing single port Tx coils. To achieve this objective, the scholar investigate the use of 3D Tx coils, planar distributed coil antennas, and array coil antennas. These approaches are analyzed using an field forming technique using MMSE-based algorithm, addressing the objectives outlined in EP-1, EP-2, and EP-3 of SO-B.

- **Chapter 5**: The aim of this chapter is to address the issue of lateral misalignment in near-field resonant WPT system by reducing magnetic flux leakage using multi-port Tx coil antennas. By integrating switchable circuits and detection coils with these antennas, the scholar discuses the design procedure to accomplish the proposed objectives in EP-4 of SO-B, as illustrated in Figure 1.7(b).

- **Chapter 6**: The focus of this chapter is to investigate receiver coil antennas with the goal of capturing all magnetic-field components to generate a uniform voltage despite lateral misalignment. This investigation is aligned with the objectives proposed in EP-5 of SO-B.

- **Chapter 7**: This chapter performs a comparative analysis of all the suggested approaches in the present study and draws overall conclusions for the thesis. It also explores the potential for future developments in order to enhance the proposed works.

# Chapter 2

# Theoretical Background of MRC-Based WPT System

In order to achieve the objectives outlined in the previous chapter, it is essential to have a clear understanding of the theory underlying the resonant near-field WPT system. Therefore, to provide a more comprehensive understanding of the mathematical analysis and implementation of the MRC-WPT system, the theoretical analysis has been divided into two parts.

The first part of the analysis focuses on the magnetic field distribution of a square coil, the derivation of induced voltage using Faraday's Law of Electromagnetic Induction, and the determination of $M$ and PTE using circuit laws. The author has demonstrated the research methodology used in this thesis by reproducing the results of the previous best literary design using computational software, simulation software, fabricational facilities, and experimental setup available in the Antenna and Microwave Research (AMR) laboratory at the institute.

The second part of the theory extensively describes the design process for creating an efficient Tx coil antenna for a perfectly aligned Rx coil antenna based on the mathematical background developed in the first part. By following this approach, it is expected that the objectives outlined in the previous chapter can be achieved more effectively.

## 2.1 PART-1: Mathematical analysis of WPT system

### 2.1.1 Magnetic-field, induced voltage and mutual inductance formulations

Using magnetostatics, the equations for the magnetic fields of the $H_x$, $H_y$, and $H_z$ components of a single-turn square coil with a side length of $2a$ carrying current of $I_T$, illustrated in Figure 2.1, have been derived in [80]. The equations are presented below:

$$H_x = \frac{I_T}{4\pi} \sum_{n=1}^{4} \left[ \frac{(-1)^{n+1}h}{r_n(r_n + P_n)} \right], \tag{2.1}$$

$$H_y = \frac{I_T}{4\pi} \sum_{n=1}^{4} \left[ \frac{(-1)^{n+1}h}{r_n(r_n + (-1)^{n+1}Q_n)} \right], \tag{2.2}$$

$$H_z = \frac{I_T}{4\pi} \sum_{n=1}^{4} \left[ \frac{(-1)^n P_n}{r_n[r_n + (-1)^{n+1} Q_n]} - \frac{Q_n}{r_n[r_n + P_n]} \right]. \tag{2.3}$$

$$Q_1 = -Q_4 = a + x - x_t, \quad Q_2 = -Q_3 = a - x + x_t,$$
$$P_1 = P_2 = a + y - y_t, \quad P_3 = P_4 = -a + y - y_t.$$

The equations utilize the variables $r_1$, $r_2$, $r_3$, and $r_4$, which represent the distances between the corners of the square loop and the observation point $O(x, y, h)$. The variables $Q_1$, $Q_2$, $Q_3$, and $Q_4$ and $P_1$, $P_2$, $P_3$, and $P_4$ are defined in the following manner: The subsequent
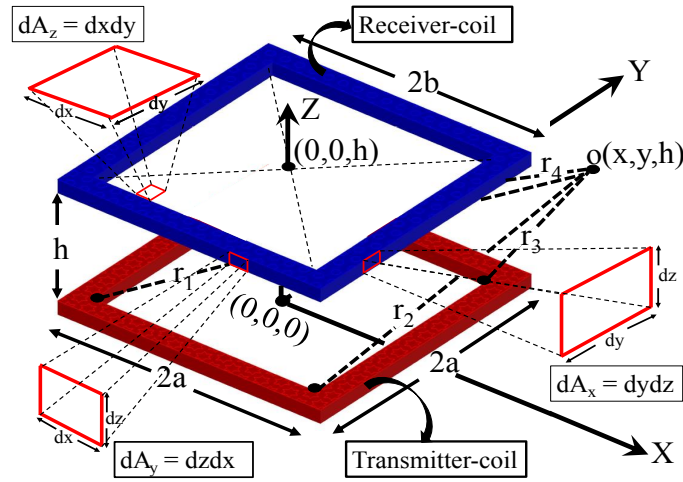


Figure 2.1: General Tx-Rx coil geometric configuration.

step involves calculating the induced voltage in the square-shaped Rx coil at angular operating frequency $\omega = 2\pi f$, which has a side length of $2b$, a transfer distance of $h$. Due to $H_x$, $H_y$, and $H_z$ present in the Rx plane a differential voltage $dV$ is induced in a differential area $dA_x$, $dA_y$, and $dA_z$. Since, the differential area are infinitesimally small, the magnetic field components along x, y, and z can be assumed constant within $dA_x$, $dA_y$, and $dA_z$. Utilizing Faraday's law of electromagnetic induction [81] the differential induced voltage equation is presented as

$$dV = -\frac{d\phi}{dt} = -\frac{d}{dt}(\mu_o \vec{H}.\vec{dA}) = -j\omega\mu_o[H_x dA_x + H_y dA_y + H_z dA_z], \tag{2.4}$$

where, $\mu_o$ is permeability in free space. The magnitude of total induced voltage $(V)$ for total number of turns $(N_r)$ concentrated at periphery of the Rx coil is given by integration of $dV$ over the area $dA$ as,

$$V = j\omega\mu_o N_r \left[ \iint_A \vec{H}.\vec{dA} \right] = j\omega\mu_o N_r \left[ \iint_{A_x} H_x dA_x + \iint_{A_y} H_y dA_y + \iint_{A_z} H_z dA_z \right], \tag{2.5}$$

For a co-axially positioned planar Rx coil with Tx coil the $dA_x$ and $dA_y$ becomes void and

the (2.5) can be modified as

$$V = j\omega\mu_o N_r \left[ \iint_A \vec{H} \cdot d\vec{A} \right] = j\omega\mu_o N_r \left[ \iint_{A_z} H_z dA_z \right], \tag{2.6}$$

Here, it is to be noted that the above induced voltage equation is valid only when $N_r$ turns are concentrated at the periphery of the Rx coil antenna. However, for equispaced Rx coil antenna for differential area $dA_{zi}$ for $i \in [1, N_r]$, the total induced voltage is evaluated as

$$V = \sum_{i=1}^{N_r} V_i(\Delta x, \Delta y) = j\omega\mu_o \sum_{i=1}^{N_r} \left[ \iint_{A_{zi}} H_z(x, y) dA_{zi} \right] \tag{2.7}$$

The mutual inductance $M$ is determined using equation (2.6) for helmoltz Rx coil and (2.7) for distributed Rx coil antenna, which is given by [82]:

$$M = \frac{V}{\omega I_T}. \tag{2.8}$$

Afterwards, the equations for PTE are mathematically derived for four different primary compensation topologies using circuit laws. These equations provide a mathematical representation of the behavior of the respective compensation topologies and help in analyzing their performance.

### 2.1.2   Power transfer efficiency evaluation using circuit analysis

The Figure. 2.2 shows the visual representation of distinct compensation topologies. These
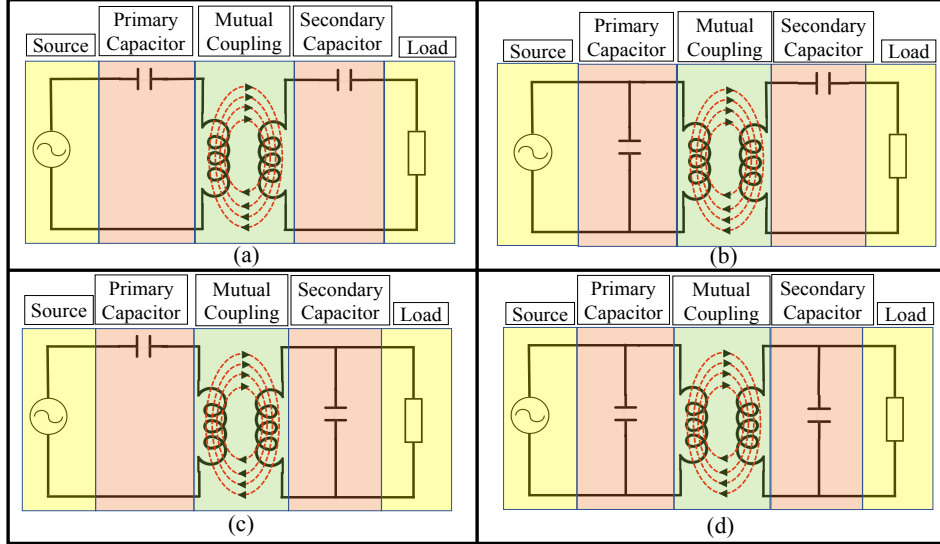


Figure 2.2: Compensation topologies (a) S-S, (b) P-S (c) S-P, and (d) P-P.

topologies, namely S-S, P-S, S-P, and P-P, enhance the performance of the WPT system in terms of PTE under different optimal load conditions.

The S-S compensation topology uses resonant capacitors that are independent of $M$ and load resistance. It is mainly used in dynamic wireless charging systems, which are prone to changes in $M$ and load resistances.

On the other hand, the compensation capacitors in S-P topology depend on $M$, making it less suitable for misalignment-prone applications. However, S-P topology requires significantly less secondary inductance, making it suitable for biomedical applications.

In contrast, the capacitors in P-S and P-P topologies depend on both $M$ and load resistance, limiting their use in many applications. Nonetheless, P-S and P-P find their use in low-power and loosely coupled applications.

## S-S Compensation Topology

Transforming the equivalent circuit to a T-network, as demonstrated in Figure. 2.3, simplifies the assessment of PTE for S-S compensation topology. The sinusoidal signal
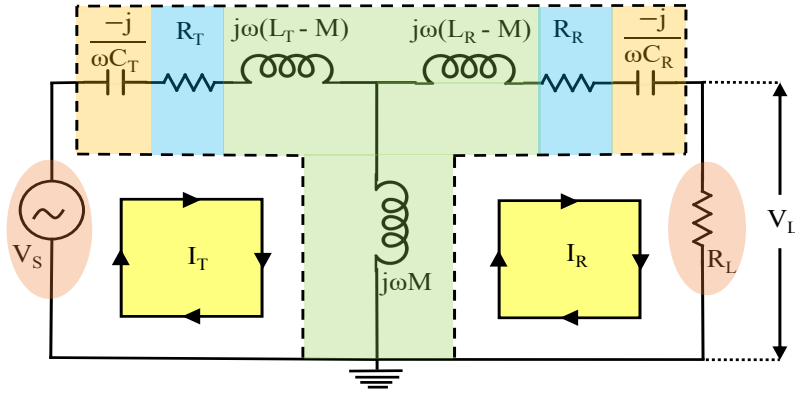


Figure 2.3: T-network equivalent circuit of WPT system for S-S topology.

source, $V_s$, supplies a signal at operating resonant frequency $f$ of the WPT system. In the circuit diagram, $R_T$, $R_R$, $L_T$, and $L_R$ represent the resistance and self-inductance of the Tx-Rx coils. Additionally, $C_T$ and $C_R$ signify the series compensation capacitors utilized to resonate the WPT system at $f$. $I_T$ and $I_R$ refer to the phasor currents circulating in the Tx-Rx coils, and the value of the load resistance, $R_L$, is dependent on the application scenario. By applying Kirchhoff's Voltage Law (KVL) in loop-1 and loop-2 of Figure. 2.3, the following equations are derived:

$$V_s = R_T I_T + (j\omega L_T - \frac{j}{\omega C_T})I_T - j\omega M I_R, \tag{2.9a}$$

$$j\omega M I_T = (j\omega L_R - \frac{j}{\omega C_R})I_R + (R_R + R_L)I_R. \tag{2.9b}$$

Let, $X_{S1} = (j\omega L_T - \frac{j}{\omega C_T})$ and $X_{S2} = (j\omega L_R - \frac{j}{\omega C_R})$. These terms, $X_{S1}$ and $X_{S2}$, represent the effective reactance of the series compensated Tx-Rx coils. By rearranging the terms

in (2.9b), we can formulate the relation between the currents in the Tx-Rx coils as:

$$I_R = \frac{j\omega M I_T}{R_R + R_L + X_{S2}}.$$ (2.10)

Thus, by substituting (2.10) into (2.9a), we can evaluate the current in the Tx coil in terms of the circuit parameters:

$$I_T = \frac{V_s(R_R + R_L + X_{S2})}{(R_T + X_{S1})(R_R + R_L + X_{S2}) + (\omega M)^2}.$$ (2.11)

Similarly, the Rx coil current is obtained by substituting (2.11) in (2.10) as

$$I_R = \frac{j\omega M V_s}{(R_T + X_{S1})(R_R + R_L + X_{S2}) + (\omega M)^2}.$$ (2.12)

Thus, the PTE is evaluated by determining the ratio of output power ($P_{out}$) and input power ($P_{in}$) as

$$\eta = \frac{P_{out}}{P_{in}} = \frac{P_{R_L}}{P_{R_T} + P_{R_R} + P_{R_L}}$$ (2.13)

Here, $P_{R_T} = I_T I_T^* R_T$ and $P_{R_R} = I_R I_R^* R_R$ denote the losses in the Tx-Rx coils, while $P_{R_L} = I_R I_R^* R_L$ represents the power consumed by the load. By examining (2.11) and (2.12), it is evident that the Tx-Rx coil currents share the same denominator. Therefore, the numerator values of power ratios in (2.13) become significant. As a result, the power ratios are evaluated under resonant system conditions, i.e., $X_{S1} = X_{S2} = 0$, as follows:

$$\begin{aligned}
P_{R_T} : P_{R_R} : P_{R_L} &= I_T I_T^* R_T : I_R I_R^* R_R : I_R I_R^* R_L \\
&= (R_R + R_L)^2 R_T : (\omega M)^2 R_R : (\omega M)^2 R_L.
\end{aligned}$$ (2.14)

The substitution of equation (2.12) into $P_{R_R} = I_R I_R^* R_R$ yields the expression for the output power as

$$P_{R_R} = \frac{\omega^2 M^2 V_s^2 R_L}{[R_T(R_R + R_L) + \omega^2 M^2]^2}.$$ (2.15)

Furthermore, by substituting the values obtained from Equation (2.14) in Equation (2.13), the PTE expression for S-S topology ($\eta_{ss}$) is obtained as

$$\eta_{ss} = \frac{(\omega M)^2 R_L}{R_T(R_R + R_L)^2 + (\omega M)^2(R_R + R_L)}.$$ (2.16)

The mathematical representation of the PTE equation for a S-S resonant WPT system is denoted by equation (2.16) and is equivalent to the expression given in [1].

### P-S Compensation Topology

The Figure. 2.4 represents the T-network equivalent representation used for computing PTE for P-S compensation topology. By connecting a capacitor ($C_T$) in parallel to the Tx-coil, an additional reactive current $I_C$ is stressed to generate by the voltage source, as
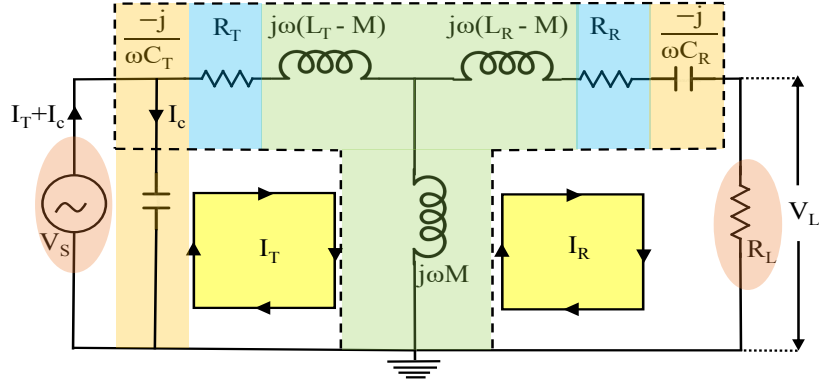
Figure 2.4: T-network equivalent circuit of WPT system for P-S topology.

shown in Figure. 2.4. KVL is then applied at loop-1 and loop-2, resulting in the following equations:

$$V_s = (R_T + j\omega L_T)I_T - j\omega M I_R, \tag{2.17a}$$

$$j\omega M I_T = X_{S2}I_R + (R_R + R_L)I_R. \tag{2.17b}$$

Thus, the relationship between the currents in the Tx-Rx coils is formulated by rearranging the terms in (2.17b), following the same approach as in (2.10). The current in the Tx coil can then be evaluated by substituting (2.10) in (2.17a) as,

$$I_T = \frac{V_s(R_R + R_L + X_{S2})}{(R_T + j\omega L_T)(R_R + R_L + X_{S2}) + (\omega M)^2}. \tag{2.18}$$

To obtain the current in the Rx coil, (2.18) is substituted in (2.10) as,

$$I_R = \frac{j\omega M V_s}{(R_T + j\omega L_T)(R_R + R_L + X_{S2}) + (\omega M)^2} \tag{2.19}$$

The power ratios are evaluated under the resonant system condition, and the resulting expression is found to be same as (2.14). Hence, the PTE for P-S Topology is equivalent to that of S-S Topology, as derived in (2.16) (i.e., $\eta_{ss} = \eta_{ps}$).

### S-P Compensation Topology

Figure. 2.5 shows the T-network equivalent circuit of the S-P topology. However, the analysis of the Rx parallel topology becomes complicated due to the parallel connection of the capacitor $C_R$ and $R_L$. Therefore, to simplify the analysis, the parallel combination of $C_R$ and $R_L$ is resolved to obtain the effective impedance $Z_{L_{eff}}$ as,

$$Z_{L_{eff}} = \frac{R_L}{1 + (\omega C_R R_L)^2} - \frac{j\omega C_R R_L^2}{1 + (\omega C_R R_L)^2}. \tag{2.20}$$

In (2.20), the effective parallel resistance $R_{L_{eff}}$ and effective parallel reactance $X_{L_{eff}}$ are
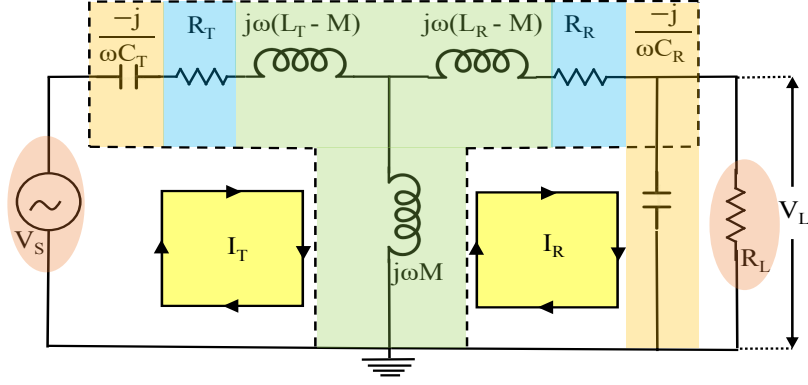
Figure 2.5: Equivalent circuit of T-network WPT system for S-P topology.

obtained as real and imaginary part of $Z_{L_{eff}}$, respectively. Consequently, by applying KVL in loop-1 and loop-2, the equations are formulated as

$$V_s = (R_T + X_{S1})I_T - j\omega M I_R, \tag{2.21a}$$

$$j\omega M I_T = j(\omega L_R - X_{L_{eff}})I_R + (R_R + R_{L_{eff}})I_R. \tag{2.21b}$$

Let $X_{P2} = (j\omega L_R - jX_{L_{eff}})$ is denoted as effective compensated reactance of parallel capacitor Rx coil. Thereby, rearranging the (2.21b), the relation between Tx-Rx coil currents is derived as,

$$I_R = \frac{j\omega M I_T}{R_R + R_{L_{eff}} + X_{P2}}. \tag{2.22}$$

Now by substituting (2.22) in (2.21a), current in the Tx coil is evaluated as,

$$I_T = \frac{V_s(R_R + R_{L_{eff}} + X_{P2})}{(R_T + X_{S1})(R_R + R_{L_{eff}} + X_{P2}) + (\omega M)^2}. \tag{2.23}$$

Now (2.23) is substituted in (2.22) to determine current in the Rx coil as

$$I_R = \frac{j\omega M V_s}{(R_T + X_{S1})(R_R + R_{L_{eff}} + X_{P2}) + (\omega M)^2} \tag{2.24}$$

The ratio of powers are evaluated under resonant condition i.e., $X_{S1} = X_{P2} = 0$ as

$$P_{R_T} : P_{R_R} : P_{R_{L_{eff}}} = (R_R + R_{L_{eff}})^2 R_T : (\omega M)^2 R_R : (\omega M)^2 R_{L_{eff}}. \tag{2.25}$$

The PTE definition of S-P topology slightly varies compared to (2.13) as

$$\eta = \frac{P_{out}}{P_{in}} = \frac{P_{R_{L_{\text{eff}}}}}{P_{R_T} + P_{R_R} + P_{R_{L_{\text{eff}}}}}. \tag{2.26}$$

It is worth noting from (2.26) that in the S-P topology, the load power ($P_{L_{eff}}$) is not only dependent on $R_L$, but also on the effective load resistance $R_{L_{eff}}$ as given in (2.20).

This effective load power also takes into account the additional loading effect caused by the discharge current of $C_R$ to $R_L$, which is dependent on the physical values of $f$ and $C_R$. Consequently, the PTE of the S-P topology ($\eta_{sp}$) is obtained by substituting (2.25) in (2.26), yielding:

$$\eta_{sp} = \frac{(\omega M)^2 R_{L_{eff}}}{R_T(R_R + R_{L_{eff}})^2 + (\omega M)^2(R_2 + R_{L_{eff}})}. \tag{2.27}$$

### P-P Compensation Topology

The T-network equivalent circuit for the P-P topology is illustrated in Figure. 2.6. The effective load impedance is transformed due to the parallel connection of primary and secondary compensation capacitors $C_T$ and $C_R$ to Tx-Rx coils, as shown in (2.20). It is noteworthy to mention that the source in the primary side generates an additional reactive current $I_C$, similar to the P-S compensation topology. KVL is applied in loop-1 and loop-2 to derive the following equations:

$$V_s = (R_T + j\omega L_T)I_T - j\omega M I_R, \tag{2.28a}$$

$$j\omega M I_T = X_{P2}I_R + (R_R + R_{L_{eff}})I_R. \tag{2.28b}$$

The relationship between Tx-Rx currents in P-P topology is same as that of S-P topology
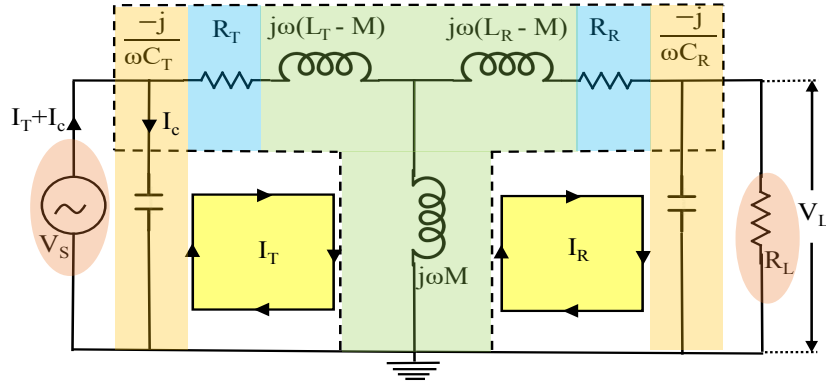


Figure 2.6: Equivalent circuit of T-network WPT system for P-P topology.

which is given in equation (2.22). Substituting this relationship in (2.28a) yields the current in the Tx coil:

$$I_T = \frac{V_s(R_R + R_{L_{eff}} + X_{P2})}{(R_T + j\omega L_T)(R_R + R_{L_{eff}} + X_{S2}) + (\omega M)^2}. \tag{2.29}$$

Substitution from (2.29) in (2.22) gives current in the Rx coil as

$$I_R = \frac{j\omega M V_s}{(R_T + j\omega L_T)(R_R + R_{L_{eff}} + X_{P2}) + (\omega M)^2}. \tag{2.30}$$

The power ratios are determined under the resonant system condition and are found to be identical to (2.25). Thus, the PTE of the P-P topology is equivalent to the S-P topology as shown in (2.27) (i.e., $\eta_{sp} = \eta_{pp}$). Table 2.1 presents a summary

Table 2.1: Comparison of PTE equations of various compensation topologies

| Compensation Topology | PTE |
|---|---|
| Series-Series | $\eta_{ss} = \frac{(\omega M)^2 R_L}{R_T(R_R+R_L)^2+(\omega M)^2(R_2+R_L)}$ |
| Parallel-Series | $\eta_{ps} = \frac{(\omega M)^2 R_L}{R_T(R_R+R_L)^2+(\omega M)^2(R_2+R_L)}$ |
| Series-Parallel | $\eta_{sp} = \frac{(\omega M)^2 R_{L_{eff}}}{R_T(R_R+R_{L_{eff}})^2+(\omega M)^2(R_2+R_{L_{eff}})}$ |
| Parallel-Parallel | $\eta_{pp} = \frac{(\omega M)^2 R_{L_{eff}}}{R_T(R_R+R_{L_{eff}})^2+(\omega M)^2(R_2+R_{L_{eff}})}$ |

of various compensation topologies based on the PTE expressions derived from circuit theory. The formulas listed in Table 2.1 suggest that the (S-S and P-S pair) and (S-P and P-P pair) have identical PTE equations. Therefore, PTE analysis of the four compensation topologies can be simplified into two configurations, namely secondary series and secondary parallel topologies, specifically for PTE analysis. Alternatively, for researchers utilizing a VNA-based experimental setup, the PTE can also be calculated by obtaining S-parameters. The mathematical computation of PTE based on S-parameters in previous literature is available only for the SS compensation topology, as follows:

### 2.1.3  Computation of S-parameter based efficiency for secondary-series topology

The evaluation of S-parameter based efficiency ($\eta_{s-conventional}$) is derived utilising the two-port S-parameter network shown in Figure. 2.7 . The Device Under Test (DUT)
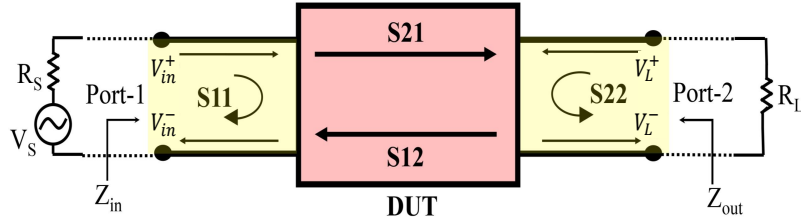


Figure 2.7: A two-port S-parameter network for $\eta_{s-conventional}$ evaluation.

comprises Tx-Rx coils where $V_s$ is applied on port-1 and $V_L$ is obtained at port-2, as depicted in Figure 2.7. The incident and reflected voltages at port-1 and port-2 are denoted by $V_{in}^+$, $V_{in}^-$, $V_L^+$, and $V_L^-$, respectively. Moreover, $R_s$ denotes the source impedance of the

supply. The input-output port voltage relationships are as follows:

$$V_s = V_{in}^+ + V_{in}^-, \ I_T = \frac{V_{in}^+ - V_{in}^-}{R_s}, \tag{2.31a}$$

$$V_s = I_1 Z_{in} = \frac{V_{in}^+ - V_{in}^-}{R_s} Z_{in}, \tag{2.31b}$$

$$V_L = V_L^+ + V_L^-, \ I_R = \frac{V_L^+ - V_L^-}{R_L}, \tag{2.31c}$$

$$V_L = I_2 Z_{out} = \frac{V_L^+ - V_L^-}{R_L} Z_{out}. \tag{2.31d}$$

Where $Z_{in}$ and $Z_{out}$ are input-output impedance which are obtained by solving (2.31b) and (2.31d) as

$$S11 = \frac{V_{in}^-}{V_{in}^+} = \frac{Z_{in} - R_s}{Z_{in} + R_s}, \tag{2.32a}$$

$$S22 = \frac{V_L^-}{V_L^+} = \frac{Z_{out} - R_L}{Z_{out} + R_L}. \tag{2.32b}$$

Where, $S11$ and $S22$ are reflection coefficients at port-1 and port-2. Moreover, $Z_{in}$ is evaluated by re-arranging (2.11) by replacing $X_{S1} = X_{S2} = 0$ under resonance to $\frac{V_s}{I_T}$ by discarding the effect of $R_s$ as

$$Z_{in} = R_T + \frac{\omega^2 M^2}{R_R + R_L}. \tag{2.33}$$

As, the WPT system is reciprocal, therefore, $Z_{out}$ is formulated similarly as

$$Z_{out} = R_R + \frac{\omega^2 M^2}{R_T + R_s}. \tag{2.34}$$

Substituting (2.33) in (2.32a) and simplifying the equation, the reflection coefficient at port-1 is given as

$$S11 = \frac{(R_T - R_s)(R_R + R_L) + \omega^2 M^2}{(R_T + R_s)(R_R + R_L) + \omega^2 M^2}. \tag{2.35}$$

Similarly, reflection coefficient at port-2 is calculated by substituting (2.34) in (2.32b) as

$$S22 = \frac{(R_T + R_s)(R_R - R_L) + \omega^2 M^2}{(R_T + R_R)(R_R + R_L) + \omega^2 M^2} \tag{2.36}$$

Equations (2.35) and (2.36) provide the expressions for $S11$ and $S22$ parameters of the R-WPT system in terms of circuit parameters. Additionally, the voltage gain ($S21$-parameter) is defined as shown in Figure 2.7.

$$S21 = \frac{V_L^-}{V_{in}^+}\bigg|_{V_L^+ = 0}. \tag{2.37}$$

The $\frac{V_L}{V_s}$ in terms of incident and reflected voltage signals is formulated as

$$\left.\frac{V_L}{V_s}\right|_{V_L^+=0} = \left.\frac{V_L^+ + V_L^-}{V_{in}^+ + V_{in}^-}\right|_{V_L^+=0} = \frac{V_L^-}{V_{in}^+(1+S11)} \tag{2.38}$$

By substituting (2.35) in (2.38) and comparing with the voltage gain using the circuit equations derived for series-series topology , the $S21$-parameter is formulated as

$$S21 = \frac{j2\omega M R_L}{(R_T + R_s)((R_R + R_L) + \omega^2 M^2)}. \tag{2.39}$$

Since R-WPT is a reciprocal network, the $S21$ and $S12$ parameters are identical. The $\eta_{s-conventional}$, which is a function of S-parameters, can be broadly categorized into transducer and power gain. The transducer gain is obtained by designing an L-section matching network for conjugate matching at the input-output ports. This nullifies the reflection coefficients, and the magnitude of the $S21$-parameter [44] alone is sufficient to evaluate $\eta_{s-conventional}$. On the other hand, the power gain is measured by allowing discontinuity in the input port impedance and compensating for the reactive component of the Tx-Rx coils. Hence, both $S21$ and $S11$ parameters are used to estimate the power gain. By incorporating the reflection loss at the source side, the conventional S-parameter-based efficiency is derived as

$$\eta_{s-conventional} = \frac{|S21|^2}{1 - |S11|^2} \times 100. \tag{2.40a}$$

The (2.35) and (2.39) are substituted in (2.40a) to obtain $\eta_{s-conventional}$ in terms of circuit parameters as

$$\eta_{s-conventional} = \frac{\omega^2 M^2 R_L}{R_T(R_R + R_L)^2 + \omega^2 M^2(R_R + R_L)}. \tag{2.40b}$$

Upon comparing equations (2.16) and (2.40b), it becomes clear that the circuit-based efficiency and S-parameter-based efficiency are identical when $R_s = 0$.

The necessary mathematical formulations and analyses required to assess the performance of a resonant WPT system have been established. As a result, the researcher employs the equations derived from field theory and circuitry laws mentioned previously to reproduce the results of the best design in the literature [1]. This approach helps to acquaint the research methodology adopted in this thesis work.

## 2.2    Design procedure of conventional literature design

The objective of the design described in [1] is to solve the issue of lateral misalignment by creating a uniform magnetic field distribution in the region of the Rx coil. The optimal parameters of Tx coil are achieved by performing parametric variation of design variables of Tx coil. The geometrical parameters of the conventional literature design can be obtained

from [1] and the layout is depicted in Figure. 2.8.
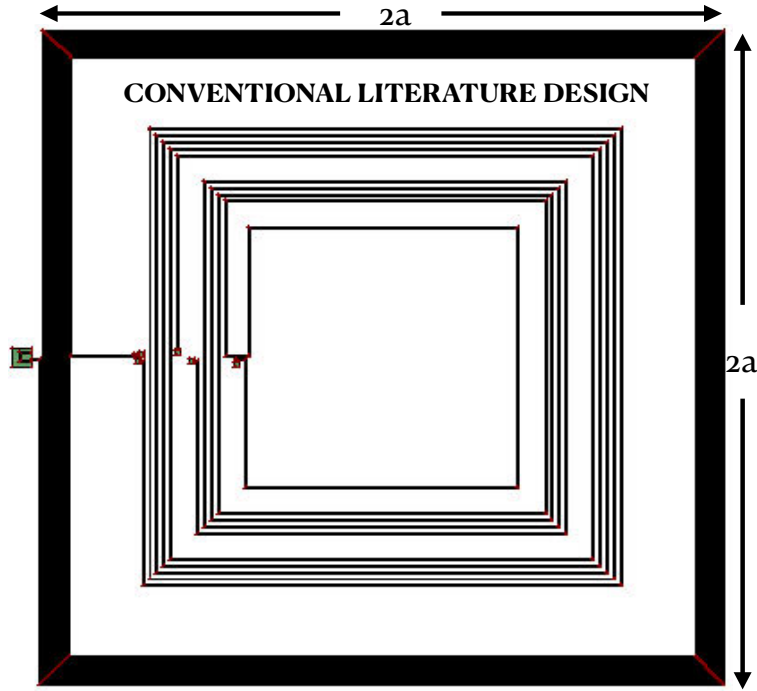


Figure 2.8: Layout of conventional literature design.

### 2.2.1   Analytical Results

The analytical values of the 3D magnetic field distribution for the optimal Tx coil parameters obtained from parametric optimization is determined by employing equation (2.3) in MATLAB software. The resulting field distribution is illustrated in Figure 2.9(a). Additionally, the scholar mathematically determined the values of $V$ and $M$ for various misalignment positions ($\Delta x$, $\Delta y$) of the Rx coil by employing equations (2.6) and (2.8), respectively. The results are shown in Figure. 2.9(b) and Figure. 2.9(c).
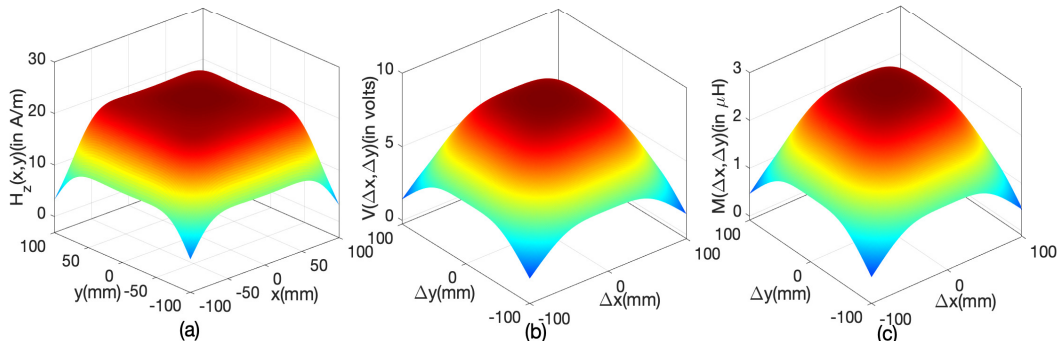


Figure 2.9: Analytical 3D distribution of literature design for (a) Magnetic field, (b) Induced voltage, and (c) Mutual Inductance.

### 2.2.2   Simulation Results

The design layout presented in [1] is additionally simulated using the ANSYS HFSS EM simulator to validate the previous analytical results. Due to the significant time required to complete the simulation, the Rx coil is only displaced along $\Delta y = 0$ with a fixed interval of 10 mm within the range of $\Delta x \in [-100, 100]$ mm. The simulated magnetic field, $V$, and $M$ results are consistent with the analytical results, as depicted in Figure. 2.10. Additionally,
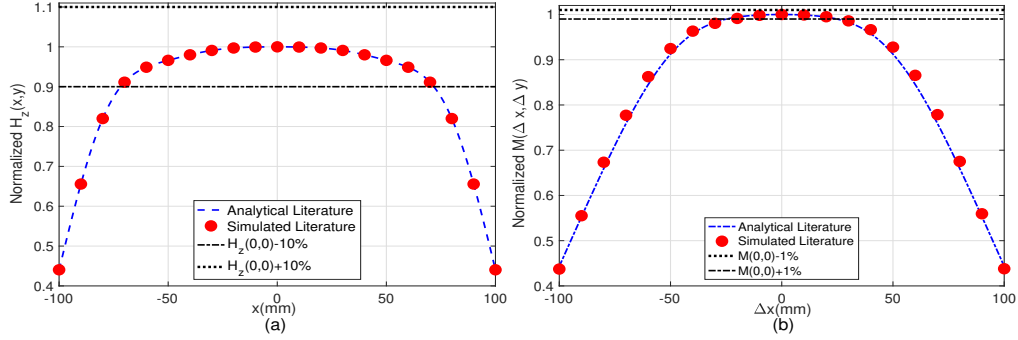


Figure 2.10: Simulated 2D distribution of literature design at $\Delta y = 0$ (a) Magnetic field, and (b) Mutual Inductance.

the Figure 2.10 illustrates the limits for magnetic-field and mutual inductance which are represented by $H_z(0,0) \pm 10\%$, and $M(0,0) \pm 1\%$. These limits are utilized to evaluate $\text{UF}(H_z(x,y))$ and $\text{UF}(\text{M}(\Delta x, \Delta y))$ as earlier defined in subsection 1.2.5.

### 2.2.3   Measurement Results

The process of creating the literary design involves the utilization of a MITS prototyping machine on an FR4 substrate at an in-house fabrication facility. An image of this design is shown in the inset of Figure. 2.11. To accurately measure and obtain data of magnetic
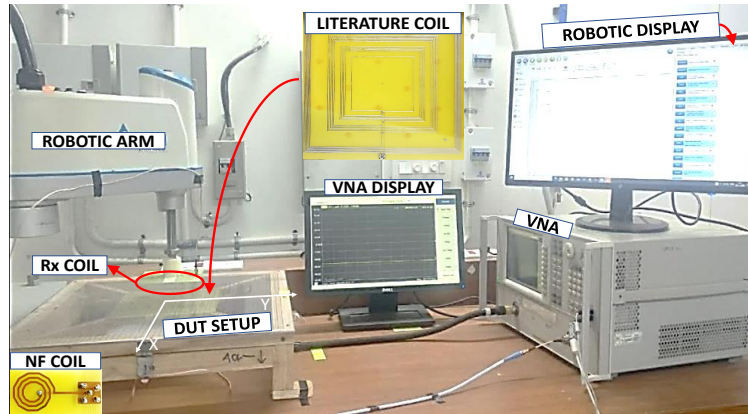


Figure 2.11: Fabricated literature design and experimental setup

fields and circuit parameters such as $M$, $R_T$, and $R_R$, an experimental setup is present at the AMR lab. This setup includes a robotic arm capable of precisely and accurately

misaligning the Rx coil to desired locations, a VNA for fetching the S-parameter data, and a near-field (NF) coil for tracing the magnetic-field profile. In order to obtain $P_{R_R}$ and $\eta_{ss}$, the measured circuit parameters are substituted into equations (2.15) and (2.16). The graphical results for the measured magnetic field, $M(\Delta x, \Delta y)$, $P_{R_R}(\Delta x, \Delta y)$, and $\eta_{ss}(\Delta x, \Delta y)$ are presented in Figure. 2.12. Moreover, the uniformity factor of various
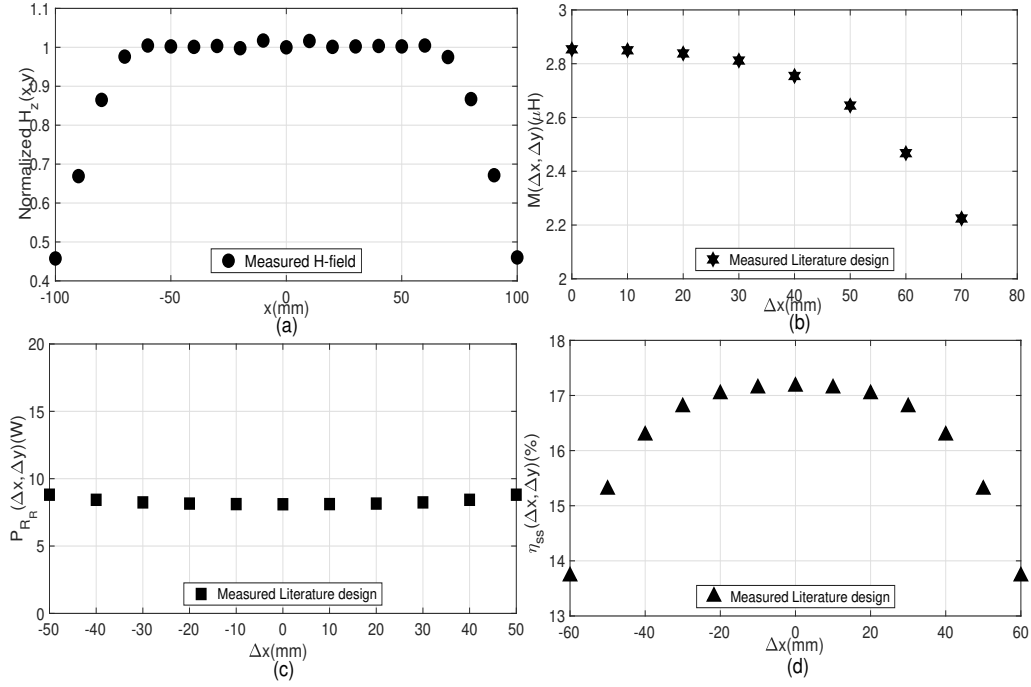


Figure 2.12: Experimental 2D distribution of literature design at $\Delta y = 0$ for (a) Magnetic field, (b) Mutual Inductance, (c) Load power, and (d) Efficiency.

performance parameters of the conventional literature design have been listed in Table 2.2.

Table 2.2: Misalignment performance metric of the design presented in [1]

| Parameter | Conventional Literature Design |
|:---:|:---:|
| $\text{UF}(H_z(x,y))$ | 51.84% |
| $\text{UF}(M(\Delta x, \Delta y))$ | 6.25% |
| $\text{UF}(P_{R_R})$ | 3.61% |

## 2.3 PART-2: Design Methodology of Selecting Tx coil Parameters

The mathematical foundation of resonant WPT system and effective utilization of the available tools is explicitly demonstrated by replicating the outcomes of literary design in the part-1. Following this, the enhancement of PTE for a perfectly aligned Rx coil is

discussed by optimizing the Tx coil antenna. The design procedure of Tx coil antenna parameters is sequentially outlined as follows:

### 2.3.1    Selection of transfer distance $h$

The $h$ between Tx-Rx coils is broadly selected based on the application scenario. Wherein for the biomedical implants (low power applications) $h$ ranges in $[10, 30]$ mm [83, 84, 85]. Whereas for mobile and portable devices (medium power applications), the transfer distance is generally fixed at $h = 50$ mm [1, 65]. Similarly, the transfer distance in drones (medium power applications) is normally rooted at $h = 50$ mm [79, 27]. Additionally, the transfer distance for electric vehicles (high power applications) ranges in $[100, 200]$ mm [86, 87, 88]. The scholar have selected a medium power application scenario to illustrate the design process. Thereby, the transfer distance is selected as $h = 50$ mm.

### 2.3.2    Selection of maximum side-length $2a$

The maximum side length, $2a$, is optimized by attaining the maximum magnetic field value at a specified $h$ (for example, at 50 mm in this case). To enhance the magnetic field at $h = 50$ mm, the analytical field equation presented in (2.3) at $O(0, 0, h)$ is differentiated with respect to $a$ as

$$\frac{\partial H_z}{\partial a} = \frac{16a(-a^5 + (ah)^2 + h^4)}{(2a^2 + h^2)^{\frac{3}{2}}(a^2 + h^2)^2} = 0. \tag{2.41}$$

Solving the fifth order equation provided in (2.41), the five roots of $a$ are evaluated as

$$a_1 = 0, \qquad a_2 = \left(\frac{(1 - \sqrt{5})h^2}{2}\right)^{\frac{1}{2}},$$
$$a_3 = \left(\frac{(1 + \sqrt{5})h^2}{2}\right)^{\frac{1}{2}}, a_4 = -\left(\frac{(1 - \sqrt{5})h^2}{2}\right)^{\frac{1}{2}}, \tag{2.42}$$
$$a_5 = -\left(\frac{(1 + \sqrt{5})h^2}{2}\right)^{\frac{1}{2}}.$$

In this case, $a_1$, $a_2$, $a_3$, $a_4$, and $a_5$ represent the five roots of equation (2.41). Of all the roots, only $a_3$ is valid as the others are either zero, negative, or imaginary, which can not fit as physical dimensional values. Moreover, by substituting $h = 50$ mm in $a_3$ of equation (2.42), the value of $a$ is determined to be $a = a_3 = 63.6$ mm. Consequently, the maximum side length is obtained as $2a = 127.2$ mm. Additionally, the parametric variation of $2a$ with $H_z$ is presented graphically in Figure. 2.13(a). By observing Figure 2.13(a), it can be seen that the peak value of $H_z$ occurs at $(x = 0, y = 0, h = 50$ mm$)$ and is maximized at $2a = 127.2$ mm, which confirms the validity of the analytical findings presented in (2.41) and (2.42). Additionally, Figure 2.13(b) shows the 3D distribution of the magnetic field for a single Tx coil turn with $2a = 127.2$ mm at $h = 50$ mm.
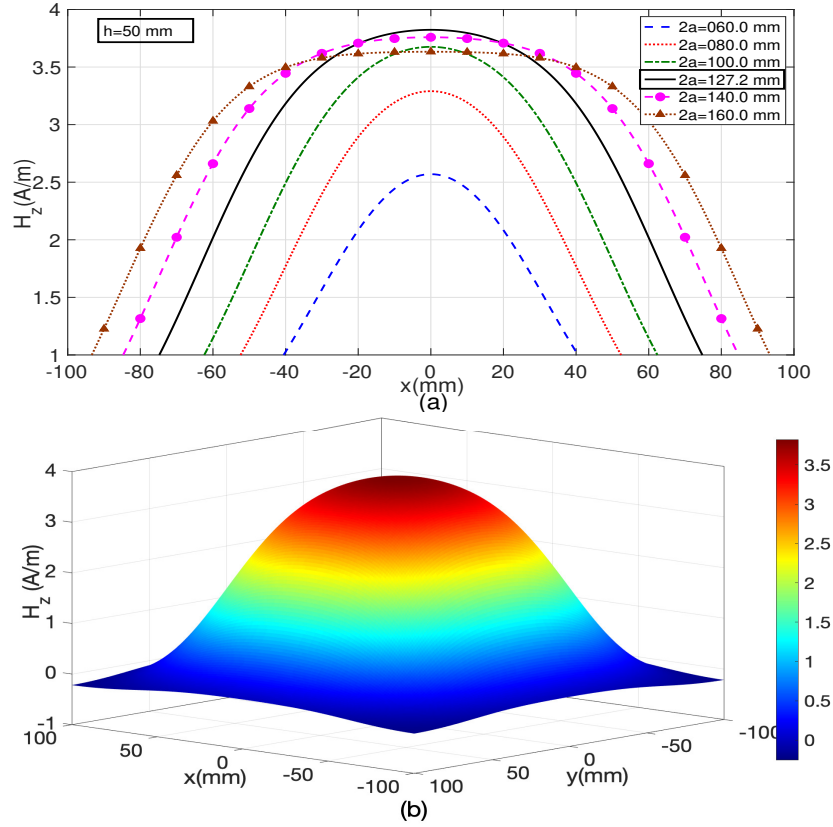
Figure 2.13: (a) Parametric variation of $2a$ with $H_z$, (b) 3D magnetic distribution for optimal $2a$.

### 2.3.3    Selection of number of turns $N_t$

The number of turns $N_t$ of square Tx coil antenna is optimized subject to ICNIRP guidelines (21 A/m or 27 $\mu$T) [89]. The value of $N_t$ is incremented until the peak value of the magnetic field reaches the ICNIRP limit of 21 A/m. The parametric variation of $N_t$ with magnetic field is displayed in Figure. 2.14. As shown in Figure 2.14, it is clear that the maximum value of the magnetic field occurs at $N_t = 5$. If $N_t$ is increased beyond this value, the ICNIRP limit will be exceeded, as demonstrated in Figure. 2.14.

### 2.3.4    Selection of operating frequency $f$

The $f$ is selected by maximizing the Q-factor using the EM simulator. The Q-factor of the Tx coil is given as $Q_T = \frac{\omega L_T}{R_T}$. Figure. 2.15 represents the variation of $f$ ranging in $[1, 20]$ MHz with $R_T$, $L_T$, and $Q_T$. Here, the $f$ is selected based on the maximum Q-factor using the data depicted in Figure. 2.15(c). The value of $R_T$ increases at higher values of $f$ due to skin and proximity effects, as shown in Figure. 2.15(a). Similarly the value of $L_T$ increases with $f$ as depicted in Figure. 2.15(b). The $Q_T$ as defined above is proportional to $L_T$, and inversely proportional to $R_T$. Therefore, the $L_T$ being dominant over $R_T$ at lower values of $f$, the $Q_T$ initially increases as seen from Figure. 2.15(c). However, after
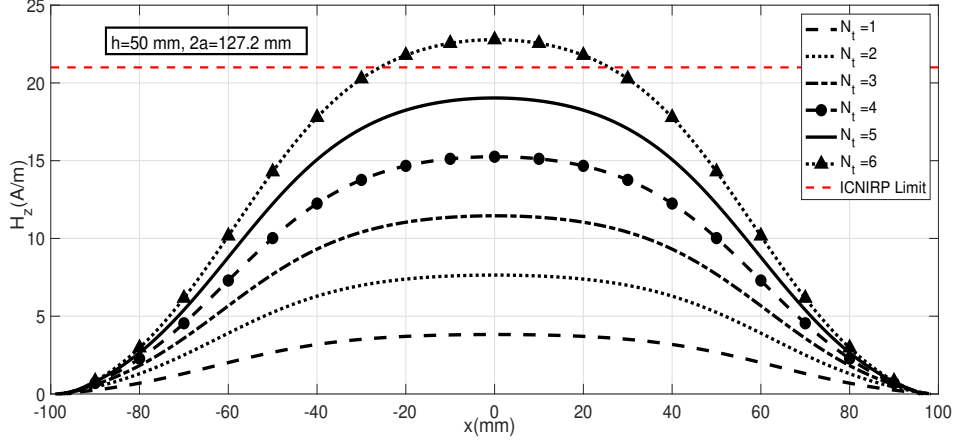
Figure 2.14: Parametric variation of $N_t$ with $H_z$.

reaching the maximum $Q_T$ at optimal $f$, the values of $R_T$ influences over $L_T$ which results in reduction of $Q_T$ as shown in Figure. 2.15(c). Moreover, the $Q_T$ values are plotted for distinct conductive tracks $w$. It is observed from Figure. 2.15(a) that increase in $w$ result in reduction of $R_T$ which augments the value of $Q_T$. Hence, it is always preferred to use large $w$ to operate at high $Q_T$. The optimal $f$ point ranges between $[12, 15]$ MHz from Figure. 2.15(c) considering all $w$. However, only Industrial, scientific and medical (ISM) frequency bands are acceptable to consider for research purposes. Here, the central frequency values of ISM are 6.78 MHz, 13.56 MHz, 27.12 MHz, 40.68 MHz etc. Therefore, the optimal $f$ is considered as 13.56 MHz at $w = 2$ mm. The summary of the above design procedure to develop a Tx coil antenna is provided in the flow chart as demonstrated in Figure. 2.16.

### 2.3.5   Rx coil selection

The Rx coil is selected based on the application scenario. The Rx coil parameters $2b$, and $N_r$ are optimized to attain user desired $V$. The application scenario selected in this work is intended for the medium power applications available in the test facility that requires a charging voltage ranging from $V \in [22.2 - 24]$ volts. Thereby, the parametric sweeping of the Rx coil is targeted to achieve the desired voltage range using the analytical equation given in (2.6). The parametric variation of $V$ with different dimensional values of $2b$ is shown in Figure. 2.17(a). Here, the Rx turns are fixed at $N_r = 1$ as further increase in it overshoots the desired $V$. Further, by observing the data shown in Figure. 2.17(a), the $2b$ value is optimized in the range $[112, 116]$ mm based on desired $V$ range. Here, the optimal Rx coil dimension is selected as $2b = 116$ mm. Moreover, the optimal 3D voltage profile distribution is plotted in Figure. 2.17(b).

### 2.3.6   Simulated Results of Resultant WPT system

The layout of resultant Tx-Rx coils is shown in Figure. 2.18 and the optimal dimensional
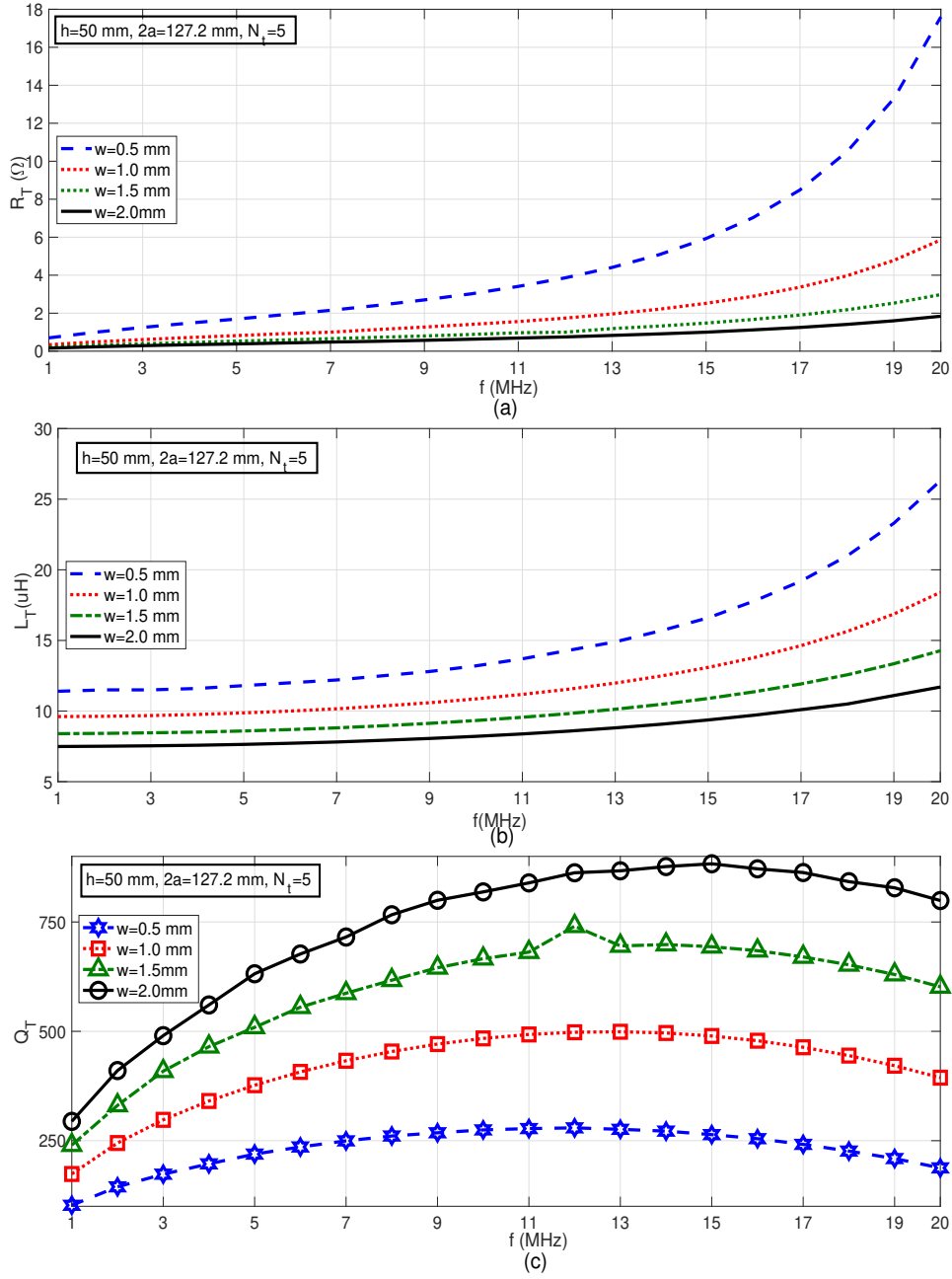
Figure 2.15: (a) Variation of $R_T$ with $f$ for different conductive track width, $w$, (b) variation of $L_T$ with $f$ for different conductive track width, $w$, (c) variation of $Q_T$ with $f$ for different conductive track width, $w$.

parameters are listed in Table 2.3. Moreover, the simulation results of magnetic field distribution corroborates with the analytical results as shown in Figure. 2.19. The input-output signals (both current and voltage) across different components of WPT system are determined through LT-Spice simulator. Further, using these signals the performance parameters such as output power ($P_{R_R}$), link efficiency ($\eta_{ss}$), and system
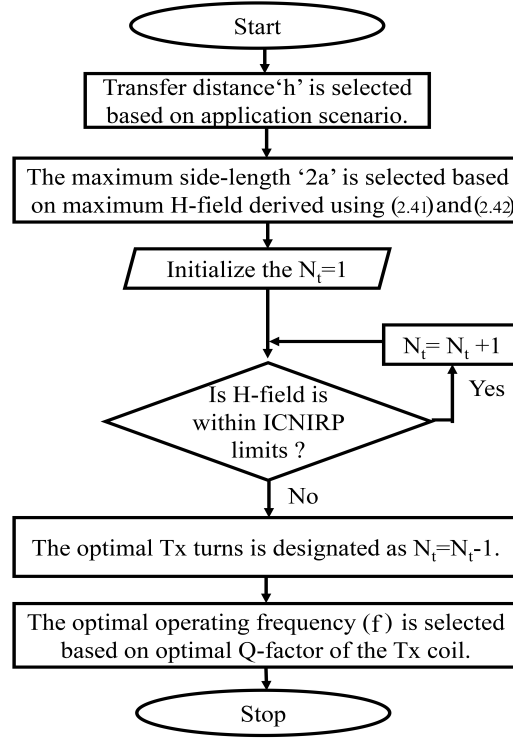
Figure 2.16: Flowchart for designing Tx Coil Antenna with Perfectly Aligned Rx Coil Antenna.

Table 2.3: The parameters of Tx-Rx coils

| **Physical dimensions of the Tx-Rx coils** | | | | | | |
|---|---|---|---|---|---|---|
| $2a/2b/h/w$ | 127.2 mm | / | 116 mm | / | 50 mm | / | 2 mm |
| $N_t/N_r/f$ | 5 | / | 1 | / | 13.56 MHz | | |

efficiency ($\eta_{dc-dc}$) are evaluated to test the quality of the resultant WPT system. The circuit simulation begins by knowing the circuit-parameters such as $R_T$, $R_R$, $L_T$, $L_R$, $M$, and coupling coefficient ($k$) which are obtained from EM simulator and are listed in Table 2.4. The circuit parameter values depicted in Table 2.4 are used in LT-Spice simulator as shown in Figure. 2.20. Here, in Figure. 2.20, the circuit schematic constitutes

Table 2.4: Circuit parameters of WPT system

| **Circuit parameters** | | | | | | |
|---|---|---|---|---|---|---|
| $R_T/R_R/L_T/L_R$ | 0.83$\Omega$ | / | 0.115$\Omega$ | / | 8.81$\mu$H | / | 0.43$\mu$H |
| $C_T/C_R/M/k$ | 15.63pF | / | 0.32nF | / | 0.31$\mu$H | / | 0.15 |

of input voltage $V_s = V_{in}$, full bridge inverter circuit consisting of four MOSFET switches, Tx-Rx coil parameters, full bridge AC-DC rectifier circuit composing of four diodes, filtering capacitor ($C_F$), and load resistance ($R_L$). The inverter is excited with $V_{in} = 36$ volts using a dc source. Thereby, the signal wave-forms such as Tx coil current $I_{Tx} = \frac{I_T}{\sqrt{2}}$,
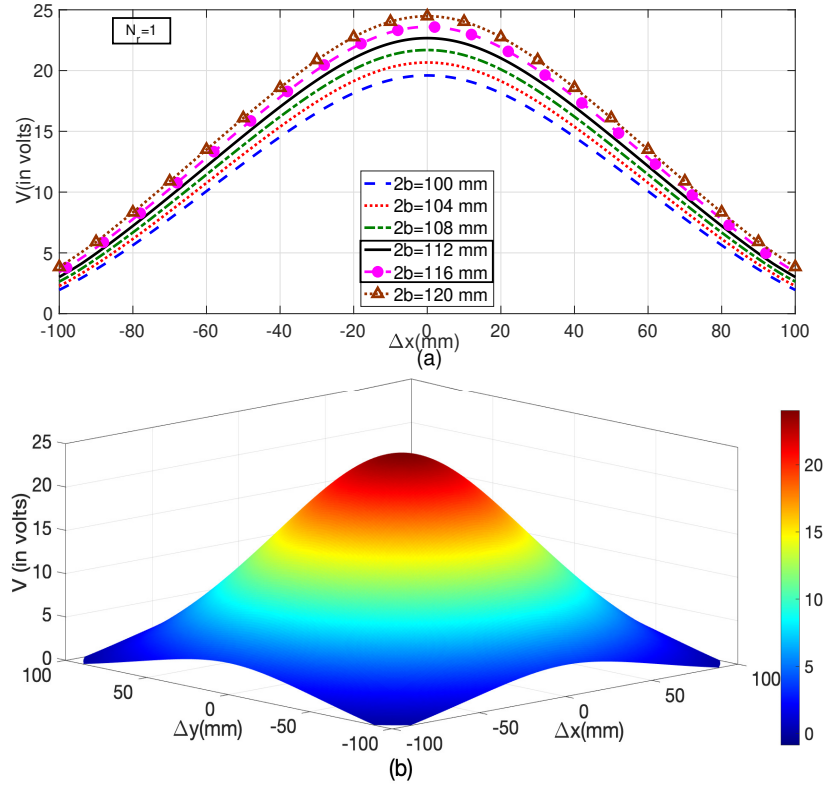
Figure 2.17: Optimizing 2*b*: (a) variation of *V* with Parametric Sweep, (b) 3D *V* Distribution for optimal 2*b*
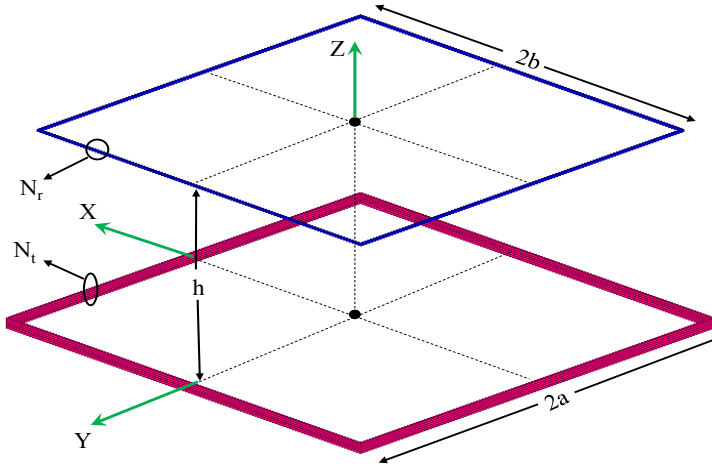


Figure 2.18: Layout of Tx-Rx coils resulted from proposed design procedure.

Rx coil current $I_{Rx} = \frac{I_R}{\sqrt{2}}$, Rx coil voltage $V_{Rx} = V_L$, DC output voltage $V_{dc}$, DC output current $I_{dc}$, MOSFET blocking voltage $V_{MOSFET}$, and diode blocking voltage $V_D$ as shown in Figure. 2.21. The input power, Rx coil power, and DC power are evaluated as $P_{in} = V_{in} \times I_{Tx} = 35.34 \times 0.862 = 30.46$W, $P_{R_R} = V_{Rx} \times I_{Rx} = 23.04 * 1.24 = 28.57$W,
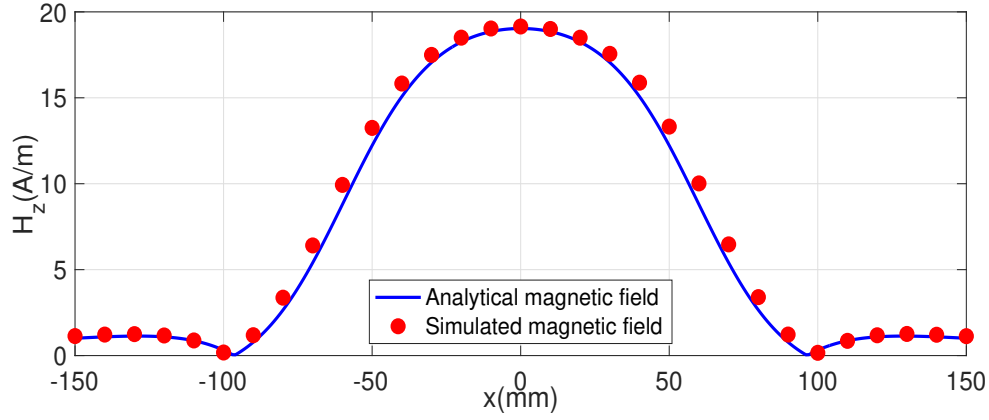
Figure 2.19: Simulated results of magnetic field ($H_z$) distribution at $y = 0$.
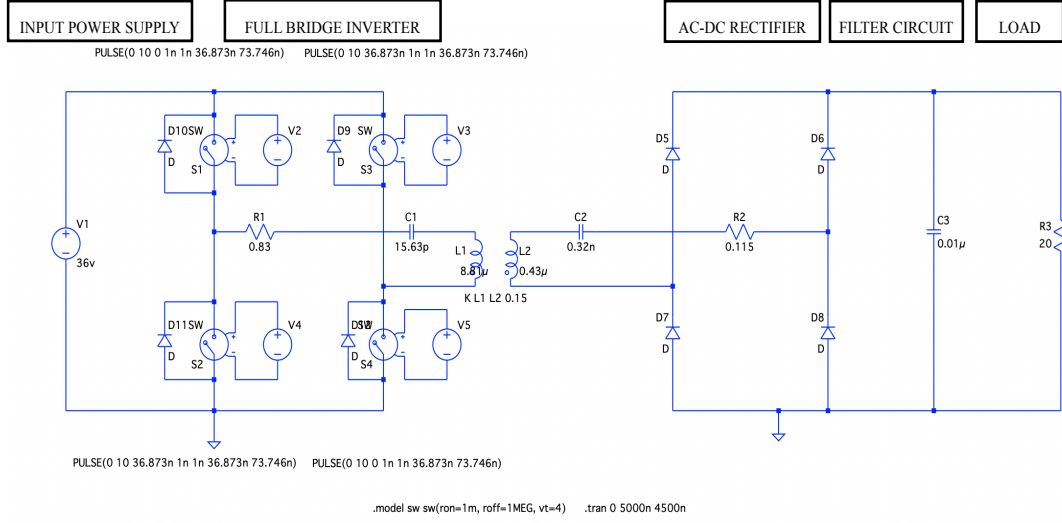


Figure 2.20: Circuit analysis of WPT system using LT-Spice simulator.

Table 2.5: Performance parameters of the WPT system

| Signal and performance parameters | |
|---|---|
| $V_{in}/I_{Tx}/V_{Rx}/I_{Rx}$ | 36 v / 0.862A / 23.04v / 1.24A |
| $V_{dc}/I_{dc}/V_{MOSFET}/V_D$ | 22.33v / 1.11A / 36v / 22.97v |
| $P_{in}/P_{R_R}/P_{DC}$ | 30.46W / 28.57W / 24.78W |
| $\eta_{ss}/\eta_{dc-dc}$ | 93.7% / 81.3% |
| Note: | $I_{Tx}$, $V_{Rx}$, $I_{Rx}$ are RMS value |
| Note: | $V_{dc}$, $I_{dc}$ are average value |
| Note: | $V_{MOSFET}$, $V_D$ are peak values |

and $P_{DC} = V_{dc} \times I_{dc} = 22.33 \times 1.11 = 24.78$W. The $\eta_{ss}$ is defined as ratio of $P_{R_R}$ and $P_{in}$, which is evaluated as 93.7%. Here, the $\eta_{ss}$ resembles the performance of Tx-Rx coils and does not include the effect of system components such as rectification and filtering
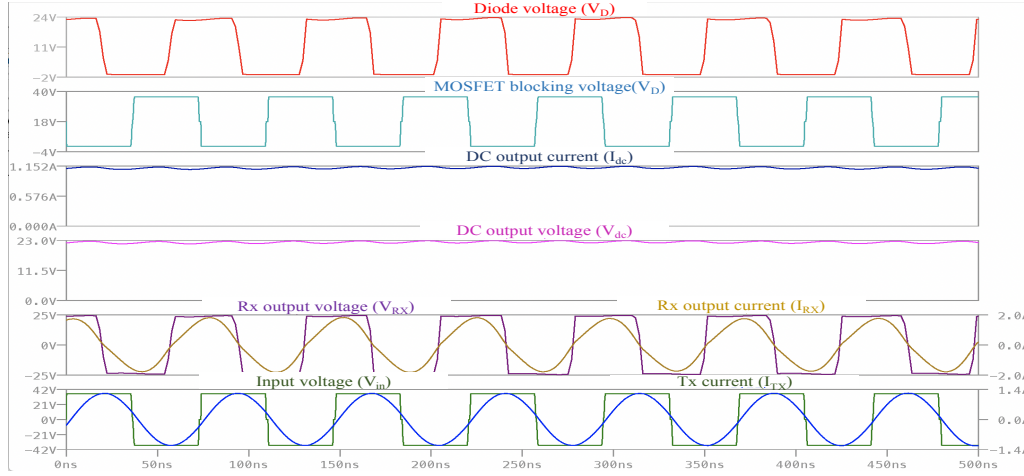
Figure 2.21: Wave-forms of various signals of proposed WPT system.

circuits. In contrast, the dc-dc efficiency or system efficiency ($\eta_{dc-dc}$) is characterized as ratio of $P_{DC}$ and $P_{in}$, which includes all the system losses of WPT system and is found to be 81.3%. All the performance parameters resulted using LT-spice simulator using Figure. 2.21 are summarized in Table 2.5.

## 2.4 Summary

This chapter establishes the mathematical foundation of a resonant WPT system using field theory and circuitry laws. Additionally, the mathematical tools, simulation setup, and experimental prototype utilized in this thesis are described by replicating the results of the best available conventional literature design [1]. The uniformity factor in terms of mutual inductance between misaligned Rx coil and Tx coil proposed in conventional literature design is found to be UF($M(\Delta x, \Delta y)$)=6.25%. Astonishingly, according to the best of author knowledge, the design presented in [1] was known to be best possible single port Tx coil antenna to mitigate lateral misalignment problem till the year 2018. However, the achieved misalignment tolerance in [1] is found to be insignificant for any practical applications. Moreover, the conventional literature design acounts for huge magnetic flux leakage outside the Rx coil operating region which results in reduced coupling and ultimately impacts the PTE of the WPT system. The above drawbacks in conventional literature design provides wide scope for improvement in enhancing lateral misalignment tolerance in wireless charging applications.

Finally in Chapter 2, a systematic design procedure is presented, outlining the justification for selecting each dimensional parameter of the Tx coil antenna, such as side length, transfer distance, number of turns, and operating frequency, to maximize the PTE for a perfectly aligned Rx coil antenna [a]. However, the experimental setup for measuring PTE using VNA does not align with the results generated from realistic power converter supply units as briefly discussed in subsection 1.2.4. Therefore, the root cause of the issue with the

VNA-based measurement setup is identified, and a novel S-parameter based measurement system is introduced, which will be exclusively dedicated to the next chapter.

CHAPTER OUTCOMES

---

[0][a] **A. Bharadwaj**, V. K. Srivastava, C. C. Reddy, and A. Sharma, "Design Methodology of Near-Field Transmitter Coil Antenna for Maximizing Efficiency of the WPT System," **accepted in 17th European Conference on Antennas and Propagation**, Florence, Italy, 2023.

# Chapter 3

# A New Measurement Method using Vector Network Analyzer

The focus of this chapter is to achieve the proposed objectives in SO-A which deals with the inadequacies of efficiency measurement systems that depend on S-parameters. These deficiencies were brought to light in the subsection 1.2.4 of the Chapter 1 and consist of two primary concerns as shown in Figure. 1.7(a). The first pertains to the lack of analytical S-parameters for secondary-parallel compensation topologies. The second involves significant differences between efficiency measurements obtained via S-parameters on a VNA and those acquired from a practical power source. The initial step in addressing these issues is the derivation of S-parameters for secondary-parallel compensation topologies using a two-port network as follows:

## 3.1 S-parameter Based Efficiency for Secondary-Parallel Topology

The S-parameters for the secondary-parallel compensation topology are determined by analyzing the two-port S-parameter network depicted in Figure 3.1. The evaluation process involves utilizing the given network to calculate the relevant S-parameters for the compensation topology. The figure serves as a visual aid in understanding the network and its components. The $Z_{in}$ is determined for secondary- parallel topology by rearranging
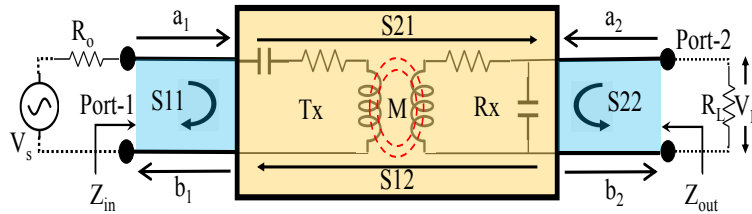


Figure 3.1: A two-port S-parameter network for PTE evaluation under secondary- parallel compensation topology.

(2.23) as

$$Z_{in} = R_T + X_{S1} + \frac{(\omega M)^2}{R_R + R_{Leff} + X_{P2}},$$

(3.1)

41

which is then substituted in (2.32a) by replacing $R_s$ with $R_o$ to obtain $S11$-parameter as

$$S11 = \frac{(R_T - R_o + jX_{S1})(R_R + R_{Leff} + jX_{P2}) + (\omega M)^2}{(R_T + R_o + jX_{S1})(R_R + R_{Leff} + jX_{P2}) + (\omega M)^2}. \tag{3.2}$$

The expression of $\frac{V_L}{V_s}$ for secondary-parallel compensation is found by multiplying $R_{Leff}$ to the both sides of (2.24) as

$$\frac{V_L}{V_s} = \frac{j\omega M R_{Leff}}{(R_T + X_{S1})(R_R + R_{L_{eff}} + X_{P2}) + (\omega M)^2}. \tag{3.3}$$

Thereupon, the equations (3.2) and (3.3) are used in (2.38), the $S21$-parameter for secondary-parallel topology is formulated as

$$S21 = \frac{j2\omega M\sqrt{R_o R_{Leff}}}{(R_T + R_o + jX_{S1})(R_R + R_{Leff} + jX_{P2}) + (\omega M)^2}. \tag{3.4}$$

The establishment of the PTE for a secondary parallel topology under resonant condition using S-parameters involves replacing equations (3.2) and (3.4) in equation (2.40a) as

$$\eta_{S-parameter}^{2parallel} = \frac{(\omega M)^2 R_{L_{eff}}}{R_T(R_R + R_{L_{eff}})^2 + (\omega M)^2(R_2 + R_{L_{eff}})}. \tag{3.5}$$

Here, $\eta_{S-parameter}^{2parallel}$ denotes S-parameter based efficiency for secondary parallel topology. Upon comparing equations (2.27) and (3.5) with the expressions provided in Table 2.1, it becomes evident that an S-parameter based analysis for secondary compensation topologies yields results that are in agreement with the circuit-based PTE.

The next issue, which pertains to discrepancies between conventional S-parameter based efficiency and the efficiency derived from practical power sources like inverters, is subsequently addressed and resolved.

## 3.2 Evaluation of modified S-parameter-based efficiency for secondary-series compensation topology

The $M$ is framed in terms of S-parameters by solving the equations (2.35), (2.36), and (2.39) as follows:

$$j\omega M = \frac{2S21R_L}{(1 - S11)(1 - S22) - S21^2}. \tag{3.6}$$

The (3.6) is substituted in (2.16) to obtain $\eta_{s-proposed}$ and formulated as

$$\eta_{s-proposed} = \frac{\left|Im\left(\frac{2S21R_L}{(1-S11)(1-S22)-S21^2}\right)\right|^2 R_{Lu}}{\left[(R_T + R_{su})(R_R + R_{Lu})^2 + \left|Im\left(\frac{2S21R_L}{(1-S11)(1-S22)-S21^2}\right)\right|^2 (R_R + R_{Lu})\right]}, \tag{3.7}$$

further, $R_{Lu}$ is divided in both numerator and denominator in (3.7) to obtain

$$\eta_{s-proposed} = \frac{\left| Im\left( \frac{2S21R_L}{(1-S11)(1-S22)-S21^2} \right) \right|^2}{\left[ (R_T+R_{su})\frac{(R_R+R_{Lu})^2}{R_{Lu}} + \left| Im\left( \frac{2S21R_L}{(1-S11)(1-S22)-S21^2} \right) \right|^2 \frac{(R_R+R_{Lu})}{R_{Lu}} \right]}, \tag{3.8}$$

the term $(R_{su}R_{Lu})$ is multiplied and divided in the first term of the denominator in (3.8) to get

$$\eta_{s-proposed} = \frac{\left| Im\left( \frac{2S21R_L}{(1-S11)(1-S22)-S21^2} \right) \right|^2}{R_{su}R_{Lu}\frac{(R_T+R_{su})}{R_{su}}\frac{(R_R+R_{Lu})^2}{R_{Lu}^2} + \left| Im\left( \frac{2S21R_L}{(1-S11)(1-S22)-S21^2} \right) \right|^2 \frac{(R_R+R_{Lu})}{R_{Lu}}}, \tag{3.9}$$

the source factor $\left( SF = \frac{R_{su}}{R_T+R_{su}} \right)$ and load factor $\left( LF = \frac{R_{Lu}}{R_R+R_{Lu}} \right)$ are introduced and replaced in (3.9) to simplify the expression as

$$\eta_{s-proposed} = \frac{\left| Im\left( \frac{2S21R_L}{(1-S11)(1-S22)-S21^2} \right) \right|^2}{\frac{R_{su}R_{Lu}}{SF \times LF^2} + \frac{\left| Im\left( \frac{2S21R_L}{(1-S11)(1-S22)-S21^2} \right) \right|^2}{LF}}. \tag{3.10}$$

Here, $R_{su}$ and $R_{Lu}$ are user-controlled internal resistances which replaced as $R_s = R_{su}$ and $R_L = R_{Lu}$. The $SF$ is the function of $R_{su}$, generally assumed according to the user-designed power supply ($R_{su} \in [0, 0.1]\Omega$). Similarly, $LF$ is the function of $R_{Lu}$ usually adjusted according to user defined application. In general, the source factor ranges in $0 < SF < 1$ depending on the $R_{su}$ value. If the user assigns the $R_{su}$ value near zero, the SF tends to zero. Similarly, if the user opts for a high $R_{su}$ value, the SF tends to one. Thus, it is advised to operate at $SF \approx 0$ to achieve higher efficiency. Moreover, the proposed S-parameter based efficiency provides users with flexible source-load conditions ($R_{su}$ and $R_{Lu}$) that matches realistic power supply units. The proposed S-parameter-based efficiency is validated by experimenting, as elaborated in the subsequent section.

## 3.3 Experimental Verification and Comparison

The proposed S-parameter-based efficiency is validated by fabricating the Tx-Rx coil with a 20 AWG single-strand copper wire as shown in the inset of Figure. 3.2(b). Notably, the circuit parameters such as resistance and self-inductance are measured using an Agilent N5230C Network analyzer at resonant frequency, $f = 400$ kHz. Following Table 3.1 summarizes the physical dimensions, circuit parameters, and operating conditions of
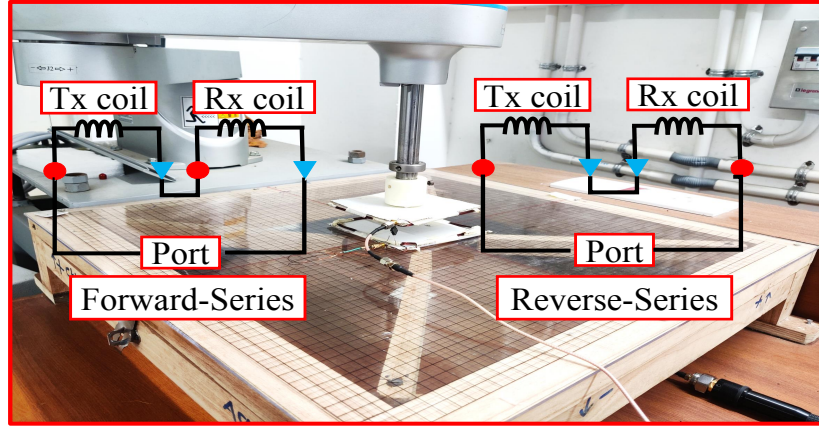
(a)
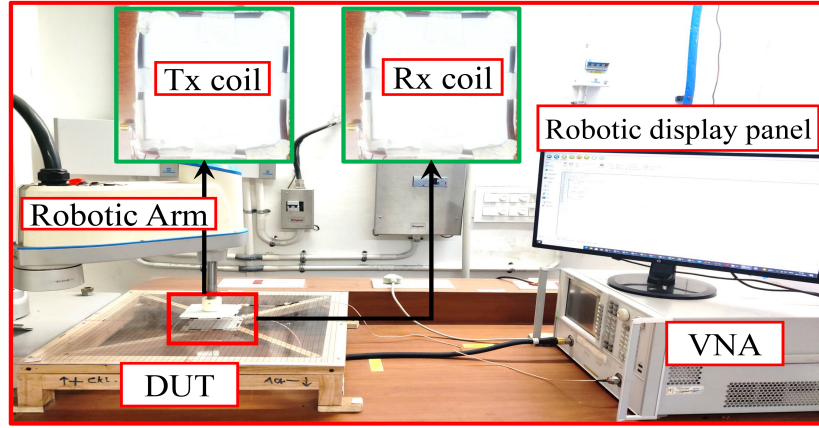


(b)

Figure 3.2: Experimental setup for measurement of (a) Mutual inductance, (b) Power transfer efficiency.

the Tx-Rx coil. The particulars of $M$ are measured in two distinct techniques. The

Table 3.1: The parameters of Tx-Rx coils

| Physical dimensions of the Tx-Rx coils | |
|---|---|
| $2a/2b/h/f$ | 108 mm/108 mm/50 mm/400 kHz |
| $N_t/N_r$ | 7/7 |
| Circuit parameters of Tx-Rx coils | |
| $R_T/R_R$ | 0.44$\Omega$/0.48$\Omega$ |
| $L_T/L_R$ | 14.23$\mu$H/14.4$\mu$H |
| Resonating capacitors of Tx-Rx coils | |
| $C_T/C_R$ | 11.1$n$H/10.99$n$F |
| Source-Load conditions for measurement of $\eta_{ss}$ | |
| $R_{su}/R_{Lu}$ | 0.01$\Omega$/10$\Omega$ |
| Source-Load conditions for measurement of $\eta_{s-conventional}$ | |
| $R_s/R_L$ | 50$\Omega$/50$\Omega$ |
| Source-Load conditions for measurement of $\eta_{s-proposed}$ | |
| $R_{su}/R_{Lu}/R_s/R_L$ | 0.01$\Omega$/10$\Omega$/50$\Omega$/50$\Omega$ |

first technique adopts the differential cumulative method (passive measurement) [38, 39] wherein the Tx-Rx coils are connected in forward and reverse series as shown in Figure. 3.2(a). In the forward series connection, the effective inductance value $L_{FC} = L_T + L_R + 2M$ is measured using the Agilent N5230C Network analyzer. However, the effective inductance value $L_{RC} = L_T + L_R - 2M$ in reverse series connection is measured by interchanging the Rx coil terminals. Thereby, the value of $M$ is determined as $M = \frac{L_{FC} - L_{RC}}{4}$. Conversely, in the second technique, the value of $M$ is experimentally acquired by connecting resonating capacitors $C_T$ and $C_R$ in series with Tx-Rx coils and by extracting S-parameters from network analyzer and further substituting in (3.6). The data of each misaligned position ($\Delta x$) is converged by averaging 1000 samples using the inbuilt averaging-factor function available in network analyzer. Further, the sample points are fetched in computational software to evaluate standard deviation as

$$\sigma_s = \left[ \frac{\left( \sum_{i=1}^{N} (S(i) - \bar{S})^2 \right)}{(N-1)} \right]^{\frac{1}{2}} \tag{3.11}$$

Here, S(i) denotes the $i$th value of S-parameter measured from the network analyzer, $N$ denotes the number of sample points and $\bar{S}$ denotes the mean of sample points acquired from VNA. The standard deviation ($\sigma_s$) of S-parameters are tabulated in Table. 3.2. In

Table 3.2: Standard deviation

| Position ($\Delta x$) | $\sigma_s$ of S11 (dB) | $\sigma_s$ of S22 (dB) | $\sigma_s$ of S21 (dB) |
|---|---|---|---|
| 0 mm | $\pm 5.1 \times 10^{-3}$ | $\pm 4.9 \times 10^{-3}$ | $\pm 0.49$ |
| 20 mm | $\pm 4.8 \times 10^{-3}$ | $\pm 5 \times 10^{-3}$ | $\pm 0.5$ |
| 40 mm | $\pm 5 \times 10^{-3}$ | $\pm 4.8 \times 10^{-3}$ | $\pm 0.48$ |
| 60 mm | $\pm 5.3 \times 10^{-3}$ | $\pm 5.1 \times 10^{-3}$ | $\pm 0.5$ |
| 80 mm | $\pm 4.7 \times 10^{-3}$ | $\pm 5.2 \times 10^{-3}$ | $\pm 0.49$ |
| 100 mm | $\pm 4.9 \times 10^{-3}$ | $\pm 4.8 \times 10^{-3}$ | $\pm 0.49$ |

addition, the magnitude of S-parameters with error bar is plotted with respect to horizontal displacement ($\Delta x$) of the Rx coil along the x-axis (i.e y=0 line) in Figure. 3.3. Respectively, the magnitude of $\{S11 \text{ and } S22\}$-parameters obtained are shown in Figure. 3.3(a), and the phase value is measured to be $180^o$. The matching network of Tx-Rx coils has been designed considering the effect of the reflected impedance of the Rx coil on the Tx coil, and thereupon, the $S11$ and $S22$ parameters have a maximum dip in a perfectly aligned state. On that account, as the Rx coil horizontally displaces ($\Delta x$ denotes misalignment), the reflected impedance alter, affecting the WPT system's resonance. This effect is observed in $S21$ and $S12$ parameters, as shown in Figure. 3.3(b), since the value of $S21$ and $S12$ parameters decrease with horizontal displacement of Rx coil. Moreover, the WPT system is reciprocal, hence the data of $S21$ and $S12$ parameters are measured to be identical as depicted in Figure. 3.3(b), and the phase value is exhibited as $90^o$. Henceforth,
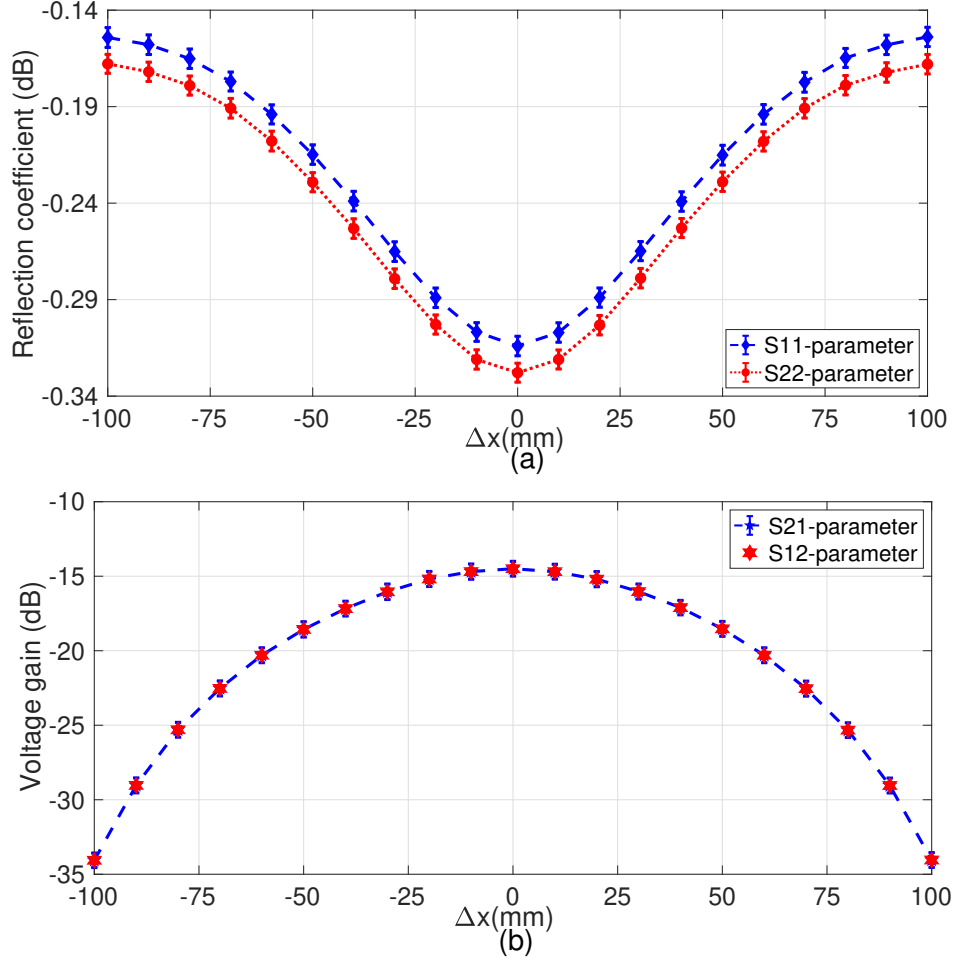
Figure 3.3: Measured results of (a) $S11$ and $S22$-parameters, (b) $S21$ and $S12$-parameters.

signal-to-noise ratio (SNR) of S-parameters is evaluated as [90]

$$SNR = 20 * log_{10} \left( \frac{S_{signal}}{S_{noise}} \right) \qquad (3.12)$$

Here, $S_{signal}$ denotes the desired signal between Tx-Rx coils, and $S_{noise}$ represents the noise signal measured when the Rx coil is displaced out of the operating region in the Rx-plane. The $S_{noise}$ is measured as $-59.8$ dB; therefore, the SNR value of S21-parameter for perfectly aligned Rx coil is determined as 45.3dB. The 2D plot of $M$ by displacing the Rx-coil horizontally at an interval of 10 mm along y=0 line is represented in Figure. 3.4. To maintain stability and accuracy in the measurement process, a DRS60L robotic arm is employed as shown in Figure. 3.2. From Figure. 3.4, it can be inferred that the measured value of $M$ from S-parameters is more accurate in comparison with the differential cumulative technique. Besides, in differential cumulative method in passive measurement, the terminals need to be physically interchanged for measuring the effective inductance value in forward and reverse series for each distinct misaligned position of the
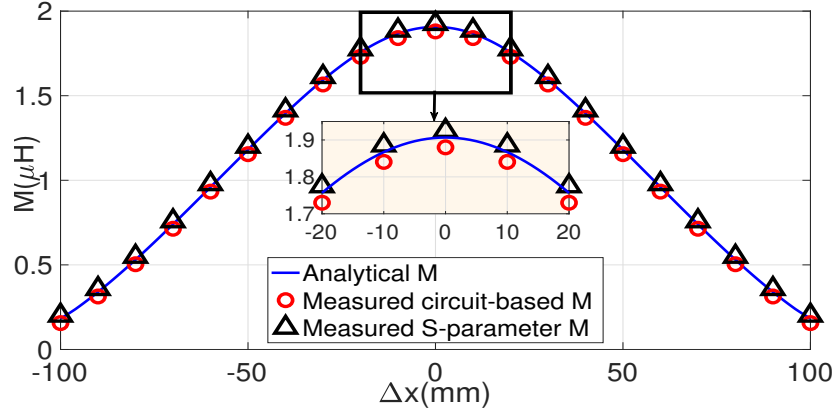
Figure 3.4: Measured results of mutual inductance.

Rx coil thereby spiraling the complexity. This proves S-parameter based measurement for determining $M$ value is simple, accurate and coherent. The $\eta_{ss}$ is determined by replacing the $M$ value using differential cumulative method and by assuming $R_s = 0.01\Omega$ and $R_L = 10\Omega$ [1] in (2.16). Subsequently, the $\eta_{s-conventional}$ is measured by determining magnitude of $S21$ and $S11$ parameters by calibrating the input-output ports at $50\Omega$ and by replacing it in (2.40a). Wherein, the ($\eta_{s-proposed}$) is determined by measuring magnitude and phase of $\{S11, S22, S21 \text{ and } S12\}$-parameter using network analyzer, and further by controlling the $SF$ and $LF$ and by replacing $R_{su} = 0.01\Omega$ and $R_{Lu} = 10\Omega$ in (3.10). The 2D plot of all the efficiencies for horizontal displacement of Rx coil at an interval of 10 mm along $y = 0$ line is shown in Figure. 3.5(a). From the Figure. 3.5(a), the $\eta_{s-proposed}$ compliments with $\eta_{ss}$, whereas, the $\eta_{s-conventional}$ shows disagreement for the WPT system which misguides the researchers in estimating the realistic performance for the same. This substantial difference occurs due to distinct operating conditions used in both the equations, $\eta_{s-conventional}$ ($R_s = R_L = 50\Omega$) and $\eta_{s-proposed}$ ($R_{su} \approx 0$ and $R_{Lu} = 10\Omega$). Moreover, the variation of $\eta$ at different transfer distances ranging $h \in [10, 50]$ mm is plotted in Figure. 3.5(b). From the plot, it is observed that the error between $\eta_{s-conventional}$ and $\eta_{ss}$ increases as the transfer distance ($h$) between Tx-Rx coils increases. Whereas, the proposed S-$\eta_{s-proposed}$ matches with the $\eta_{ss}$ for all transfer distances $h$. To assess the degree of deviation with respect to realistic power source efficiency, $\eta_{ss}$, an error rate ($\epsilon$) is defined for each misalignment data $\Delta x$ as

$$\epsilon_1 = \left| \frac{\eta_{ss} - \eta_{s-conventional}}{\eta_{ss}} \right|, \tag{3.13a}$$

$$\epsilon_2 = \left| \frac{\eta_{ss} - \eta_{s-proposed}}{\eta_{ss}} \right|. \tag{3.13b}$$

Where, $\epsilon_1$ represents error between circuit and conventional S-parameter based efficiencies, and $\epsilon_2$ denotes the error deviation between circuit and proposed S-parameter based efficiencies. The error rate ($\epsilon$) is evaluated for each misalignment ($\Delta x$) as depicted in Figure. 3.6. Here, the $\epsilon$ increases with misalignment ($\Delta x$), as the Tx-Rx coils are resonated
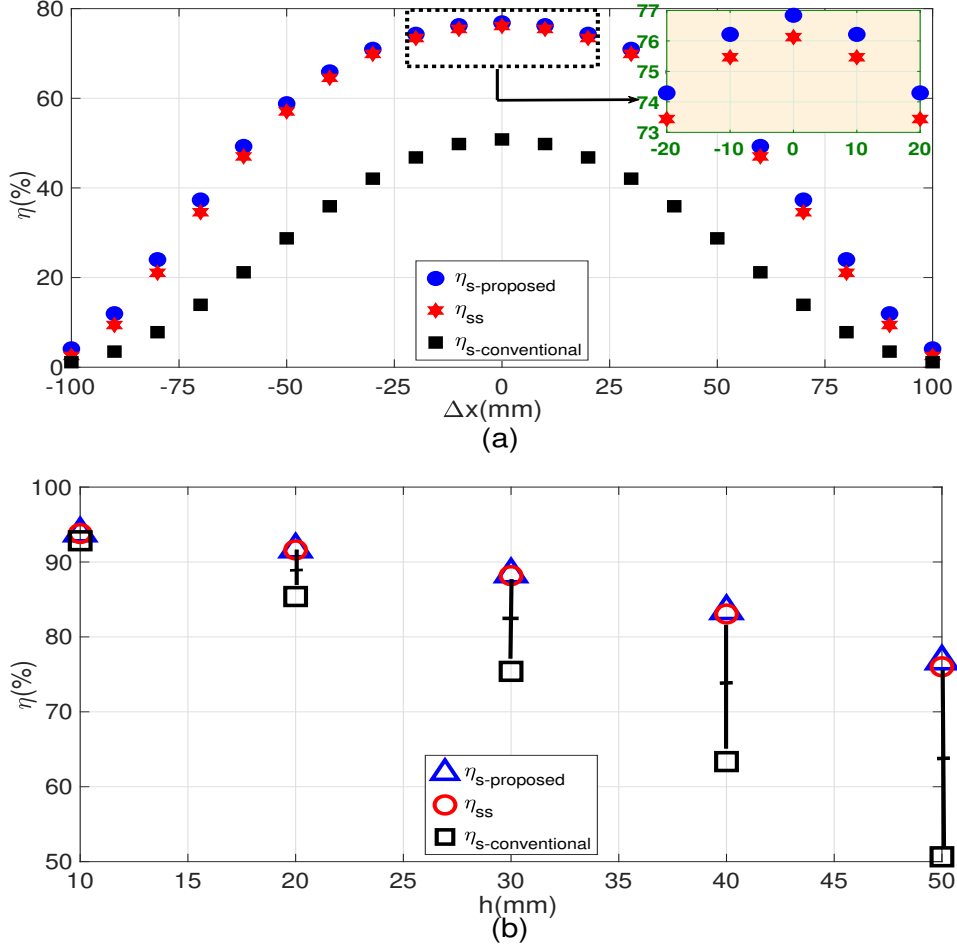
Figure 3.5: Measured results of efficiency for (a) Horizontal misalignment ($\Delta x$), (b) Transfer distance ($h$).

under a perfectly aligned state (i.e., $\Delta x = 0$). Therefore, when the Rx coil displaces from its intended position, the reflected impedance of the Rx coil on the Tx coil alters, disturbing the resonant frequency. The error rate for conventional s-parameters ($\epsilon_1$) from Figure. 3.6 is above 30% for entire misalignment range. In contrast, the error rate observed for proposed S-parameter based efficiency ($\epsilon_2$) is at most 5%. Therefore, the $\eta_{s-proposed}$ measurement technique paves a novel path for researchers to estimate realistic performance parameters for coil designs using S-parameters.

### 3.3.1 Comparison with state of the art equations

The proposed $\eta_{s-proposed}$ equation is compared with various literature works as tabulated in Table 3.3, wherein $\eta_{ss}$ is measured by considering $R_{su} = 0.01\Omega$ and $R_{Lu} = 10\Omega$ [1]. Thereby, the losses due to the source-load effect are significantly minimized. Consequently, the attained value of $\eta_{ss}$ is greater than 70%. In contrast, the $\eta_{s-coventional}$ is measured under fixed source-load conditions given as $R_s=R_L=50\Omega$ [91, 92, 93, 94, 95]. The value
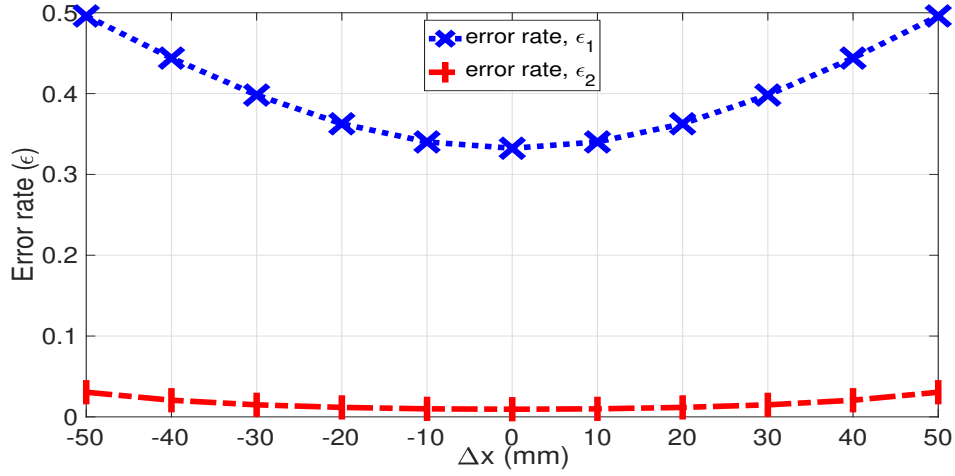
Figure 3.6: Error rate ($\epsilon$) of $\eta_{s-conventional}$ and $\eta_{s-proposed}$ for Horizontal misalignment ($\Delta x$) of Rx coil.

Table 3.3: Comparison of the proposed S-parameter based efficiency with the efficiency equations available in the literature.

| Ref | Efficiency type | Source-Load conditions | Efficiency value |
|---|---|---|---|
| [1] | $\eta_{ss}$ | $R_{su} = 0\Omega, R_{Lu} = 10\Omega$ | 91% |
| [91] | $\eta_{s-conventional}$ | $R_s = R_L = 50\Omega$ | 24% − 29% |
| [92] | $\eta_{s-conventional}$ | $R_s = R_L = 50\Omega$ | 50% |
| [93] | $\eta_{s-conventional}$ | $R_s = R_L = 50\Omega$ | 53% |
| [94] | $\eta_{s-conventional}$ | $R_s = R_L = 50\Omega$ | 47.2% |
| [95] | $\eta_{s-conventional}$ | $R_s = R_L = 50\Omega$ | 35% |
| Proposed work | $\eta_{s-proposed}$ | $R_s = R_L = 50\Omega,$ $R_{su} = 0.01\Omega, R_{Lu} = 10\Omega$ | $\approx 80\%$ |

of $\eta_{s-conventional}$ in the literary works is less than 55% because of high source-load losses. Therefore, a modified S-parameter-based efficiency is proposed, allowing the user to control the terminal resistances by calibrating $SF$ and $LF$. From Table 3.3, it is evident that by using $\eta_{s-proposed}$, the value is obtained close to 80%, equivalent to $\eta_{ss}$. The proposed equations permit the researchers to estimate the realistic performance of Tx-Rx coils using S-parameters at very high frequencies.

## 3.4 Summary

This chapter of the thesis introduces an exciting and cutting-edge approach to predicting the PTE of a secondary-series resonant WPT system using S-parameters obtained from VNA. The results of this study are truly remarkable, as the accuracy achieved by this new measurement methodology is comparable to that of realistic power sources that utilize power electronic converters. This breakthrough in VNA based measurement technique is poised to revolutionize the development and optimization of WPT systems, particularly for practical applications across a wide range of frequencies and the publication pertinent

to this achievement is given below in [b].

Furthermore, this chapter represents a major milestone in the field of resonant WPT systems, as it presents the first-ever analytical S-parameters for secondary-parallel compensation topologies [c]. This achievement adds to the growing body of knowledge in this field and opens up exciting new possibilities for future research in resonant WPT system. Moreover, the proposed measurement technique is used in subsequent chapters of this thesis work for measuring efficiency between newly designed Tx-Rx coils.

The next chapter addresses the misalignment problem by exploring distinct objective functions, including uniform magnetic-field formation and uniform induced voltage at the Rx coil region. Various single port Tx coil designs, such as 3D Tx coils, singular distributed coil antennas, and array coil antennas, are optimized using these approaches. For the first time, structured mathematical analysis is provided to determine the optimal magnetic-field distribution, which holds great promise for addressing the lateral misalignment problem. These groundbreaking approaches offer potential for designing lateral misalignment-insensitive Tx coils in near-field WPT systems, benefiting the research community.

CHAPTER OUTCOMES

---

[b] **A. Bharadwaj**, A. Sharma and C. C. Reddy, "An Unconventional Measurement Technique to Estimate Power Transfer Efficiency in Series–Series Resonant WPT System Using S-Parameters," in **IEEE Transactions on Instrumentation and Measurement**, vol. 71, pp. 1-9, 2022, Art no. 8004009, doi: 10.1109/TIM.2022.3181291.

[c] **A. Bharadwaj**, A. Sharma and C. C. Reddy, "Analytical Framework of S-parameter Based Efficiency for Secondary-Parallel Compensation WPT system to Authenticate Data Using VNA," in **IEEE Transactions on Instrumentation and Measurement**, doi: 10.1109/TIM.2023.3240224.

# Chapter 4

# Single Port Tx Coil Antennas

This chapter is dedicated to the development of an objective function that addresses the lateral misalignment problem in WPT systems using single port Tx coil antennas. As part of this process, novel mathematical formulations are developed to determine the optimal magnetic-field distribution in the Rx coil, with the aim of improving the system's lateral misalignment tolerance. Additionally, this chapter presents the evolution and optimization of three distinct Tx coil designs, designated as Design-1A, Design-1B, and Design-1C, which fulfill the objectives outlined in EP-1, EP-2, and EP-3 of SO-B, respectively.

## 4.1 Evolution of Design-1A (SO-B: EP-1)

In WPT applications like EVs, angular misalignment is typically not a problem since the Rx and Tx are always coplanar in conventional planar structures. This is demonstrated in Figure. 4.1, which depicts possible Rx misalignment when the vehicle is displaced.
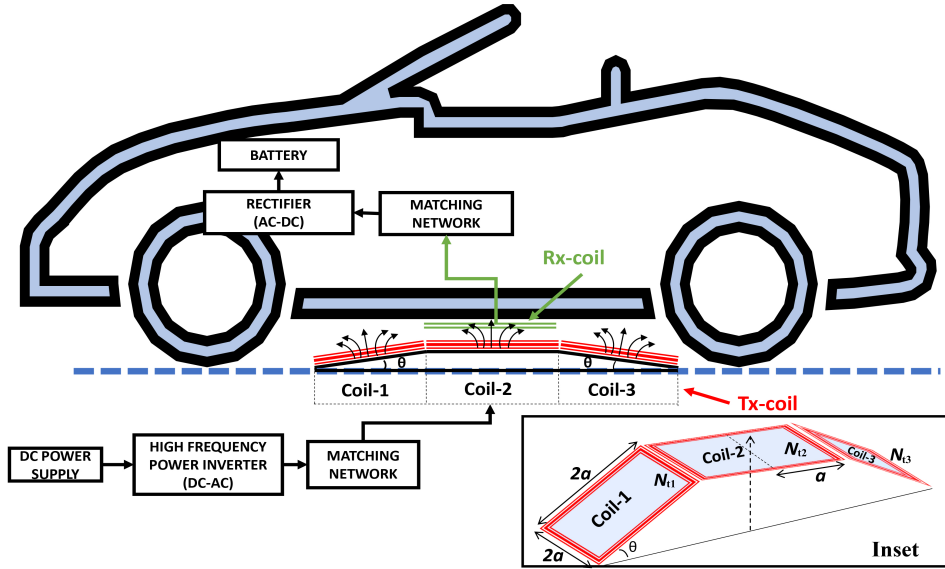


Figure 4.1: Schematic diagram of WPT system and the proposed Tx coil: Design-1A.

As a result, stabilizing the output voltage of the misaligned Rx coil to improve battery life becomes a primary objective, with mitigation of lateral misalignment being crucial. Achieving this requires forming the uniform magnetic field in such a way that constant induced voltage is obtained in the Rx coil, regardless of its displacement.

### 4.1.1 The proposed Tx antenna and magnetic field analysis

A prototype of the Design-1A Tx coil antenna is shown in Figure 4.1. The structure of Design-1A comprises three coils, each in the shape of a square Helmholtz coil with $2a = 100$mm, as detailed in the inset of Figure 4.1. The three coils are connected in series, and coil-2 is coplanar with the Rx coil. Whereas, coils-1 and 3 are placed on inclined faces of an isosceles trapezoid at an angle $\theta$ from the ground plane. Let the number of turns in the three coils be denoted by $N_{t1}$, $N_{t2}$, and $N_{t3}$, respectively. The magnetic field components $H_x$, $H_y$, and $H_z$ along the $x$, $y$, and $z$ axes, as given in equations (2.1), (2.2), and (2.3), are evaluated for the three coils of Design-1A at each coil center, denoted by $(x_{tm}, y_{tm}, z_{tm})$, where $m = 1, 2, 3$. The total magnetic field of each component due to $N_{t1}, N_{t2}$, and $N_{t3}$ turns of each coil for a conventional planar antenna with $\theta = 0°$ is given by

$$H_x = N_{t1}H_x^1 + N_{t2}H_x^2 + N_{t3}H_x^3 \tag{4.1a}$$

$$H_y = N_{t1}H_y^1 + N_{t2}H_y^2 + N_{t3}H_y^3 \tag{4.1b}$$

$$H_z = N_{t1}H_z^1 + N_{t2}H_z^2 + N_{t3}H_z^3 \tag{4.1c}$$

where subscript '$m$' in $H^m$ represent contribution of field due to coil-$m$.

### 4.1.2 Analysis of magnetic-field distribution

Now the magnetic field distribution originated by the proposed structure is analyzed. Since the coil-1 and coil-3 are tilted by an angle $\theta$, (4.1a), (4.1b) and (4.1c) are no longer valid directly for these coils, hence, the coordinates are translated according to observation point $P(x_p, y_p, z_p)$ in the space. To determine the total magnetic field in the Rx-plane, the adopted geometrical configuration of the proposed idea is shown in Figure. 4.2. The coil-2 is assumed coinciding with the global coordinate system (X,Y,Z), hence, coil-2 center is located at the origin, and its plane lies in x-y plane. Whereas, coil-1 and coil-3 have local coordinate axis $X^1, Y^1, Z^1$ and $X^3, Y^3, Z^3$ as shown in Figure. 4.2(a). We note that all the coordinate systems have x-axis common due to geometry of the structure. The translated coordinates of observation point $P$ in coil-1 local coordinate system is $(x_{p1}, y_{p1}, z_{p1})$ which is found with respect to global coordinate system from Figure. 4.2(a) and evaluated as

$$x_{p1} = x_p \tag{4.2a}$$

$$y_{p1} = (y_p + y_e)\cos(\theta) + (z_p + z_e)\sin(\theta) \tag{4.2b}$$

$$z_{p1} = (z_p + z_e)\cos(\theta) - (y_p + y_e)\sin(\theta) \tag{4.2c}$$

where,

$$y_e = a + a\cos(\theta)$$
$$z_e = a\sin(\theta) \tag{4.3}$$
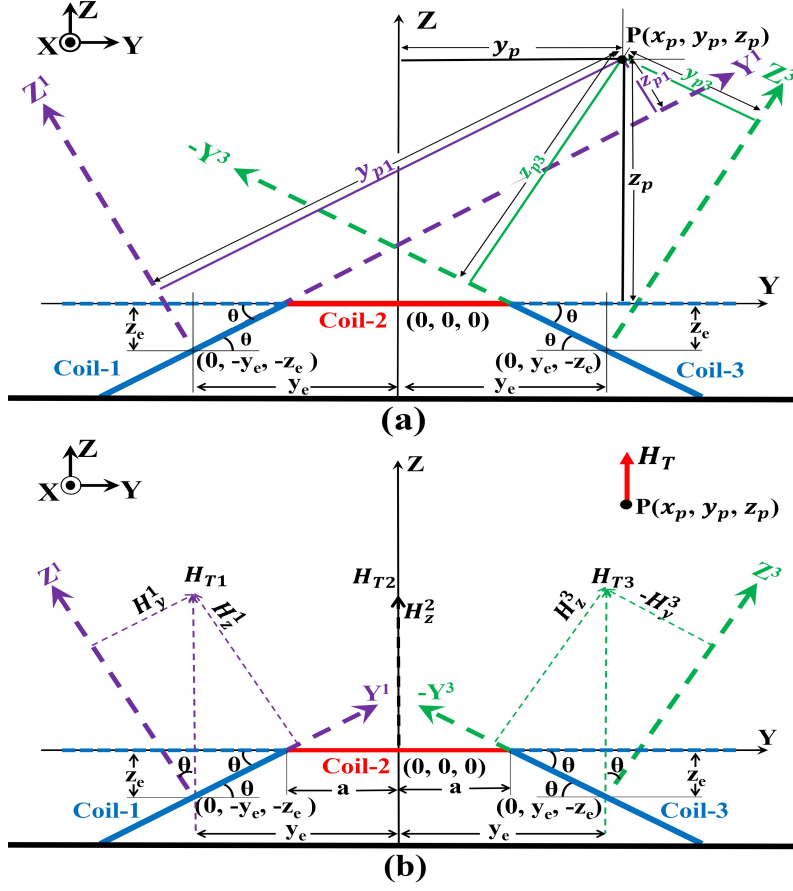
Figure 4.2: Geometrical configuration of Design-1A (a) the translation of coordinates due to Tx modules, (b) Components of magnetic field due to Tx modules.

Similarly, the translated coordinates of observation point $P$ in coil-3 local coordinate system are evaluated as

$$x_{p3} = x_p \tag{4.4a}$$

$$y_{p3} = (y_p - y_e)\cos(\theta) - (z_p + z_e)\sin(\theta) \tag{4.4b}$$

$$z_{p3} = (z_p + z_e)\cos(\theta) + (y_p - y_e)\sin(\theta) \tag{4.4c}$$

Since the Rx coil lies parallel to xy-plane, only $H_z$ component of the total magnetic field will induce voltage in the Rx coil. By using (4.2) and (4.4), the vertical magnetic field perpendicular to Rx plane $H_T$ due to each of the three coils are found at the observation point $P(x_p, y_p, z_p)$. The vertical field component $H_{Tm}$ due to coil-m at the observation point is characterized from Figure. 4.2(b) and formulated as

$$H_{T1} = H_z^1\cos(\theta) + H_y^1\sin(\theta) \tag{4.5a}$$

$$H_{T2} = H_z^2 \tag{4.5b}$$

$$H_{T3} = H_z^3\cos(\theta) - H_y^3\sin(\theta) \tag{4.5c}$$

where $H^m$ denotes the field component due to coil-$m$ in its local coordinate system as shown in Figure. 4.2(b). Now from (4.5a)-(4.5c), the total vertical magnetic field that influence the Rx coil is given as

$$H_T = H_{T1} + H_{T2} + H_{T3} \tag{4.6}$$

### 4.1.3   Formulation of induced voltage

The Rx antenna is assumed as square Helmholtz coil located at $z = h$ plane with $2b = 100$mm and $N_r = 12$. The effective height from ground of the Rx coil is $Z_{eff} = h + 2z_e$, where $Z_{eff} = 200$mm is the height between the Tx and Rx when $\theta = 0^o$. Due to $H_T$ distribution in the Rx-plane, a $dV$ is induced in a differential area $dA_z$ of the Rx coil as given in (2.4). The Rx coil is assumed misaligned to location $(\Delta x, \Delta y)$. Here, the lateral misalignment is only considered along y-axis, hence, $\Delta x = 0$. When the Rx is perfectly aligned with the Tx-module $\Delta x = 0$ and $\Delta y = 0$. The $V$ in the misaligned Rx is computed for entire Rx area by replacing $H_T$ with $H_z$ in (2.6). We observe from above defined equations that $V$ depends on tilt angle $\theta$ of the proposed design, hence, an optimal choice of $\theta$ may achieve $V$ independent of $\Delta y$ misalignment. Here the $V$ is evaluated at $f = 488.6$kHz.

### 4.1.4   Parametric Analysis

The parametric variation is done for $V$ by varying tilt angle ($\theta$) along with variation in number of turns. Due to symmetry, $N_{t1}=N_{t3}$, and the parametric study is conducted by varying normalized number of turns in coil-1 or coil-3 as $N = \frac{N_{t1}}{N_{t2}}$ or $\frac{N_{t3}}{N_{t2}}$. As a performance metric the UF is consider for $V(0, \Delta y)$ i.e, uniformity in only single dimension. Here, the UF is defined as the ratio of misaligned distance ($\Delta y = u$) up to which $V(0, \Delta y)$ varies within $\pm 1\%$ of $V(0,0)$ to the target misaligned distance ($\Delta y = u_o$). By using computational software (MATLAB 9.5 R2018b) the analytical model is investigated and UF is calculated with variation of $N$ for different tilt $\theta$ values and the result is shown in Figure. 4.3(a). For a corresponding peak UF, the induced voltage $V(0, \Delta y)$ for various $\theta$ is plotted in Figure. 4.3(b). From Figure. 4.3(a) it is evident that the uniformity in induced voltage is optimized at $\theta = 14^o$ and $N = 4$ and the corresponding $\text{UF}(V(\Delta x))$ is found as 55.33% as compared to 28.66% obtained by conventional design with $\theta = 0^o$ at the same value of $N$. As the Tx-coil is optimized at non-zero $\theta$, hence, the resulting design takes shape of a trapezoid in contrast to planar design of $\theta = 0^o$. It is also observed that Figure. 4.3(b) that, for $\theta = 14^o$, $V$ shows a better flatness for a wider misalignment $\Delta y$. The optimized parameters and performance metric based on normalized turns with respect to coil-2 is given in Table 4.1. The desired voltage for charging EV $V = 12V$ is obtained by increasing number of turns proportional to the voltage. For instance, we increased the number of turns in coil-2 to 30 turns, proportionally the number of turns in coil-1 and coil-3 are increased to 120 turns to maintain the optimal ratio $N = 4$. The data consisting of optimized parameters in Table. 4.1 is generic and can be used to calculate
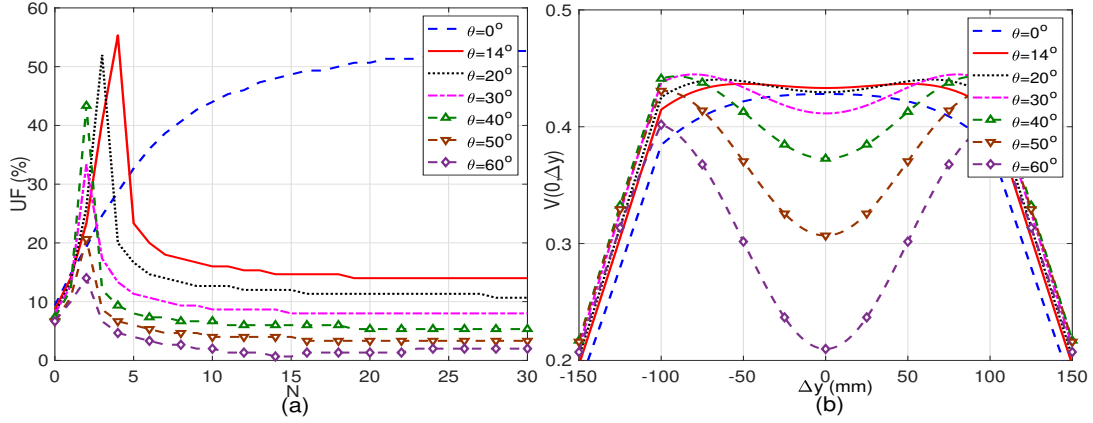
Figure 4.3: Parametric variation of Design-1A (a) variation of UF for various tilt angles, (b) variation of $V(0, \Delta y)$ for various tilt angles.

actual data according to the specifications of the required parameters such as battery voltage, maximum output power, maximum current etc. Whereas, the data consisting of performance metric does not change as the ratio always remain constant.

Table 4.1: Optimized parameters of Design-1A

| Normalized turns (N) | Optimized tilt angle $\theta$ | V |
|:---:|:---:|:---:|
| 4 | $14^o$ | $12V$ |
| **$N_{t1}$** | **$N_{t2}$** | **$N_{t3}$** |
| 120 | 30 | 120 |
| **Optimized UF** | **Conventional UF** | **% improvement** |
| 55.33% | 28.66% | 93.00% |

### 4.1.5    Analytical and simulated results of Design-1A

The analytically obtained 3D plots of magnetic-field and induced voltage distributions are shown in Figure. 4.4(a) and Figure. 4.4(b). The value of $V(0, \Delta y)$ remains constant within the misalignment region of $u = 166$mm, resulting in a significant improvement in the stability of $V(0, \Delta y)$ and mitigating the problem of lateral misalignment. The 3D plot clearly shows that EVs can freely park in the parking slot with a misalignment tolerance of $[-83, 83]mm$, which implies a total misalignment tolerance of $166mm$ along the y-direction. In contrast, the total misalignment tolerance of the conventional design is observed to be $86mm$. The results are compared with the conventional planar coil design ($\theta = 0^o$) and are presented in 2D plots shown in Figure 4.5. Later simulation is performed in Ansys HFSS v18.0 where the proposed structure is designed and then exported to Ansys simplorer as shown in Figure. 4.6. The Tx and Rx coils are resonated by connecting external capacitors, $C_T$ and $C_R$, respectively. The source voltage, $V_s$, is adjusted to achieve a current of $1A$ through the Tx-coil, which is measured by an ammeter indicating current $I_T$. To measure the induced voltage for different misaligned positions of the Rx, a voltmeter is connected across its terminals. The simulation results are validated and well-corroborated with the
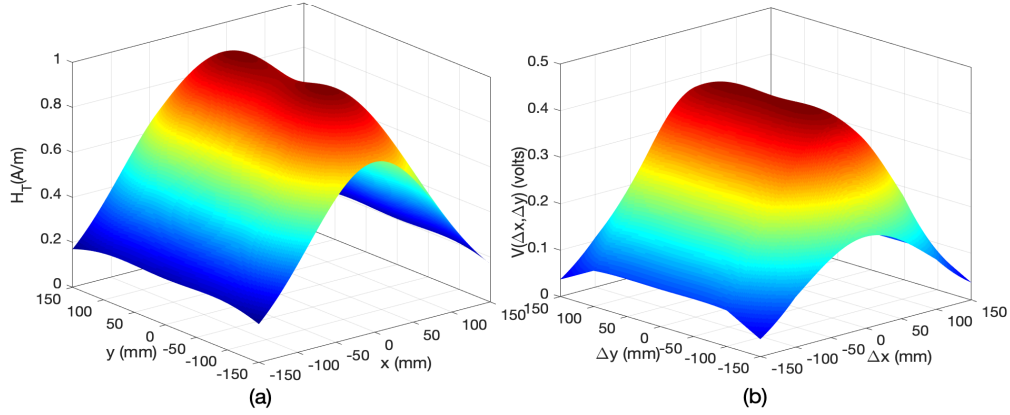
Figure 4.4: Optimal trapezoidal multi-coil antenna (Design-1A) (a) $H_T$, (b) $V(0, \Delta y)$.
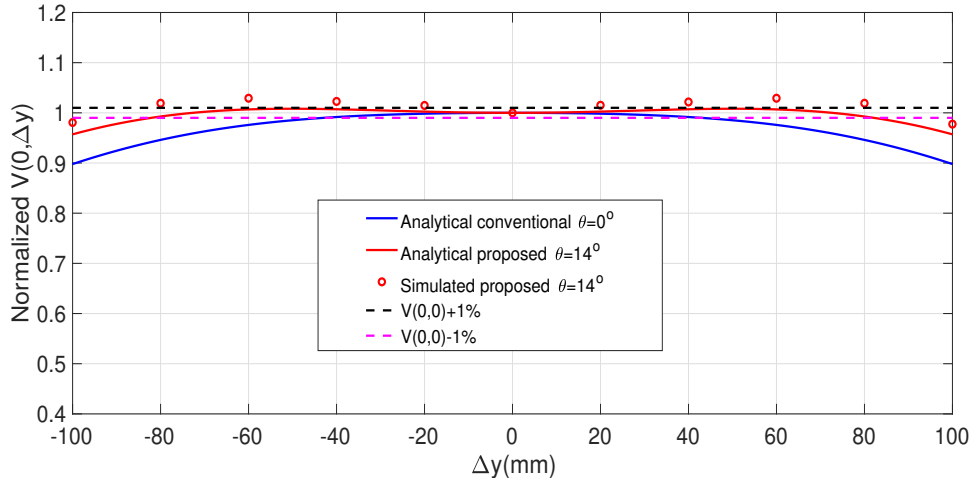


Figure 4.5: Normalized $V(0, \Delta y)$ versus Rx misalignment along y-direction.
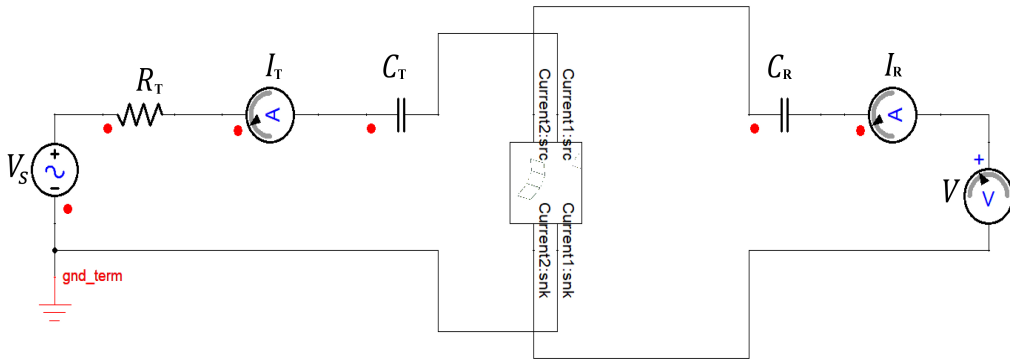


Figure 4.6: Circuit simulation of Design-1A using Ansys simplorer.

analytical results, as depicted in Figure 4.5. However, the UF of Design-1A is evaluated for only one dimension, i.e., along the y-direction, which does not guarantee its true

misalignment tolerance in the Rx coil region in 2D coverage. Moreover, due to the 3D trapezoidal structure, practical challenges in terms of positioning persist with Design-1A. These limitations made us to evolve towards planar Tx coil Design-1B. .

## 4.2   System Configuration of Design-1B (SO-B: EP-2)

A prototype of planar Tx and misaligned Tx coil is depicted in Figure. 4.7. In the proposed
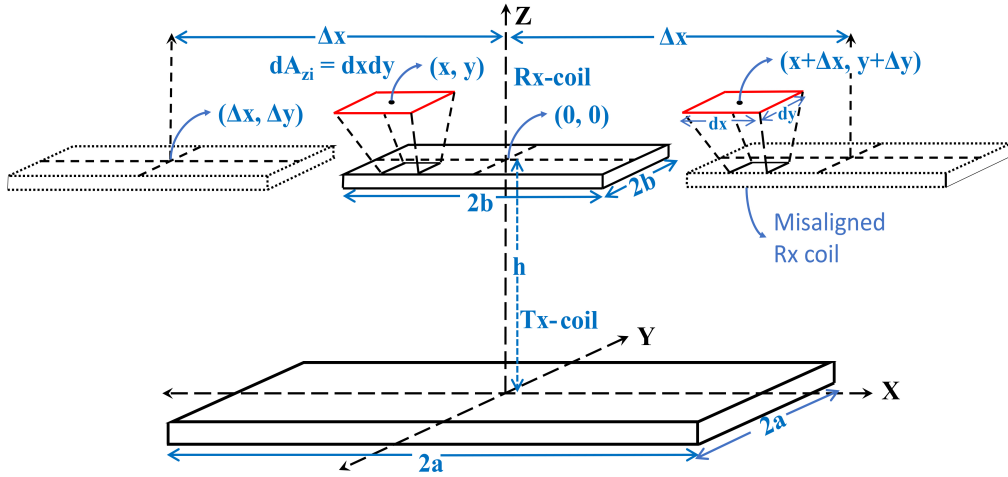


Figure 4.7: A generic WPT system under lateral misalignment condition.

analytical model, the Tx coil with $N_t$ number of equispaced square turns of side length $2a_n \forall$ integer $n \in [1, N_t]$. The dimensions of the turns are evaluated as $2a_n = 2a - 2(n - 1)(g_T + w_T)$, where $g_T$ is turn-to-turn spacing and $w_T$ is width of the conductor strip of the Tx coil. For a multi-turn Tx, total magnetic-field is evaluated by replacing $H_z(x, y)$ with $H_z^n(x, y)$ in (2.3) and by summing the magnetic field distribution due to individual turn each carrying a current $I_T$. Using (2.3), the total magnetic-field in the Rx plane can be obtained as

$$H_z(x, y) = \sum_{n=1}^{N_t} \xi_n . H_z^n(x, y) \tag{4.7}$$

To optimize the Design-1B of the Tx coil and improve its performance, the approach involves defining the coefficient of current circulation for the $n^{th}$ turn, which is represented by $\xi_n$. The value of $\xi_n$ is assigned as either 0, +1, or -1, where a value of $\xi_n = 0$ indicates that the corresponding turn does not exist, while $\xi_n = \pm 1$ represents the constructive or destructive contribution of the $n^{th}$ turn to the total magnetic field. This approach allows the Tx coil to adopt a non-uniformly distributed turns structure, which is optimized to meet the desired performance criteria. It is worth noting that turns with $\xi_n = 0$ are not included in the actual number of turns, and therefore, the realized Tx coil consists of $N't = \sum 1^{N_t} |\xi_n|$ turns in practice. This optimization technique enables the Tx coil to achieve better performance and efficiency compared to conventional designs. At the Rx side, a

square coil having dimensional parameters $2b$ units and number of turns $N_r$ is located in $z = h$ plane as shown in Figure. 4.7. However, in this case Rx coil consists of equispaced square turns of side length $2b_i \forall$ integer $i \in [1, N_r]$ evaluated as $2b_i = 2b - 2(i-1)(g_R + w_R)$, where $g_R$ and $w_R$ are turn-to-turn spacing and width of the conductor strip of the Rx coil, respectively. Let $A_{zi}$ is the area of $i^{th}$ turn and the Rx is located in $z = h$ plane at (0,0) in perfectly aligned position. The Rx is now assumed laterally misaligned to location $(\Delta x, \Delta y)$ as shown in Figure. 4.7. The total induced voltage due to misaligned Rx coil antenna for $i^{th}$ turn of the Rx coil can be evaluated by substituting (4.7) in (2.7) as

$$V(\Delta x, \Delta y) = j\omega\mu_o \sum_{i=1}^{N_r} \iint_{A_{zi}} \left[ \sum_{n=1}^{N_t} \xi_n . H_z^n(x,y) \right] dA_{zi} \qquad (4.8)$$

Hence for the misaligned Rx, the $M(\Delta x, \Delta y)$ can be evaluated by substituting (4.8) in(2.8) as

$$M(\Delta x, \Delta y) = \frac{\mu_o}{I_T} \sum_{i=1}^{N_r} \iint_{A_{zi}} \left[ \sum_{n=1}^{N_t} \xi_n . H_z^n(x,y) \right] dA_{zi} \qquad (4.9)$$

The output-power and PTE equations for a misaligned Rx coil $(\Delta x, \Delta y)$ in the Rx-plane region can be obtained by replacing (4.9) in (2.15) and (2.16).

The above formulated equations are valid for a range of frequencies for which the current is uniformly distributed along the tracks, which implies that the Tx coil is electrically small for the frequency of the single tone transmitting signal. It can be observed from equation (2.16) that the PTE is a function of both $M$ and the Rx misalignment distance $(\Delta x, \Delta y)$. Furthermore, equation (4.9) indicates that, for a given Rx, the variation of $M(\Delta x, \Delta y)$ with respect to $(\Delta x, \Delta y)$ is solely determined by the $H_z^n(x,y)$ and $\xi_n$ distributions. Since the $H_z^n(x,y)$ function in equation (4.7) is fixed for a predefined turn, the only parameters available for optimization are the number of turns $N_t'$ and the current coefficients $\xi_n$. Following this observation, the proposed field-forming technique is applied to equation (4.7) in order to find the optimal $N_t'$ and $\xi_n$ distribution by optimizing the Tx coil parameters.

### 4.2.1 Optimization problem for the magnetic field forming

The proposed optimization problem is based on field forming technique using Q-assisted MMSE algorithm where the MMSE is calculated between the targeted magnetic field $(H_T(x,y))$ distribution and the calculated magnetic field $(H_z(x,y))$ formed in the desired range $x, y \in [-r, r]$ within the Rx plane. The value of $r$ determines the displacement range (maximum working region) of the Rx coil and defines the area in the Rx plane within which uniform magnetic field is targeted. The objective is to achieve a uniform magnetic field in the Rx plane to mitigate lateral misalignment, therefore, $H_T(x,y) = H_o \quad \forall \ x, y \in [-r, r]$ is set where $H_o$ is the targeted peak magnetic field required at the location $(0, 0, h)$. To maximize the Q-factor which is constrained by minimizing MSE for forming uniform magnetic field, an optimization problem is formulated to synthesize the Tx coil antenna

(to find $N_t^{'}$, $\xi_n$) below:

$$\max_{N_t^{'},\xi_n} \quad Q(N_t^{'},\xi_n)$$

$$\text{s.t.} \quad \Delta \left| \left( \min_{N_t^{'},\xi_n} \quad MSE = \overline{[H_z(x,y) - H_T(x,y)]^2} \right) \right| \leq 1\%$$

$$\text{s.t.} \quad S_{Tn} \leq 2a, \quad \xi_n \in (-1,0,1)$$

$$H_T(x,y) = \begin{cases} H_o & \text{for} \quad -r \leq x,y \leq r \\ 0 & \text{otherwise} \end{cases} \tag{4.10}$$

where, $\Delta(.)$ denotes percentage deviation. The steps for magnetic field forming are described in the following.

- Define the target function $H_T(x,y)$ for desired range $[-r,r]$ and physical dimension limits $2a$ and $2b$.

- Evolution of Tx coil antenna (Design-1B) to achieve the defined objective function (4.10) using the Q-assisted MMSE based optimization.

- Determine the $V(\Delta x, \Delta y)$ under lateral misalignment using (4.8).

- Determine $M(\Delta x, \Delta y)$ using (4.9) and quantify the uniformity.

- Validate the improvement in lateral misalignment by the proposed Design-1B Tx coil antenna.

To solve the optimization problem (4.10), an algorithm is adopted in Section-4.2.3.

### 4.2.2   Proposed Design-1B coil for Q-assisted widespread uniformity of the magnetic field distribution

The solution to the optimization problem (4.10) is presented in this section. As a result, a Q-assisted Tx coil (Design-1B) is proposed to form the targeted field with wide uniformity. For a fair comparison with the coventional literature design discussed in chapter-2, the maximum dimension of the Design-1B Tx coil antenna is constrained and the results are compared with the design proposed in [1]. The algorithm is initialized with a set of design constraints and initial values of the optimization parameters.

The design constraints on the Tx parameters $2a$, minimum inner side length $S_{Tm}$, $g_T$, $w_T$, and the Rx parameters $2b$, inner side length $S_{Rm}$, $N_r$, $g_R$, $w_R$ and general parameters are selected based on fabrication limit and comparative study with [1] and listed in Table 4.2. The target magnetic field parameter is set to $H_o = 23.55\text{A/m}$ assuming the feed current is 1A, and aimed uniformity is considered in the range 70 mm $\leq r \leq$ 100 mm during optimization. The algorithm adopted here is an iterative process based on Q-assisted MMSE as given in (4.10) and summarized in a flow chart presented in Figure. 4.8. By the algorithm initialized with these values, the optimization reveals optimal design parameters

Table 4.2: Design parameter values of the Design-1B Tx coil and the distributed Rx coil

| Tx parameters | Rx parameters | General parameters |
|---|---|---|
| $2a = 200$ mm | $2b = 100$ mm | $f = 488.6$ kHz |
| $S_{Tm} = 16$ mm | $S_{Rm} = 77$ mm | $I_T = 1$ A |
| $w_T = 0.5$ mm | $w_R = 0.5$ mm | $h = 50$ mm |
| $g_T = 1.5$ mm | $g_R = 0.5$ mm | |
| $H_o = 23.5521$ A/m | $N_r = 12$ | |
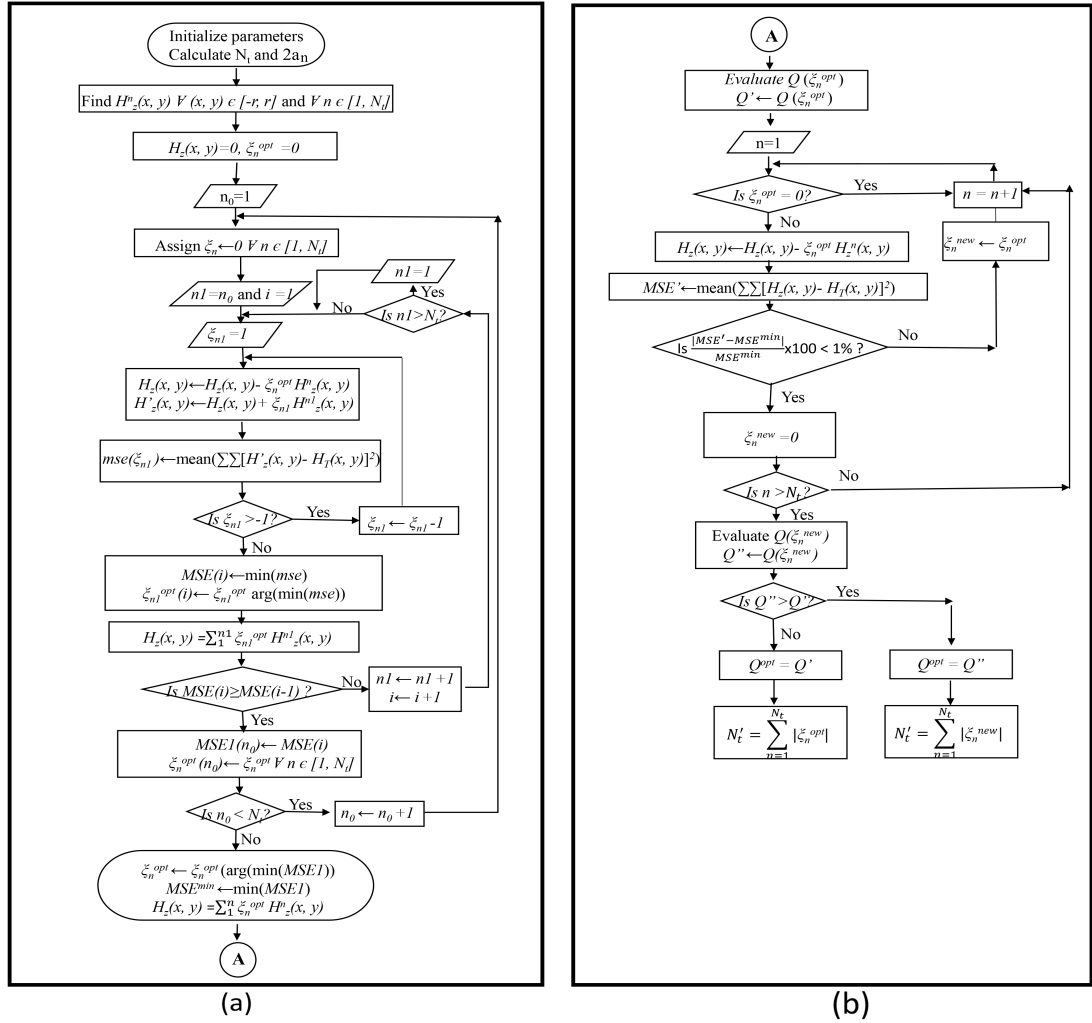


Figure 4.8: Flow chart for developing Design-1B (a) Step-1 to Step-7 (b) Step-8 to Step-14.

$N_t'$ and $\xi_n$ of the proposed Tx antenna. A detailed description of the adopted design algorithm summarized in Figure. 4.8 is now presented.

### 4.2.3   Optimization algorithm for the Tx coil design

**Step-1:** Initiate the parameter values for $2a$, $S_{Tm}$, $w_T$, and $g_T$. Determine the maximum number of turns possible for the Tx coil as

$$N_t = \frac{2a - S_{Tm}}{2(w_T + g_T)} + 1.$$

Compute the dimensions of each turn, $S_{Tn}$, where $n$ is an integer in the range of $[1, N_t]$, using the formula $2a_n = 2a - 2(n-1)(w_T + g_T)$.

**Step-2:** The magnetic field of each turn $H_z^n(x, y)$ at the $z = h$ plane can be evaluated using equation (2.3), where $x$ and $y$ are in the range $[-r, r]$. To obtain numerical results, we discretize samples at intervals of $dx = dy = 0.1$ mm for each point $(x, y)$. These values are stored in a matrix $H_z^n(x, y)$ for $1 \leq n \leq N_t$. The total number of samples stored is $N_s = \frac{4r^2}{dxdy}$. Additionally, the matrix $H_T(x, y)$ can be discretely defined based on the condition given in equation (4.10).

The total magnetic field $H_z(x, y)$ at a point $(x, y)$ is determined by the current coefficient $\xi_n$ of each turn using equation (4.7). To evaluate the accuracy of $H_z(x, y)$, we calculate the mean square error (MSE) between $H_z(x, y)$ and $H_T(x, y)$ for all discrete samples using optimization problem (4.10). The MSE is computed as $MSE = \left( \sum_x \sum_y [H_z(x, y) - H_T(x, y)]^2 \right) / N_s$. In subsequent steps, we determine the optimal $\xi_n$ values that correspond to minimum MSE (MMSE).

**Step-3:** Setting $\xi_n = 0$ for $n \in [1, N_t]$ results in $H_z(x, y) = 0$ for all $(x, y)$.

**Step-4:** For each turn $n$, the $H_z(x, y)$ is updated by adding the contribution of $\xi_n H_z^n(x, y)$ using the formula $H_z(x, y) \leftarrow H_z(x, y) + \xi_n H_z^n(x, y)$. We then calculate the $MSE(\xi_n)$ separately for three cases where $\xi_n$ takes values of $0$, $+1$, and $-1$. The optimal $\xi_n$ value for that particular turn is chosen based on the minimum $MSE(\xi_n)$ value. Finally, we update $\xi_n$ with the chosen optimal value.

**Step-5:** Starting from an arbitrary turn $n_0$, we run Step-4 for all turns from $n = N_t$ to $n = 1$. During this process, we add the optimal contribution $\xi_n H_z^n(x, y)$ of each turn to $H_z(x, y)$, while simultaneously computing the MMSE with the cumulative effect of all the optimized previous turns. For each subsequent turn, we select the corresponding optimal $\xi$ and store the corresponding $MSE$ value. As the process iterates, the stored $MSE$ decreases, and the cumulative $H_z(x, y)$ approaches $H_T(x, y)$. This process continues cyclically from the outermost to the innermost turn until the $MSE$ converges. As a result, we reveal the optimal profile $\xi \rightarrow \xi^{opt}$ for a particular initial $n_0$, and store the final $MSE$ in $MSE(n_0)$.

**Step-6:** Repeat Step-5 for all possible starting points $n_0 \in [1, N_t]$ and evaluate the corresponding $MSE(n_0)$. We then select the $\xi^{opt}$ profile that corresponds to the minimum $MSE(n_0)$ and update it as the optimal solution.

**Step-7:** Repeat Steps 2 to 6 for all uniformity target ranges $r$ and select the $\xi^{opt}$ profile with the minimum overall $MSE^{min}$.

**Step-8:** Evaluate the quality factor for the $\xi_n^{opt}$ profile and designate it as $Q' \leftarrow Q(\xi_n^{opt})$.

**Step-9:** Initialize $n = 1$ (outermost turn) where $n \in [1, N_t]$. For each value of $n$ check the condition $\xi_n^{opt} = 0$. If the condition is true, then move to the next turn.

**Step-10:** If the condition in Step-10 fails (i.e. $\xi_n^{opt} \neq 0$), then the effect of magnetic field due to that corresponding $n^{th}$ turn is removed as $H_z(x,y) \leftarrow H_z(x,y) - \xi_n^{opt} H_z^n(x,y)$ and calculate $MSE'(\xi_n^{opt})$.

**Step-11:** The percentage deviation between $MSE'$ (calculated in Step-10) and $MSE^{min}$ (calculated in Step-7 ) is found as shown in Figure. 4.8(b). If the percentage deviations is greater than 1% then skip the turn.

**Step-12:** In contrast to Step-11, if the percentage deviation is under 1% limit, the corresponding $n^{th}$ turn is designated as the insignificant turn in the formation of widespread uniform magnetic field and thus, discard it from the $\xi_n^{opt}$ profile and update the $\xi_n^{opt}$ profile.

**Step-13:** Repeat Step-10 to Step-12 until all the turns $N_t$ given in Step-1 has been exploited to check the insignificant turns to be discarded from $\xi_n^{opt}$ profile.

**Step-14:** Evaluate quality factor corresponding to modified $\xi^{opt}$ profile and assign it as $Q'' \leftarrow Q(\xi_n^{opt})$. Select the optimal quality factor from $Q^{opt} \leftarrow max(Q', Q'')$.

### 4.2.4   Resulting design as an outcome of the algorithm

The procedure of Figure. 4.8 generates an optimum $\xi_n$ profile and we note that $\xi_n = 0$ implies the absence of the turn. Hence, the total number of turns in the realized coil $N_t' = \sum_1^{N_t} |\xi_n^{opt}|$ is obtained. The coil resulted from this procedure is consisting of multiple non-uniformly distributed turns having current flow in similar (for $\xi_n = +1$) or opposite (for $\xi_n = -1$) circulations. Moreover, the distribution of the turns is such that it forms several clusters of continuous turns having $\xi_n \neq 0$ and each member turn of a cluster has the same current circulation. The optimized square coil is designated as Design-1B. The proposed optimal design has $N_t' = 28$ turns distributed among four clusters. Each cluster has dimensions given by outer turn side length $2a^c$, inner turn side length $S_{Tm}^c$, number of turns $N_T^c$, and current coefficient $\xi^c$ as listed in Table 4.3. The optimal Design-1B coil

Table 4.3: Design-1B coil optimal geometrical parameters

| cluster | $2a^c$(mm) | $S_{Tm}^c$(mm) | $N_T^c$ | $\xi^c$ |
|---------|------------|----------------|---------|---------|
| cluster-1 | 200 | 152 | 13 | +1 |
| cluster-2 | 144 | 116 | 08 | -1 |
| cluster-3 | 080 | 068 | 04 | +1 |
| cluster-4 | 044 | 036 | 03 | -1 |

antenna is simulated using commercial EM simulator and its layout is shown in Figure. 4.9. The simulated Tx coil circuit parameters are $L_T = 67.707\mu H$, $R_T = 18.417\Omega$ and $Q_T = 11.28$, respectively. To note that the Q-factor is low due to high resistance of the printed tracks in the PCB technology, in contrast, a high Q-factor can be achieved for the designs by using Litz or copper wires which are later experimentally verified. Similarly, the Rx coil parameters are $L_R = 32.066\mu H$, $R_R = 5.054\Omega$, and $Q_R = 19.47$, respectively. Further
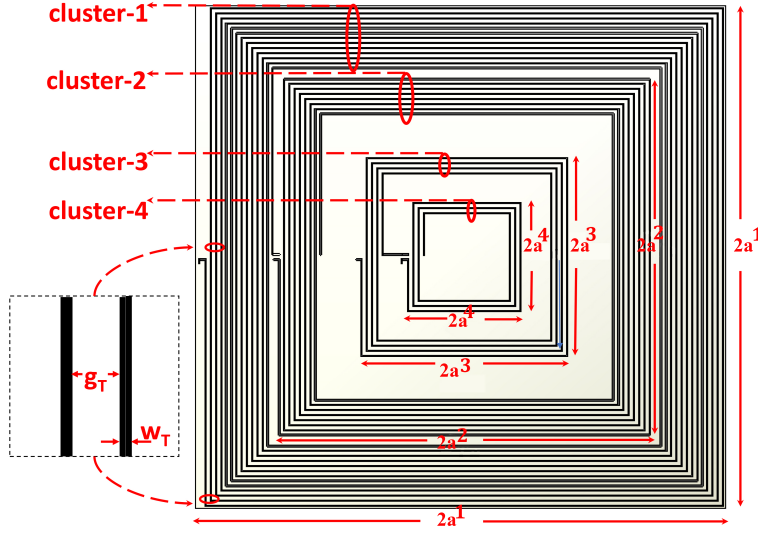
Figure 4.9: Layout of the proposed Design-1B.

analysis and result verification using EM simulator is addressed in the subsequent section.

### 4.2.5    Equispaced and Literature design

Two designs are used to compare the performance of the proposed scheme. The first is an equispaced design which is evaluated by forcing $\xi_n = 1$ in the proposed MMSE algorithm shown in Figure. 4.8 for a target $H_o = 23.55 A/m$. The resulting equispaced design consists of 7 turns with $0.5mm$ gap between the turns. The second is a convetional literature design [1] which was presented in detail in subsection 2.2 of Chapter-2. Here both the designs are simulated to evaluate their performance parameters. The simulated equispaced coil circuit parameters are $L_{equ} = 31.21\mu H$, $R_{equ} = 11.083\Omega$ and $Q_{equ} = 8.645$, respectively. Similarly, the literature coil circuit parameters are $L_{lit} = 54.56\mu H$, $R_{lit} = 15.92\Omega$, and $Q_{lit} = 10.52$, respectively.

### 4.2.6    Performance analysis and results

The performance of the Tx coil antennas is evaluated in terms of improvement in uniformity of $H_z(x,y)$ and $M(\Delta x, \Delta y)$ distributions to compare the extent of mitigation of lateral misalignment problem. The effect is reflected on PTE which is elaborated in Section 4.2.7. In Figure. 4.10, optimal 3D plots of the $H_z(x,y)$ and $M(\Delta x, \Delta y)$ distributions in the entire Rx plane are shown. As observed from Figure. 4.10(a), the values of $H_z(x,y)$ at corners for the proposed design are slightly greater in comparison to $H_o$, however, those are under the limit of UF for magnetic field. The $M(\Delta x, \Delta y)$ distributions obtained for the proposed design is similar.

The evaluation of $\text{UF}(H_z(x,y))$ and $\text{UF}(M(\Delta x, \Delta y))$ can be better visualized through 2D plots. The performance of the conventional literature design [1] and equispaced coil antenna is also evaluated and results are included for comparison purpose. The 2D
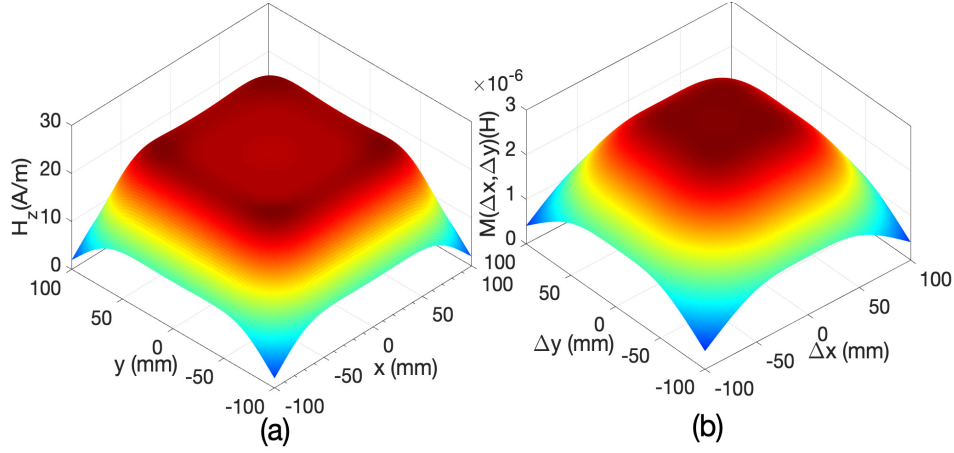
Figure 4.10: Calculated distributions of optimal Design-1B coil antenna (a) magnetic field intensity, (b) mutual inductance.

distribution of the $H_z(x,y)$ in $h = 50$ mm and $y = 0$ cut is shown in Figure. 4.11 where
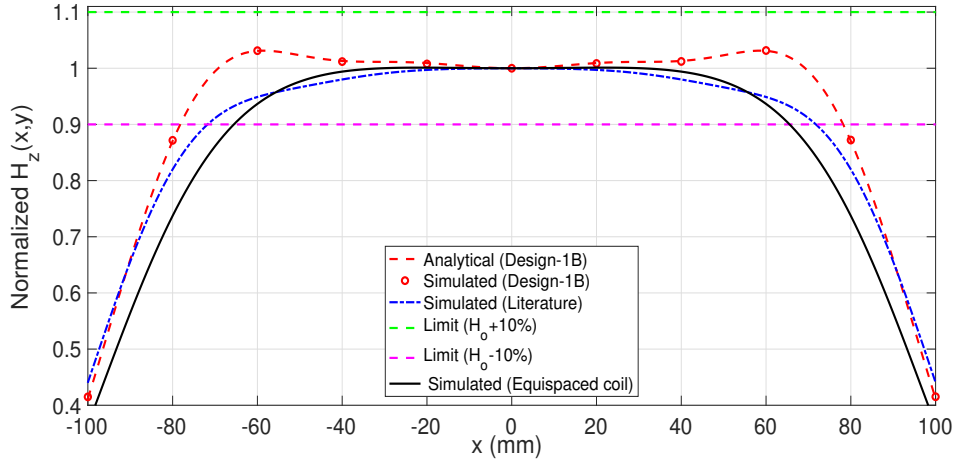


Figure 4.11: Normalized $H_z(x,y)$ distribution in $h = 50$ mm plane $y = 0$.

the values are normalized by the central value $H_o$. The results demonstrate that the uniformity of $H_z(x,y)$ is improved significantly by the proposed design compared to the design available in literature. Similarly, to quantify the performance, the $\text{UF}(H_z(x,y))$ is evaluated and calculated as 60.8%, 51.8% and 42.25% for the optimal Design-1B, the literature, and the equispaced coil designs, respectively.

The proposed design layout of Figure. 4.9 is simulated using Ansys HFSS v18.0 and the result obtained for the $H_z(x,y)$ distribution corroborates the analytical results as shown in Figure. 4.11. To evaluate performance in the lateral misalignment case, the normalized 2D variation of $M(\Delta x, \Delta y)$ with the Rx misalignment in $h = 50$ mm plane is presented in Figure. 4.12. The results indicate a significantly improved uniformity in $M$ achieved by the proposed design over the designs available in literature. In Figure. 4.12(a), for the Rx moving along $x$ direction ($\Delta y = 0$), the $M$ is uniform in the range $\Delta x \in [-38, 38]$
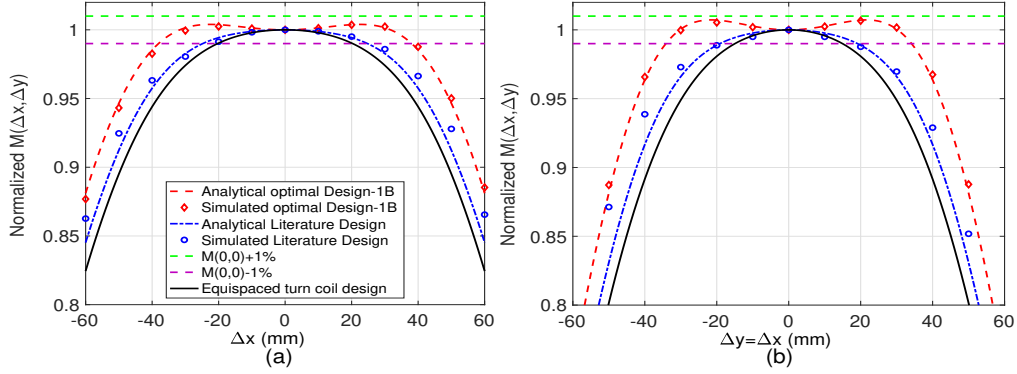
Figure 4.12: The $M(\Delta x, \Delta y)$ distribution result for the misaligned Rx (a) $\Delta y = 0$ (b) $\Delta y = \Delta x$.
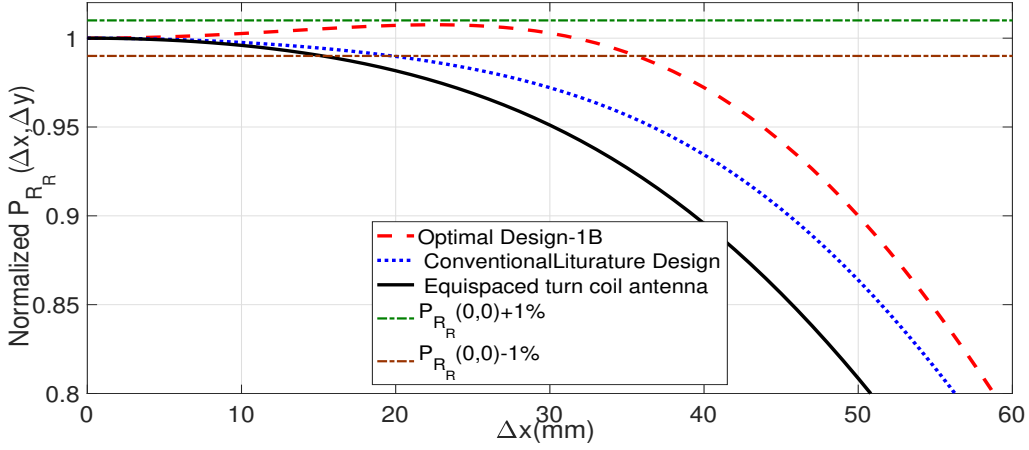


Figure 4.13: Normalized $P_{R_R}(\Delta x, \Delta y)$ in $h = 50$ mm plane for $y = 0$.

mm for the proposed optimal Design-1B coil antenna as compared to $\Delta x \in [-25, 25]$ mm range achieved by the literature design. The $UF(M(\Delta x, \Delta y))$ evaluated for the entire $h = 50$ mm plane is found as 14.44%, 6.25% and 4% for the optimal Design-1B, the literature, and the equispaced designs, respectively. The $P_{R_R}(\Delta x, \Delta y)$ is evaluated using (2.14) by considering $R_s = 0\Omega$, $R_L = 10\Omega$, and $V_s = 10V$ from [1]. The 2D plots of $P_{R_R}(\Delta x, \Delta y)$ are shown in Figure. 4.13 and its stability region is designated as $UF(P_{R_R}(\Delta x, \Delta y))$ and has similar definition as $UF(H_z(x, y))$ and $UF(M(\Delta x, \Delta y))$. From Figure. 4.13, the uniformity of normalized $P_{R_R}$ for the proposed design is in the range $\Delta x \in [-38, 38]$ mm as compared to $\Delta x \in [-19, 19]$ mm for the literature design and $\Delta x \in [-15, 15]$ mm for the equispaced design. This proves that, for the proposed design, $P_{R_R}(\Delta x, \Delta y)$ is more stable to lateral misalignment compared to the other designs. The performance is summarized and compared in Table 4.4 for the three designs.

Hence, the proposed design is shown to have high tolerance for the lateral misalignment. The simulated result of $M$ for the optimal Design-1B is included in Figure. 4.12 showing a good agreement with the analytically obtained results. The proposed antenna has improved the $UF(H_z(x, y))$ and $UF(M(\Delta x, \Delta y))$ by 17.36% and 131.04% in comparison

Table 4.4: Performance comparison of the proposed design

| Parameter | Literature design [1] | Equispaced coil design | Optimal Design-1B |
|---|---|---|---|
| UF($H_z(x,y)$) | 51.84% | 42.25% | 60.84% |
| UF($M(\Delta x, \Delta y)$) | 6.25% | 4% | 14.44% |
| UF($P_{R_R}(\Delta x, \Delta y)$) | 3.61% | 2.25% | 12.25% |

to the literature design which is a significant improvement in terms of mitigation of lateral misalignment and shows a higher PTE over the literature design for the aligned Rx case as proved in the next section.

### 4.2.7    Experimental verification of Design-1B

To prove the proposed MMSE algorithm is valid for a wide range of applications, the measurement is performed by fabricating the designs in low cost PCB materials which are preferred in low power applications such as biomedical implants [96]. Moreover, the same designs are fabricated using low loss single strand copper wire which are suitable for medium power applications such as mobile devices [1, 65].

### 4.2.8    Designs Printed in PCB

The proposed Design-1B having layout shown in Figure. 4.9 is fabricated using MITS FP-21 prototyping machine on FR4 substrate having thickness 1.6 mm, relative permittivity 4.4, loss tangent 0.02 and copper deposition of $35\mu$m. Moreover, the literature design is fabricated to have unbiased comparison with the proposed design under the same experimental conditions. The fabricated prototypes are shown in Figure. 4.14(a) exhibiting the experimental setup. The measurements are performed using Agilent N5230C Network Analyzer. The measured circuit parameters of the proposed Tx design and the Rx coil are $L_T = 68.128\mu H$, $R_T = 15.77\Omega$, $L_R = 32.68\mu H$ and $R_R = 4.96\Omega$. To resonate the WPT system at $f = 488.6$kHz, tuning capacitors $C_T = 1.55$nF and $C_R = 3.24$nF are connected in series with the proposed Tx and Rx coils, respectively. An in-house near field probe as shown in the inset of Figure. 4.14(a) is used to measure the magnetic field experimentally using a network analyzer and validate the widespread uniformity of the magnetic field resulted in the analysis. The measured $H_z(x,y)$ results plotted in Figure. 4.14(b) corroborate with the analytical results. Moreover, the power factor ($\cos(\phi)$) of the proposed system is measured as 0.99 (the phase angle between voltage and current is $\phi = 1.584^o$) which is close to unity. The $M(\Delta x, \Delta y)$ of the proposed and literature designs are measured using forward series and reverse series connection between Tx-Rx coils as aldready explained in chapter-2. The $M(\Delta x, \Delta y)$ between Tx and Rx coils is measured along y=0 line in the Rx-plane at an interval of 10 mm using DRS60L robotic arm as shown in Figure. 4.15(a) which moves the Rx precisely along the desired path From the results it can be inferred that the enhancement of max$\{M(\Delta x, \Delta y)\}$ achieved by the proposed design over the literature design whose fabricated structure is shown in the

**(a)**



**(b)**
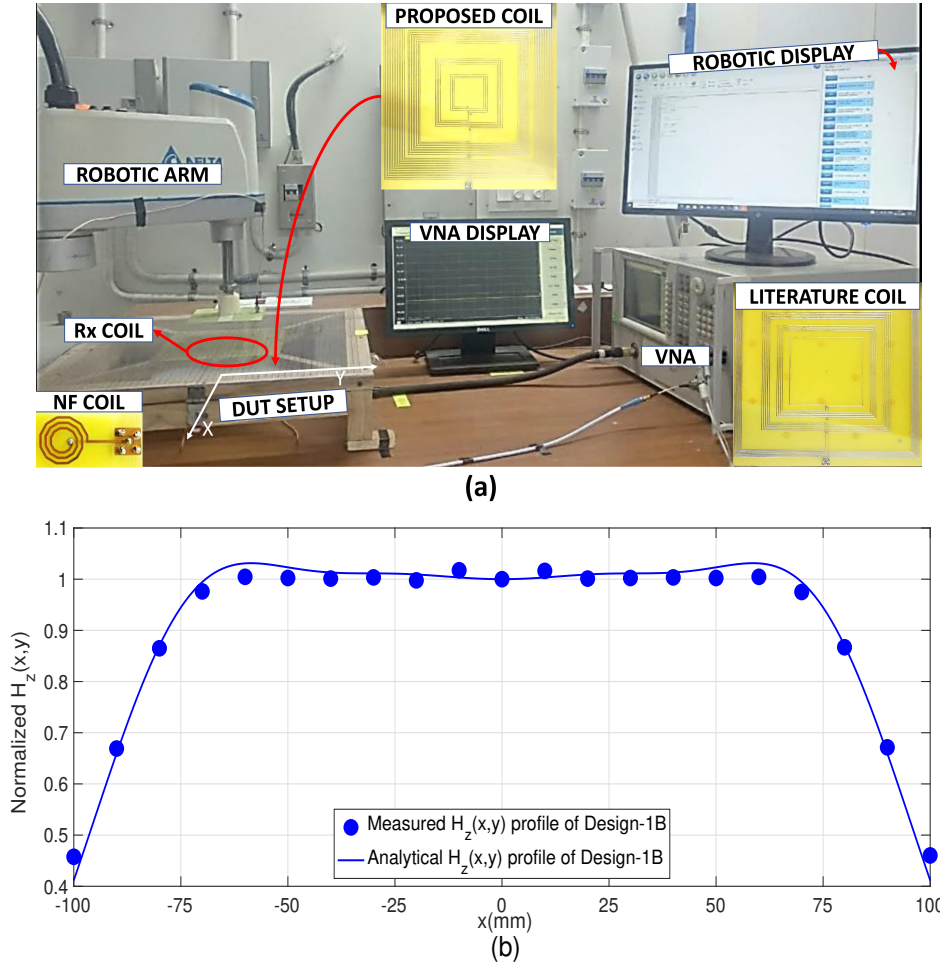
Figure 4.14: (a) Fabricated prototypes and experimental setup. (b) Measured $H_z(x,y)$ distribution for the proposed design.
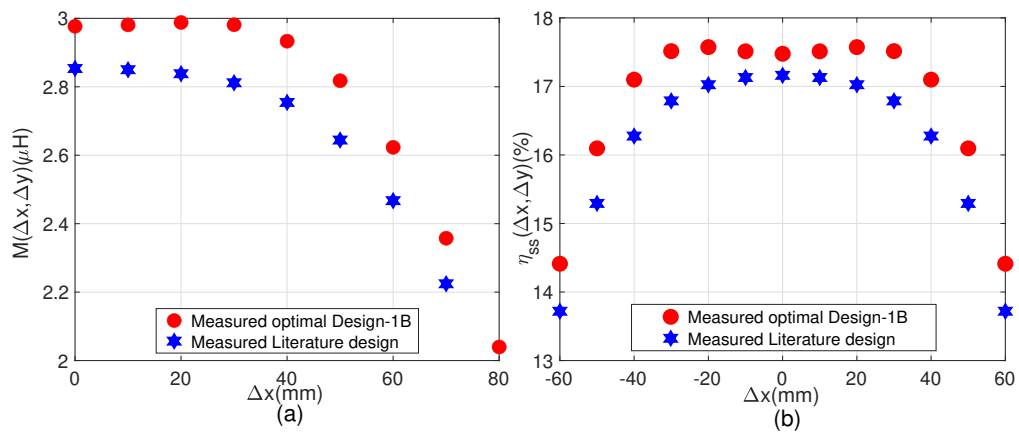


Figure 4.15: Measured results (a) $M(\Delta x, \Delta y)$ in $\mu$H along $\Delta y = 0$, (b) $\eta_{ss}(\Delta x, \Delta y)$ in % along $\Delta y = 0$.

Table 4.5: Parameters of experimental design

| Optimal Design-1B: PCB | |
|---|---|
| $R_T/L_T/R_R/L_R$ | $15.77\Omega/68.12\mu H/4.96\Omega/32.68\mu H$ |
| $C_T/C_R$ | $1.55nF/3.24nF$ |
| $M(0,0)/k/R_{ref}$ | $2.97\mu H/0.0629/5.55\Omega$ |
| $Q_T/\eta_{ss}(0,0)/P_{R_R}(0,0)$ | $13.26/17.41\%/816.7mW$ |
| **Optimal Design-1B: Enameled copper** | |
| $R_T/L_T/R_T/L_T$ | $1.94\Omega/51.66\mu H/0.72\Omega/28.91\mu H$ |
| $C_T/C_R$ | $2nF/3.6nF$ |
| $M(0,0)/k/R_{ref}$ | $2.98\mu H/0.077/7.8\Omega$ |
| $Q_T/\eta_{ss}(0,0)/P_{R_R}(0,0)$ | $81.74/74.7\%/7.66W$ |
| **Literature design: PCB** | |
| $R_{lit}/L_{lit}/M(0,0)/k/R_{ref}$ | $14.85\Omega/52.49\mu H/2.85\mu H/0.0689/5.12\Omega$ |
| $Q_{lit}/\eta_{ss}(0,0)/P_{R_R}(0,0)/C_{lit}$ | $10.85/17.16\%/859mW/2nF$ |
| **Literature design: Enameled copper** | |
| $R_{lit}/L_{lit}/M(0,0)/k/R_{ref}$ | $1.92\Omega/46.05\mu H/2.84\mu H/0.077/7.09\Omega$ |
| $Q_{lit}/\eta_{ss}(0,0)/P_{R_R}(0,0)/C_{Lit}$ | $73.63/73.4\%/8.1W/2.3nF$ |

inset of Figure. 4.14(a). This enhancement is a result of increase in the uniformity of the magnetic-field region within the region bounded by the Rx coil. The measured $\eta_{ss}(\Delta x, \Delta y)$ of the Design-1B and literature coil antennas are depicted in Figure. 4.15(b) by substituting measured circuit parameters in (2.16) under the conditions $R_s = 0\Omega$ and $R_L = 10\Omega$ [1]. The increment in peak value of $\eta_{ss}(\Delta x, \Delta y)$ is achieved due to higher Q-factor of proposed design which is measured using network analyzer as 13.26 in comparison with 10.85 for the literature design, respectively. The slight disparity in the Q values determined by simulation earlier and experiment is due to fabrication and measurement tolerances. The results show that the $\eta_{ss}(\Delta x, \Delta y)$ is stabilized (for $\pm 1\%$ variation from peak value) in range $[-36, 36]$ mm and $[-20, 20]$ mm for the proposed optimal design and the literature design, respectively. In the entire Rx plane, the lateral misalignment is mitigated in area of $72 \times 72$ mm$^2$ by the proposed design in contrast to $40 \times 40$ mm$^2$ by the literature design. The low efficiency in Figure. 4.15(b) is a result of fabricating the design in a low cost PCB layer which are suitable for biomedical and small electronic applications. Nevertheless, the proposed Q-assisted MMSE algorithm can achieve high efficiency and high Q-factor by manufacturing the designs using low loss conductive materials such as copper wires, litz wires, super conductors etc., which is explained next.

### 4.2.9   Designs Manufactured using Copper Wires

The Design-1B and literature coil antennas are manufactured through a process of engraving a conductive track on a wooden sheet using 3D laser printing, followed by the manual insertion of 20 AWG enameled copper wire into the engraved track. These steps are illustrated in Figure 4.16(a) and Figure. 4.16(b). The figures in Figure.4.16(c) and Figure.4.16(d), present the measured data of $P_{R_R}(\Delta x, \Delta y)$ and $\eta_{ss}(\Delta x, \Delta y)$ along the $y = 0$ line at an interval of 10 mm. These figures were obtained by substituting the
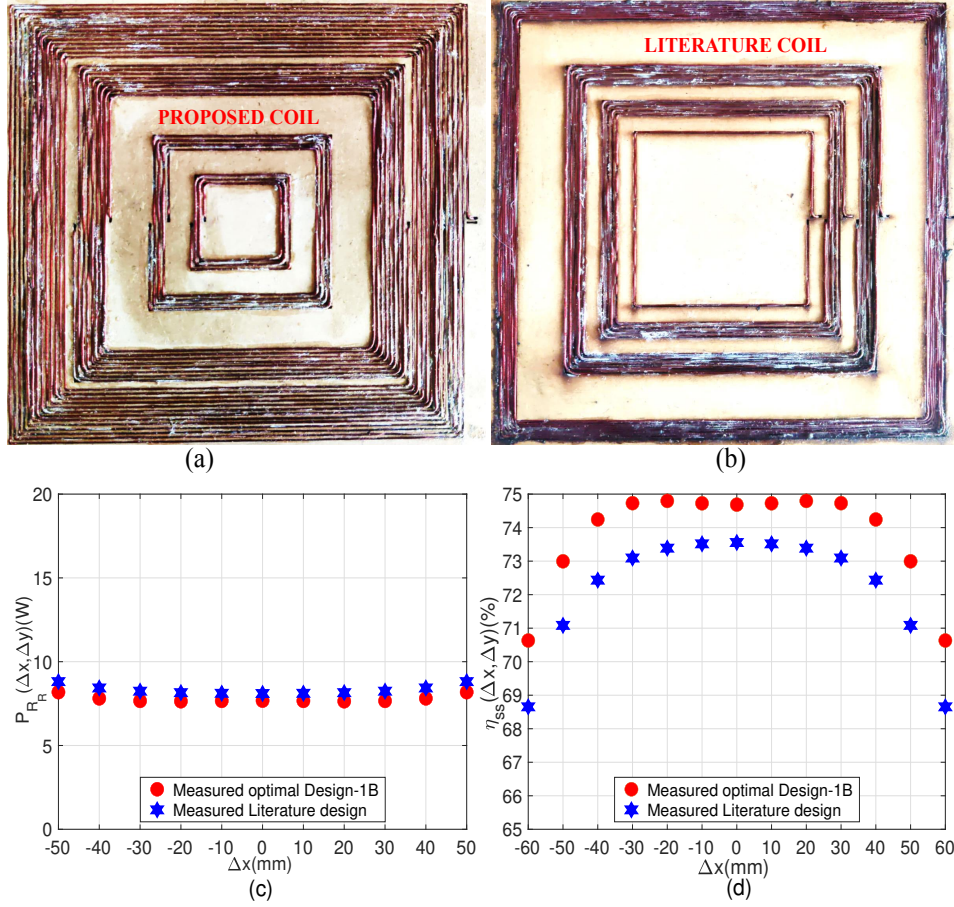
Figure 4.16: (a) Fabricated prototype of Design-1B, (b) fabricated prototype of Literature design, (c) measured $P_{R_R}(\Delta x, \Delta y)$ along $\Delta y = 0$, (d) measured $\eta_{ss}(\Delta x, \Delta y)$ along $\Delta y = 0$.

measured circuit parameters using the experimental setup depicted in Figure. 4.14(a) into (2.15) and (2.16). The proposed design's (Design-1B) $\eta_{ss}(\Delta x, \Delta y)$ surpasses that of the conventional literature design in terms of peak value, while the stability region remains the same as in the PCB design. Conversely, the measured stability of $P_{R_R}(\Delta x, \Delta y)$ is uniform within the range of $\Delta x \in [-38, 38]$ mm, unlike the conventional literature design, which is limited to $\Delta x \in [-20, 20]$ mm. The $\max\{P_{R_R}(\Delta x, \Delta y)\}$ value of the proposed design is slightly less than conventional literature design to achieve the higher misalignment tolerance compared to literature design. This proves the proposed Q-assisted MMSE based optimized design namely Design-1B Tx coil antenna has a good potential to mitigate the lateral misalignment problem in the desired Rx region. The circuit parameters of the proposed design are summarized in Table 4.5. Where $k$ is the coefficient of coupling, and $R_{ref}$ is the reflected impedance. Despite the enhanced lateral misalignment tolerance achieved through the use of Design-1B, which forms a widely spread uniform magnetic field, there is still a lack of mathematical justification for ensuring that the optimal magnetic field distribution is indeed uniform. To address this issue, an analytical framework with the aim to determine the optimal magnetic field distribution resulting in a uniform induced voltage

for a misaligned Rx coil antenna is explored. This framework adopts a target objective that is specifically tailored towards achieving the desired uniformity in the induced voltage, thereby providing a more comprehensive understanding of the relationship between the magnetic field distribution and its impact on the uniformity on induced voltage. As a result a new Tx coil antenna Design-1C is investigated.

## 4.3   WPT system configuration of Design-1C (SO-B: EP-3)

A general configuration of prototype of Design-1C Tx coil antenna which consists of a spatially distributed multi coil array is depicted in Figure. 4.17. Similar to Figure. 4.7,
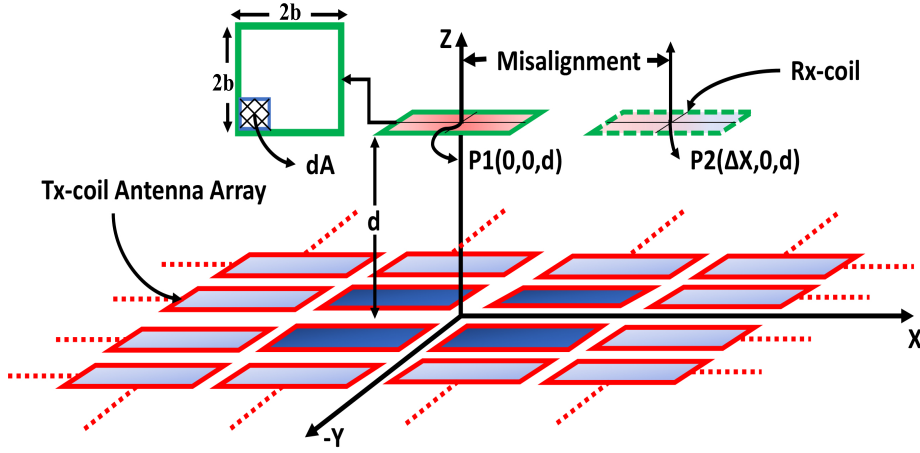


Figure 4.17: Schematic diagram of the considered WPT system.

in Figure. 4.17, the Rx coil location at P1 denotes perfectly aligned with the Tx and the misaligned Rx coil location is shown at P2. As per the Design-1B, the magnetic-field distribution should be uniform to achieve a uniform $V(\Delta x, \Delta y)$ over the entire area where the Rx is expected to move. However, when the Rx coil is misaligned laterally along the x-axis as shown in Figure. 4.17, the value of $V(\Delta x, \Delta y)$ is not as uniform as magnetic field distribution from previous designs.

### 4.3.1   Significance of the induced voltage as design objective

From the observation of equations (2.6), (2.8), and (2.16) the misalignment of Rx coil $(\Delta x, \Delta y)$ mainly depends on $V(\Delta x, \Delta y)$ for a given Tx and a Rx antenna. Therefore, for predefined Tx and Rx designs, the variation in $V(\Delta x, \Delta y)$ with the Rx displacement is the cause of lateral misalignment problem. To obtain a stable $\eta_{ss}(\Delta x, \Delta y)$ and mitigate lateral misalignment problem, the $V(\Delta x, \Delta y)$ should be position insensitive of the Rx coil. Hence, uniformity in $V(\Delta x, \Delta y)$ is adopted as design objective.

### 4.3.2    Induced voltage analysis for perfectly aligned Rx

The $V$ given in (2.6) is modified for a perfectly aligned Rx coil area $A_z = 2b \times 2b$ as,

$$V = j\omega\mu_o N_r \int_{-b}^{b}\int_{-b}^{b} H_z(x,y)dxdy \tag{4.11}$$

which represents the total $V$ when the Rx coil is in complete alignment with its center located at $(0, 0, h)$. In case of misalignment, the $V$ may vary due to change in $H_z(x,y)$ distribution enclosed within the Rx coil area.

### 4.3.3    Proposed analytical model for Induced voltage and magnetic field for misaligned Rx

**Analysis of $V$ in case of the misaligned Rx**

To analyze the effect of misalignment on $V$, the Rx coil center is assumed shifted by $\Delta x$ and $\Delta y$ along the x and y directions, respectively, with new location $(\Delta x, \Delta y, h)$ of its center. Now, the Rx area $A_z$ is defined in terms of a 2D unit step function as

$$A_z = \int_{-\infty}^{+\infty}\int_{-\infty}^{+\infty} A_r(x,y)\,dx\,dy, \tag{4.12}$$

$$A_r(x,y) = \begin{cases} 1 & \text{for } -b \leq x \leq b \text{ and } -b \leq y \leq b \\ 0 & \text{otherwise} \end{cases} \tag{4.13}$$

where $A_r(x,y)$ represents area function of the Rx in space. The $A_r(x,y)$ is a rectangular function since we considered that the Rx coil is a square. For other shapes of the Rx coil e.g., circular, the $A_r(x,y)$ can be defined accordingly. Using the definitions (4.12)-(4.13), induced voltage, $V'(0,0)$, in the Rx coil under perfectly aligned condition is re-formulated from (4.11) as

$$V'(0,0) = j\omega\mu_o N_r \int_{-\infty}^{+\infty}\int_{-\infty}^{+\infty} H_z(x,y)A_r(x,y)\,dx\,dy. \tag{4.14}$$

Now the Rx coil is assumed shifted to $(\Delta x, \Delta y, h)$. The misaligned Rx coil can be represented by corresponding shift in the area function as $A_r(x - \Delta x, y - \Delta y)$. The induced voltage, $V'(\Delta x, \Delta y)$, for misalignment case is obtained

$$V'(\Delta x, \Delta y) = j\omega\mu_o N_r \int_{-\infty}^{+\infty}\int_{-\infty}^{+\infty} [H_z(x,y)A_r(x-\Delta x, y-\Delta y)]dxdy \tag{4.15}$$

Further, for analytical equivalence, the $V'$ is normalized by a factor $V_0 = j\omega\mu_o N_r$ to give normalized induced voltage $V = V'/V_0$. Since the general expression of a continuous space domain 2D convolution $[*]$ is given by [97]

$$\begin{aligned} g(X',Y') &= f_1(X,Y) * f_2(X,Y) \\ &= \int_{-\infty}^{+\infty}\int_{-\infty}^{+\infty} f_1(X,Y)f_2(X - X', Y - Y')\,dX\,dY \end{aligned} \tag{4.16}$$

A careful comparison of (4.15) with (4.16) reveals that **the normalized induced voltage function for misalignment case is convolution of H-field distribution and Rx area function**, hence,

$$V(\Delta x, \Delta y) = H_z(x, y) * A_r(x, y) \tag{4.17}$$

Here, $(x, y)$ and $(\Delta x, \Delta y)$, both are space variables, however, former denotes coordinate of any point in the Rx plane, whereas, latter represents misalignment of the Rx coil center from the original location in the coordinate system.

**Optimal $H_z(x, y)$ solution for any objective $V(\Delta x, \Delta y)$**

It is noted from (4.17) that the $V$ is a function of misalignment $(\Delta x, \Delta y)$ and its shape is determined by the shapes of $H_z(x, y)$ and $A_r(x, y)$. Since $A_r(x, y)$ is predefined as rectangular shapes in (4.13), the $V(\Delta x, \Delta y)$ shape in (4.17) depends solely on $H_z$ distribution. Therefore, a solution of optimal $H_z$ distribution to achieve any objective $V(\Delta x, \Delta y)$ shape is now derived using Fourier analysis. Applying Fourier Transform (FT) on (4.17) gives $\text{FT}[V(\Delta x, \Delta y)] = \text{FT}[H_z(x, y) * A_r(x, y)]$ which is further solved for optimal $H_z$ by using convolution property $\text{FT}[X * Y] = \text{FT}[X].\text{FT}[Y]$ to obtain

$$
\begin{aligned}
\text{FT}[V(\Delta x, \Delta y)] &= \text{FT}[H_z(x, y)].\text{FT}[A_r(x, y)] \\
\Rightarrow \text{FT}[H_z(x, y)] &= \frac{\text{FT}[V(\Delta x, \Delta y)]}{\text{FT}[A_r(x, y)]} \\
\Rightarrow H_z(x, y) &= \text{IFT}\left[ \frac{\text{FT}[V(\Delta x, \Delta y)]}{\text{FT}[A_r(x, y)]} \right]
\end{aligned}
\tag{4.18}
$$

where IFT is the inverse Fourier transform operation. Since 2D Fourier analysis is involved, (4.18) is solved numerically, however, a closed form solution can be obtained using separation of variables method by dividing the problem in to 1D. For instance, the 2D spacial functions, $V(\Delta x, \Delta y)$ and $A_r(x, y)$, are realized being separable in $x$ and $y$ directions. Let $V(\Delta x, \Delta y) = V^x(\Delta x) \cdot V^y(\Delta y)$. Therefore, to define an objective $V$, $V^x$ and $V^y$ can be defined individually. Similarly, $A_r(x, y) = A^x(x) \cdot A^y(y)$ is separable from (4.13) into

$$
A^{x/y}(x/y) = \begin{cases} 1 & -b \le x/y \le b \\ 0 & \text{otherwise} \end{cases}
\tag{4.19}
$$

This is used in (4.18) to simplify optimal $H_z$ solution as

$$
H_z(x, y) = \text{IFT}\left[ \frac{\text{FT}\left[V^x(\Delta x) \cdot V^y(\Delta y)\right]}{\text{FT}\left[A^x(x) \cdot A^y(y)\right]} \right]
$$

Using separability and linearity property of the FT we obtain

$$
H_z(x, y) = \text{IFT}\left[ \frac{\text{FT}\left[V^x(\Delta x)\right] \cdot \text{FT}\left[V^y(\Delta y)\right]}{\text{FT}\left[A^x(x)\right] \cdot \text{FT}\left[A^y(y)\right]} \right]
\tag{4.20}
$$

Hence, the optimal solution of $H_z(x,y)$ distribution to achieve any objective $V(\Delta x, \Delta y)$ function is obtained in (4.20). Now, the $H_z$ solution to obtain specific $V$ distribution is presented.

### 4.3.4   Objective function for an ideal $V(\Delta x, \Delta y)$ in the Rx coil

As discussed in Section 4.3.1, ideally, $V$ should be independent of $(\Delta x, \Delta y)$. To mitigate lateral misalignment for Rx displacement range $|\Delta x|, |\Delta y| \leq v$, the ideal target $V(\Delta x, \Delta y)$ shape defines the objective function as,

$$\text{Find} \quad H_z(x,y)$$
$$\text{s.t. } V(\Delta x, \Delta y) = \begin{cases} 1 & -v \leq (\Delta x, \Delta y) \leq v \\ 0 & \text{otherwise} \end{cases} \tag{4.21}$$

whose corresponding separable 1D functions $V^x(\Delta x)$ and $V^y(\Delta y)$ are given by

$$V^{x/y}(\Delta x/\Delta y) = \begin{cases} 1 & -v \leq \Delta x/\Delta y \leq v \\ 0 & \text{otherwise} \end{cases} \tag{4.22}$$

The optimal $H_z$ solution of (4.21) is found by substituting FT of (4.19) and (4.22) in (4.20) as

$$H_z(x,y) = \text{IFT} \left[ \frac{\text{sinc}(v\omega_x) \cdot \text{sinc}(v\omega_y)}{\text{sinc}(b\omega_x) \cdot \text{sinc}(b\omega_y)} \right] \tag{4.23}$$

where $\omega_{x/y}$ are spacial angular frequencies along $x/y$ directions. To obtain a closed form solution of (4.23), the range, for which the lateral misalignment is mitigated, is assumed to be an integer multiple of the Rx maximum dimension i.e., $v = nb$, where $n$ is an integer. Therefore, (4.23) is expanded to

$$H_z(x,y) = \text{IFT} \left[ \frac{\text{sinc}(nb\omega_x) \cdot \text{sinc}(nb\omega_y)}{\text{sinc}(b\omega_x) \cdot \text{sinc}(b\omega_y)} \right] \tag{4.24}$$

which by using separability is written as

$$H_z(x,y) = \text{IFT} \left[ \frac{\text{sinc}(nb\omega_x)}{\text{sinc}(b\omega_x)} \right] \cdot \text{IFT} \left[ \frac{\text{sinc}(nb\omega_y)}{\text{sinc}(b\omega_y)} \right] \tag{4.25}$$

$$H_z(x,y) = H_n(x) \cdot H_n(y) \tag{4.26a}$$

$$\text{where } H_n(x/y) = \text{IFT} \left[ \frac{\text{sinc}(nb\omega_{x/y})}{\text{sinc}(b\omega_{x/y})} \right] \tag{4.26b}$$

The $H_z(x,y)$ is also separable in two identical 1D functions, $H_n(x)$ and $H_n(y)$, each in $x$ and $y$ direction, respectively. Hence, analysis of any one function in (4.26b) is sufficient and further performed to obtain the final solution. To analyze $H_n(x)$ further from (4.26b),

solution is observed for specific $n$, e.g., for $n = 1$, $H_1(x) =$ IFT[1]$= \delta(x)$, for $n = 2$,

$$H_2(x) = \text{IFT}\left[\frac{\text{sinc}(2b\omega_x)}{\text{sinc}(b\omega_x)}\right] = \delta(x - b) + \delta(x + b),$$

and for $n = 3$,

$$H_3(x) = \text{IFT}\left[\frac{\text{sinc}(3b\omega_x)}{\text{sinc}(b\omega_x)}\right] = \delta(x) + \delta(x - 2b) + \delta(x + 2b).$$

Hence, for general $n$, the solution of $H_n(x)$ is obtained as

$$H_n(x) = \begin{cases} \delta(x) + \sum_{m=1}^{\lfloor \frac{n}{2} \rfloor}[\delta(x - 2mb) + \delta(x + 2mb)] & \text{for odd } n \\ \sum_{m=1}^{\lfloor \frac{n}{2} \rfloor}[\delta(x - (2m-1)b) + \delta(x + (2m-1)b)] & \text{for even } n \end{cases} \tag{4.27}$$

The $H_n(y)$ is also given by (4.27). Hence, the $H_z(x, y)$ distribution is evaluated by substituting (4.27) in (4.26a) and represents the closed form solution of the objective (4.23). To further investigate the solution, a condition on $A_r(x, y)$ is derived to satisfy the solution (4.27) of the objective function (4.23). For this, (4.17) is rewritten in terms of separable 1D functions as

$$V^x(\Delta x) \cdot V^y(\Delta y) = [H_n(x) \cdot H_n(y)] * [A^x(x) \cdot A^y(y)]$$
$$\text{hence} \quad V^{x/y}(\Delta x/\Delta y) = \left[H_n(x/y) * A^{x/y}(x/y)\right] \tag{4.28}$$

which, in conjunction with (4.22) and for $v = nb$, shows

$$V^x(\Delta x) = 1 \ \forall \ -v \leq \Delta x \leq v$$
$$\Rightarrow A^x(x) * H_n(x) = 1 \ \forall \ -nb \leq x \leq nb \tag{4.29}$$

Substitution of $H_n(x)$ from (4.27) in (4.29) results in conditions

$$A^x(x) + \sum_{m=1}^{\lfloor \frac{n}{2} \rfloor}[A^x(x - 2mb) + A^x(x + 2mb)] = 1 \tag{4.30a}$$
$$\forall \ -nb \leq x \leq nb \quad \text{for odd } n$$

$$\sum_{m=1}^{\lfloor \frac{n}{2} \rfloor}[A^x(x - (2m-1)b) + A^x(x + (2m-1)b)] = 1 \tag{4.30b}$$
$$\forall \ -nb \leq x \leq nb \quad \text{for even } n$$

The conditions (4.30a) and (4.30b) are graphically demonstrated in Figure. 4.18. The ideal solution of $H_z(x)$ obtained in (4.27) is consisting of impulse train which upon convolution with $A^x(x)$ generates a rectangular function corresponding to a uniform $V^x(\Delta x)$ (since $V = H * A$) achieving the ideal objective function as demonstrated in Figure. 4.18. Similarly for total 2D functions, the $H_z(x, y)$ follows the same properties and corresponding
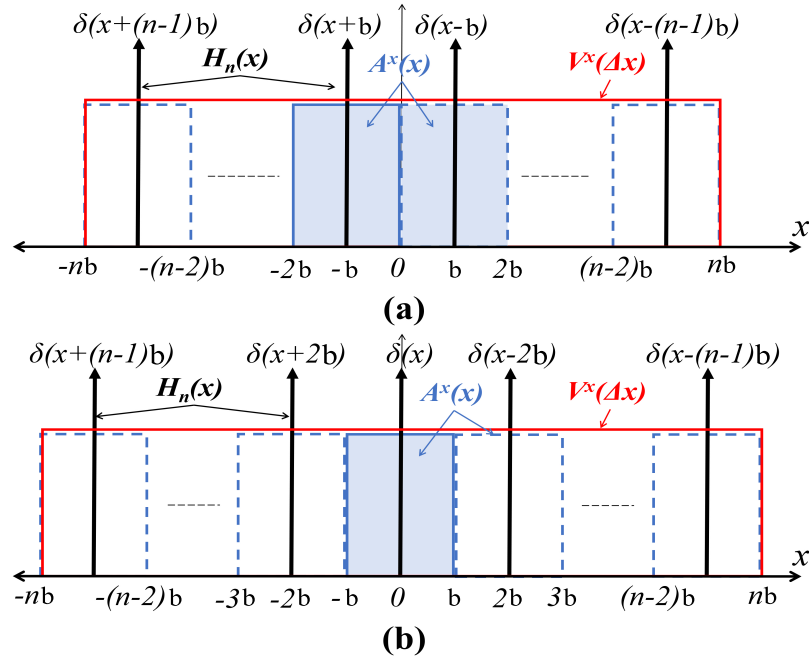
Figure 4.18: Ideal objective solution: 1D function for (a) even $n$ (b) odd $n$.

condition on $A_r(x, y)$ is visualized in Figure. 4.19 in 3D as a proof. Apparently, the uniform
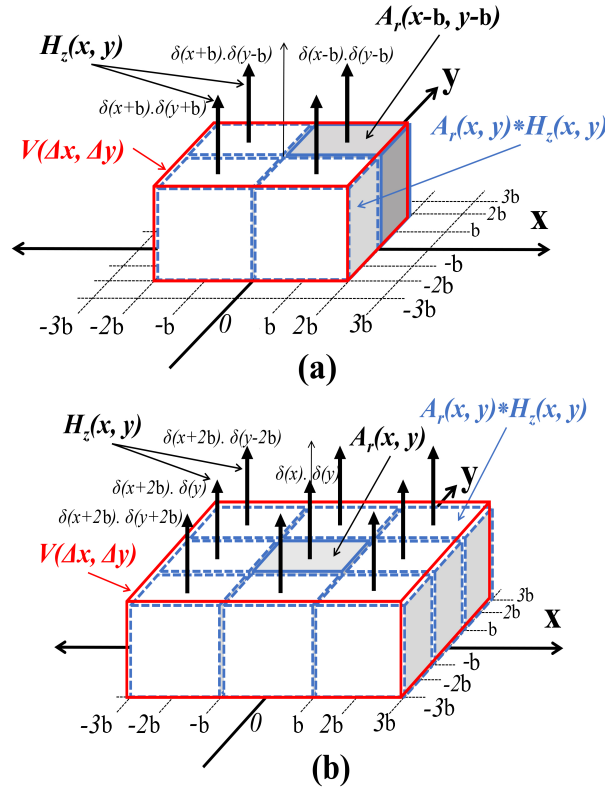


Figure 4.19: Ideal objective solution: total function for (a) $n = 2$ (b) $n = 3$.

$V$ is achieved by the optimal $H_z$ solution of (4.27).

Let us revisit the $H_z$ solution obtained in (4.27) for the ideal case where $\delta(x)$ is located at an integer multiple of $b$. Now, if we shift the $\delta(x)$ locations to an integer multiple of $b \pm \partial x$, where $\partial x$ is a fraction, the targeted range of uniformity in $V$ becomes $v = nb \pm \partial x$. In this case, if (4.27) still represents the $H_z$ solution to produce uniform $V$ in the range of $-v$ to $v$, the conditions (4.30a) and (4.30b) must be satisfied. However, these conditions encounter discontinuities (gaps) for the $v = nb + \partial x$ case and an aliasing effect for the $v = nb - \partial x$ case, respectively. These effects are demonstrated graphically for $n = 2$ in Figure.4.20 for $v = nb - \partial x$ and in Figure.4.21 for $v = nb + \partial x$. The figures presented in
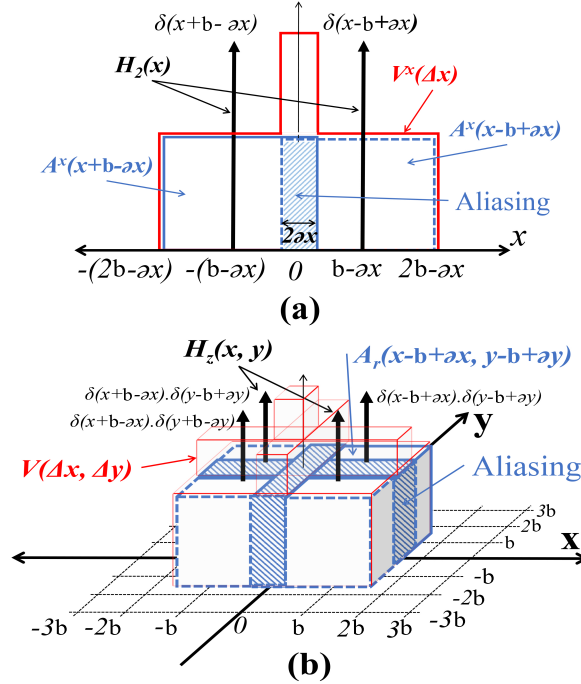


Figure 4.20: Aliasing effect for $v = 2b - \partial(x)$ (a) 1D (b) total 2D functions.

this study depict the occurrence of aliasing and discontinuity effects for both the 1D and total 2D functions. These effects create problems with the impulse train of $H_z$ in (4.27) as it is unable to produce constant $V$ values in the desired range of Rx misalignment after convolution with the rectangular function $A_r$. Thus, it is necessary to adopt periodic functions other than $\delta(x)$ to achieve a constant $V$ function. However, generating the ideal $H_z(x)$ solution of (4.27) is not feasible due to the fact that realistic distributions should not have abrupt variations.

Therefore, the objective $V$ function, which is ideally assumed to be rectangular, must be redefined to have a gradual change for a practically realizable $H_z(x)$ solution. This redefinition is crucial in ensuring that the function remains stable and produces reliable results. In summary, it is important to consider the effects of aliasing and discontinuity when designing functions and to redefine the objective function to suit realistic distributions with gradual changes.
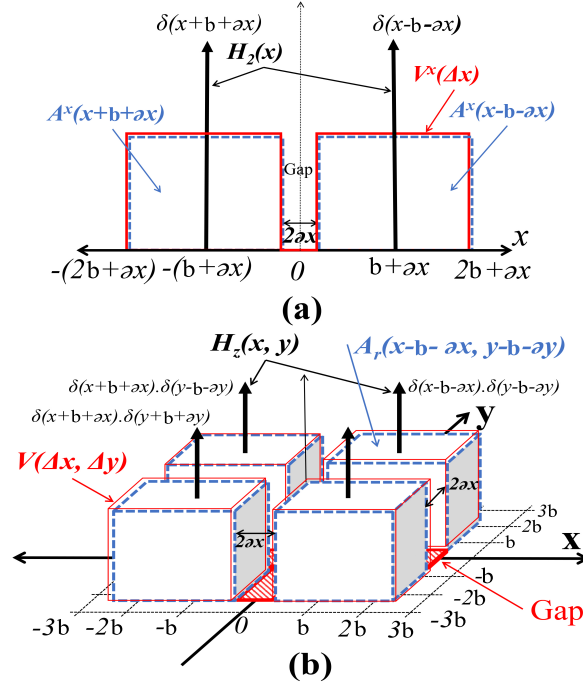
Figure 4.21: Discontinuity effect for $v = 2b + \partial(x)$ (a) 1D (b) total 2D functions.

### 4.3.5    Objective for a realistic $V(\Delta x, \Delta y)$ function

To address lateral misalignment, the objective has been modified to define a realistic $V(\Delta x, \Delta y)$ function, as shown in (4.20). Since the 2D functions are fully separable, only 1D functions in $x$ are analyzed for brevity, and the total functions can be computed by multiplication. The aim is to achieve uniformity in the range $-(v - c) \leq \Delta x \leq (v - c)$, and an arbitrary roll-off region of size $2c$ is defined by a function $K(x)$, as illustrated in Figure 4.22.

It should be noted that the uniformity in $V(\Delta x, \Delta y)$ is essential for the proper functioning of wireless power transfer systems. Therefore, a gradual change in the objective function is necessary to avoid abrupt variations in the realistic distributions. To achieve this, the arbitrary roll-off region is defined using $K(x)$, which ensures that the function smoothly changes from the uniformity region to the discontinuity region. By defining a realistic $V(\Delta x, \Delta y)$ function, it is possible to obtain a practically realizable $H_z(x)$ solution that can produce a constant $V$ function in the desired range of Rx misalignment. The objective
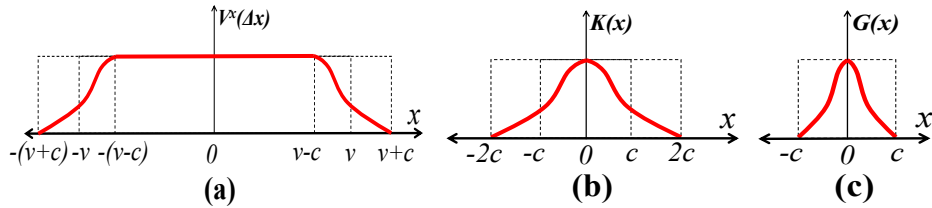


Figure 4.22: (a) Realistic $V^x(\Delta x)$ objective function (b) Roll off $K(x)$ (c) $G(x)$.

function with realistic target $V$ is defined as

$$
\text{Find} \quad H_z(x) \quad \text{s.t.}
$$

$$
V^x(\Delta x) = \begin{cases}
0 & -\infty < \Delta x \leq -(v+c) \\
K(\Delta x + v - c) & -(v+c) < \Delta x \leq -(v-c) \\
1 & -(v-c) < \Delta x \leq (v-c) \\
K(\Delta x - v + c) & (v-c) < \Delta x \leq (v+c) \\
0 & (v+c) < \Delta x < +\infty
\end{cases} \tag{4.31}
$$

The function $K(x)$ in this context represents an even function within the range $x \in [-2c, 2c]$, and its purpose is to effect gradual change, or roll-off, in $V^x(\Delta x)$ as depicted in Figure. 4.22(b). In order to determine $H_z$ to achieve the objective stated in (4.31), it is necessary to derive certain relationships that will be used later in the analysis.

**Derivation of a useful relation to find $H_z$ solution**

Define a function $G(x)$ which is related to $K(x)$ by

$$
K(x) = G(x) * rect\left(\frac{x}{2c}\right) \tag{4.32}
$$

$$
\text{hence} \quad K(x) = \int_{-c+x}^{c} G(x-\tau)d\tau \quad \text{for} \ x > 0, \tag{4.32a}
$$

$$
\text{and} \quad K(x) = \int_{-c}^{c+x} G(x-\tau)d\tau \quad \text{for} \ x < 0. \tag{4.32b}
$$

Since $K(x)$ is an even function limited in range $x \in [-2c, 2c]$, the $G(x)$ function has a range $[-c, c]$ and satisfies conditions

$$
G(x) = G(-x) \text{ and } \int_{-\infty}^{\infty} G(x)dx = \int_{-c}^{c} G(x)dx = 1 \tag{4.33}
$$

Graphical illustrations of $V^x$, $K$, and $G$ defined in (4.31), (4.32) and (4.33) are depicted in Figure. 4.22. Further, let $B(x)$ is a rectangle function defined as

$$
B(x) = rect\left(\frac{x}{2v}\right) = \begin{cases} 1 & -v \leq x \leq v \\ 0 & \text{otherwise} \end{cases} \tag{4.34}
$$

The $G(x)$ is defined in such a way that its convolution with $B(x)$ equals to the function $V^x(\Delta x)$ defined in (4.31). Hence, the useful relation between $V^x(\Delta x)$ and $G(x)$ is defined by

$$
V^x(\Delta x) = G(x) * B(x) = \int_{-\infty}^{\infty} G(\Delta x - \tau)B(\tau)d\tau \tag{4.35}
$$

The proof of this useful relation (4.35) is now presented.

Since $V^x$ is a piecewise function as defined in (4.31), the relation (4.35) is proved for various range of $V^x(\Delta x)$.

a) For range $-\infty < \Delta x \leq -(v+c)$ and $(v+c) \leq \Delta x < \infty$

Using convolution property, since $G(x) = 0$ outside range $-c \leq x \leq c$ and $B(x) = 0$ outside range $-v \leq x \leq v$, the result of $G(x) * B(x)$ is zero outside the range $-(v+c) \leq x \leq (v+c)$. Hence, this is equated with $V(\Delta x) = 0$ in (4.31) for the mentioned range.

b) For range $-(v+c) < \Delta x \leq -(v-c)$

The function $G(\Delta x - \tau)$ in (4.35) is non-zero $\forall\, \tau \in [\Delta x - c, \Delta x + c]$ and $B(\tau)\, \forall\, \tau \in [-v, v]$. Both are illustrated in Figure. 4.23. The maximum range of $\tau$ where $G(\Delta x - \tau) \neq 0$ for
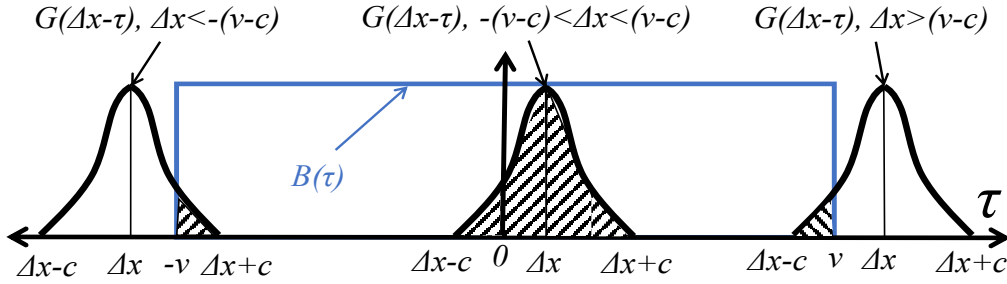


Figure 4.23: Graphical illustration of $G(\Delta x - \tau)$ and $B(\tau)$.

$-(v+c) < \Delta x \leq -(v-c)$ is

$$
\begin{aligned}
G(\Delta x - \tau) \neq 0\ &\Rightarrow \forall\, \tau \in [-(v+2c), -v]\ \text{ for } \Delta x = -(v+c) \\
G(\Delta x - \tau) \neq 0\ &\Rightarrow \forall\, \tau \in [-v, -(v-2c)]\ \text{ for } \Delta x = -(v-c)
\end{aligned}
\tag{4.36}
$$

As shown in Figure. 4.23, $G(\Delta x - \tau)$ overlaps with $B(\tau)$ from left side and the range of (4.36) is used in (4.35) to evaluate

$$
V^x(\Delta x) = \int_{-v}^{(\Delta x + c)} G(\Delta x - \tau) d\tau
$$

which by change of variable $\tau = (\eta - v + c)$ converted to

$$
V^x(\Delta x) = \int_{-c}^{(\Delta x + v)} G(\Delta x + v - c - \eta) d\eta
\tag{4.37}
$$

Since for this case $\Delta x < -(v-c) \Rightarrow (\Delta x + v - c) < 0$, (4.32b) is used with substitution $\Delta x \Rightarrow (\Delta x + v - c)$ to conclude (4.37) as $V(\Delta x) = K(\Delta x + v - c)$ which is matched to (4.31). Hence, the relation (4.35) is true for $-(v+c) < \Delta x \leq -(v-c)$ range.

c) For range $(v-c) < \Delta x \leq (v+c)$

Similar to the above analysis, in this case, $G(\Delta x - \tau)$ and $B(\tau)$ functions are demonstrated in Figure. 4.23. For $\Delta x \geq (v-c)$, the $G(\Delta x - \tau)$ will overlap with $B(\tau)$ from right side. For the extreme values of $\Delta x$, the $G(\Delta x - \tau)$ range is given by

$$
\begin{aligned}
G(\Delta x - \tau) \neq 0\ &\Rightarrow \forall\, \tau \in [(v-2c), v]\ \text{ for } \Delta x = (v-c) \\
G(\Delta x - \tau) \neq 0\ &\Rightarrow \forall\, \tau \in [v, (v+2c)]\ \text{ for } \Delta x = (v+c)
\end{aligned}
\tag{4.38}
$$

Analysis of the extreme range of (4.38) in Figure. 4.23, suggests to rewrite (4.35) for this range as

$$V^x(\Delta x) = \int_{(\Delta x - c)}^{v} G(\Delta x - \tau)d\tau$$

which by change of variable $\tau = (\eta + v - c)$ converted to

$$V^x(\Delta x) = \int_{(\Delta x - v)}^{c} G(\Delta x - v + c - \eta)d\eta \tag{4.39}$$

In this case, $\Delta(v - c) < x \Rightarrow (\Delta x - v + c) < 0$, therefore, (4.32b) is applicable and used (after substitution $\Delta x \Rightarrow (\Delta x - v + c)$) in (4.39) to conclude $V(\Delta x) = K(\Delta x - v + c)$ which is matching with (4.31) for this range.

d) Range $-(v - c) < \Delta x \leq (v - c)$

Similarly, this range is also demonstrated in Figure. 4.23 and for the extreme values of $\Delta x$, the maximum range of $G(\Delta x - \tau)$ is determined as

$$\begin{aligned} G(\Delta x - \tau) \neq 0 &\Rightarrow \forall \, \tau \in [-v, -(v - 2c)] \text{ for } \Delta x = -(v - c) \\ G(\Delta x - \tau) \neq 0 &\Rightarrow \forall \, \tau \in [(v - 2c), v] \text{ for } \Delta x = (v - c) \end{aligned} \tag{4.40}$$

The convolution is same at both extreme ranges as per (4.40) and demonstrated in Figure. 4.23. Hence, (4.35) for this range becomes

$$V^x(\Delta x) = \int_{(\Delta x - c)}^{(\Delta x + c)} G(\Delta x - \tau)d\tau$$

which by change of variable $\tau = (\eta + \Delta x)$ followed by use of property (4.33) gives $V^x(\Delta x) = \int_{-c}^{c} G(-\eta)d\eta = 1$ showing matched value with (4.31) for this range also.

Hence, the useful relation (4.35) is proved to be true and used further to obtain the solution of the objective (4.31), next.

**Optimal $H_z$ solution of the objective (4.31)**

The optimal $H_z$ solution obtained by (4.20) is used to achieve any objective $V$ function. However, due to complexity of the realistic $V$ objective defined in (4.31), a direct solution is cumbersome. At this point, the relation (4.35) is found very useful to obtain a closed form solution. Substitution from (4.35) in (4.20) gives

$$\begin{aligned} H_z(x, y) &= \text{IFT}\left[\frac{\text{FT}\left[B(x) * G(x)\right] \cdot \text{FT}\left[B(y) * G(y)\right]}{\text{FT}\left[A^x(x)\right] \cdot \text{FT}\left[A^y(y)\right]}\right] \\ &= \text{IFT}\left[\frac{\text{FT}\left[B(x)\right] \cdot \text{FT}\left[G(x)\right]}{\text{FT}\left[A^x(x)\right]}\right]\text{IFT}\left[\frac{\text{FT}\left[B(y)\right] \cdot \text{FT}\left[G(y)\right]}{\text{FT}\left[A^y(y)\right]}\right] \\ &= H(x) \cdot H(y) \end{aligned} \tag{4.41}$$

Hence, the $H_z(x, y)$ is separable into 1D identical functions $H_z$ in $x$ and $y$. The $H_z$ is further solved to obtain closed form solution. By substituting $A^x(x)$ from (4.19) and $B(x)$

from (4.34)

$$H_z(x) = \text{IFT} \left[ \frac{\text{FT}\left[rect\left(\frac{x}{2v}\right)\right] \cdot \text{FT}\left[G(x)\right]}{\text{FT}\left[rect\left(\frac{x}{2b}\right)\right]} \right]$$

$$= \text{IFT} \left[ \frac{\text{sinc}(v\omega_x) \cdot \text{FT}\left[G(x)\right]}{\text{sinc}(b\omega_x)} \right] = \text{IFT} \left[ \frac{\text{sinc}(v\omega_x)}{\text{sinc}(b\omega_x)} \right] * G(x) \quad (4.42)$$

To solve (4.42) further, $v = nb$ is assumed where $n$ is an integer, and solution pattern from (4.27) is adopted. Hence, the solution of optimal $H_z$ distribution is achieved as

$$H_n(x) = \begin{cases} \left( \delta(x) + \sum_{m=1}^{\lfloor \frac{n}{2} \rfloor} [\delta(x-2mb) + \delta(x+2mb)] \right) * G(x) \\ \qquad\qquad\qquad\qquad \text{for odd } n \\ \left( \sum_{m=1}^{\lfloor \frac{n}{2} \rfloor} [\delta(x-(2m-1)b) + \delta(x+(2m-1)b)] \right) * G(x) \\ \qquad\qquad\qquad\qquad \text{for even } n \end{cases}$$

$$\qquad (4.43)$$

$$= \begin{cases} \left( G(x) + \sum_{m=1}^{\lfloor \frac{n}{2} \rfloor} [G(x - 2mb) + G(x + 2mb)] \right) \\ \qquad\qquad\qquad\qquad \text{for odd } n \\ \left( \sum_{m=1}^{\lfloor \frac{n}{2} \rfloor} [G(x - (2m - 1)b) + G(x + (2m - 1)b)] \right) \\ \qquad\qquad\qquad\qquad \text{for even } n \end{cases}$$

It is observed from (4.43) that the optimal $H_z(x)$ solution of objective (4.31) is given by copies of $G(x)$ at different locations $x = \pm bm$ as graphically demonstrated in Figure. 4.24. Similarly, the final solution of $H_z(x, y)$ will be copies of $G(x)G(y)$ at locations $(\pm bm, \pm bm)$.
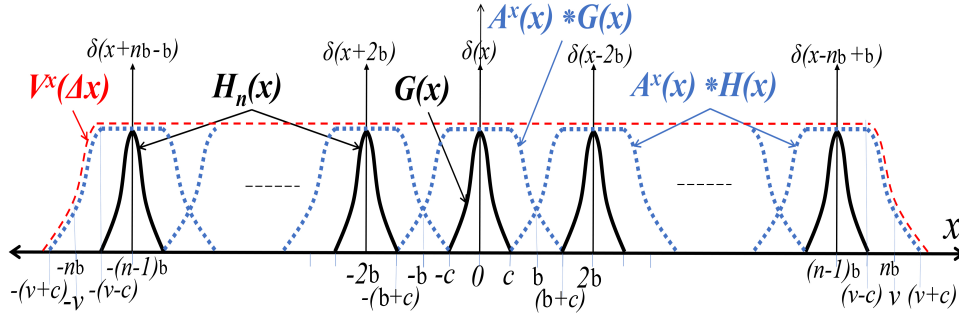


Figure 4.24: Optimal solution for real objective, 1D functions for odd $n$.

Since, $V = A * H_z$, it is observed from the figure that the overlapping area of various copies of $A * G$ ensures uniformity in the solution of $V$. Hence, $A_r(x, y) * H_z(x, y) = V(\Delta x, \Delta y) = 1 \ \forall \ x, y \in [-(v - c), (v - c)]$ where $v = bn$ is achieved and the corresponding optimal $H(x)$ distribution is given by (4.43).

### 4.3.6   Summary of the proposed design procedure

**Proposed step-wise procedure for Tx coil antenna design to mitigate lateral misalignment problem**

S1 Define objective $V(\Delta x)$ function and set $n$ for its desired uniformity for a given Rx dimension $b$.

S2 Obtain $K(x)$ function from $V(\Delta x)$ as

$$K(\Delta x) = \begin{cases} V(\Delta x - v + c) & -c \leq \Delta x \leq 0 \\ V(\Delta x + v - c) & 0 \leq \Delta x \leq c \end{cases}$$

S3 Derive $G(x)$ function graphically or by using (4.32) as

$$G(x) = \text{IFT}\left(\frac{\text{FT}(K(\Delta x))}{\text{FT}(rect(\frac{\Delta x}{2c}))}\right) \tag{4.44}$$

S4 Use $G(x)$ in (4.43) derived from Step-3 to obtain the optimal $H_z x, y)$ distribution mitigating lateral misalignment.

S5 For a given $n$, design the Tx coil array antenna using magnetic field forming technique to generate the desired $H_z(x, y)$ distribution in the Rx plane.

S6 Simulate the transmitter coil and adjust parameters further to obtain the desired $H_z(x, y)$.

As a result, the procedure reveals a Tx antenna for lateral misalignment mitigated in the range $(x, y) \in -(v - c)$ to $(v - c)$ where $v = nb$.

### 4.3.7   Illustration of the proposed analysis with simple functions

In the proposed analysis, $G(x)$ can adopt any arbitrary shape depending on $K(\Delta x)$, however, for illustration purpose, simple mathematical functions such as rectangular, triangular, raised cosine, etc., can be chosen. In this section, the procedure is demonstrated assuming $K(\Delta x)$ to be a triangular function.

For this example, in Step-1, the 1D function of objective $V(\Delta x, \Delta y)$ from (4.31) is defined in Figure. 4.25(a). In Step-2, the corresponding $K(\Delta x)$ function is obtained by graphical interpretation as $K(\Delta x) = tri(\frac{\Delta x}{4c})$ and plotted in Figure. 4.25(b). In Step-3, $G(x)$ is derived using (4.44) as

$$\begin{aligned} G(x) &= \text{IFT}\left[\frac{\text{FT}\left[tri(\frac{\Delta x}{4c})\right]}{\text{FT}\left[rect(\frac{\Delta x}{2c})\right]}\right] \\ &= \text{IFT}\left[\frac{\text{FT}\left[rect(\frac{\Delta x}{2c}) * rect(\frac{\Delta x}{2c})\right]}{\text{FT}\left[rect(\frac{\Delta x}{2c})\right]}\right] = rect\left(\frac{x}{2c}\right) \end{aligned} \tag{4.45}$$

The calculated $G(x)$ is plotted in Figure. 4.25(c). In Step-4, the $H_z(x)$ solution is obtained by substituting $G(x) = rect(\frac{x}{2c})$ in (4.43) for any $n$. The values of $n$ and $c$ determines misalignment range $(v - c)$ of the Rx which is the uniformity range of $V$ since $v = nb$. The $n = 2$ and $n = 3$ cases are discussed now.
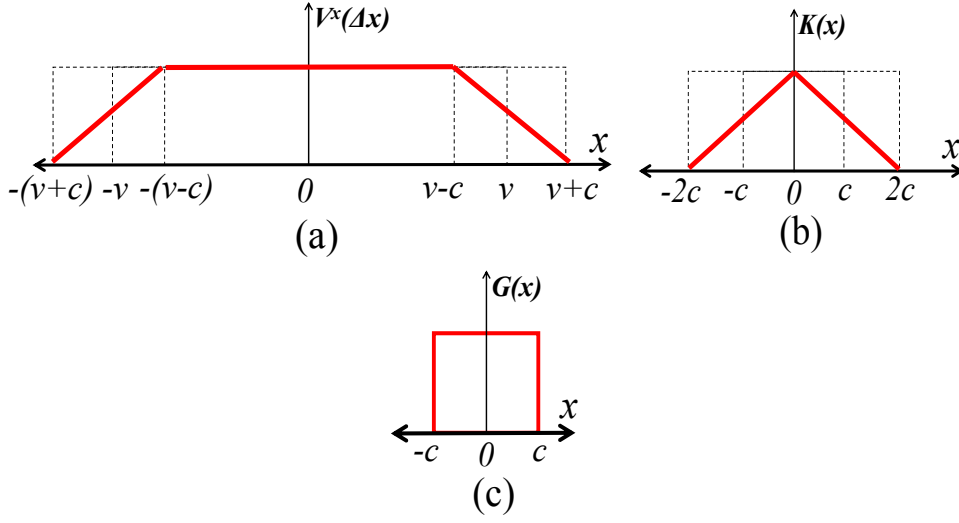
Figure 4.25: Illustration (a) objective $V^x(\Delta x)$ (b) $K(x)$ (c) $G(x)$.

**For n=2**: the $H_n(x)$ is calculated using (4.43) as $H_2(x) = G(x - b) + G(x + b)$ which by substitution becomes $H_2(x) = rect(\frac{x-b}{2c}) + rect(\frac{x+b}{2c})$ and depends upon $c$. The optimal solution (1D functions) is plotted in Figure. 4.26 specifically for $c < b$ and $c = b$. As a
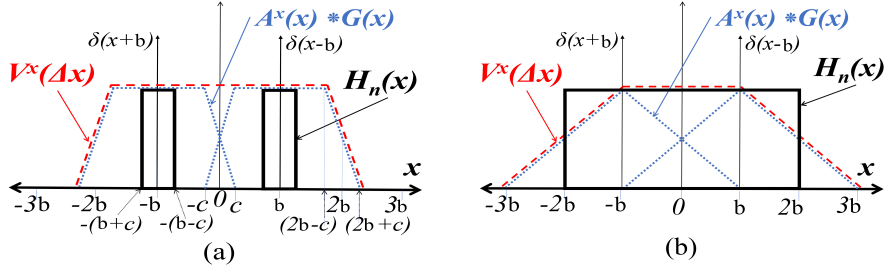


Figure 4.26: Illustration: Optimal $H(x)$ for $n = 2$ and (a) $c < b$ (b) $c = b$.

result, a uniform $V^x$ in misalignment range $2b - c$ is achieved by optimal $H_2$ for $n = 2$.
**For n=3**, the calculated solution from (4.43) is $H_3(x) = G(x) + G(x - 2b) + G(x + 2b) \Rightarrow rect(\frac{x}{2c}) + rect(\frac{x-b}{2c}) + rect(\frac{x+b}{2c})$ and plotted in Figure. 4.27 as $c$ varies. In this case, the uniformity of $V^x$ is achieved in misalignment range $3b - c$. Similarly, the total function
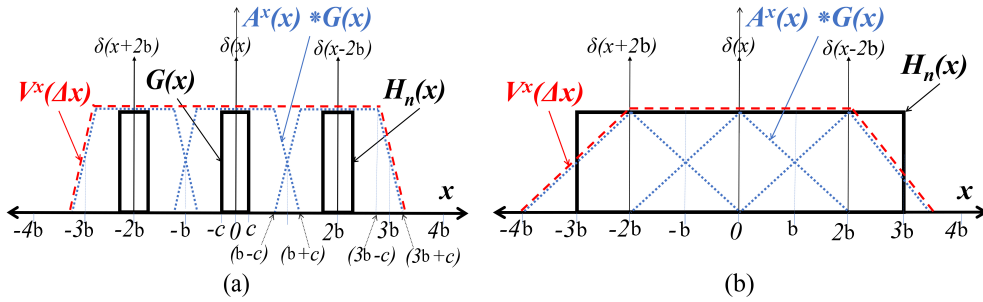


Figure 4.27: Illustration: Optimal $H(x)$ for $n = 3$ and (a) $c < b$ (b) $c = b$.

$V(\Delta x, \Delta y)$ is obtained and the solutions for $n = 2$ and 3 are depicted in Figure. 4.28 for $c < b$ . It is to be noted that the uniformity range $(nb - c)$ and corresponding optimal $H_z$
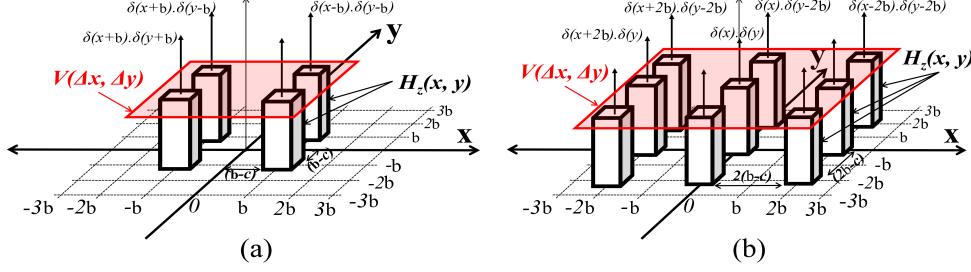


Figure 4.28: Illustration: Optimal $H(x, y)$ for (a) $n = 2$ (b) $n = 3$.

shapes depend on $c$ value. A maximum value of $c$ $(= b)$ results in a minimum uniformity as demonstrated in Figure. 4.26(b) and Figure. 4.27(b). In the case $c = b$, the $H_z$ solution is uniform which is adopted as the design objective in the literature works [1]. However, the proposed analysis is general and reveals that the $c = b$ is just one possible solution to mitigate lateral misalignment and may not be an optimal solution. Hence, a minimum $c$ is desired to achieve wider uniformity in $V$ and this corresponds to the non-uniform magnetic field distributions demonstrated in Figure. 4.28 as optimal solution. Although, designing antennas which can generate the optimal $H_z$ corresponding to lower $c$ values is a challenge. Next, we propose the coil array antennas which are designed by using the proposed procedure for non-uniform field forming.

### 4.3.8   Proposed coil array for non-uniform magnetic field forming

The proposed analytical model is now implemented for a realistic $V(\Delta x, \Delta y)$ profile depicted in Figure. 4.22(a). The Rx coil is considered with side length 100mm ($b = 50$mm), $N_r = 12$ concentrated turns, and located in $z = h = 50$mm plane. Uniformity for $n = 2$ and $n = 3$ cases are presented and correspondingly two designs are proposed for generating non-uniform magnetic field solutions of (4.43) achieved by the proposed analytical model. Further, in the design objective, the roll-off region extension is considered as $c = 50$mm in Figure. 4.22(a). Hence, for $n = 2$ design, the targeted uniformity range of $V$ is $\Delta x, \Delta y \in [-50, 50]$ ($v - c = nb - c = 50$mm) and roll-off extends upto 150mm for $x \geq 0$. Similarly, for $n = 3$ design, the targeted uniformity in $V$ range is $\Delta x, \Delta y \in [-100, 100]$ and roll-off extension is 200mm. Hence, the objective $V(\Delta x, \Delta y)$ is completely defined in Step-1. In Step-2, now the $K(\Delta x, \Delta y)$ is determined. As shown in Figure. 4.22(b), $K(\Delta x, \Delta y)$ resembles to a bell shape of width 200mm and its peak represents the desired voltage $V_0 = 10.96V$ [1] induced in the perfectly aligned Rx.

Now before $G(x, y)$ is evaluated in Step-3, it is noted from Figure. 4.24 and Figure. 4.28 that the optimal $H(x, y)$ distribution is superposition of the copies of $G(x, y)$ at various spatial locations $(x, y) = (\pm bm, \pm bm)$ at $z = h$. Hence, we propose that the final Tx array located in $z = 0$ plane consists of spatially distributed coils with their centers at $(x, y) = (\pm bm, \pm bm)$ where each coil is capable of generating magnetic field equal

to $G(x, y)$ individually. As a result, the total $H(x, y)$ is obtained as superposition of the individual $G(x, y)$. This way, the $n = 2$ design consists of a total of 4 coils with their centers located ideally at $(-50, 50)$, $(50, 50)$, $(-50, -50)$ and $(50, -50)$ in mm, respectively, as per the illustration of Figure. 4.28(a). Similarly, the n=3 design requires 9 coils with their centers ideally at $(-100, 100)$, $(0, 100)$, $(100, 100)$, $(-100, 0)$, $(0, 0)$, $(100, 0)$, $(-100, -100)$, $(0, -100)$ and $(100, -100)$ in mm, respectively, as per the illustration of Figure. 4.28(b). In Step-3, the $G(x, y)$ which represents the $H_z$ distribution generated by a single coil of the Tx array is now derived from roll-off function $K(\Delta x, \Delta y)$. As evident from Figure. 4.22(c), the $G(x, y)$ also follows a bell shape which can be obtained by designing a square spiral coil. The $H_z(x, y)$ field produced by a single turn square coil with side length $2a$ with current $I_T$ given in (2.3) is adopted in MATLAB based analysis to implement the field-forming technique. The coil geometry ($2a$ and $N_t$) is optimized that produces field distribution equal to $G(x, y)$ at the Rx plane $h = 50$mm and achieves the desired $K(\Delta x, \Delta y)$. The track width and the gap between adjacent turns is assumed to be 0.5mm according to the available fabrication process limitations. The result of parametric analysis for a single multi-turn coil is conducted in Figure. 4.29 having feed current of 1A. This shows the
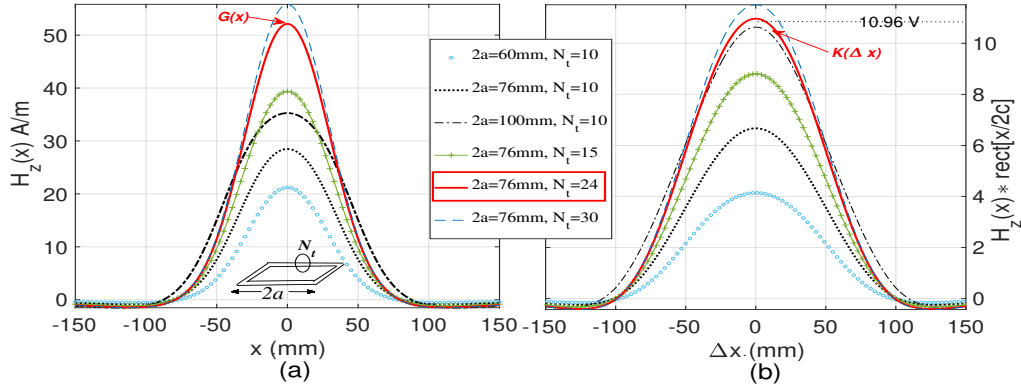


Figure 4.29: Analytical optimization of a single multi-turn coil geometry. (a) $H_z(x, y)$ distribution. (b) $V(\Delta x)$ distribution in h=50mm plane and $y = 0$ cut.

optimized parameters of a multi-turn square coil as $2a = 76$mm and $N_t = 24$ achieving the desired $K(\Delta x, \Delta y)$ (with peak $V_0 = 10.96V$ and bell width 200mm). The corresponding optimal $H_z(x, y)$ will serve as $G(x, y)$ solution as highlighted in Figure. 4.29(a) for $y = 0$ cut.

In Step-4, the total $H_z(x, y)$ can be obtained as superposition of $G(x, y)$ distributions due to individual coil. In Step-5, the complete Tx array is obtained by placing individual coil at the fixed locations mentioned earlier for both the designs. To note that, in general, the analytically obtained coil array may comprise overlapping coils because they exist in a common plane. Therefore, an another round of customization with constrained coil size can be performed. However, in the proposed Design-1C, this is not required. Furthermore, due to negative magnetic field at the edges beyond bell width as shown in Figure. 4.29(a), the objective $V(\Delta x, \Delta y)$ may vary slightly within uniformity range. However, this is eliminated in the analytical design itself by adjustments in the optimal coil parameters.

As a result, the final parameters of the proposed Design-1C Tx coil array antenna are found and listed in Table 4.6 for the design $n = 2$ and $n = 3$ having four (coil-1 to 4) and nine (coil-1 to 9) coils, respectively. The outer and inner turn side lengths $2a_o$ and $2a_i$ of

Table 4.6: The proposed Design-1C Tx coil array antenna design parameters.

| Design $n = 2$ | | | |
|---|---|---|---|
| Tx coil | Center location $(x, y)$ mm | $2a_o$, $2a_i$ (mm) | $N_t$ |
| coil-1,2,3,4 | (-51,51) (51,51) (-51,-51) (51,-51) | 76, 29 | 24 |
| Design $n = 3$ | | | |
| Tx coil | Center location $(x, y)$ mm | $2a_o$, $2a_i$ (mm) | $N_t$ |
| coil-1,3,7,9 | (-101,101) (101,101) (-101,-101) (101,-101) | 78, 25 | 27 |
| coil-2,4,6,8 | (0,101) (-101,0) (101,0) (0,-101) | 80, 29 | 26 |
| coil-5 | (0,0) | 80, 23 | 29 |

the proposed designs are listed and the track width $w$ and separation $s$ is 0.5mm.

### 4.3.9    Analytical Results

The performance evaluation of the proposed designs is now presented. Figure. 4.30 shows
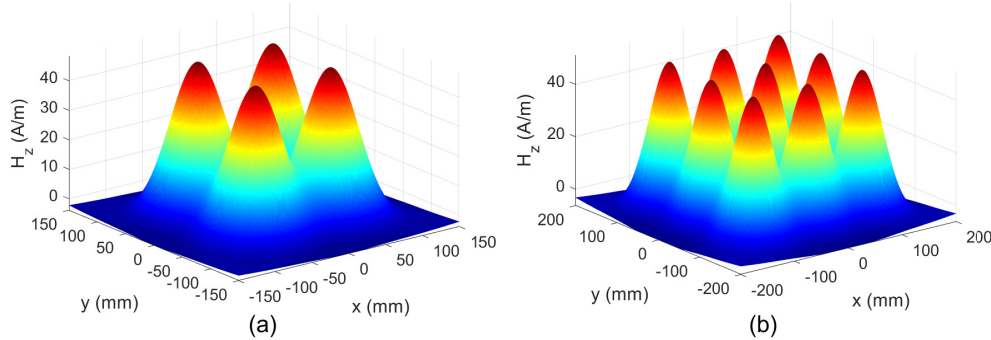


Figure 4.30: $H(x, y)$ distributions of the proposed Design-1C for (a) $n = 2$ (b) $n = 3$.

the $H_z(x, y)$ distribution in the Rx plane $h = 50$mm calculated using (4.43) for the two designs. The result demonstrates the non-uniform fields formed by the proposed Design-1C $n = 2$ and $n = 3$. The $V(\Delta x, \Delta y)$ distribution with Rx misalignment is plotted in Figure. 4.31 where the attained uniformity in the induced voltage is proved.

To exhibit the effectiveness for mitigation of lateral misalignment, the proposed designs are compared with the literature antenna [1] which was designed to form uniform magnetic field. For a better visualization of improvement in $V$ uniformity, 1D functions $H(x)$ and $V(\Delta x)$ are plotted for $y = 0$ cut in Figure. 4.32 and compared results with the literature design. The results in Figure. 4.32 show that the magnetic field formed by individual set of coils of the proposed designs corresponds to copies of $G(x)$ presented in Figure. 4.29. Moreover, the proposed $n = 2$ design shows a better uniformity in $V(\Delta x)$ compared to the literature design, and further the uniformity is enhanced by the proposed $n = 3$ design. From Figure. 4.32, we calculated the total misalignment tolerance region where change in
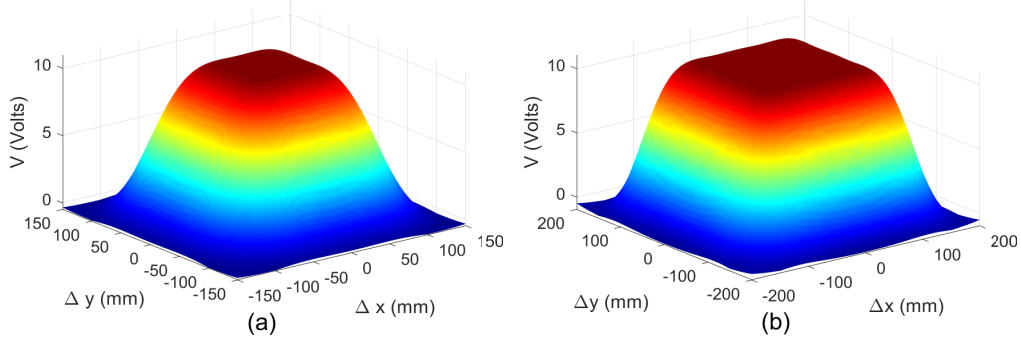
Figure 4.31: $V(\Delta x, \Delta y)$ distributions of the Design-1C for (a) $n = 2$ (b) $n = 3$.
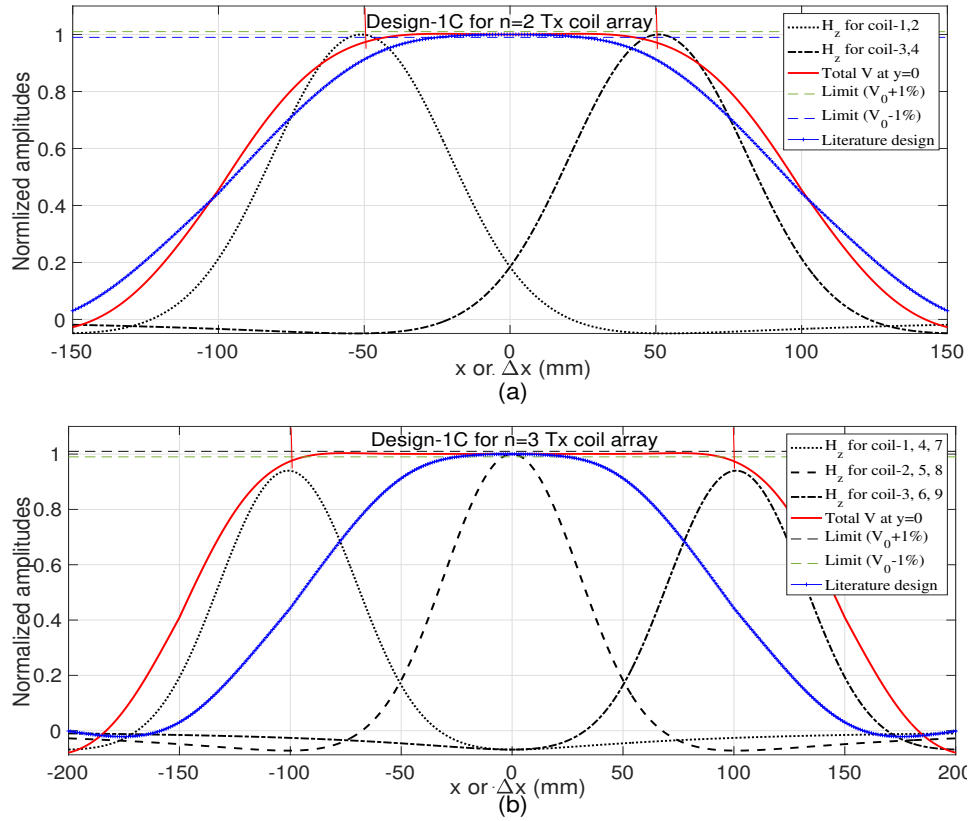


Figure 4.32: Analytical results of $H_z(x)$ and $V^x(\Delta x)$ distributions at $h = 50$mm and $y = 0$ cut for (a) n=2, and (b) n=3.

$V$ is within 1% limit of $V_0$ value as [-24, 24]mm, [-42.6, 42.6]mm, and [-93, 93]mm for the literature, the $n = 2$, and the $n = 3$ designs, respectively.

Since the large size Tx are intended to achieve wider uniformity, for fair comparison, the size of Tx should also be considered in performance metric. To quantify performance, a UF($V(\Delta x, \Delta y)$) can be defined as the ratio of total area in $z = h$ plane where change in the $V(\Delta x, \Delta y)$ is within 1% of $V_0$ to the total size of the Tx. Where $V_0 = V(0,0)$ corresponds to the Rx voltage in perfectly aligned position i.e., $\Delta x = \Delta y = 0$. The

dimensions are $179 \times 179$mm$^2$, $276 \times 276$mm$^2$, and $200 \times 200$mm$^2$ of the Tx for the $n = 2$, the $n = 3$, and the literature designs, respectively. Hence, from Figure. 4.31, we calculated that the proposed $n = 2$ design has percentage UF($V(\Delta x, \Delta y)$)=22.65% and for the literature UF($V(\Delta x, \Delta y)$)=5.76% is calculated. The proposed $n = 3$ design achieves UF($V(\Delta x, \Delta y)$)=45.41%. Therefore, the improvement shown by the proposed designs in UF($V(\Delta x, \Delta y)$) is 293.23% ($n = 2$) and 688.36% ($n = 3$) over the literature design.

### 4.3.10    Realization of the proposed coil array antennas

The proposed Tx arrays are realized in Printed Circuit Board (PCB) technology. For this purpose a two-sided FR4 substrate of height=1.6mm, $\epsilon_r = 4.4$, $tan\delta = 0.02$, and copper deposition of 35 micron is used. Figure. 4.33 shows the PCB layouts of the proposed
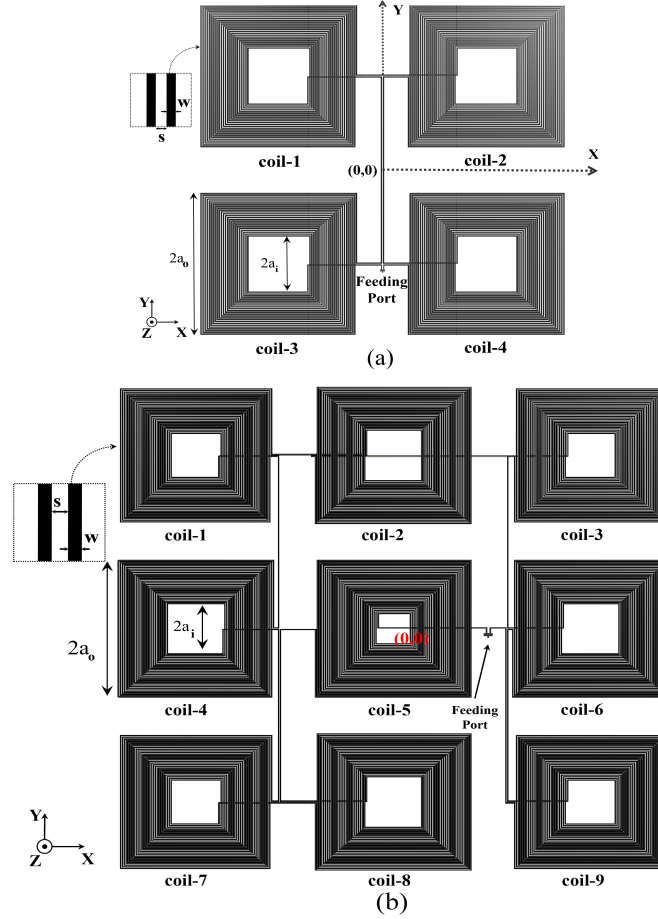


Figure 4.33: Layout of the proposed coil array designs (a) $n = 2$ (b) $n = 3$.

designs having dimensions listed in Table 4.6. The coils are etched on the front-layer of the PCB. The feed lines connecting the coils in series are present at the bottom-layer. The vias facilitate connections between the two layers. To resonate the Tx and Rx coils at the operating frequency 488.6KHz, matching capacitors are used at the feeding ports. The designs are validated through simulations using commercial EM software Ansys HFSS

v18.0.

### 4.3.11    Simulation and results

The proposed designs are simulated for $H_z(x, y)$ distributions which are found similar to the analytical results shown in Figure. 4.30 and omitted here for brevity. Next, the Rx misalignment analysis is performed. In the simulations, the Rx located in the plane $h = 50$mm is displaced in the range $\Delta x, \Delta y \in [-150, 150]$mm and readings are noted for the two cuts central ($y = 0$) and diagonal ($x = y$) to cover the misalignment area. Figure. 4.34 shows the simulated $V(\Delta x, \Delta y)$ variation along with the analytical results
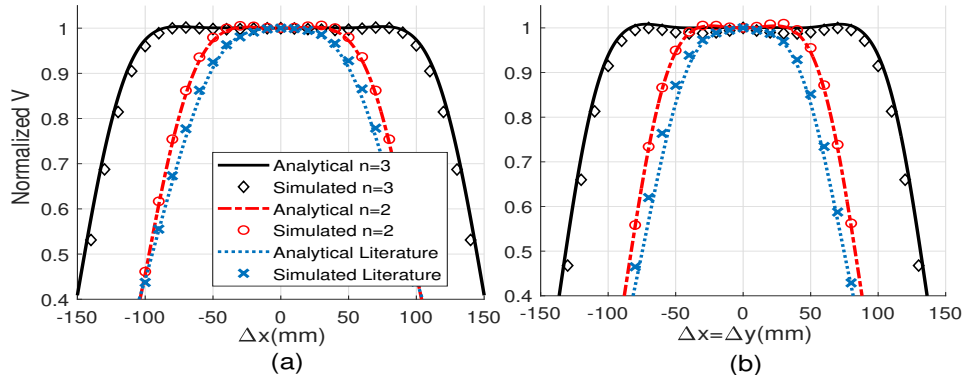


Figure 4.34: Simulation of misalignment analysis (a) $y = 0$ cut (b) $x = y$ cut.

and the literature design for comparison. The simulation results are well corroborated with the analysis for both the cuts. The improvement achieved by the proposed designs shown in the simulation results is found in agreement with the analysis. Hence, the UF($V(\Delta x, \Delta y)$) values achieved in the analysis are validated by the simulations. The designs are fabricated and the results are further validated experimentally.

### 4.3.12    Experimental validation of Design-1C for n=2 and n=3 designs

The antenna layouts of Figure. 4.33 are fabricated and prototypes are shown in inset of Figure. 4.35 demonstrating the experimental setup. The measurements are performed with Agilent N5230C Network Analyzer. The $|S21|$ parameter between the Tx-Rx coils is measured which is later used to determine $\eta_{s-conventional}$ by substituting $|S11| = 0$ in (2.40a). The measurements are conducted for various displacements of the Rx coil which is precisely performed using DRS60L robotic arm as depicted in Figure. 4.35. An in-house near-field probe as shown in the inset of Figure. 4.35 is used to measure the magnetic field distribution of the proposed antennas. The measured $H_z(x, y)$ results are plotted in Figure. 4.36(a) showing good agreement between the measured and simulated data, and demonstrating the non-uniform magnetic field formed by the proposed designs. To measure $|S21|$, the Rx coil is displaced along central $y = 0$ and diagonal $y = x$ lines and the normalized $S21$ based efficiency are shown in Figure. 4.36(b). This validates the proposed model and proves its potential to mitigation the lateral misalignment problem
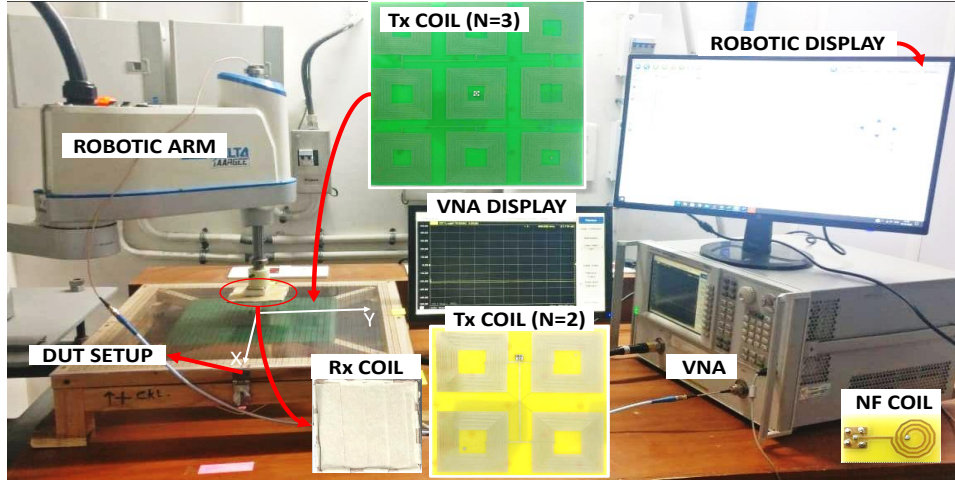
Figure 4.35: Fabricated prototypes and experimental setup.
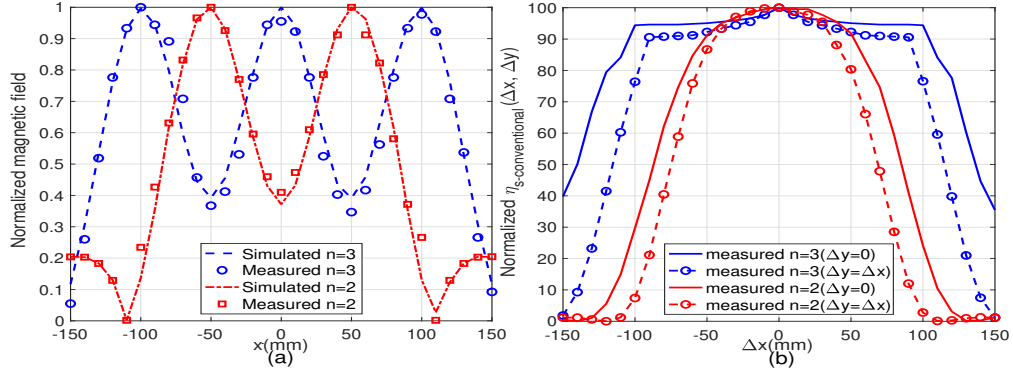


Figure 4.36: Measured results (a) normalized $H_z(x, y)$ (b) normalized $\eta_{s-conventional}$.

in the desired Rx region.

Table 4.7: Comparison of proposed single-port Tx coil antennas.

| Designs | Tx size (mm) | UF($M(\Delta x, \Delta y)$)/ UF($V(\Delta x, \Delta y)$) | Flux control | Misalignment dimension | Tx type |
|---|---|---|---|---|---|
| Literature-[1] | $200 \times 200$ | 5.76% | No | $(\Delta x, \Delta y)$ | planar |
| Design-1A | $300 \times 100$ | 55.33% | No | $(\Delta x)$ | 3-D |
| Design-1B | $200 \times 200$ | 14.4% | No | $(\Delta x, \Delta y)$ | planar |
| Design-1C (n=2) | $179 \times 179$ | 22.65% | No | $(\Delta x, \Delta y)$ | planar |
| Design-1C (n=3) | $276 \times 276$ | 45.41% | No | $(\Delta x, \Delta y)$ | planar |

## 4.4    Summary

This chapter delves into the evolution of single port Tx coil antennas to address lateral misalignment problems. The chapter begins with the investigation of a 3D Tx coil antenna,

which is optimized based on parametric variation of distinct dimensional parameters to produce a widespread uniform magnetic field. Here, the 3D design is designated as Design-1A [d]. However, misalignment tolerance ($UF(\Delta x) = 55.33\%$) is improved in only 1D Rx coil misalignment (i.e, along $\Delta x$) which does not give misalignment freedom in entire X-Y plane. Additionally, the practical challenges arise in positioning this antenna in many applications, leading to the development of a planar Tx coil. For this, a nove field forming technique using Q-assisted MMSE based algorithm is employed for a target objective of producing a widespread and uniform magnetic field. The resultant planar design is named as Design-1B [e]. The stability of $\eta_{ss}(\Delta x, \Delta y)$ (PCB and copper wire) for the Design-1B is achieved in the Rx area $72 \times 72$ mm$^2$ incontrast to $40 \times 40$ mm$^2$ shown by the conventional literature design. The overall misalignment tolerance in terms of the $\eta_{ss}(\Delta x, \Delta y)$ is improved by   224% by implementing the proposed Design-1B in comparison to the design proposed in the literature [1].

While a uniform magnetic field is desirable, it does not necessarily guarantee optimal field distribution to mitigate lateral misalignment problems. To determine the optimal magnetic field distribution, an analytical framework is newly derived to target uniform induced voltage with Rx misalignment. Surprisingly, the analytical justifications reveal that a non-uniform magnetic field is optimal for mitigating lateral misalignment problems. As a result, two designs are developed to generate a non-uniform magnetic field in the Rx region, namely Design-1C (n=2) and Design-1C (n=3) [f]. Compared to the conventional literature design, the size of the Design-1C (n = 2) is reduced by   19.89%, and the misalignment tolerance is improved by $\sim 293\%$. Moreover, the achieved misalignment tolerance by the Design-1C (n = 3) is improved by $\sim 688\%$. A summary of performance parameters of the proposed designs evolved from the objectives proposed in EP-1, EP-2 and EP-3 are tabulated in Table 4.7.

Despite achieving excellent misalignment tolerance with single port Tx coils such as Design-1A, Design-1B, and Design-1C, these designs suffer from significant flux leakage. This leakage leads to reduced coupling between Tx-Rx coils and significantly affects the PTE of WPT systems. Therefore, multi-port Tx coil antenna with a switching and detection system is investigated to control flux leakage in Chapter 5. Overall, this chapter provides valuable insights into the evolution of single port Tx coil antennas and their optimization to mitigate lateral misalignment problems.

CHAPTER OUTCOMES

---

[d] **A. Bharadwaj**, V. K. Srivastava, A. Sharma and C. C. Reddy, "A Novel Trapezoidal Multi-Coil Antenna for Wireless Charging of Electric Vehicles," **2020 IEEE 15th International Conference on Industrial and Information Systems (ICIIS)**, RUPNAGAR, India, 2020, pp.  13-17, doi: 10.1109/ICIIS51140.2020.9342635.

[e] **A. Bharadwaj**, A. Sharma and C. C. Reddy, "A Multi-Turn Coil Antenna With Nonuniform Clustered Turns Optimized Using Q-Assisted MMSE Procedure to Enhance Misalignment Tolerance in WPT Systems," in **IEEE Transactions on Antennas and Propagation**, vol. 70, no. 7, pp. 5302-5311, July 2022, doi: 10.1109/TAP.2022.3146433.

[f] A. Sharma, **A. Bharadwaj** and V. K. Srivastava, "An Analytical Framework to Design Planar Transmitting Array Antennas to Mitigate Lateral Misalignment in Wireless Power Transfer Systems," in **IEEE Transactions on Antennas and Propagation**, vol. 69, no. 9, pp. 5559-5569, Sept. 2021, doi: 10.1109/TAP.2021.3069518.

# Chapter 5

# Multi Port Tx Coil Antennas

In the previous chapter, designs were proposed to mitigate the lateral misalignment problem in WPT systems. However, a trade-off is associated with these designs. Specifically, they lead to a significant increase in flux leakage outside the Rx coil operating region, which in turn causes a reduction in the coupling coefficient and link efficiency between the Tx and Rx coils.

To overcome this challenge, this chapter puts forward a solution in which multi-port Tx coil antennas are optimized to minimize flux leakage as targeted in EP-4 of SO-B. To achieve this, a switching circuit is utilized, which activates the appropriate Tx coil antenna based on the location of the Rx coil antenna, as determined by a detection system. This approach involves the development of two designs, namely Design-2A and Design-2B, which are aimed at reducing flux leakage. The ultimate goal of this proposed approach is to enhance the overall efficiency and performance of the WPT system.

## 5.1 System configuration of Design-2A (SO-B: EP-4)
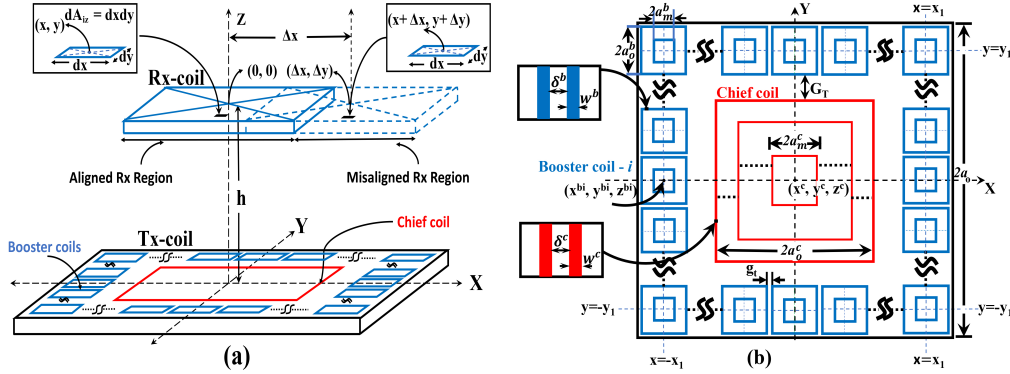


Figure 5.1: (a) A two-coil WPT system under lateral misalignment, (b) the proposed Design-2A Tx coil antenna profile for analysis.

The Tx coil antenna with two-port configuration under misaligned Rx coil is depicted in Figure. 5.1(a) and the coordinate system is defined. Here, similar to design-1A, 1B, and 1C, the Tx-Rx coils are magnetically coupled at $f = 488.6$kHz. The structure of the proposed Design-2A is detailed in Figure. 5.1(b). The proposed Design-2A Tx coil antenna is designed to operate in dual mode for an efficient generation of the magnetic field in the Rx coil working region ($z{=}h$ plane). The dual-mode is achieved by incorporating a simple

two-state switching operation. The proposed antenna is primarily consisting of a chief coil centered at location $(x^c, y^c, z^c)$ which is the same as the origin $(0, 0, 0)$ of the coordinate system. The chief coil is responsible to generate a concentrated magnetic field distribution within the aligned Rx region as marked in Figure. 5.1(a). Further to generate widespread uniform magnetic field up to the misaligned Rx region as marked in Figure. 5.1(a), the proposed antenna contains a set of small booster coils, as depicted in Figure. 5.1(b), circumscribing the chief coil. For a perfectly aligned Rx, the Tx operates in mode-1 in which only the chief coil is excited to generate the magnetic field distribution confined within the Rx area. In case the Rx is misaligned, the Tx is switched to mode-2 in which, additionally, all the booster coils are excited along with the chief coil to form an extensively uniform magnetic field in the entire Rx region to mitigate lateral misalignment problem. The equivalent circuit model of the WPT system in mode-2 is shown in Figure. 5.2. The
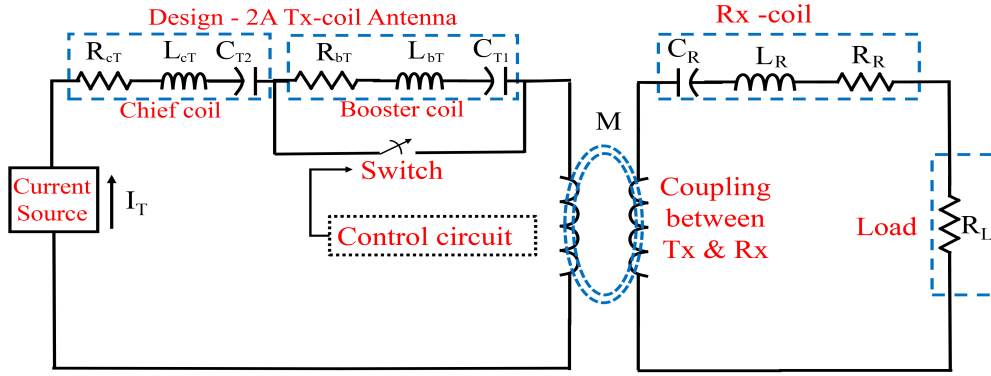


Figure 5.2: Equivalent circuit model to evaluate WPT performance of the Design-2A Tx coil antenna.

proposed Tx antenna under mode-2 (when the switch is OFF) is represented as a series connection of the chief coil and the booster coils. Here, $R_{cT}$, $R_{bT}$, $L_{cT}$, and $L_{bT}$ denote the resistances and self-inductances of the chief coil and booster coils, respectively. The same circuit model is applicable for operation in mode-1 (when the switch is ON) by omitting the booster coil parameters $R_{bT}$ and $L_{bT}$ in the equivalent circuit. To resonate the Tx at frequency $f$, capacitors $C_{T1}$ and $C_{T2}$ are used as shown in Figure 5.2.

Interoperability between the two modes can be achieved by adopting various detection systems proposed in the literature, such as coil-based sensors [98, 99], radio frequency detection [100], reflected impedance [101], or tunneling magnetoresistive (TMR) sensor matrix [102]. For example, a TMR sensor array can be integrated with the proposed Tx antenna to detect the Rx coil's position. To detect the Rx in perfect alignment, a sensor is placed at the chief coil, and for Rx misalignment detection, other sensors are placed at the booster coils. The sensor array is integrated into the control circuit, as shown in Figure 5.2, which changes the switch to the 'ON' or 'OFF' state based on the Rx coil's alignment. The number of TMR sensors and their locations can be judiciously chosen and calibrated

according to the desired degree of misalignment tolerance for practical applications.

The geometrical parameters of the chief coil include maximum side length, $2a_o^c$, minimum side length, $2a_m^c$, number of turns, $N_t^c$, width of the conductive strip, $w^c$, and inter-turn spacing, $\delta^c$. The side length of the $n^{th}$ turn of the chief coil is determined as $2a_n^c = 2a_o^c - 2(n-1)(w^c + \delta^c) \ \forall \ n \in \{1, 2, ..N_t^c\}$. Let $n_b$ denotes number of booster coils centered at locations $(x^{bi}, y^{bi}, z^{bi}) \ \forall \ i \in \{1, 2, ..n_b\}$ encompassing the chief coil. Each booster coil-$i$ identically has maximum side length, $2a_o^b$, minimum side length, $2a_m^b$, width of conductive strip, $w^b$, inter-turn spacing, $\delta^b$, number of turns, $N_t^{bi}$. The side length of the $n^{th}$ turn is determined as $2a_n^{bi} = 2a_o^b - 2(n-1)(w^b + \delta^b) \ \forall \ n \in \{1, 2, ..N_t^{bi}\}$ and $\forall \ i \in \{1, 2, ..n_b\}$. The magnetic field generated by the proposed Design-2A Tx coil antenna along z-direction is evaluated using (2.3) by re-labelling $H_z(x, y)$ with $H_z^{nt}(x, y)$. Where $H_z^{nt}$ with superscript $t \Leftarrow c$ and $t \Leftarrow bi$ represent magnetic fields due to the chief coil and the booster coil-$i$, respectively, and the coil positions are defined as $(x^t, y^t, z^t)$ from Figure. 5.1(b). The longitudinal separation between the Tx-Rx coil is $h$. The total magnetic field, $H_z(x, y)$, in the Rx region is given by the superposition of the individual magnetic fields due to all the turns of the chief coil as well as the booster coils and obtained as

$$H_z^c(x, y) = \sum_{n=1}^{N_t^c} H_z^{nc}(x, y)\chi_n^c, \tag{5.1a}$$

$$H_z^b(x, y) = \sum_{i=1}^{n_b} \sum_{n=1}^{N_t^{bi}} H_z^{nbi}(x, y)\gamma_o^b, \tag{5.1b}$$

$$H_z(x, y) = H_z^c(x, y) + H_z^b(x, y), \tag{5.1}$$

where $H_z^c(x, y)$ and $H_z^b(x, y)$ are calculated to be individual magnetic field distributions generated by the chief coil and the set of booster coils, respectively. The coefficients $\chi_n^c$ and $\gamma_o^b$ are incorporated to assist the optimization for the proposed magnetic field forming. Here, the $\chi_n^c = 0, \pm 1$ is characterized as coefficient of current circulation in the $n^{th}$ turn of the chief coil which is same as previously used in optimization of Design-1B. The value $\chi_n^c = 0$ represents the absence of the $n^{th}$ turn and $\chi_n^c = +1/-1$ represents constructive/destructive contribution of the $n^{th}$ turn in $H_z^c(x, y)$. This permits the optimization to analytically design the chief coil as the structure of a non-uniformly distributed turn with relatively opposite current circulations. The booster coils are constrained to acquire uniformly distributed turns to boost the magnetic field around the border of the Rx working region. For this, the coefficient $\gamma_o^b$, a non zero positive integer, is defined as boosting factor and supports amplification of the $H_z(x, y)$ in the misaligned Rx region. For instance, if $\gamma_o^b = 1$ in (5.1b) implies the magnetic field due to the multi-turn booster coils, then, $\gamma_o^b > 1$ signifies the requirement to generate a $\gamma_o^b$ times more magnetic field by the booster coils. This amplifying effect, in practice, can be realized by feeding the booster coils separately with a source having $\gamma_o^b$ times higher magnitude of the current (i.e, $\gamma_o^b I_T$). However, in the proposed design, this effect is judiciously incorporated within the antenna structure itself as presented later in Section 5.1.4.

### 5.1.1 Optimization procedure of the proposed design

In order to optimize the antenna design, the relationships between the various design variables and constraints are formulated based on the geometrical parameters. The design constraints are determined by fabrication limits and comparative study, and include parameters such as $w^c$, $w^b$, $\delta^c$, $\delta^b$, the gap between successive booster coils ($g_T$), and the maximum dimension ($2a_o$) of the Tx antenna, as depicted in Figure 5.1(b). Since $2a_o$ sets the upper limit on the dimensions of the chief coil and the booster coils, as shown in Figure 5.1(b), it is related to $2a_o^c$, $2a_o^b$, and $G_T$ by visualizing the $x = 0$ or $y = 0$ line in Figure 5.1(b) as follows:

$$2a_o = 2a_o^c + 2(2a_o^b) + 2G_T, \tag{5.2}$$

where $G_T$ represents the separation between the chief coil and the booster coils. The total number of booster coils, $n_b$, is determined by the geometric values of $2a_o$, $2a_o^b$, $g_T$, and $\gamma_o^b$, and the relationship is formulated as follows:

$$n_b = \left\lfloor \frac{4(2a_o - 2a_o^b)}{g_T + 2a_o^b}\gamma_o^b \right\rfloor, \tag{5.3}$$

where $\lfloor . \rfloor$ represents the greatest integer function and is used to obtain the required integer value. The booster coil centers $(x^{bi}, y^{bi})$ lie on the lines $\pm X_1$ and $\pm Y_1$ as shown in Figure. 5.1(b) and are related with $2a_o^c$, $2a_o^{bi}$, and $G_T$ as

$$X_1 = \pm\frac{2a_o^c + 2a_o^{bi}}{2} + G_T \quad \text{and} \quad Y_1 = \pm\frac{2a_o^c + 2a_o^{bi}}{2} + G_T. \tag{5.4}$$

Therefore, the total number of coils, $n_T$, in the Tx antenna is given by $n_T = n_b + 1$. To be noted for the chief coil that the entries to the vector $2a_n^c$ represent side lengths of all the possible turns considered in the analytical optimization. However, once the values $\chi_n^c$ are known, the corresponding turns having $\chi_n^c = 0$ do not exist physically in the realized design. The absence of such turns in $2a_n^c$ implies a non-uniformly distributed turns profile of the coil which is denoted as $2a_n^{c'}$. Therefore, the actual side length vector $2a_n^{c'}$ of the optimised chief coil is given by

$$2a_n^{c'} = |\chi_n^c| \, 2a_n^c = |\chi_n^c| \, (2a_o^c - 2(n-1)(w^c + \delta^c)) \tag{5.5}$$

$$\text{where,} \quad 2a_n^c = (2a_o^c - 2(n-1)(w^c + \delta^c)). \tag{5.6}$$

In the vector, $2a_n^{c'} \quad \forall \quad n \in \{1, 2, ..N_t^c\}$, the difference between the values of successive turns is $(w^c + \delta^c)$ and the difference between the values of successive turns around continuos zero entries represents non-uniform turn spacing denoted as $\Delta_m^c$. The total number of turns in the realized chief coil and booster coils are determined as

$$N_t^{c'} = \sum_{n=1}^{N_t^c} |\chi_n^c|, \quad N_t^{bi} = \frac{2a_o^b - 2a_m^b}{2(\delta^b + w^b)} + 1 \, \forall i \in \{1, 2, ..n_b\}. \tag{5.7}$$

Firstly, the known parameters are defined, which include the values of $I_T$, $2a_o$, $g_T$, $w^c$, $w^b$, $2a_m^b$, $2a_m^c$, $\delta^c$, and $\delta^b$. Then, the other design parameters, such as $x^{bi}$, $y^{bi}$, $N_t^{bi}$, $2a_o^c$, $2a_o^b$, $G_T$, $n_b$, $\chi_n^c$, $\gamma_o^b$, $2a_n^c$, $2a_n^{c'}$, $N_t^{c'}$, and $\Delta_m^c$, are optimized. Since the design parameters are interdependent and constrained by relations (5.2)-(5.7), only $2a_o^c$ and $\chi_n^c$ for the chief coil and $x^{bi}$, $y^{bi}$, $2a_o^b$, and $\gamma_o^b$ for the booster coils are available for optimization. Moreover, the optimization of these two types of coils is not independent but constrained by (5.2). Once the design variables and their relationships are defined, the following optimization based on the proposed field-forming technique is performed.

### 5.1.2   Formulating optimization problem based on field-forming

The optimization of the proposed design is now presented. The proposed field-forming technique is based on MMSE algorith which is same as used previously in optimizing Design-1B. The MMSE is evaluated between the targeted and the calculated magnetic field distributions. Since the proposed structure operates in two different modes, the global optimization objective is therefore consisting of a sub-objective which is defined to achieve concentrated magnetic field by the chief coil in the aligned Rx area in mode-1. For the sub-objective, the target magnetic field function $H_T^c(x,y)$ is defined as

$$H_T^c(x,y) = \begin{cases} H_o & \text{for} \quad -p \leq x, y \leq p \\ 0 & \text{otherwise} \end{cases} \tag{5.8}$$

where $p$ is the parameter defined to confine the magnetic field within the aligned Rx region. The MSE for this sub-objective, $MSE^c$, is evaluated between the $H_z^c(\text{x,y})$ calculated using (5.1a) and the $H_T^c(x,y)$ defined in (5.8). Hence, the sub-objective for the optimization is formulated as

$$\min_{2a_o^c, \chi_n^c} \quad MSE^c = \overline{\left(H_z^c(2a_o^c, \chi_n^c) - H_T^c(x,y)\right)^2} \tag{5.9}$$
$$\text{s.t.} \quad 2a_m^c \leq 2a_o^c \leq 2a_o, \quad \chi_n^c \in \{-1, 0, 1\}$$

where $\overline{(\cdot)}$ denotes the mean function. Subsequently, under the global objective, the booster coils are optimized for the given sub-optimized chief coil resulting from (5.9). For the global objective, the targeted magnetic field, $H_T(x,y)$ is same as (4.10), is thus defined as

$$H_T = \begin{cases} H_o & \text{for} \quad -r \leq x, y \leq r \\ 0 & \text{otherwise.} \end{cases} \tag{5.10}$$

where $r > p$ implies spreading the magnetic field uniformity in the misaligned Rx region in mode-2. The overall MSE is determined between the calculated $H_z(x,y)$ using (5.1) and the $H_T(x,y)$ defined in (5.10). The optimization problem for the global objective is

formulated as

$$\min_{2a_o^b, x^{bi}, y^{bi}, \gamma_o^b} \quad MSE = \overline{\left(H_z(x,y)(2a_o^b, x^{bi}, y^{bi}, \gamma_o^b) - H_T(x,y)\right)^2}$$

$$\text{s.t.} \qquad 2a_m^b \leq 2a_o^b \leq \frac{2a_o - 2a_o^c}{2}, \quad \gamma_o^b \geq 1 \tag{5.11}$$

To solve the formulated optimization problem, an algorithm is developed which is an iterative process based on MMSE defined in (5.9) and (5.11).

### 5.1.3 Design algorithm for the proposed field-forming

The design algorithm flow chart is presented in Figure. 5.3. The procedure begins with the set of design constraints and terminates with the optimal geometrical parameters of the proposed Design-2A antenna. By sweeping the design parameters in the optimization process, the solutions of (5.9) and (5.11) are obtained. The algorithm summarized in Figure. 5.3 is described in detail as follows.
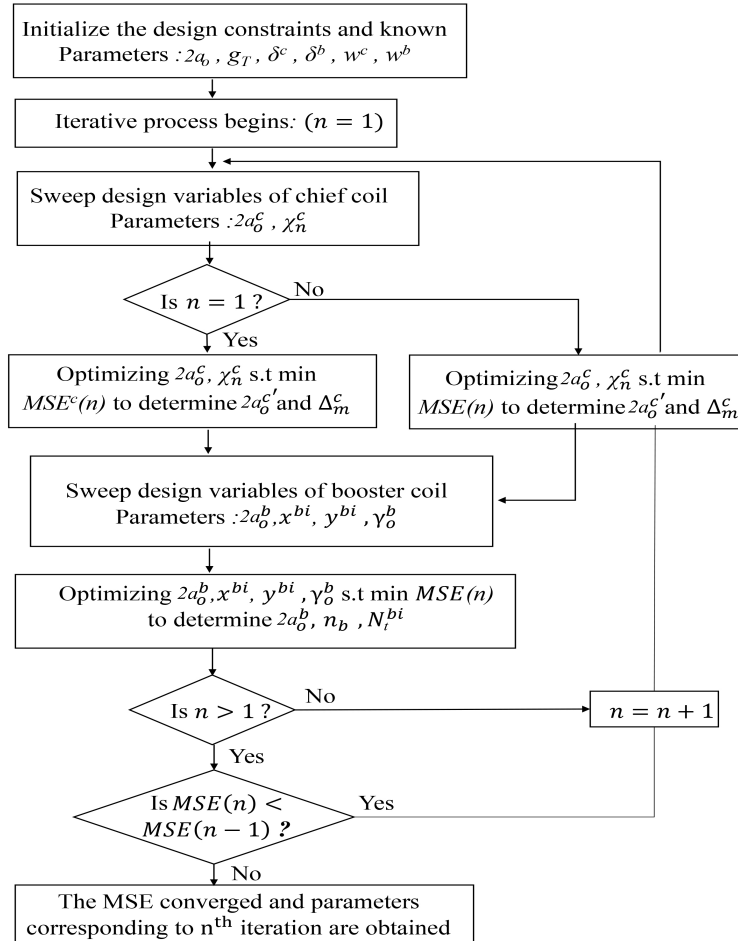


Figure 5.3: Iterative design algorithm flowchart for developing Design-2A.

**Step-1:** The known parameters are initialized.

**Step-2:** The chief coil optimization process begins in the first iteration based on MMSE problem defined in (5.9) by initializing and sweeping design variables $2a_o^c$ and $\chi_n^c$. Let the $2a_o^c$ is a vector. For each entry of $2a_o^c$ vector, the $MSE$ is saved as defined in (5.9) and progressively stored in $MSE^c$ vector. The design parameters corresponding to the minimum $\{MSE^c\}$ are evaluated as sub-optimized chief coil parameters.

**Step-3:** The sub-optimum $2a_o^c$ and $\chi^c$ results are then used in (5.5) and (5.6) to determine non-uniform side length profile $2a_o^{c'}$ and spacing $\Delta_m^c$ of the chief coil. The $N_t^{c'}$ value is determined using (5.7).

**Step-4:** The booster coils are then optimized based on the MMSE problem defined in (5.11) by initializing and sweeping design variables $2a_o^b$, $x^{bi}$, $y^{bi}$ and $\gamma_o^b$ for the fixed sub-optimized chief coil obtained in Step-2. The $G_T$ is determined using (5.2) for different values of $2a_o^b$ where the value of $2a_o^c$ is fixed to the sub-optimum value obtained in Step-2. Let the $2a_o^b$ is a vector. For each index of $2a_o^b$ vector, $MSE$ is evaluated as per (5.11) for $\gamma_o^b \geq 1$. The result is stored for each index in vector $MSE$. The value of minimum $\{MSE\}$ is stored in $MSE(n)$ for $n^{th}$ iteration of the algorithm and corresponding design parameters are extracted to form a sub-optimized Design-2A antenna.

**Step-5:** The $2a_o^b$, $G_T$ and $\gamma_o^b$ are used in (5.3) to determine $n_b$ and $N_t^{c'}$ and $N_t^{bi}$ are obtained from (5.7).

**Step-6:** The Step-2 to Step-5 are repeated for several times until MMSE converges i.e $MSE(n) = MSE(n-1)$. Upon termination, the parameters of the chief coil and the booster coils corresponding to the final iteration are obtained and represent optimal geometrical parameters.

### 5.1.4 Realization of the proposed design

The resultant antenna design using the algorithm of Figure. 5.1 is now presented. The target magnetic field parameter is set to $H_o = 23.55A/m$ [1] and the field forming is desired in the range $p \leq 50mm$ for the sub-objective (5.9) and $70mm < r \leq 100mm$ for the global objective (5.11). The known parameters are initialized based on fabrication limits as $g_T = 1mm$, $\delta^c = 0.5mm$, $\delta^b = 0.5mm$, $w^c = 0.5mm$, $w^b = 0.5mm$, $2a_m^c = 16mm$, $2a_m^b = 8mm$ and the Tx size constraint based on comparative study with [1] as $2a_o = 200mm$.

The algorithm reveals optimum values of $2a_o^{c'}$, $\chi_n^c$, and $\Delta_m^c$ for the chief coil and $2a_o^b$, $n_b$, $N_t^{bi}$, $G_T$ and $\gamma_o^b$ for the booster coils. The obtained parameter values for the proposed Design-2A antenna are listed in Table 5.1. The chief coil has $N_t^{c'} = 11$ turns in which the outer eight turns have $\chi^c = +1$ and the inner three turns have $\chi^c = -1$. There are $n_b = 20$ booster coils each having $N_t^{bi'} = 13$ turns and their center locations are listed in Table 5.1. The booster coils have $\gamma_o^b = 2$ which represents the requirement of a doubled current. The requirement of $\gamma_o^b = 2$ is incorporated within the structure by cloning the booster coils on a double-sided PCB. Hence, the booster coils are placed at the front side and their replicas are etched at the bottom side of the PCB all connected in series with vias and having the same current circulation. The realized PCB layout of the proposed Design-2A

Table 5.1: The proposed Design-2A parameters

| Cheif coil | |
|---|---|
| $\Delta_1^c - \Delta_7^c/\Delta_8^c/\Delta_9^c/\Delta_{10}^c$ | 2mm/34mm/4mm/2mm |
| $2a_o^c/N_t^{c'}/\chi_{1-8}^c/\chi_{9-11}^c$ | 126mm/11/+1/-1 |
| **Booster coil** | |
| $2a_o^b/n_b/G_T/\gamma_o^b$ | 32mm/40/5mm/2 |
| Coil-$i$ | Coil location $(x^{bi}, y^{bi})$ in mm |
| Coil-1 to 20 | $(-83, +17)(-83, +50)(-83, +83)$ |
| | $(-50, +83)(-17, +83)(+17, +83)$ |
| | $(+50, +83)(+83, +83)(+83, +50)$ |
| | $(+83, +17)(+83, -17)\ (+83, -50)$ |
| | $(+83, -83)\ (+50, -83)\ (+17, -83)$ |
| | $(-17, -83)(-50, -83)\ (-83, -83)$ |
| | $(-83, -50)\ (-83, -17)$ |

is presented in Figure. 5.4 marked with the geometrical dimensions of the chief coil and the booster coils. Moreover, the interconnection between chief coil and booster coils is given in Figure. 5.4(e). An analytical model is required to evaluate the PTE performance of the proposed Design-2A antenna.

### 5.1.5 Analytical model to evaluate performance of the proposed Design-2A Tx coil antenna

At the Rx side, an equispaced square coil antenna is employed which has identical dimensions as one used while evaluating $V(\Delta x, \Delta y)$ for Design-1B. The effective magnetic field equation (5.1) is substituted in (2.7) to get total induced voltage in all the turns of the misaligned Rx is computed as

$$V(\Delta x, \Delta y) = \sum_{i=1}^{N_r} V_i = \sum_{i=1}^{N_r} \left[ -j2\pi f\mu_o \iint_{A_{iz}} H_z(x,y)dA_{iz} \right] \tag{5.12}$$

Analogously, using (5.1a) and (5.1b) in (5.12), the induced voltages $V^c(\Delta x, \Delta y)$ and $V^b(\Delta x, \Delta y)$ due to the chief coil and the booster coils, respectively, can be determined as

$$V^c(\Delta x, \Delta y) = -j2\pi f\mu_o \sum_{i=1}^{N_r} \iint_{A_{iz}} H_z^c(x,y)dA_{iz} \tag{5.13a}$$

$$V^b(\Delta x, \Delta y) = -j2\pi f\mu_o \sum_{i=1}^{N_r} \iint_{A_{iz}} H_z^b(x,y)dA_{iz} \tag{5.13b}$$

$$\text{and} \quad V(\Delta x, \Delta y) = V^c(\Delta x, \Delta y) + V^b(\Delta x, \Delta y). \tag{5.13}$$

For the misaligned Rx coil antenna, using $V(\Delta x, \Delta y)$ expression obtained in (5.13), $M(\Delta x, \Delta y)$ is formulated for mode-1 operation as

$$M(\Delta x, \Delta y) = \frac{|V^c(\Delta x, \Delta y)|}{2\pi fI_T} = \frac{\mu_o}{I_T} \sum_{i=1}^{N_r} \iint_{A_{iz}} H^c(x,y)dA_{iz} \tag{5.14}$$
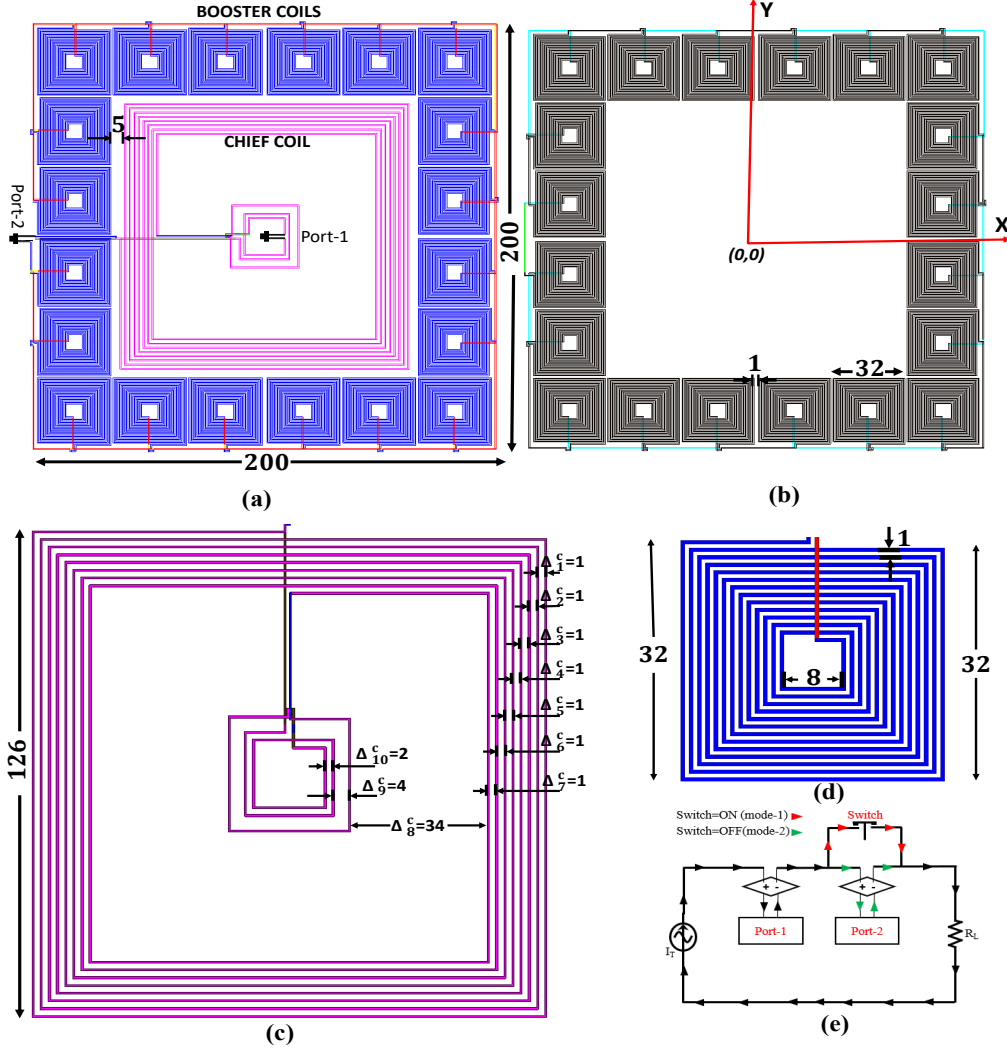
Figure 5.4: Layout of the proposed Design-2A (a) Front view (b) Back view (c) Chief coil (d) Booster coil (e) Switching operation.

and for mode-2 operation when the Rx is misaligned as

$$M(\Delta x, \Delta y) = \frac{\mid V(\Delta x, \Delta y)\mid}{2\pi f I_T} = \frac{\mu_o}{I_T}\sum_{i=1}^{N_r}\iint_{A_{iz}}[H^c(x,y)+H^b(x,y)]dA_{iz} \qquad (5.15)$$

The PTE is characterized in terms of $|S21|$ parameter (given in (2.35)) between the Tx-Rx coil input ports by evaluating $\eta_{s-conventional}$ by substituting $|S11| = 0$ in (2.40a). It is obvious from (2.40a) that the stability of the $S21$ parameter with respect to the Rx misalignment ($\Delta$x, $\Delta$y) depends on $M(\Delta x, \Delta y)$, since, all other parameters such as $R_{cT}$, $R_{bT}$, $R_s$ and, $R_L$ are fixed values. The optimized Design-2A antenna improves uniformity of the magnetic field distribution significantly by optimizing $H_z^c(x,y)$ and $H_z^b(x,y)$ which improves the uniformity of $M(\Delta x, \Delta y)$ from (5.15) in mode-2 operation. Hence, an improved stability of $S21(\Delta x, \Delta y)$ is expected under misaligned condition. Intensive analysis and simulations are performed for proper validation of the proposed Design-2A

Tx coil antenna, which is presented in the subsequent section.

### 5.1.6 Performance evaluation and results

The performance is assessed in terms of improvements achieved in the uniformity of $H_z(x,y)$, $M(\Delta x, \Delta y)$, and $S21(\Delta x, \Delta y)$ distributions to evaluate the extent of mitigation of the lateral misalignment problem. In Figure. 5.5, the analytically obtained field
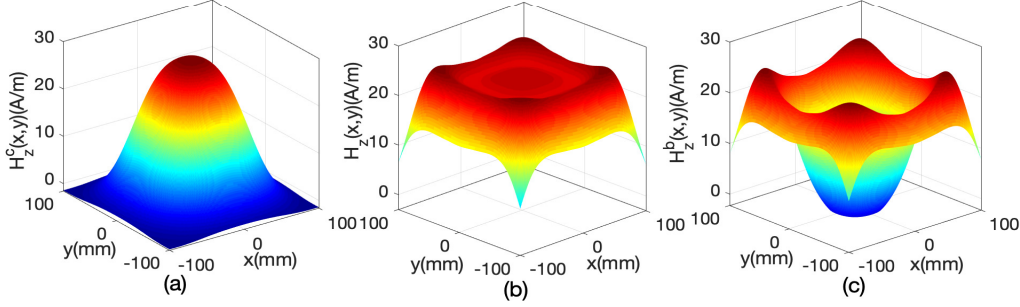


Figure 5.5: Calculated magnetic field distributions of (a) $H_z^c(x,y)$(Tx in mode-1), (b) $H_z(x,y)$ (Tx in mode-2), (c) $H_z^b(x,y)$ (booster coils).

distributions are plotted. From Figure. 5.5(a), it is observed that the magnetic field distribution, in mode-1, originating from the chief coil ($H_z^c(x,y)$) is concentrated in the aligned Rx area. Whereas, Figure. 5.5(b) shows that the proposed Design-2A antenna operating in mode-2 generates a widespread uniform magnetic field ($H_z(x,y) = H_z^c(x,y) + H_z^b(x,y)$). The $H_z(x,y)$ in mode-2 is emanating from the chief coil and the booster coils jointly whose individual field distributions $H_z^c(x,y)$ and $H_z^b(x,y)$ are depicted in Figure. 5.5(a) and Figure. 5.5(c), respectively. It can be observed that the $H_z^b(x,y)$ is maximum around the edges of the Rx region, hence, the $H_z(x,y)$ is boosted by the use of booster coils as per their denoted name. As a result of the applied algorithm, a slightly higher $H_z(x,y)$ is observed near the corners, however, those are under the defined UF($H_z(x,y)$) limits. A notable observation from the analytical results is that the slope of the $H_z^c(x,y)$ and $H_z^b(x,y)$ distributions are complementary to each other such that the locations where the $H_z^c(x,y)$ attains its maxima, the $H_z^b(x,y)$ has its minima, this leads to an overall uniform $H_z(x,y)$. The $M(\Delta x, \Delta y)$ distribution for the Rx misalignment ($\Delta x$, $\Delta y$) is calculated using (5.14) for $2b = 100$mm, $N_r = 12$, and plotted in Figure. 5.6(a) in case only the chief coil is excited. Apparently, the $M(\Delta x, \Delta y)$ is not uniform by the use of the chief coil alone. However, the proposed Design-2A antenna operating in dual-mode achieves uniform $M(\Delta x, \Delta y)$ distribution as plotted in Figure. 5.6(b) implying a better tolerance for the Rx misalignment.

To further inspect the uniformity, the 2D distributions of the $H_z^c(x,y)$ (Tx in mode-1), $H_z(x,y)$ (Tx in mode-2), and $H_z^b(x,y)$ in $h = 50$mm Rx plane for $y = 0$ cut are plotted in Figure. 5.7, where curves are normalized by the $H_o$ value. The performance of the literature design [1] is also evaluated and results are included for comparison purpose. The results indicate that the uniformity of $H_z(x,y)$ is improved by the proposed design
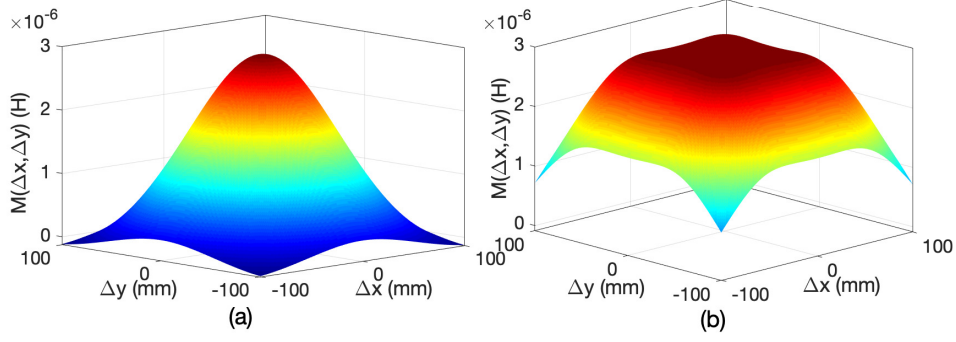
Figure 5.6: Calculated $M(\Delta x, \Delta y)$ of (a) the proposed Design-2A antenna due to only chief coil, (b) optimal Design-2A.
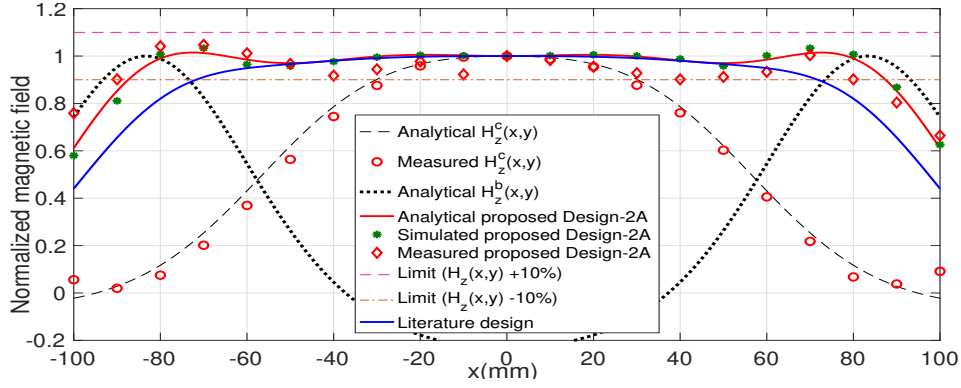


Figure 5.7: Normalized magnetic field distribution in $h = 50mm$ plane and $y = 0$ cut.

over the literature design. To quantify the performance, the $\text{UF}(H_z(x,y))$ is evaluated in the entire $h = 50mm$ plane and found to be 79.65% for the proposed Design-2A antenna as compared to 51.8% calculated for the literature design. The proposed design having layout shown in Figure. 5.4 is simulated using Ansys HFSS v18.0 and the results obtained for the $H_z(x,y)$ distribution corroborate with the analytical results as shown in Figure. 5.7. To evaluate the performance under misalignment case, the normalized 2D variations of $M(\Delta x, \Delta y)$ for the Rx displaced along lateral ($\Delta y = 0$ cut) and diagonal ($\Delta y = \Delta x$ cut) directions are presented in Figure. 5.8. The results indicate a significant improvement in the $M(\Delta x, \Delta y)$ uniformity by the proposed design over the literature design. For instance, in case of the Rx displaced along lateral direction ($\Delta y = 0$), the $M(\Delta x)$ is uniform in the range $\Delta x \in [-48, 48]$mm for the proposed Design-2A antenna as compared to $\Delta x \in [-25, 25]$mm range shown by the literature design. The overall $\text{UF}(M(\Delta x, \Delta y))$ for the entire $h = 50mm$ plane is analytically evaluated as 23.04% and 6.25% for the Design-2A and the literature designs, respectively. The simulated results are also included in Figure. 5.8 showing a good agreement with the analytical results. The performance is compared and summarized in Table 5.2. The obtained analytical and simulated results are validated experimentally in the subsequent section.
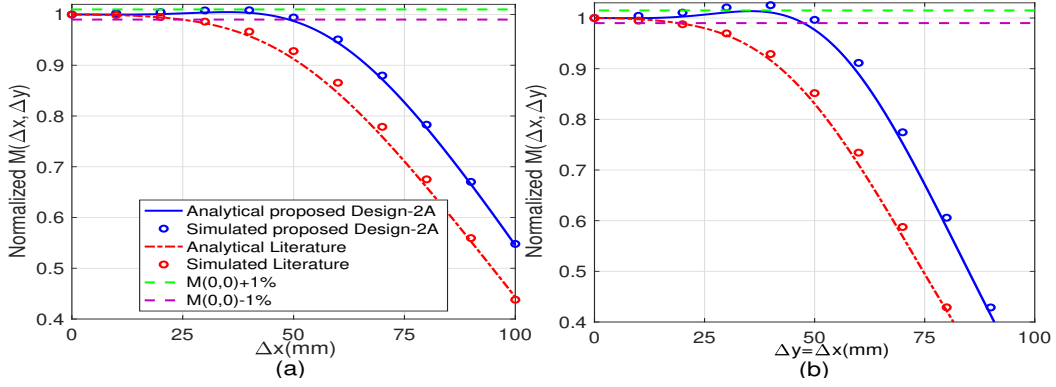
Figure 5.8: The $M(\Delta x, \Delta y)$ distribution results for the misaligned Rx (a) $\Delta y=0$ (b) $\Delta y=\Delta x$.

Table 5.2: Performance comparison of the proposed design

| Performance parameter | Literature design [1] | Proposed Design-2A |
|---|---|---|
| UF($H_z(x,y)$) | 51.84% | 79.65% |
| UF($M(\Delta x, \Delta y)$) | 6.25% | 23.04% |

### 5.1.7 Experimental validation of Design-2A Tx coil antenna

The proposed design is experimentally verified in the laboratory using a measurement setup shown in Figure. 5.9. The layout of proposed Design-2A Tx coil antenna is realized and fabricated on FR4 substrate having thickness $1.6mm$, relative permittivity 4.4, loss tangent 0.02 and copper deposition of $35\mu m$. The fabricated prototypes are shown in the inset of Figure. 5.9 and the measurements are performed using Agilent N5230C Network Analyzer. To minimize the effect of observational error, a DRS60L robotic arm is used to automate the movement of the Rx precisely along the desired path.

An in-house near field probe with outer diameter $2cm$ and number of turns three, as shown in the inset of Figure. 5.9, is used to measure the magnetic field distribution and the measured results are included in Figure. 5.7. The measured magnetic field distribution of the proposed antenna are validated and corroborated with the analytical results for both the modes of operation. A slight mismatch observed for some samples can be attributed to measurement errors.

### 5.1.8 PTE performance evaluation

Using the analytical model presented in Section 2.1.3, the $S21$ is calculated using (2.39) for the Rx displaced along the paths $\Delta y=0$ and $\Delta y=\Delta x$ and the results are shown in Figure. 5.10. The $S21$ is measured by using setup shown in Figure. 5.9 and the results are corroborated well with the analysis as presented in Figure. 5.10. When the Rx is perfectly aligned, only the chief coil is activated to conserve the leakage flux as claimed in the proposed approach. Moreover, the input power drawn by the proposed antenna in mode-1 is significantly reduced for the same output power in the Rx-coil due to low
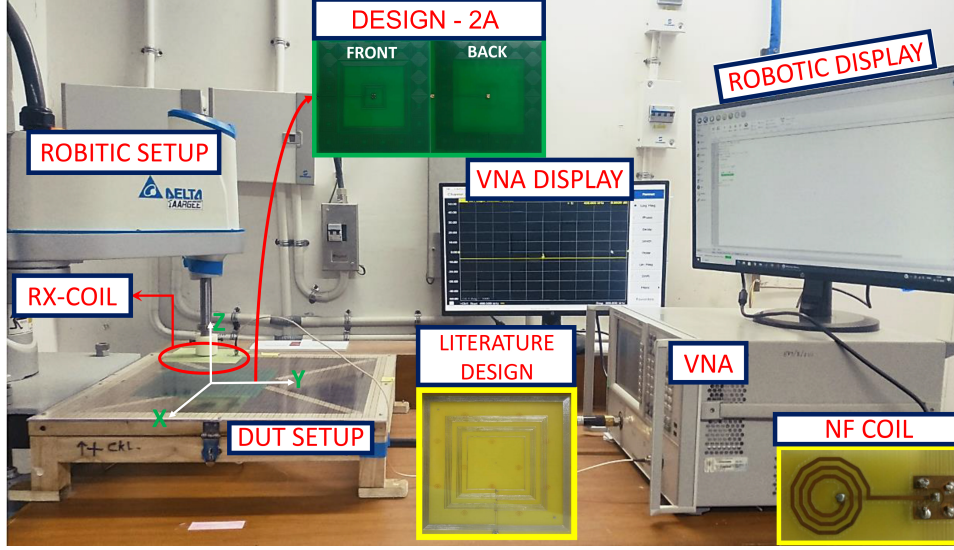
Figure 5.9: Fabricated prototypes and experimental setup.

resistance measured as $4\Omega$ of the excited chief coil in mode-1 as compared to $43.4\Omega$ resistance measured for mode-2 of the proposed Design-2A antenna. The stable region of $S21(\Delta x, \Delta y)$ parameter for the cheif coil antenna alone is $[-7, 7]$mm. Whereas, the stable region for the proposed Design-2A under misaligned state is $[-49, -49]$mm. For comparison, the literature design, fabricated as shown in Figure. 5.9, is measured and the results included in Figure. 5.10 shows $S21$ stability range as $[-26, 26]$mm. The uniformity of S21 parameter which has similar definition as $UF(M(\Delta x, \Delta y))$, is calculated as $24\%$ and $6.76\%$ for the proposed Design-2A antenna and the literature design, respectively. Therefore, the misalignment tolerance in $S21(\Delta x, \Delta y)$ parameter is $255\%$ improved by the proposed antenna over the literature design, the same improvement is realized on the link efficiency of the WPT system according to the expression $\eta_{s-conventional} = |S21|^2 \times 100$ by assuming port-1 is perfectly matched ($|S11| = 0$) in (2.40a).

The Design-2A Tx coil antenna has a major setback in its asymmetric structure. Although both modes of operation yield identical values of $M(\Delta x, \Delta y)$, the resistive parts of the chief coil and booster coils, namely $R_{cT}$ and $R_{bT}$, are not identical, resulting in instability in $\eta_{s-conventional}$ while using de-normalized values. This instability in $\eta_{s-conventional}$ leads to an increase in operating costs for WPT systems when the Rx coil is misaligned from its intended position due to poor human motor skills. Moreover, the system composed of Design-2A does not provide a working model for the operation of switching circuits. To counter the drawbacks of Design-2A, a novel 4-port symmetrical Tx coil antenna designated as Design-2B is proposed to maintain uniformity in PTE even with a misaligned Rx coil antenna. Furthermore, the system composed of Design-2B is equipped with a realistic detection system to activate the Tx modules based on the position of the Rx coil antenna.
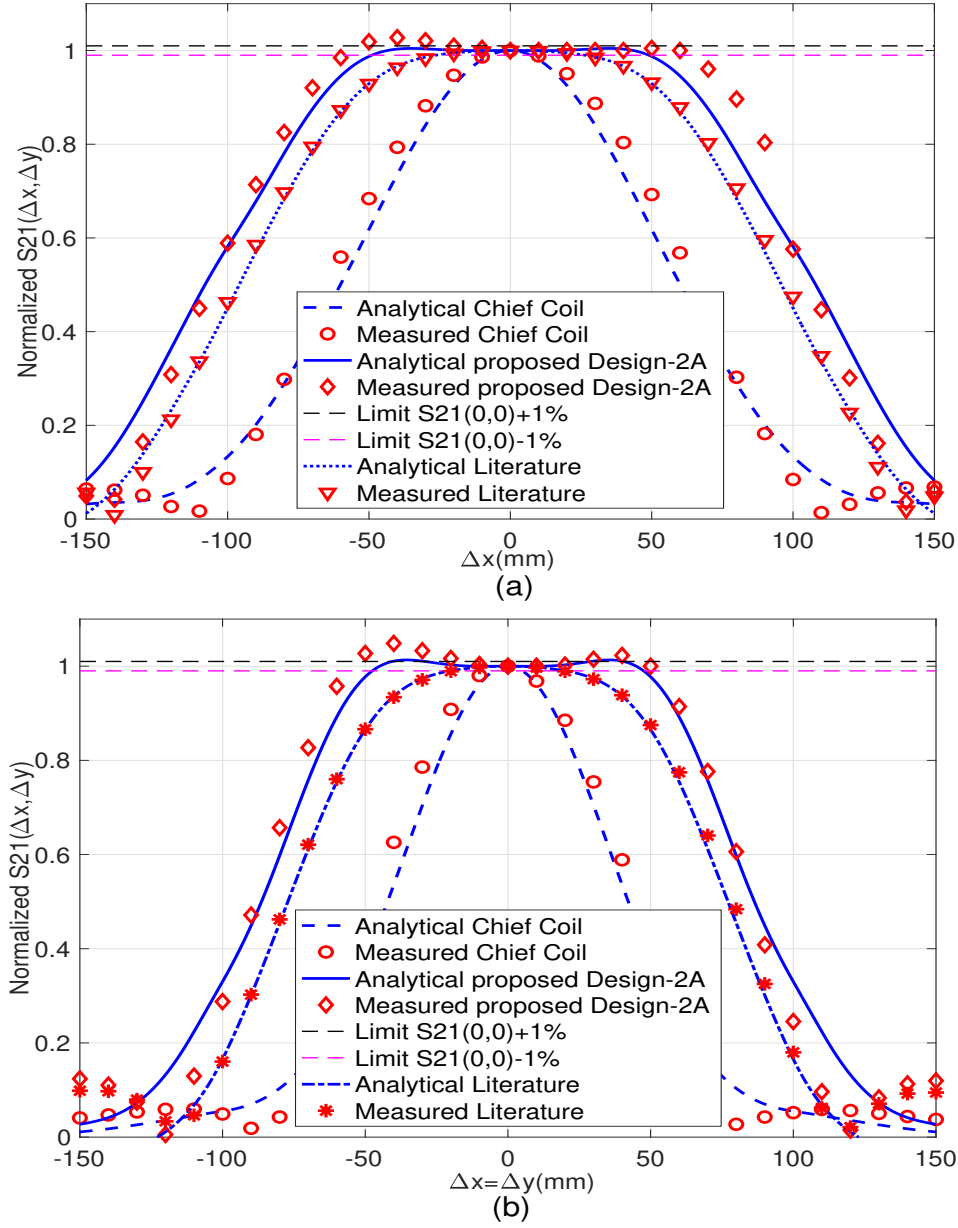
Figure 5.10: Performance results of $S21$ parameter (a) $\Delta y=0$, (b) $\Delta y=\Delta x$.

## 5.2   System Description of Design-2B (SO-B: EP-4)

Figure 5.11(a) illustrates a prototype of a Design-2B Tx coil antenna in a two-coil resonant WPT system that operates at a frequency of $f = 300$ kHz. This frequency was chosen to facilitate a fair comparison with the system presented in [79]. As with all previous designs, the distance between the Tx and Rx coils is fixed at $h = 50$ mm. Figure 5.11(b) provides a detailed illustration of the proposed Design-2B charging pad. The Tx pad is composed of four independent planar sub-array coil modules labeled A, B, C, and D. Each coil module, denoted by $m \in$ A, B, C, D, is centered at $(x_m, y_m)$ as depicted in
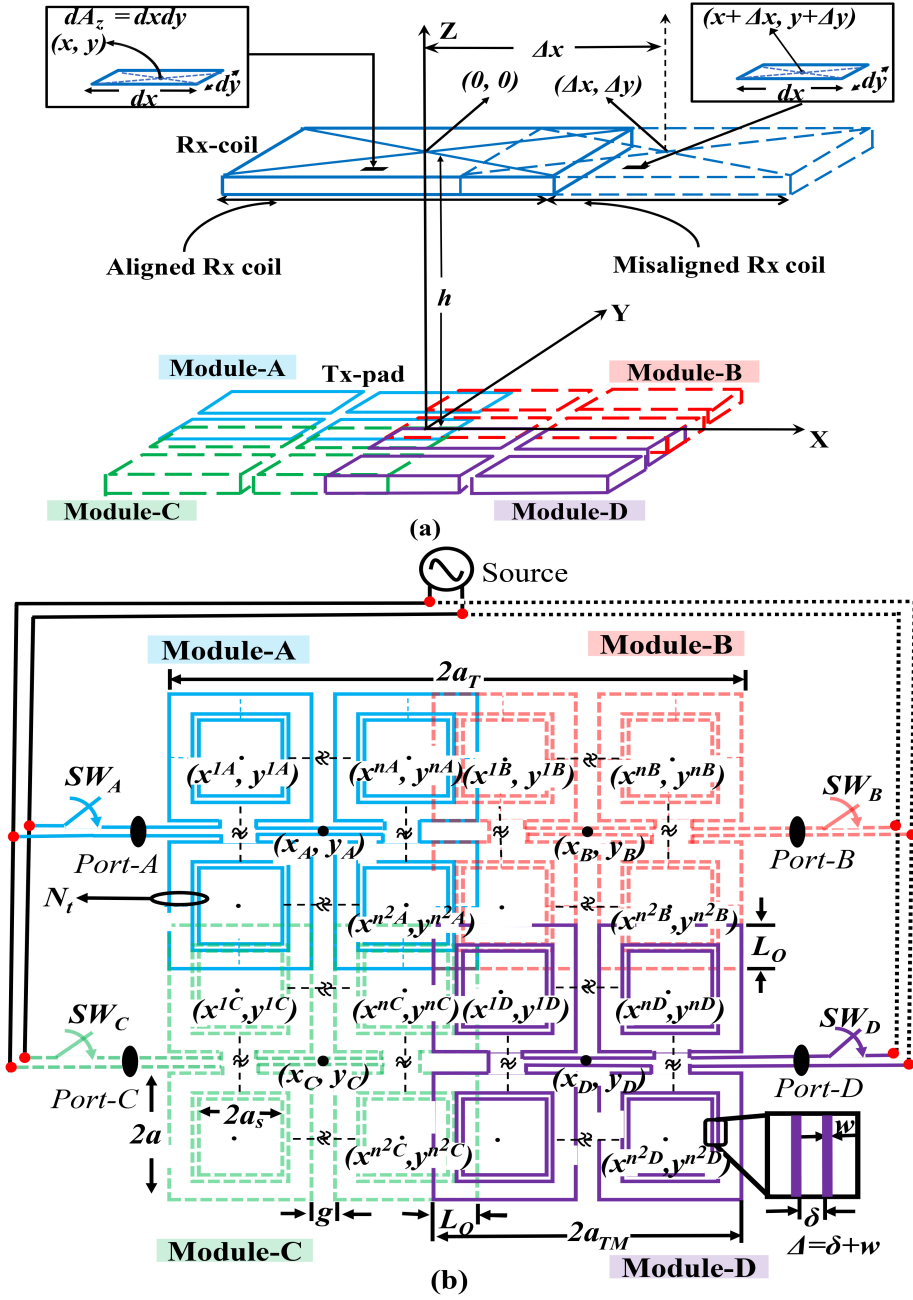
Figure 5.11: (a) A schematic WPT system under lateral misalignment, (b) the proposed Design-2B charging pad scheme for analysis.

Figure 5.11(b). It contains an $n \times n$ array of multi-turn coils located at $(x_t = x^{im}, y_t = y^{im}); \forall; i \in 1, 2, ..n^2$. Thus, each module consists of $n^2$ coils. The Design-2B charging pad is optimized to generate a piece-wise non-uniform magnetic field distribution similar to design-1C, resulting in a pseudo-uniform voltage induction in the Rx region, regardless of misalignment. Here, the terms "piece-wise" and "pseudo" indicate that even if only one of the Tx modules is activated by integrating the switching operation, a uniform voltage in

the Rx coil is ensured throughout and within the operating region of the misaligned Rx.

The corresponding coil module-$m$ can be activated based on the position of the Rx coil using four switches $(\mathrm{SW}_A, \mathrm{SW}_B, \mathrm{SW}_C, ; \mathrm{and}; \mathrm{SW}_D)$ connected to the feeding ports of the coil modules, as shown in Figure 5.11(b). Additionally, the equivalent circuit diagram of the proposed two-coil series-series resonant WPT system is presented in Figure 5.12. In
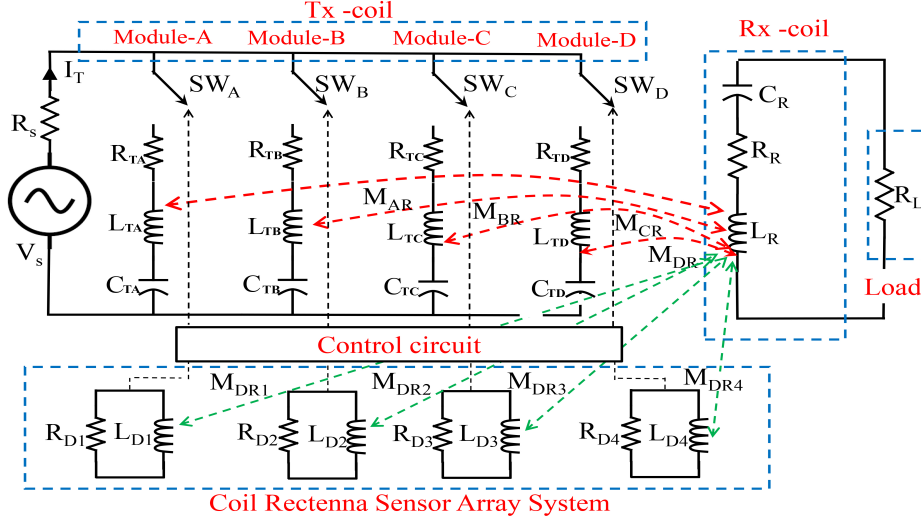


Figure 5.12: Schematic circuit diagram of the proposed WPT system Design-2B of modular Tx and sensor array.

the circuit, $R_{Tm}$ and $L_{Tm}$ represent effective series resistance and self-inductance of Tx module-$m \in \{$A, B, C, D$\}$, respectively. To resonate the Tx-Rx coils at $f$, capacitors $C_{Tm}$ and $C_R$ are connected in series as a compensation network. Mutual inductance between the Tx module-$m$ and the Rx coil is denoted as $M_{mR}$. Cross-coupling between adjacent Tx modules is nullified since only one Tx module-$m$ at a time is excited and switched using a control circuit. A coil rectenna sensor array system, as shown in Figure. 5.12, is integrated with the micro-controller-based control circuit, which implements a state machine for switching operation by sensing the Rx misalignment state. The rectenna sensor array design is proposed later in Section 5.2.10.

To design the proposed Tx charging pad by field-forming technique, the geometrical parameters defined in Figure. 5.11(b) include the maximum side length of the Tx charging pad, $2a_T$, the maximum side length of the Tx module-$m$, $2a_{TM}$, single-coil side length, $2a$, the minimum side length of single-coil, $2a_s$, trace width, $\Delta$, track width, $w$, inter-turn spacing, $\delta$, and module overlapping length, $L_o$. The side length of the $j^{th}$ turn of a coil is determined as $2a^j = 2a - 2(j-1)\Delta \ \forall \ j \in \{1, 2, ..N_t\}$. Here, $\Delta = w + \delta$, and $N_t$ denotes the number of turns in a single coil as shown in Figure. 5.11(b). The z-component of the magnetic-field given in (2.3) is relabelled as $H_z(x, y) = H_{zim}^j(x, y)$ for single turn-$j$ of the coil-$im$ of the Tx module-$m$. Moreover, the side-length of Tx-coil in (2.3) is re-labelled as $2a = 2a^j$. The magnetic field generated by the Tx module-$m$, $H_{zT}^m(x, y)$, in the Rx region

due to $n \times n$ sub-array coils is evaluated as

$$H_{zT}^m(x,y) = \sum_{i=1}^{n^2} \sum_{j=1}^{N_t} H_{zim}^j(x,y) \quad \forall \quad m \in \{A, B, C, D\} \tag{5.16}$$

The magnetic field originated by the entire Tx charging pad, $H_{zT}(x,y)$, depends on the status of the switching circuit and is formulated as

$$H_{zT}(x,y) = S_A \cdot H_{zT}^A(x,y) + S_B \cdot H_{zT}^B(x,y) + S_C \cdot H_{zT}^C(x,y) + S_D \cdot H_{zT}^D(x,y) \tag{5.17}$$

where $S_m \in \{0,1\}$ represents the state of the switch $SW_m$ corresponding to the module-$m$ which depends on the Rx position. Due to the involvement of the switching states, the expression in (5.17) represents a piece-wise magnetic field distribution which is optimized further to generate non-uniform distribution by the individual Tx module. For analysis, the Rx coil is assumed misaligned by $(\Delta x, \Delta y)$ from its aligned position as depicted in Figure. 5.11(a). The switching state is set to $S_m = 1$ when the Rx stays within the uniform voltage region of the module-$m$. Thus, the states $S_m$ of the switches are assigned based on the Rx position as

$$S_m = \begin{cases} 1 & \text{for } m = \begin{cases} A & \text{for } \Delta x \leq 0, \Delta y \geq 0 \\ B & \text{for } \Delta x > 0, \Delta y \geq 0 \\ C & \text{for } \Delta x \leq 0, \Delta y < 0 \\ D & \text{for } \Delta x > 0, \Delta y < 0 \end{cases} \\ 0 & \text{for other } m \end{cases} \tag{5.18}$$

By using the unit step function, $u(x)$, the switching states $S_m$ defined in (5.18) can be expressed in a unified manner to indulge the switching boundaries as

$$\begin{aligned} S_A &= u(-\Delta x)u(\Delta y), \quad S_B = u(\Delta x)u(\Delta y) \\ S_C &= u(-\Delta x)u(-\Delta y), \ S_D = u(\Delta x)u(-\Delta y) \end{aligned} \tag{5.19}$$

### 5.2.1   Induced Voltage Analysis for Misaligned Rx Coil

At the Rx side, a square coil having side length, $2b$, is considered to have a number of turns, $N_r$, concentrated at its periphery. Knowing the magnetic field distribution expression (5.17), the induced voltage in the misaligned Rx coil is formulated using (2.4)-(2.6) to conduct the design optimization. By substituting (5.17) in (2.6), the $V(\Delta x, \Delta y)$ is determined in terms of switching states as,

$$V(\Delta x, \Delta y) = -j2\pi f \mu_o N_r \left[ \iint_{A_z} \left( S_A \cdot H_{zT}^A + S_B \cdot H_{zT}^B \quad + S_C \cdot H_{zT}^C + S_D \cdot H_{zT}^D \right) dA_z \right] \tag{5.20}$$

which is further written as

$$V(\Delta x, \Delta y) = \sum_{m \in \{A,B,C,D\}} S_m \cdot V_m(\Delta x, \Delta y) \tag{5.21}$$

where $V_m(\Delta x, \Delta y)$ represents the induced voltage in the misaligned Rx due to individual Tx module-$m$ and is given as

$$V_m(\Delta x, \Delta y) = -j2\pi f \mu_o N_r \iint_{A_z} H_{zT}^m(x,y) dA_z, \ \forall \ m \in \{A,B,C,D\} \tag{5.22}$$

Substitution from (5.19) in (5.21) gives

$$\begin{aligned}
V(\Delta x, \Delta y) = \Big[ &u(-\Delta x)u(\Delta y)V_A(\Delta x, \Delta y) + u(\Delta x)u(\Delta y)V_B(\Delta x, \Delta y) \\
&+u(-\Delta x)u(-\Delta y)V_C(\Delta x, \Delta y) + u(\Delta x)u(-\Delta y)V_D(\Delta x, \Delta y) \Big]
\end{aligned} \tag{5.23}$$

Since each module is identical and symmetric, the $V_m(\Delta x, \Delta y)$ of the module-$m$ can be realized as shifted replicas of a voltage distribution function, $V_o(\Delta x, \Delta y)$, corresponding to a hypothetical module which is identical to the other modules however located at the origin. To express this in formulation, the $V_m(\Delta x, \Delta y)$ can be written as

$$V_m(\Delta x, \Delta y) = V_o(\Delta x - x_m, \Delta y - y_m), \quad \forall \ m \in \{A,B,C,D\} \tag{5.24}$$

Similarly, the $H_{zT}^m(x,y)$ are realized as the shifted replicas of the field distribution $H_{zT}^o(x,y)$ generated by the hypothetical module as

$$H_{zT}^m(x,y) = H_{zT}^o(x - x_m, y - y_m), \quad \forall \ m \in \{A,B,C,D\} \tag{5.25}$$

and the relationship between $H_{zT}^o(x,y)$ and $V_o(\Delta x, \Delta y)$ is given by (5.22) with $m \implies o$ replacement. Observing (5.23) and (5.24) together, it is inferred that the optimization of any one module (e.g., the hypothetical module located at the origin) is sufficient to realize the complete Tx pad. This can greatly simplify the computational time of the numerical optimization which only requires to focus on generating optimal non-uniform magnetic field distribution of $H_{zT}^o$ to achieve uniform $V_o$. However, an overall uniform $V(\Delta x, \Delta y)$ for the entire Tx pad can be realized only when this procedure is followed by an optimal overlapping region selection constraint.

To illustrate the procedure, let the uniformity in $V_o(\Delta x, \Delta y)$ due to a hypothetical module is optimized, which ideally achieves a target voltage ($V_p$) with $\pm 1\%$ maximum variation in the Rx misalignment range $-p \leq (\Delta x, \Delta y) \leq p$ and defined as,

$$V_o(\Delta x, \Delta y) = \begin{cases} V_p \pm 1\% & \text{for} \quad -p \leq (\Delta x, \Delta y) \leq p, \\ < (V_p - 1\%) & \text{otherwise} \end{cases} \tag{5.26}$$

The distribution of $V_o(\Delta x, \Delta y)$ is replicated at $(x_m, y_m)$ given as

$$x_m = \pm \left( \frac{2a_{TM} - L_o}{2} \right), \quad y_m = \pm \left( \frac{2a_{TM} - L_o}{2} \right), \tag{5.27}$$

to realize the $V_m(\Delta x, \Delta y)$ from (5.24) for each module-$m$ and thereby the overall $V(\Delta x, \Delta y)$ from (5.23) for the Tx pad is obtained as

$$
\begin{aligned}
V(\Delta x, \Delta y) = &\left[ u(-\Delta x)u(\Delta y)V_o \left( \Delta x + \frac{2a_{TM} - L_o}{2}, \Delta y - \frac{2a_{TM} - L_o}{2} \right) \right. \\
&+ u(\Delta x)u(\Delta y)V_o \left( \Delta x - \frac{2a_{TM} - L_o}{2}, \Delta y - \frac{2a_{TM} - L_o}{2} \right) \\
&+ u(-\Delta x)u(-\Delta y)V_o \left( \Delta x + \frac{2a_{TM} - L_o}{2}, \Delta y + \frac{2a_{TM} - L_o}{2} \right) \\
&\left. + u(\Delta x)u(-\Delta y)V_o \left( \Delta x - \frac{2a_{TM} - L_o}{2}, \Delta y + \frac{2a_{TM} - L_o}{2} \right) \right].
\end{aligned}
\tag{5.28}
$$

To achieve the uniform voltage in the operating Rx region, the $V(\Delta x, \Delta y)$ must be uniform with value $V_p \pm 1\%$ for the inter-modular movement Rx. Hence, the $V(\Delta x, \Delta y)$ must be uniform, particularly at the boundaries where the switching occurs. To derive the uniformity constraint, the Rx is assumed to move from module-$A$ (or module-$C$) to module-$B$ (or module-$D$) crossing the boundary at $\Delta x = 0$. Due to the switching at the boundary, voltages for the two cases, $\Delta x = 0^+$ and $\Delta x = 0^-$ are equated to $V_p \pm 1\%$. Due to symmetry, only the $\Delta x = 0^+$ case is sufficient to derive the constraint. For the Rx located in module-A region at the boundary $\Delta x = 0$, the voltage $V(\Delta x = 0^-)$ is given from (5.28) as

$$
\begin{aligned}
V(\Delta x = 0^-, \Delta y) &= (V_p \pm 1\%) \\
\implies V_o \left( \frac{2a_{TM} - L_o}{2}, \Delta y - \frac{2a_{TM} - L_o}{2} \right) &= (V_p \pm 1\%),
\end{aligned}
\tag{5.29}
$$

this is true from (5.26) if following constraint is satisfied as

$$-p \leq \frac{2a_{TM} - L_o}{2} \leq p, \tag{5.30}$$

which is solved further to obtain

$$2a_{TM} - 2p \leq L_o \leq 2a_{TM} + 2p, \tag{5.31}$$

where $L_o \leq 2a_{TM} + 2p$ is trivial since the extension of overlap can not exceed $2a_{TM}$ due to geometry of Tx pad in Figure. 5.11(b). Therefore, the the overlapping region is constrained as

$$L_o \geq 2a_{TM} - 2p, \tag{5.32}$$

and the corresponding total misalignment tolerance range ($-r$ to $r$) of the Tx pad is

$$-p - \left(\frac{2a_{TM} - L_o}{2}\right) \le (\Delta x, \Delta y) \le p + \left(\frac{2a_{TM} - L_o}{2}\right). \tag{5.33}$$

Hence, a higher $L_o$ results in a lower misalignment tolerance range, therefore to be minimized. However, the $L_o$ constraint in (5.32) limits the minimum value. Thus the optimal overlapping region selection is constraint by

$$L_o = 2a_{TM} - 2p. \tag{5.34}$$

Also, a higher $p$ improves the misalignment tolerance range from (5.33) which is targeted in the proposed optimization. The value of $p$ is optimized using the field forming technique which is based on MMSE algorithm defined later in (5.38) which assists in determining the optimal $L_o$ value using (5.34).

## 5.2.2 Mutual Coupling, Link Efficiency, and Load Power Formulation for the Misaligned Rx Coil

The Tx-Rx mutual coupling $M_{mR}$, defined in Figure. 5.12, is generally formulated in terms of $V$ using (2.8). However, for the proposed switched design, the $M_{mR}$ between the Tx module-$m$ and the Rx also depends on the switching states $S_m$ (incorporated in $V(\Delta x, \Delta y)$) as well as Rx misalignment $(\Delta x, \Delta y)$ and determined using

$$M_{mR}(\Delta x, \Delta y) = \frac{V(\Delta x, \Delta y)}{2\pi f I_T} \quad \forall \quad m \in \{A, B, C, D\} \tag{5.35}$$

Thus, the Tx modules that do not have an Rx coil are not activated and do not have any coupling with the Rx coil. To obtain the performance parameter $\eta_{s-conventional}$, which is defined in (2.40a), we substitute (5.35) in (2.35) and (2.39). Similarly, to obtain the $P_{R_R}(\Delta x, \Delta y)$ for series-series resonant topology, we replace (5.35) in (2.15). Note that the $M_{mR}(\Delta x, \Delta y)$ depends on $V(\Delta x, \Delta y)$, and therefore, the uniformity of $\eta_{s-conventional}$ and $P_{R_R}(\Delta x, \Delta y)$ depends on the output profile of the induced voltage, provided that the resistive losses are constant for all Tx modules. Therefore, uniformity in $V$ implies uniformity in $M_{mR}$, $\eta_{s-conventional}$, and $P_{R_R}$, which is formulated as an optimization problem, and the design algorithm is detailed in the subsequent section.

## 5.2.3 Objective Function and Optimization Design Procedure to form Pseudo Uniform Voltage

The proposed optimization problem is based on the MMSE algorithm aldready discussed in Chapter 4. Since the optimization problem solely depends on the geometrical parameters of the Tx modules, the relationships among various design parameters are first defined, serving the design constraints.

### 5.2.4   Design Constraints and Parameter Relationships

The geometrical parameters of the Design-2B charging pad as defined in Figure. 5.11(b)
are inter-related as

$$
\begin{cases}
2a_T = 2(2a_{TM}) - L_o, \\
2a_{TM} = |x^{nm} - x^{1m}| + 2a, \\
N_t = \frac{2a - 2a_s}{2(\Delta)} + 1, \\
x_m = \frac{x^{nm} + x^{1m}}{2}, \ y_m = \frac{y^{n^2m} + y^{nm}}{2}.
\end{cases}
\tag{5.36}
$$

The known parameters such as $2a_s$ and $\Delta$ are initialized based on fabrication limits. Due to
inter-dependency of the parameters given by the constraints (5.36), the only independent
design parameters available for optimization of the Tx module-$m$ are $(x^{im}, y^{im})$, $2a$, and
$n$. The same is correspondingly available for the hypothetical module optimization. From
(5.24), it is mentioned that only the hypothetical module parameters are sufficient for
defining optimization problem for uniform $V(\Delta x, \Delta y)$.

### 5.2.5   Formulation of Optimization Problem Based on Field-forming Technique

The optimization of the hypothetical module of the Tx antenna is now presented. The MSE
is evaluated between the target voltage $V_T(\Delta x, \Delta y)$ and the calculated voltage $V_o(\Delta x, \Delta y)$
induced in the desired range of misalignment $\Delta x, \Delta y \in \ [-\frac{2a_{TM}}{2}, \frac{2a_{TM}}{2}]$ within the Rx
plane. The value of $2a_{TM}$ governs the misalignment tolerance range ($-p$ to $p$) of the Rx
coil and defines the area within which uniform $V_o(\Delta x, \Delta y)$ is targeted in the Rx plane due
to the hypothetical module. The target induced voltage function $V_T$ is defined as

$$
V_T(\Delta x, \Delta y) =
\begin{cases}
V_p & \text{for} \quad -\frac{2a_{TM}}{2} \leq \Delta x, \Delta y \leq \frac{2a_{TM}}{2}, \\
0 & \text{otherwise.}
\end{cases}
\tag{5.37}
$$

In practice the misalignment range is limited as $2p < 2a_{TM}$ because it is not possible to
achieve voltage uniformity in region equivalent to the size of the Tx coil [79]. Therefore, the
compromised misalignment range is reflected in the overlapping length defined in (5.34).
For optimization, the MSE is evaluated between the $V_o(\Delta x, \Delta y)$ calculated using (5.24)
and the $V_T$ defined in (5.37). Hence, the objective for the optimization is formulated as

$$
\min_{x^{io}, y^{io}, 2a, n} \quad MSE = \overline{[V_o(\Delta x, \Delta y) - V_T(\Delta x, \Delta y)]^2}
$$
$$
\text{s.t.} \quad 2a_s \leq 2a \leq 2a_T
\tag{5.38}
$$

where $\overline{[\cdot]}$ represents the mean function. Following the optimization, the complete Tx
pad parameters are obtained by determining the optimal $L_o$ value from the overlapping
constraint (5.34). To solve the optimization problem defined in (5.38) and design the
complete Design-2B charging pad, an algorithm is developed which is an iterative process
based on minimum {MSE} and is now illustrated.
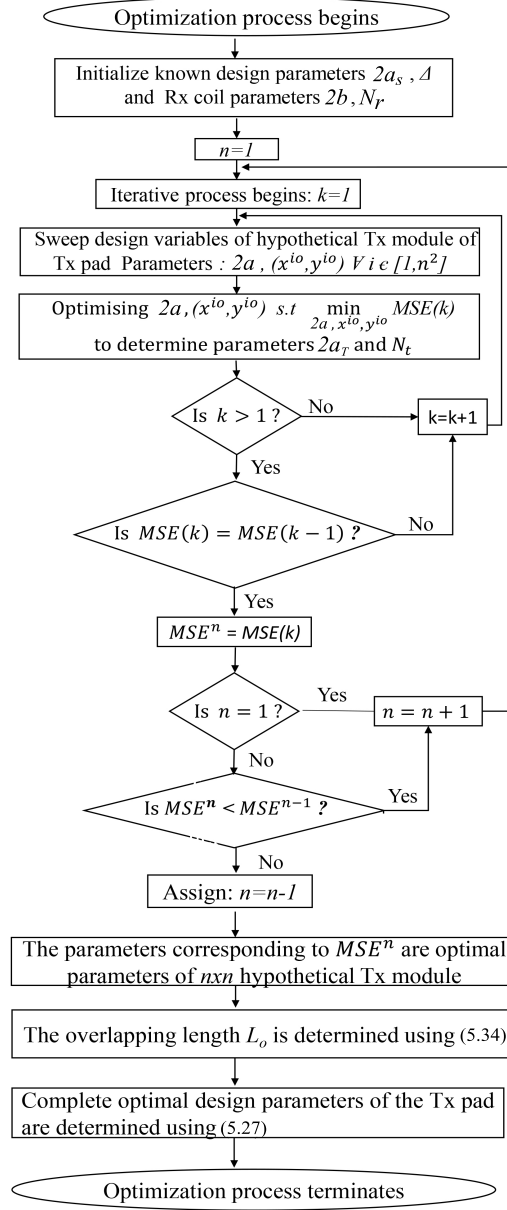
Figure 5.13: Iterative design algorithm to fabricate Design-2B Tx coil antenna.

## 5.2.6   Design Procedure for Design-2B Charging Pad

An iterative design algorithm based on (5.38) is adopted and summarized in the flow chart shown in Figure. 5.13. The algorithm begins with initializing the set of known design constraints and terminates with optimal geometrical parameters of Tx pad by sweeping the independent design parameters in the optimization procedure. The design steps of the algorithm are detailed as follows.

**Step-1:** The optimization process begins by initializing the known parameters based on the fabrication limit of a hypothetical Tx module ($m \Longleftarrow o$) and Rx coil.

**Step-2:** The optimization process for $n \times n$ array coils for a hypothetical Tx module is initiated for $n = 1$.

**Step-3:** The optimization process begins for first iteration ($k = 1$) based on the MMSE problem defined in (5.38) by sweeping design variables $2a$ and $x^{io}, y^{io} \quad \forall \quad i \in [1, n^2]$. The design parameters corresponding to minimum {MSE} are evaluated.

**step-4:** From the optimized design variables of hypothetical Tx module resulted in Step-3, dependent design parameters such as $2a_{TM}$, $N_t$, $x_o$, and $y_o$ are determined from (5.36).

**Step-5:** The Step-2, 3, and 4 are repeated for several iterations until minimum MSE converges i.e. MSE(k)=MSE(k-1). The MSE value corresponding to $k^{th}$ iteration is stored in $MSE^n$.

**Step-6** The Step-2, 3, 4 and 5 are repeated for array coils $n > 1$ in hypothetical Tx module.

**Step-7:** The design parameters and misalignment range ($2a$) corresponding to $\min\{MSE^n\}$ are designated as optimal design parameters of $n \times n$ hypothetical Tx module.

**Step-8:** The optimal overlapping length ($L_o$) as shown in Figure. 5.11(b) is evaluated using (5.34).

**Step-9:** Given that, the hypothetical Tx module is identical to the Tx modules-A, B, C, and D, the design parameters of the entire Tx pad are determined with the aid of optimal parameters of the hypothetical Tx module and overlapping length ($L_o$). Wherein, the positions of the proposed Tx pad are evaluated using (5.27) to achieve the voltage distribution defined in (5.28).

**Step-10:** The optimization algorithm terminates.

The realization of the optimized design is exemplified in the next section.

### 5.2.7   Proposed Design-2B Charging Pad Realization and Results

The optimization procedure of Figure. 5.13 is executed by considering $2b = 150$ mm and $N_r = 18$ to achieve output voltage rating ($V_o = 16.96$ V) in (5.38) same as that achieved in [79] to have a fair comparison. Moreover, the required output voltage for drones ranges in $12 - 24$ V [103], which ensures the achieved voltage is within the limiting range. The known parameters such as $2a_s = 16$ mm, $\Delta = 1$ mm, $w = 1$ mm, and $\delta = 0$ mm are initialized based on the fabrication limits. The algorithm primarily unveils the independent optimal parameters $2a$, $n$, $L_o$ and $(x^{im}, y^{im})$. Later, the dependent parameters $2a_{TM}$, $N_t$, $2a_T$, and $(x_m, y_m)$ are determined using (5.36). The optimized design parameters obtained for the proposed charging pad are listed in Table 5.3. The $n \times n$ sub-array of Tx module-$m$ is optimized for $n = 2$. To facilitate the overlapping between adjacent Tx modules-$m$, the proposed Tx pad is realized using Litz wires with a diameter of 1 mm. The layout of the final design is depicted in Figure. 5.14 and the performance is evaluated subsequently.

### 5.2.8   Analytical Results

The magnetic field distribution $H_{zT}(x, y)$ of each Tx module-$m$ is displayed in Figure. 5.15, and it is verified that the optimal magnetic field generated by the $2 \times 2$ sub-array has a

Table 5.3: The optimized design parameters of proposed Design-2B charging pad

| Physical dimensions of Design-2B Tx pad | |
|---|---|
| $2a_T/2a_{TM}/2a$ | 428.1 mm/241.8 mm/93.2 mm |
| $L_o/N_t/n$ | 55.5 mm/39/2 |
| **Position of sub-array coils in Tx module-A** | |
| $P_{A1}, P_{A2}$ | (-167.3, 167.6) mm, (-18.7, 167.6) mm |
| $P_{A3}, P_{A4}$ | (-167.3, 19) mm, (-18.7, 19) mm |
| **Position of sub-array coils in Tx module-B** | |
| $P_{B1}, P_{B2}$ | (19, 167.6) mm, (167.6, 167.6) mm |
| $P_{B3}, P_{B4}$ | (19, 19) mm, (167.6, 19) mm |
| **Position of sub-array coils in Tx module-C** | |
| $P_{C1}, P_{C2}$ | (-167.3, -18.7) mm, (-18.7, -18.7) mm |
| $P_{C3}, P_{C4}$ | (-167.3, -167.3) mm, (-18.7, -167.3) mm |
| **Position of sub-array coils in Tx module-D** | |
| $P_{D1}, P_{D2}$ | (19, -18.7) mm, (167.6, -18.7) mm |
| $P_{D3}, P_{D4}$ | (19, -167.3) mm, (167.6, -167.3) mm |
| **Geometric center of Tx module-m** | |
| $(x_A, y_A), (x_B, y_B)$ | (-93, 93.3) mm, (93.3, 93.3) mm |
| $(x_C, y_C), (x_D, y_D)$ | (-93, -93) mm, (93.3, -93) mm |
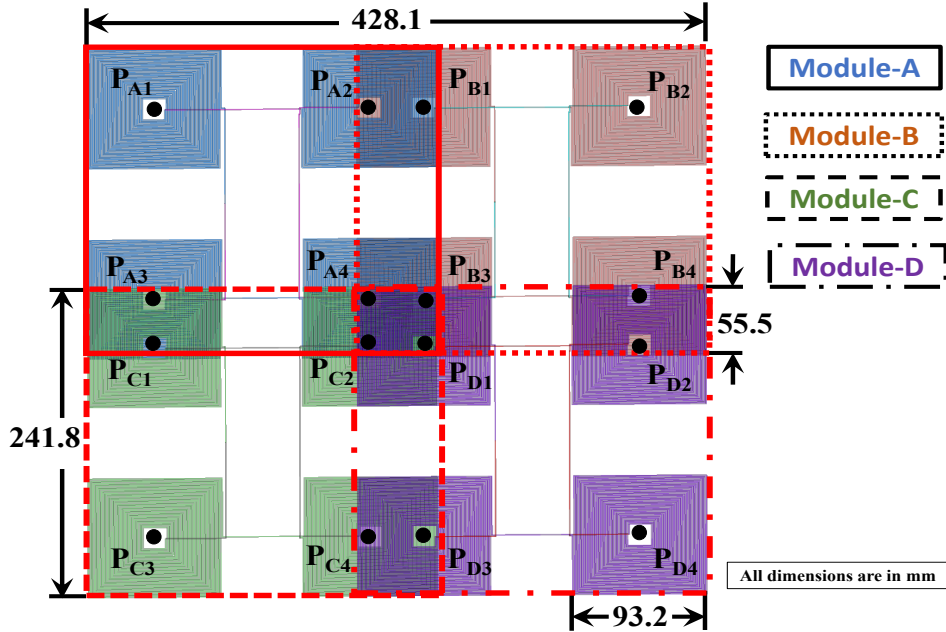


Figure 5.14: Layout of the proposed Design-2B modular multi-coil array charging pad.

piece-wise non-uniform distribution in the Rx plane. Moreover, at any given instant, only the $H_{zT}(x, y)$ of one single Tx module-(A or B or C or D) is activated based on the position of the Rx coil, which reduces the undesired field leakage. This optimal magnetic field links with the Rx coil to locally mitigate the lateral misalignment. Integrated with the switching control, the optimal magnetic field distribution forms pseudo uniform $V(\Delta x, \Delta y)$ in the
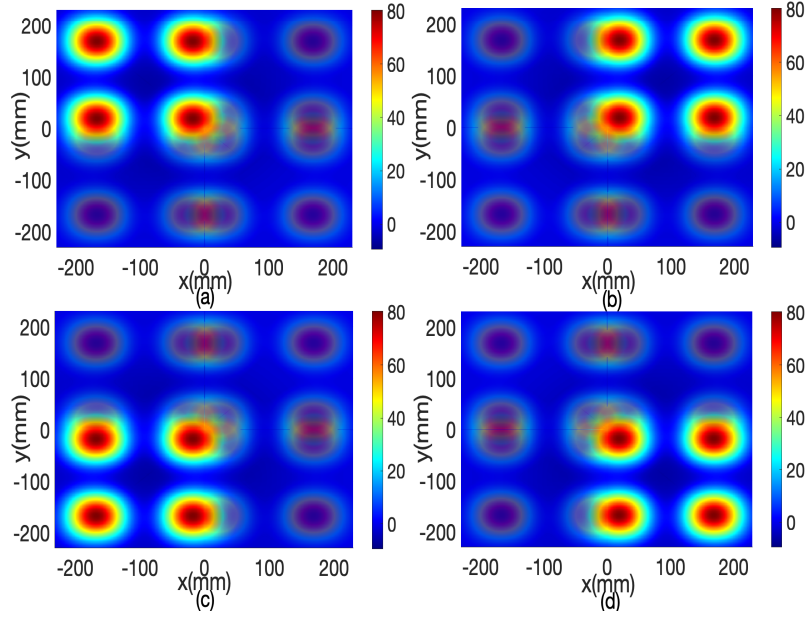
Figure 5.15:  $H_{zT}(x, y)$ distribution of (a) Tx module-A, (b) Tx module-B, (c) Tx module-C, (d) Tx module-D.
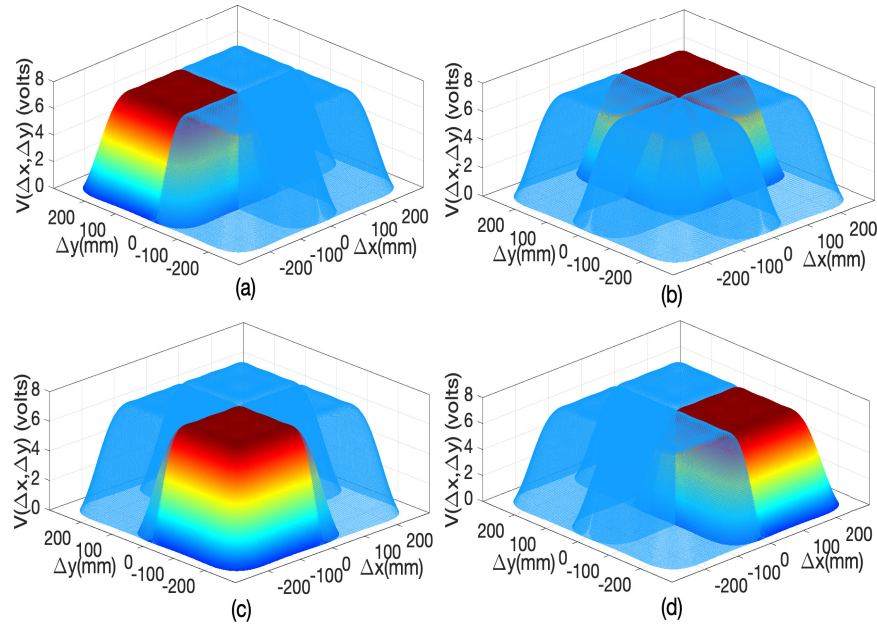


Figure 5.16:  $V(\Delta x, \Delta y)$ distribution in the misaligned Rx coil by switching on (a) Tx module-A, (b) Tx module-B, (c) Tx module-C, (d) Tx module-D.

misaligned Rx coil as shown in Figure. 5.16. The uniformity of voltage is maintained in the total Rx operating region by activating suitable Tx module-$m$ where the Rx lies.
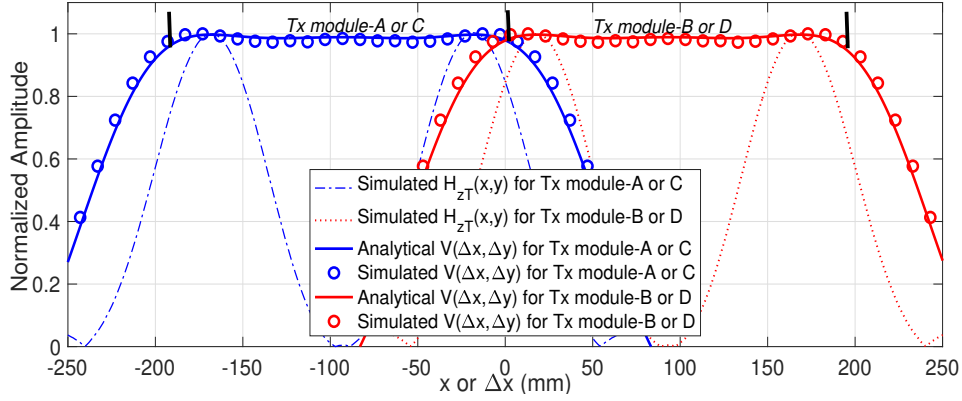
Figure 5.17: Normalized $H_{zT}(x,y)$ and $V(\Delta x, \Delta y)$ distribution in $h = 50$ mm.
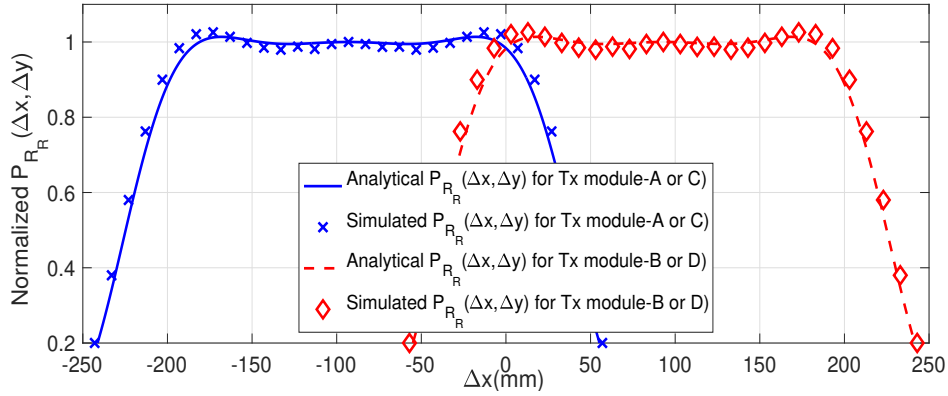


Figure 5.18: Normalized $P_{R_R}(\Delta x, \Delta y)$ distribution in $h = 50$ mm.

### 5.2.9   Simulation Result of Design-2B

The optimized design layout of Figure. 5.14 is simulated using commercial EM software, and the simulated results for $H_{zT}(x,y)$ and $V(\Delta x, \Delta y)$ are corroborated with the analytical results as shown in Figure. 5.17. The results indicate significant improvement in uniformity of $V(\Delta x, \Delta y)$ in the Rx region. For the Rx moving along x-direction ($\Delta y = 93.3$ mm), the $V(\Delta x, \Delta y)$ versus $\Delta x$ is uniform in the range $\Delta x \in [-186, 186]$ mm and the Tx module-A and -B are excited in sequence. Further, a similar uniformity in $V(\Delta x, \Delta y)$ is observed when the Rx moves along the x-direction ($\Delta y = -93$ mm) over the Tx module-C and -D in sequence. Through simulations, the circuit parameters are extracted as $R_{TA} = R_{TB} = R_{TC} = R_{TD} \approx 2.3\Omega$ and $L_{TA} = L_{TB} = L_{TC} = L_{TD} \approx 303.07\mu$H. The analytically evaluated $P_{R_R}$ using (2.15) is corroborated with the $P_{R_R}$ determined using the simulated parameters in Figure. 5.18. The uniformity of $P_{R_R}(\Delta x, \Delta y)$ is observed in the Rx misalignment range $\Delta x \in [-184, 184]$ mm from Figure. 5.18. The misalignment performance parameters analytically optimized for the proposed design corroborate the simulation results. To detect the Rx misalignment, the sensor array system is utilized. The detection system encompassing the rectenna coils for automatic switching of Tx module-m based on the position of the Rx coil is now detailed.

### 5.2.10    Detection System with Coil Rectenna Sensors Array

The interoperability between the adjacent Tx modules is achieved using an array of coil rectennas (a combination of sensing coil and rectifier circuit) by sensing the Rx coil position and further processing with a microcontroller to operate the switches. Simulation-based optimization is conducted to analyze the response of the coil rectenna sensor array system, which is further verified through measurements. The location of sensor coils is primarily optimized by finding the void regions (where the magnetic field generated by the Tx coil is low, as seen from Figure. 5.15) to reduce the cross-coupling and interference from the Tx coil on the sensor array system. As a result, mainly the Rx coil contributes to exciting voltages in the sensor coils. Among the various void regions on the Tx-coil, the locations of the sensor coils are judiciously selected within each Tx module area, and each sensor is shared with the adjacent neighbors. In this manner, the overlapped region is exploited well for shared placement of the rectennas to effectively minimize the number of sensors in the design to one per module. Moreover, the optimal locations of the coil rectennas in the overlapped region achieve a maximum response from the sensors to effectively detect the crossover movement of the Rx compared to sensing the Rx coil staying within a module. The resultant detection system comprises four sensing coils, namely coil rectenna (AB, BD, DC, and CA) placed within the overlapping region between the modules where the Rx coil is to be detected, crossing the module boundaries. As demonstrated in Figure. 5.19, the centers of the optimized coil rectennas are approximately located at coordinates $(0, 93), (93, 0), (0, -93)$, and $(-93, 0)$ in mm. Each sensor coil has dimension $S_D = 10$ mm and a number of turns $N_D = 20$. Here, the values of $S_D$ and $N_D$ are optimized by performing parametric variation to have a minimum sensitivity to operate the microcontroller for activating the switching mechanism to detect the misalignment of the Rx coil.z

The output voltage readings of the rectenna sensors are fetched into the microcontroller, where a decision state machine is implemented. The state machine keeps track of the previous state of the switches and triggers the switching circuit based on the comparisons of the rectenna output voltages with the decision thresholds. To illustrate this, the coil rectenna responses with the Rx coil misalignment are analyzed. The output voltage readings, $V_X(\Delta x, \Delta y)$, of the rectenna-X, are simulated with respect to the Rx coil misalignment along $\Delta y = 93$ mm (i.e., the Rx moving from module-A to module-B) and the variations are plotted in Figure. 5.20(a). It is interpreted from Figure. 5.20(a) that when the Rx coil lies within the Tx module-A area ($\Delta x \leq 0$), $\{V_{AB}$ or $V_{CA}\} \geq V_{TH1}$ and $V_{BD} < V_{TH1}$, where $V_{TH1}$ is the first decision threshold voltage. The $V_{TH1}$ indicates the presence of the Rx coil within a particular Tx module area based on the voltage variation in rectenna sensors. Similarly in Figure. 5.20(a), when the Rx coil lies within the Tx module-B area ($\Delta x > 0$), $\{V_{AB}$ or $V_{BD}\} \geq V_{TH1}$ and $V_{CA} < V_{TH1}$. This can also be verified by observing the variation of output voltage in the coil rectenna-(BD, AB, and DC) when the Rx coil is misaligned along $\Delta x = 93$ mm (i.e., the Rx moving from module-B to module-D) from the simulated responses presented in Figure. 5.20(b). Hence,
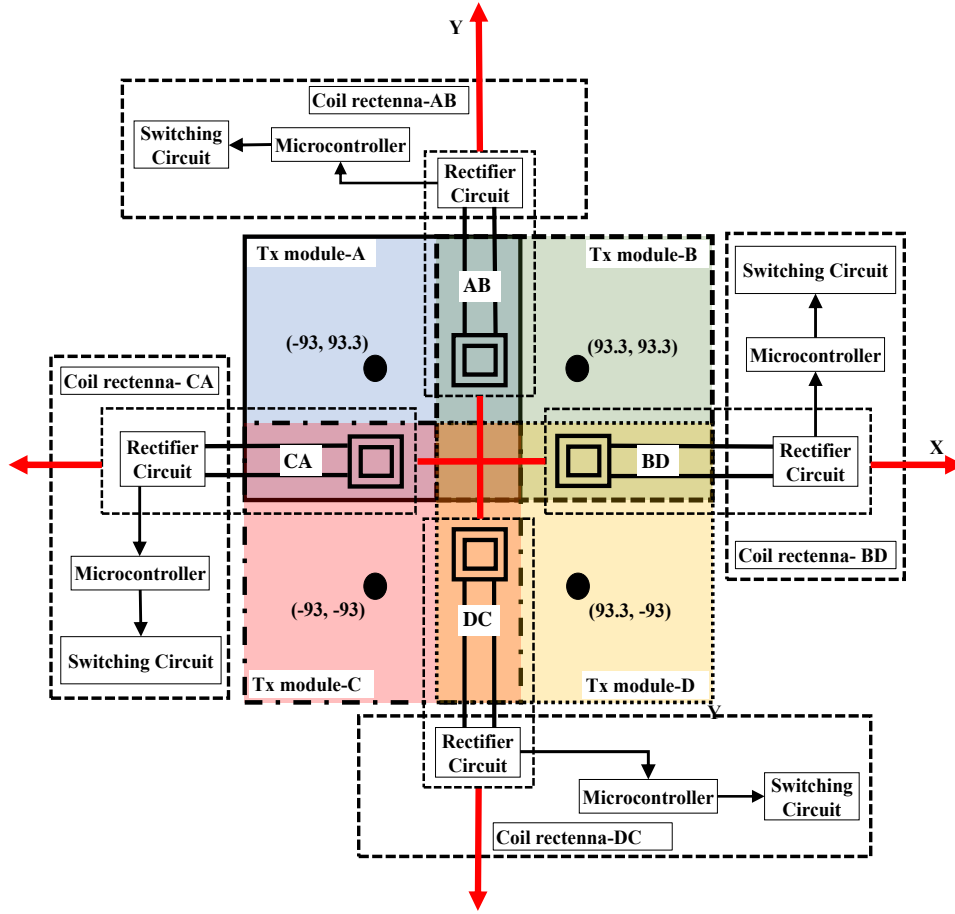
Figure 5.19: Coil rectenna sensor array system.
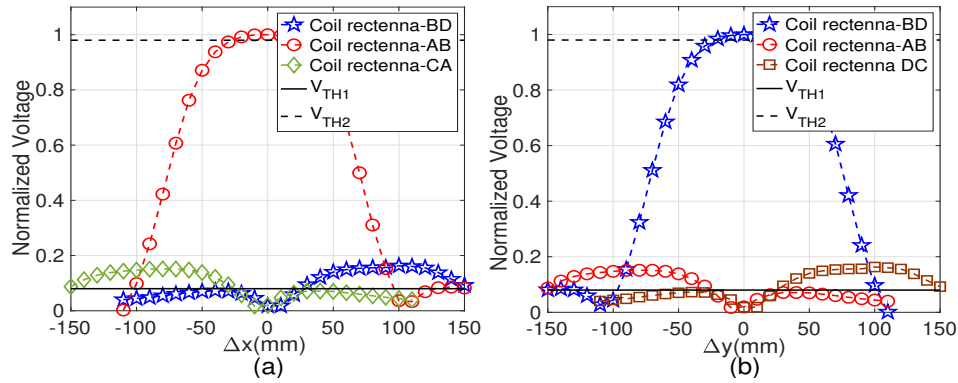


Figure 5.20: Voltage variation along (a) $\Delta y = 93$ mm, (b) $\Delta x = 93$ mm.

based on the voltage comparisons, the decision state machine can operate the switching states as detailed in Table 5.4 for the Rx coil misaligned within a particular module area. Further, when the Rx is misaligned from module-A to module-B, Figure. 5.20 (a) indicates that the rectenna-AB located at the crossing boundary shows $V_{AB} \geq V_{TH2}$ while the $V_{CA} \approx V_{BD}$. Here, the $V_{TH2}$ is the second decision threshold voltage which indicates

Table 5.4: Switching States of the Rx coil staying within a particular module

| Sensor voltage reading | $SW_A$ | $SW_B$ | $SW_C$ | $SW_D$ |
|---|---|---|---|---|
| $\{V_{AB}$ or $V_{CA}\} \geq V_{TH1}$ <br> $\{V_{BD}$ & $V_{DC}\} < V_{TH1}$ | **ON** | OFF | OFF | OFF |
| $\{V_{AB}$ or $V_{BD}\} \geq V_{TH1}$ <br> $\{V_{CA}$ & $V_{DC}\} < V_{TH1}$ | OFF | **ON** | OFF | OFF |
| $\{V_{CA}$ or $V_{DC}\} \geq V_{TH1}$ <br> $\{V_{AB}$ &$V_{BD}\} < V_{TH1}$ | OFF | OFF | **ON** | OFF |
| $\{V_{BD}$ or $V_{DC}\} \geq V_{TH1}$ <br> $\{V_{CA}$ &$V_{AB}\} < V_{TH1}$ | OFF | OFF | OFF | **ON** |

the presence of the Rx coil within the overlapped region of the Tx modules for which the corresponding common rectenna sensor shows voltage reading $\geq V_{TH2}$. The same can be observed in Figure. 5.20(b) for the Rx movement from module-B to module-D where $V_{BD} \geq V_{TH2}$ along with $V_{AB} \approx V_{DC}$ representing the crossover event. Hence, the state machine can decide to trigger the switching circuit to new states by knowing previous states as detailed in Table 5.5 for the Rx coil moving to the adjacent module area. The triggering of the new switching state is not abrupt. A gradual switching can

Table 5.5: Triggering of switches when Rx coil crosses module boundary

| Detection voltage | Previous State | | | | Current State | | | |
|---|---|---|---|---|---|---|---|---|
| | $SW_A$ | $SW_B$ | $SW_C$ | $SW_D$ | $SW_A$ | $SW_B$ | $SW_C$ | $SW_D$ |
| $V_{AB} \geq V_{TH2}$ | **ON** | **OFF** | OFF | OFF | **OFF** | **ON** | OFF | OFF |
| $V_{CA} \approx V_{BD}$ | **OFF** | **ON** | OFF | OFF | **ON** | **OFF** | OFF | OFF |
| $V_{BD} \geq V_{TH2}$ | OFF | **ON** | OFF | **OFF** | OFF | **OFF** | OFF | **ON** |
| $V_{AB} \approx V_{DC}$ | OFF | **OFF** | OFF | **ON** | OFF | **ON** | OFF | **OFF** |
| $V_{DC} \geq V_{TH2}$ | OFF | OFF | **ON** | **OFF** | OFF | OFF | **OFF** | **ON** |
| $V_{BD} \approx V_{CA}$ | OFF | OFF | **OFF** | **ON** | OFF | OFF | **ON** | **OFF** |
| $V_{CA} \geq V_{TH2}$ | **ON** | OFF | **OFF** | OFF | **OFF** | OFF | **ON** | OFF |
| $V_{AB} \approx V_{DC}$ | **OFF** | OFF | **ON** | OFF | **ON** | OFF | **OFF** | OFF |

be implemented at the crossover boundary by intentionally providing some delay time in switching, for instance, first activating the next module and then deactivating the previous module in sequence during the Rx passing the overlapped region. Initially, the Tx module-A, Tx module-B, Tx module-C, and Tx module-D are periodically activated until one among the many conditions provided in Table 5.4 and Table 5.5 is satisfied. Additionally, the above discussion on the decision state machine used for activating the switching circuit is graphically illustrated in a flowchart shown in Figure. 5.21. Although this simulation study illustrates the working principle of the detection system based on the decision thresholds, it further explains the state-machine implementation. However, the actual values of $V_{TH}$ are better perceived through proper calibrations over the realistic system, which is performed experimentally next. These states and the detection system are further validated experimentally along with the Design-2B charging pad in the subsequent section.
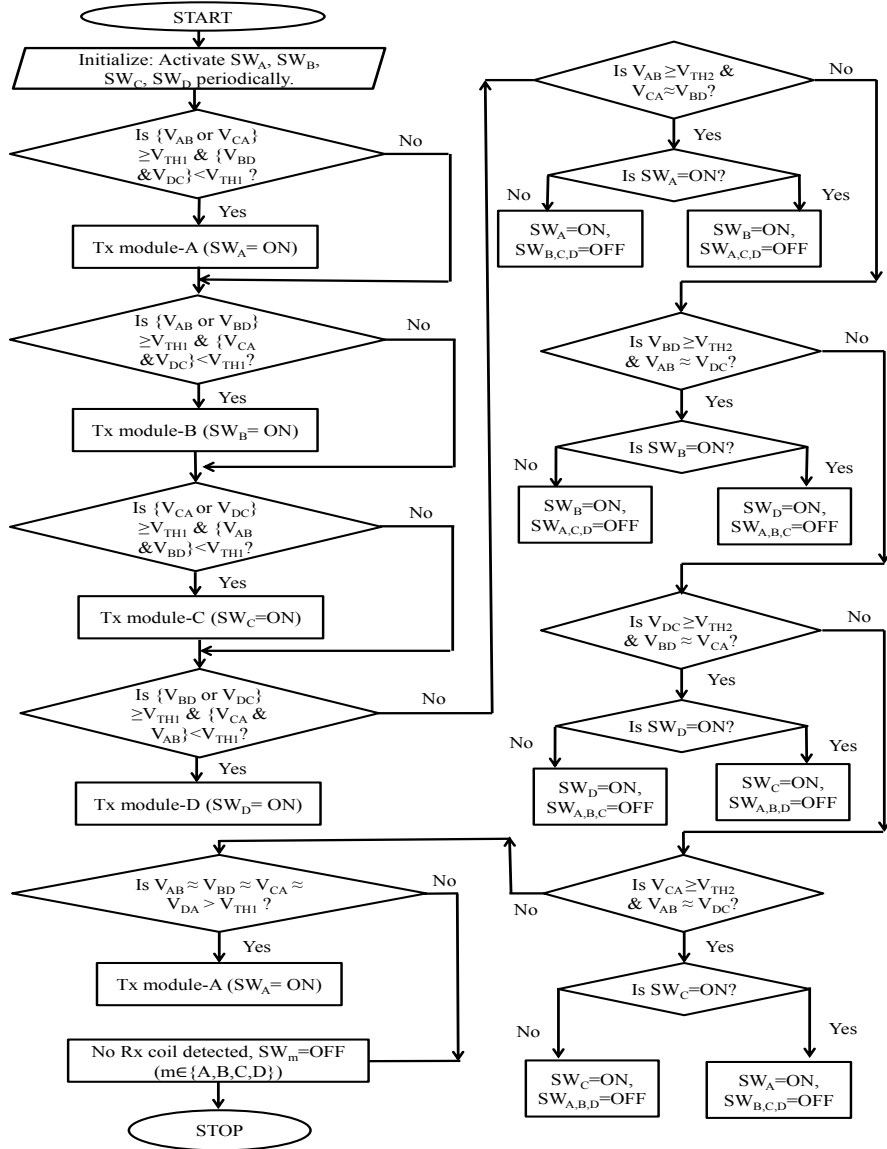
Figure 5.21: Flow chart of decision state-machine to activate switching circuit.

### 5.2.11 Experimental verification and results of Design-2B Tx charging pad

**Design-2B Charging Pad Performance Measurement**

The proposed Design-2B charging pad has the layout shown in Figure. 5.14 and the Rx coil is fabricated using Litz wire having 25 strands, 37 SWG diameter to reduce the high-frequency losses. The circuit parameters of the coils are measured using Agilent PNA-L N5230C Network Analyzer and listed in Table 5.6. The experimental setup demonstrated in Figure. 5.22 is used to evaluate the misalignment performance of the proposed Design-2B charging pad in terms of link efficiency ($\eta_{s-conventional}$) using (2.40a)

Table 5.6: Measured circuit parameters of the Design-2B Tx pad

| Circuit parameters | Measured values |
|---|---|
| $R_{TA}/R_{TB}/R_{TC}/R_{TD}$ | $2.42\Omega/2.49\Omega/2.48\Omega/2.45\Omega$ |
| $L_{TA}/L_{TB}/L_{TC}/L_{TD}$ | $303.6\mu$H$/304.1\mu$H$/303.9\mu$H$/303.68\mu$H |
| $C_{TA}/C_{TB}/C_{TC}/C_{TD}$ | $927pF/925.5pF/926.1pF/926.8pF$ |
| $R_R/L_R/C_R$ | $1.55\Omega/196.75\mu H/1.43nF$ |
| $R_s/R_L$ | $50\Omega/14\Omega$ |
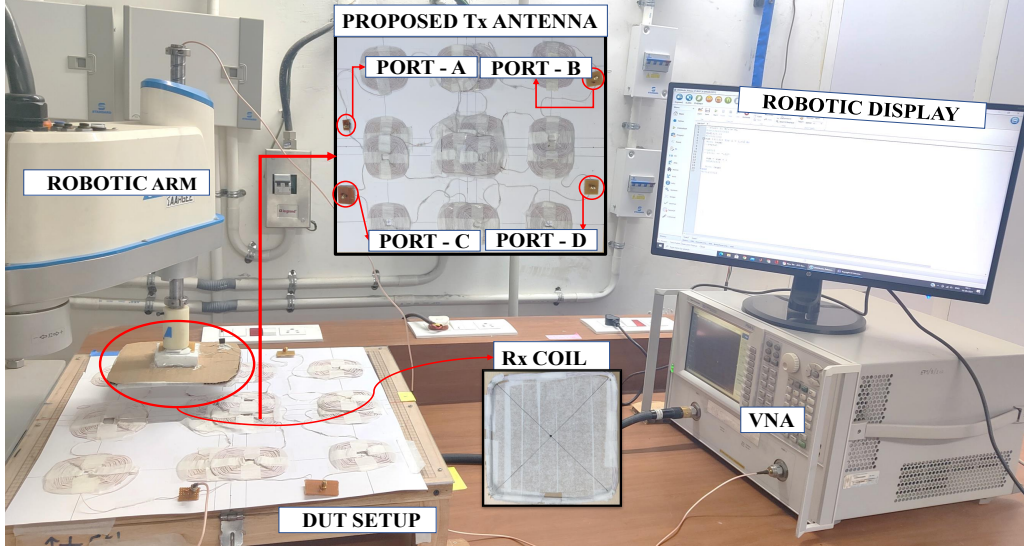


Figure 5.22: Setup for misalignment performance measurements of the Design-2B Tx coil antenna.

from measured $S11$ and $S21$ parameters. This measurement is conducted by using the DRS60L robotic arm, as shown in Figure. 5.22, is utilized to move the Rx coil precisely along the desired path to accurately determine $\eta_{s-conventional}(\Delta x, \Delta y)$. The data is acquired by Network Analyzer for the Rx moving along $y = 93$ mm at an interval of 10 mm in $h = 50$ mm plane. The measured $\eta_{s-conventional}$ distribution results are depicted in Figure. 5.23. The results indicate uniformity of $\eta_{s-conventional}$ achieved in the Rx misalignment range $\Delta x \in [-184, 184]$ mm. The measured value of the maximum $\eta_{s-conventional}$ shown by the design is $\eta_{s-conventional} = 79.91\%$, respectively. Further, the $\eta_{s-conventional}(\Delta x, \Delta y)$ is estimated for two different cases of conductive materials. In case-1, a low loss litz wire [79] is considered. The resistance (R) per unit length (l) $(\alpha = \frac{R}{l})$ of the low loss wire is evaluated by determining the ratio of total conductive wire length of Tx pad to the measured resistance value and is determined as $\alpha_1 = 16.6\mu\frac{\Omega}{\text{mm}}$ from [79]. Therefore equivalent resistance of the proposed Tx module-m (Let m $\impliedby$ A) and Rx-coil are calculated as

$$R_{TA}^{case1} = l_A \times \alpha_1 = 0.574\Omega$$
$$R_R^{case1} = l_R \times \alpha_1 = 0.18\Omega. \tag{5.39}$$
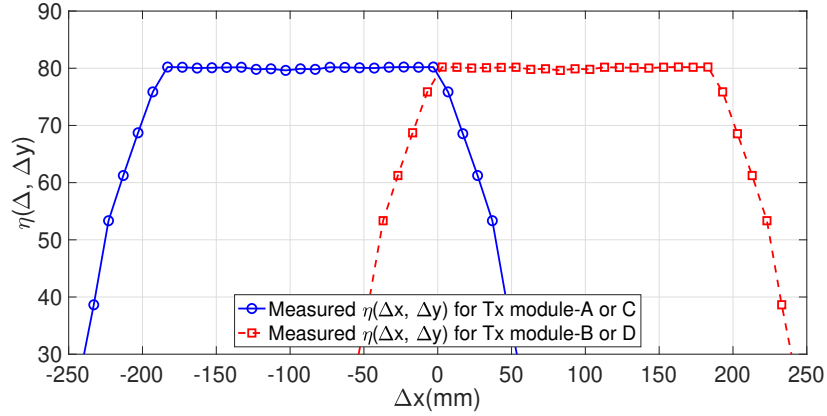
Figure 5.23: Measured $\eta_{s-conventional}(\Delta x, \Delta y)$ distribution in $h = 50$ mm.

Where $l_A = 34445$ mm and $l_R = 10800$ mm are the effective length of the conductive track of Tx module-A and Rx coil. The maximum $\eta_{sa-conventional}$ of case-1 is 96.096% which is determined by substituting $R_R^{case1}$ in (2.35), (2.39) and (2.40a). Moreover, the value of $P_{R_R}$ under a perfectly aligned Rx coil is 109.99W which is determined by substituting (5.39) in (2.15) assuming $V_s = 48$V and $R_s = 0\Omega$ to have a fair comparison with [79]. In case-2, the proposed Litz wire is replaced with PCB design [79] for estimation of $\eta_{s-conventional}(\Delta x, \Delta y)$. Similarly, the resistance (R) per unit length (l) of PCB design is determined as $\alpha_2 = 909\mu\frac{\Omega}{\text{mm}}$ from [79] and the equivalent resistances are obtained as

$$R_{AT}^{case2} = l_A \times \alpha_2 = 31.31\Omega$$
$$R_R^{case2} = l_R \times \alpha_2 = 9.81\Omega. \tag{5.40}$$

The maximum $\eta_{s-conventional}$ of case-2 is evaluated as 16.744%. It is evident that the value of $\eta$ depends on the conductive track material which can be replaced according to the specific applications.

**The Detection System Realization and Measurements**

A real-application model of the detection system is demonstrated using the fabricated coil rectenna sensor array system in Figure. 5.24. The signal generator is used to feed the power to the Tx as shown in Figure. 5.24(a). The measurement is performed by displacing the Rx coil from the initial position $P_1$ up to $P_{12}$ through a path defined in Figure. 5.24(b). The sensor coil positions are calibrated accommodating the fabrication errors. A control unit (Arduino board) is programmed and a state machine is implemented by setting calibrated threshold voltages ($V_{TH1}$ and $V_{TH2}$) which are determined experimentally by observing the measured variation of voltage readings in the rectenna sensors. While moving the Rx from $P_1$ to $P_{12}$, the switching status of Tx module-m is indicated by glowing LED to demonstrate real application as depicted in Figure. 5.24(c), thus, the switching states are verified. For this, the recorded responses of the rectennas are plotted in Figure. 5.25 where the $V_{TH1}$ and $V_{TH2}$ are marked for the state machine to activate the switching
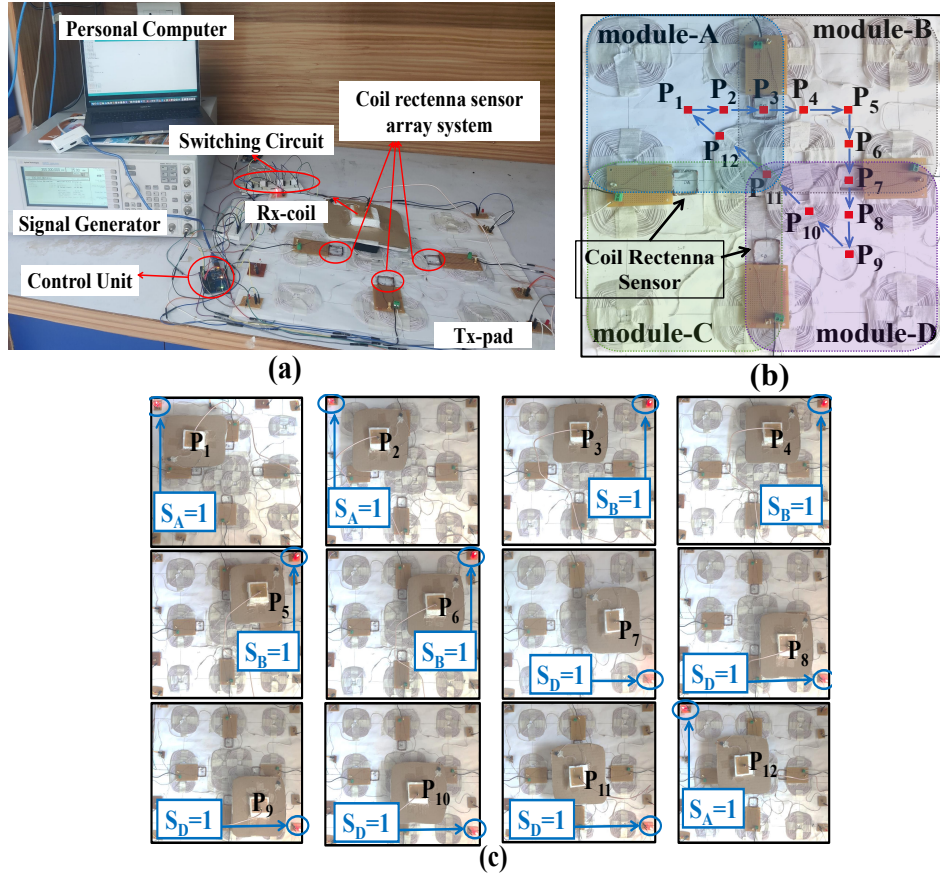
Figure 5.24: The realized detection system with rectenna sensors, (a) experimental setup with the prototype, (b) path for Rx movement, and (c) switching states.
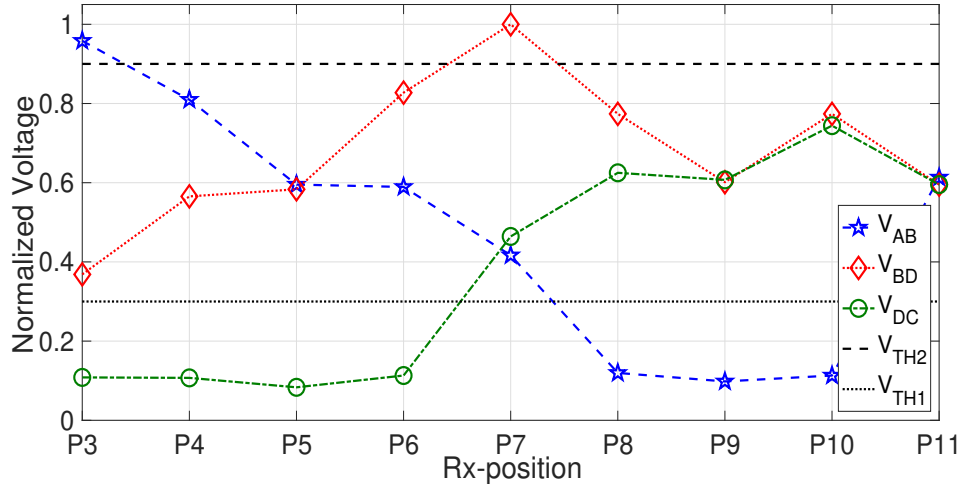


Figure 5.25: Measured output voltages of coil rectenna sensor array system.

circuit (relays) shown in Figure. 5.24(a) based on the position of the Rx coil. To illustrate the switching, the Rx movement from $P5$ to $P11$ which consists of in-module as well as

crossover movement is discussed in detail. The plots in Figure. 5.25 showcase that when the Rx coil is aligned to $P_5$ (i.e., within module-B), the detection rectenna-AB and -BD placed in Tx module-B show similar readings $V_{AB} \approx V_{BD} \geq V_{TH1}$ and the other sensors ($V_{DC}$ and $V_{CA}$) read noise signal, this activates the $SW_B$ ($S_B = 1$) as per Table 5.4. In the next position $P_6$, the same readings in the sensors keep the status of the switch unchanged. Further movement to $P_7$ (the Rx coil crosses the boundary and the previous state is $S_B = 1$) causes $V_{BD} > V_{TH2}$ and $V_{AB} \approx V_{DC}$ as shown in Figure. 5.25, the state machine triggers the switching state to $S_B = 0$ and $S_D = 1$ as per the rule of Table 5.5. This crossover is demonstrated in Figure. 5.24(c) for the Rx positions $P_6$ and $P_7$. Further, for the Rx movement from $P_7$ to $P_{11}$, the switching state $S_D = 1$ remains unchanged as $V_{BD}$ and $V_{DC}$ lie within the threshold regions. Although, in the position $P_{11}$ all the sensors read similar value ($V_{AB} \approx V_{BD} \approx V_{CA} \approx V_{DA}$) $> V_{TH1}$, the switching status remains constant since none of the readings are $< V_{TH1}$. Moreover, if the Rx coil lands directly on $P_{11}$, the default Tx module-$A$ is activated using the switching circuitry. The calibrated denormalized values of $V_{TH2}$ and $V_{TH1}$ in the working model are 151.2 mV and 50.4 mV, respectively. The uniformity factor in terms of induced voltage due to proposed Design-2B Tx coil antenna in the Rx coil antenna is achieved by UF($V(\Delta x, \Delta y)$)=75.5%.

Table 5.7: Comparison of proposed multi-port Tx coil antennas.

| Designs | Tx size in mm | UF($M(\Delta x, \Delta y)$)/ UF($V(\Delta x, \Delta y)$) | Flux control | Misalignment dimension | Tx type | Detection |
|---------|---------------|----------------------------|--------------|------------------------|---------|-----------|
| Literature-[1] | $200 \times 200$ | 5.76% | No | ($\Delta x, \Delta y$) | planar | No |
| Literature-[79] | $700 \times 700$ | 31.36% | Yes | ($\Delta x, \Delta y$) | planar | Yes |
| Design-2A | $200 \times 200$ | 23.41% | Yes | ($\Delta x, \Delta y$) | planar | No |
| Design-2B | $428 \times 428$ | 75.5% | Yes | ($\Delta x, \Delta y$) | planar | Yes |

## 5.3 Summary

In this chapter, the focus was on reducing flux leakage between Tx-Rx coils by adopting switching and detection circuitries, with an additional objective to enhance lateral misalignment tolerance. Aiming to achieve this, a two-port Tx coil antenna called Design-2A [g] was initially developed to control the flux leakage. The misalignement tolerence shown by the Design-2A Tx coil antenna in terms of UF($H_z(x, y)$) and UF($M(\Delta x, \Delta y)$) is improved by 53.06% and 268.64% respectively over to that of conventional literature design presented in subsection 2.2. However, the asymmetric nature of the chief and booster coils of Design-2A resulted in distinct resistive losses, causing difficulty to maintain stability in PTE. Besides, a practical approach to operate the switching circuit in Design-2A was unexplored.

As an alternative, a four-port symmetric multi-coil antenna designated as Design-2B [h] was proposed as part of an evolutionary process to ensure stability in PTE while controlling the flux leakage. A realistic detection system was implemented to run the prototype. The

proposed Design-2B charging pad achieves 75.5% uniformity in the $V(\Delta x, \Delta y)$, which is higher than the previous literary works [79]. Moreover, the Design-2B achieves uniform efficiency in the Rx misalignment range, $-184$ mm $\leq \Delta x, \Delta y \leq 184$ mm by significantly miniaturized Tx pad, $428.1 \times 428.1$ mm$^2$ compared to [79]. In addition, only 25% of the Tx pad is activated to reduce the undesired magnetic field by suitable switching circuitry. The performance metrics achieved by Design-2B is considered to be best results in this thesis work and accomplishes the proposed objectives mentioned in EP-4. The comparison of performance parameters of Design-2A and Design-2B are given in Table. 5.7. Despite the significant achievements of Design-2B, including its ability to tolerate high misalignments, reduce flux leakage, enhance PTE, and miniaturize the Tx charging pad, it was mandatory to consider the limitations of this design. One such disadvantage of Design-2B is its inherent complexity, which makes it challenging to implement and maintain. In addition, there seems to be a significant growth in cost of the WPT system over time, which could pose a financial burden.

As a result, the focus of the next chapter will be on optimizing the Rx coil antenna instead of the Tx coil, with an hope to offer a more efficient and cost-effective solution. By doing so, we aim to address the limitations of previous designs and create cost-effective WPT system.

CHAPTER OUTCOMES

---

[g] **A. Bharadwaj**, V. K. Srivastava, A. Sharma and C. C. Reddy, "A Switchable Multicoil Antenna With Booster Coil to Improve Coverage in WPT Systems," in **IEEE Transactions on Antennas and Propagation**, vol. 70, no. 4, pp. 2490-2498, April 2022, doi: 10.1109/TAP.2021.3137379.

[h] **A. Bharadwaj**, A. Sharma and C. R. Chandupatla, "A Switched Modular Multi-Coil Array Transmitter Pad With Coil Rectenna Sensors to Improve Lateral Misalignment Tolerance in Wireless Power Charging of Drone Systems," in **IEEE Transactions on Intelligent Transportation Systems**, 2022, doi: 10.1109/TITS.2022.3220793.

# Chapter 6

# Receiver Coil Antenna

In the previous chapters of this thesis, we discussed the limitations of designing Tx coil antennas in terms of their complexity and high maintenance costs. These limitations have inspired us to investigate the optimization of Rx coil antennas. As a result, we propose a novel Rx coil antenna in this chapter, which is designed to harvest both vertical $(H_z(x,y))$ and horizontal $(H_x(x,y)$, and $H_y(x,y))$ magnetic field components to address the issue of lateral misalignment tolerance. Thereby, the development of Design-3 completes the targeted objectives mentioned in EP-5 of SO-B.

The key objective of this chapter is to compensate for the reduction in $H_z(x,y)$ in the misaligned region of the Rx coil by utilizing either $H_x(x,y)$ or $H_y(x,y)$. This is achieved through the development of an efficient and effective Rx coil antenna that can harness these magnetic field components. By doing so, we aim to improve the overall performance and reliability of WPT systems. The novel Rx coil antenna is designated as Design-3 in this chapter.

## 6.1 Structural Configuration of the Design-3 Rx coil Antenna (SO-B: EP-5)

Figure. 6.1 renders the configuration of the proposed Rx coil antenna and conventional Tx coil for a near-field resonant WPT system. The center of the Tx-Rx coils is set apart at a transfer distance, $h$. The Design-3 Rx coil antenna as shown in Figure. 6.1 is bifurcated in two parts as $Rx_1$ and $Rx_2$ operating at single tone resonating frequency, $f = 400$ kHz. The tilt angle of $Rx_1$ ranges in $0^o \leq \theta \leq 90^0$ for $\phi = 0^o$ (i.e, tilted towards x-axis) to capture $\{x$ and $z\}$-components of magnetic field. Similarly, the tilt angle provided for $Rx_2$ ranges between $0^o \leq \theta \leq 90^o$ at $\phi = 90^o$ (i.e, tilted towards y-axis) to capture $\{y$ and $z\}$-components of magnetic field generated by Tx coil antenna. The physical dimensions of Tx-Rx coils defined in Figure. 6.1 include side-length of Tx coil, $2a$, side-length of Rx coil, $2b$, number of Tx coil turns, $N_t$, number of turns for $Rx_1$, $N_{r1}$, number of turns of $Rx_2$, $N_{r2}$, and conductive track width, $\delta$. Moreover, a factor termed as relative charging height $\epsilon$ [1] is defined as the ratio of $h$ and $2a$ of the square coil antenna. The value of $\epsilon$ is fixed at 0.25 [1] to obtain maximum uniformity along the z-component of the magnetic field. The tilt in the Rx coil antenna leads to a slight decline in the effective clearance height which turns into 3D shape. Moreover, placement of 3D Rx coils are more feasible for drones [104]. Therefore, the proposed work is primarily pertinent to drone based WPT systems.
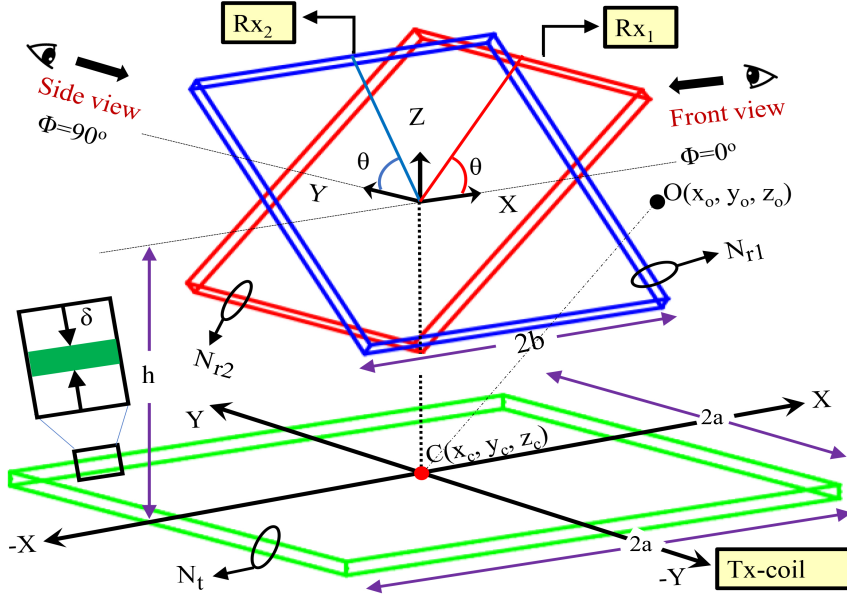
Figure 6.1: Structural configuration of the proposed Design-3 Rx coil antenna.

### 6.1.1 Equivalent circuit of Tx coil and Design-3 Rx coil antenna

The equivalent circuit diagram of the Tx and Design-3 Rx coil antenna is drawn in Figure. 6.2. The Tx coil antenna is excited with $V_s$ having $R_s$. In the circuit, $R_T$ and $L_T$
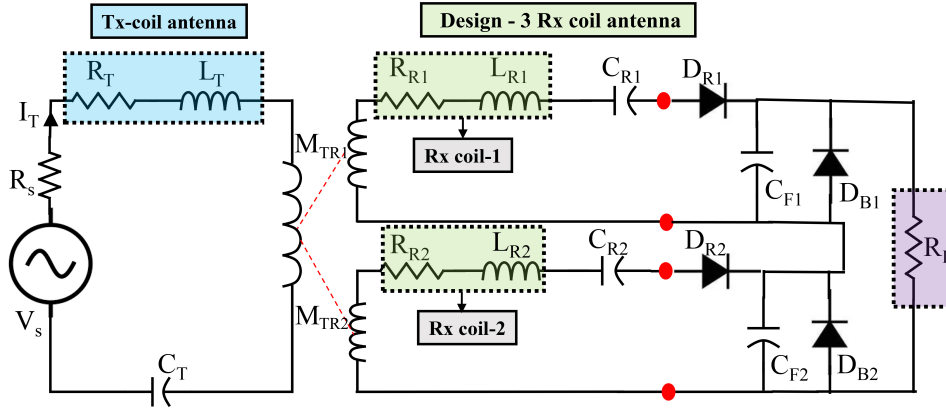


Figure 6.2: Equivalent circuit diagram of the WPT system composed with proposed Design-3 Rx coil antenna.

denote the Tx resistance and self-inductance, whereas, $R_{R1}$, $L_{R1}$, $R_{R2}$, and $L_{R2}$ depict resistance and self-inductance of $Rx_1$ and $Rx_2$ respectively. To enhance the coupling, resonating capacitors at Tx-Rx side is denoted as $C_T$, $C_{R1}$ and $C_{R2}$ as shown in Figure. 6.2. The output response of individual voltages are rectified using rectification diode (i.e., $D_{R1}$, and $D_{R2}$) integrated with filtering capacitor (i.e., $C_{F1}$, and $C_{F2}$). Thereby, the resultant DC responses are combined by connecting in series. Moreover, a bypassing diodes ($D_{B1}$,

and $D_{B2}$) are connected at the end of Rx$_1$ and Rx$_2$ in anti-parallel direction with the load as shown in Figure. 6.2. The operation of bypassing diodes is to divert under-performing Rx coil between Rx$_1$ and Rx$_2$ to reduce the effective copper losses. Further, $R_L$ is quantified according to the application. Moreover, from Figure. 6.2, $M_{TR1}$, and $M_{TR2}$ are mutual inductance due to Rx$_1$ and Rx$_2$. The analytical evaluation of magnetic field and induced voltage is detailed in next section.

### 6.1.2 Mathematical Analysis of Magnetic Field and Induced Voltage

For the considered application, since the Rx coil has large dimensions and is tilted, the magnetic field components are non-uniformly distributed throughout the area of the Rx coil. Therefore, field distribution generated by the Tx antenna in the 3-D space around the Rx coil is essentially required to analyze the proposed system mathematically. The magnetic field component along (x, y, and z)-direction due to single-turn square coil, carrying current, $I_T$ is determined by replacing the observation point O$(x, y, h)$ with O$(x_o, y_o, z_o)$ in the (2.1), (2.2), and (2.3). Here, the Tx coil center is located at C$(x_t, y_t, z_t)$
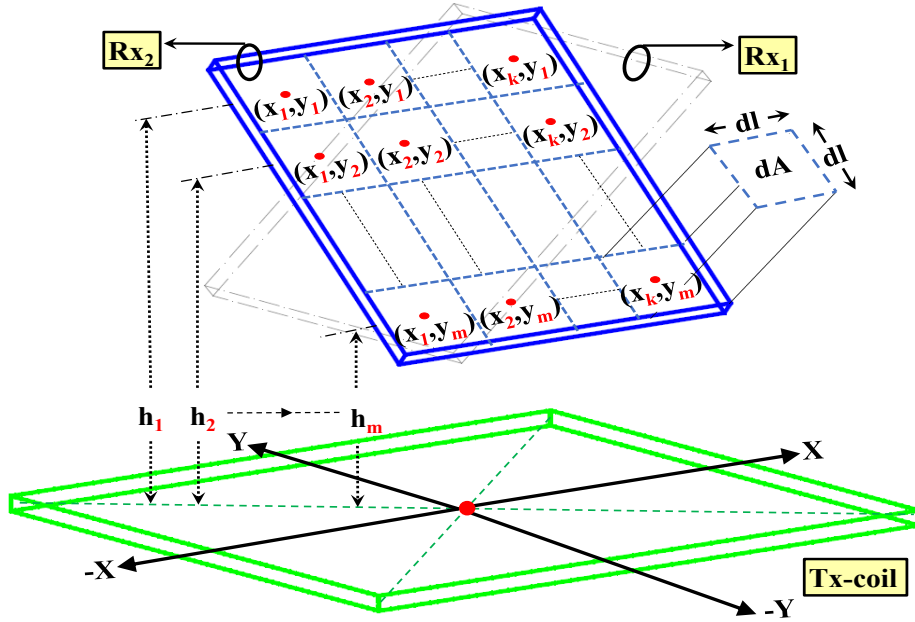


Figure 6.3: Design-3 Rx coil antenna segmented with small differential area units for mathematical deduction of performance parameters.

of the coordinate system as shown in Figure. 6.1, where $(x_t = 0, y_t = 0)$. As the postion of Tx-coil turns can be positioned at different $z_c$, therefore, the $h$ in (2.1), (2.2), and (2.3) is replaced with $z_o - z_c$. Moreover, due to the physical nature of Rx coil, the magnetic field distribution is evaluated by segmenting Rx coil in small differential area units $dA = (dl \times dl)$ as shown in Figure. 6.3. Where $dl$ is differential side-length unit of $dA$. Further, the observation points O$(x_o, y_o, z_o)$ is evaluated in terms of the physical

dimensions of the of Rx coil, $dl$, and $\theta$ using Figure. 6.3 as

$$
\begin{aligned}
x_o =x_k &= -b + \left( k - \frac{1}{2} \right) dl, \\
y_o =y_m &= \left( b + \left( \frac{1}{2} - m \right) dl \right) \cos \theta, \\
z_o =h_m &= h + \left( \frac{1}{2} \left( \frac{2b}{dl} + 1 \right) - m \right) dl \sin \theta.
\end{aligned}
\tag{6.1}
$$

The Tx coil is helical in shape; therefore, each turn has different $z_c$. Hence, the effective magnetic field due to each component is calculated at the center position of $dA$ as

$$
H_x^{mk} = \sum_{z_c=0}^{N_T-\zeta} H_x^{z_c}, \quad H_y^{mk} = \sum_{z_c=0}^{N_T-\zeta} H_y^{z_c}, \quad H_z^{mk} = \sum_{z_c=0}^{N_T-\zeta} H_z^{z_c}.
\tag{6.2}
$$

Here in (6.2) $\zeta = \frac{\delta}{1mm}$, knowing the magnetic field distribution of the tilted-orthogonal Rx coil region, the induced voltage is evaluated by considering differential induced voltage $dV^\phi$ due to $dA$ in the Rx coil is formulated using (6.2) from Faraday's law of electromagnetic induction as

$$
\begin{aligned}
dV^\phi = -N_r \frac{\partial \psi}{\partial t} = &- j\omega\mu_o N_r [(H_x^{mk} dA \sin\theta + H_z^{mk} dA \cos\theta) \cos\phi \\
&+ (H_y^{mk} dA \sin\theta + H_z^{mk} dA \cos\theta) \sin\phi]
\end{aligned}
\tag{6.3}
$$

Here, $\omega = 2\pi f$, $\psi$, and $\mu_o$ are angular frequency, magnetic flux, and permeability in free space respectively. Whereas, $C = \omega\mu_o N_r$ is proportional constant of $dV^\phi$. As the Rx-coil is separated in two parts, the effective differential voltage is calculated by performing superposition of $dV^\phi$ due to $Rx_1$ at $\phi = 0^o$ and $Rx_2$ at $\phi = 90^o$ as

$$
dV = |dV^{0^o}| + |dV^{90^o}|.
\tag{6.4}
$$

Here, absolute value of individual voltage response of each Rx coil is taken to mimic the equivalent response of DC combining shown in Figure. 6.2. Thereby, the total voltage $V$ of tilted-orthogonal Rx coil antenna is evaluated by summing $dV$ due to each $dA$ of $Rx_1$ and $Rx_2$ as shown in Figure. 6.3. The accuracy of analytical value of $V$ is inversely proportional to area of the $dA$. Whereas, the total number of $dA$ are originated to be $\frac{2b \times 2b}{dA}$. In this study, $dA$ is considered as $1mm^2$ (i.e, $dl = 1mm$). The magnitude of $V$ due to magnetic field for misaligned Rx coil antenna at the location $(x_k + \Delta x, y_m + \Delta y)$ is calculated as

$$
\begin{aligned}
|V_T(\Delta x, \Delta y)|, &= \iint_{A=2b \times 2b} dV \\
&= \left| \iint_{A=2b \times 2b} dV^{0^o} \right| + \left| \iint_{A=2b \times 2b} dV^{90^o} \right|, \\
&= |V_{Rx_1}| + |V_{Rx_2}|.
\end{aligned}
\tag{6.5}
$$
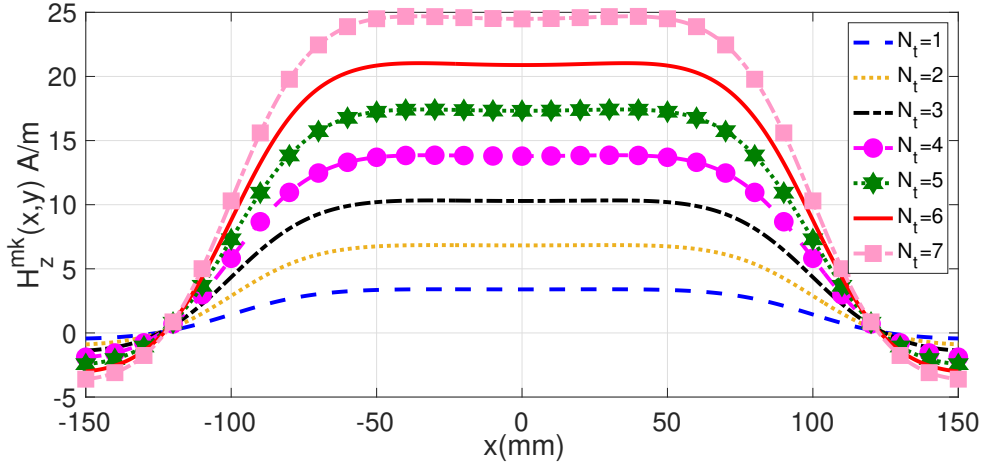
Figure 6.4: Variation of $H_z^{mk}(x, y)$ in accordance with number of turns $(N_t)$

Whereof, $|V_{Rx_1}|$ and $|V_{Rx_2}|$ are voltages due to $\mathrm{Rx}_1$ and $\mathrm{Rx}_2$ which mimics the response of DC combining.   Moreover, $|V(\Delta x, \Delta y)|$ is the total voltage virtue of misaligned tilted-orthogonal Rx coil antenna which captures (x, y and, z)-components of magnetic field. Furthermore, the mutual coupling $M$ between Tx-Rx coils is obtained from (2.8) in terms of individual mutual inductances such as $|M_{TR1}|$ and $|M_{TR2}|$ as

$$M(\Delta x, \Delta y) = \frac{|V_{Rx_1}| + |V_{Rx_2}|}{\omega I_T} = |M_{TR1}| + |M_{TR2}|. \tag{6.6}$$

Based on the equations mentioned above, i.e. (6.2)-(6.6), the established fact is that the physical dimensions of the Tx-Rx coil are the critical parameters to avail the stability in $M(\Delta x, \Delta y)$ in the misaligned Rx coil. Consequently, the physical parameters of the Tx-Rx coils are parameterized to ensure stability in mutual inductance. The parametric optimization is detailed in the next section.

### 6.1.3   Parametric Optimization of Design-3 Rx Coil Antenna

Prior to the parametric optimization of Rx coil antenna, it is vital to optimize the physical parameters of the Tx coil antenna in accordance with $\epsilon = 0.25$. Moreover, the application scenario adopted for this work includes drone wireless charging system wherein the transfer distance chosen is $h = 50$ mm. Therefore, the maximum side-length of Tx-coil is determined as $2a = 200$ mm. Conclusively, the number of turns $(N_t = 6)$ of square shaped Helical Tx coil antenna is optimized subjected to ICNIRP guidelines (21 A/m or 27 $\mu$T) [89] at $Z_o = h$ plane. The parametric variation of $N_t$ with respect to $H_z^{mk}(x, y)$ is demonstrated in Figure. 6.4. At the Rx side, the parametric sweep of $\theta$ is executed for Rx coil parameters such as $2b = 100$ mm, $N_{r1} = 6$, $N_{r2} = 6$, and $\delta = 1$ mm. Since, the $\theta$ varies in the range $0^o \le \theta \le 90^o$ in (6.6), the optimal $\theta$ is attained subject to a condition that maximum UF$(M(\Delta x, \Delta y))$ is achieved. The analytical results of parametric variation are demonstrated in Figure. 6.5. Based on the results, it can be inferred that at $\theta = 0^o$,
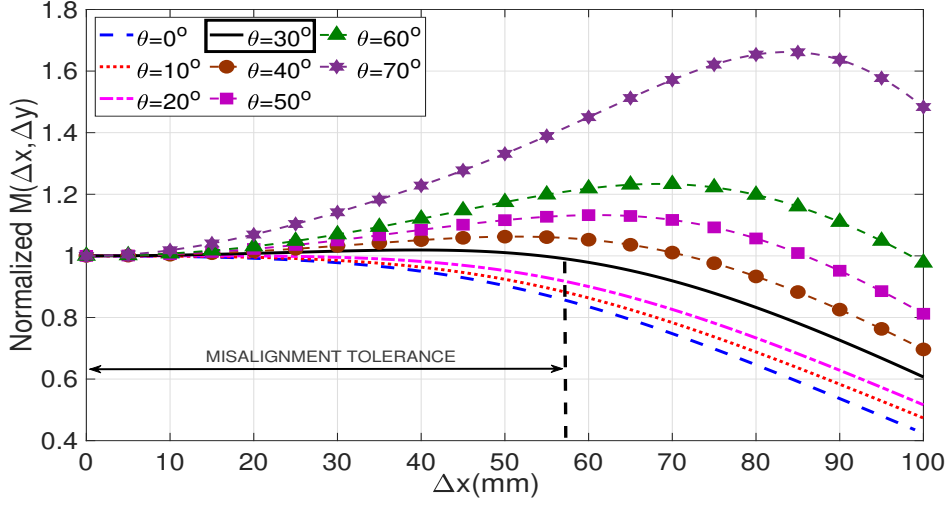
Figure 6.5: Normalized mutual inductance $M(\Delta x, \Delta y)$ when Rx coil is tilted at (a) $\theta = 0^o$, (b) $\theta = 10^o$, (c) $\theta = 20^o$, (d) $\theta = 30^o$, (e) $\theta = 40^o$, (f) $\theta = 50^o$, (g) $\theta = 60^o$, and (h) $\theta = 70^o$.
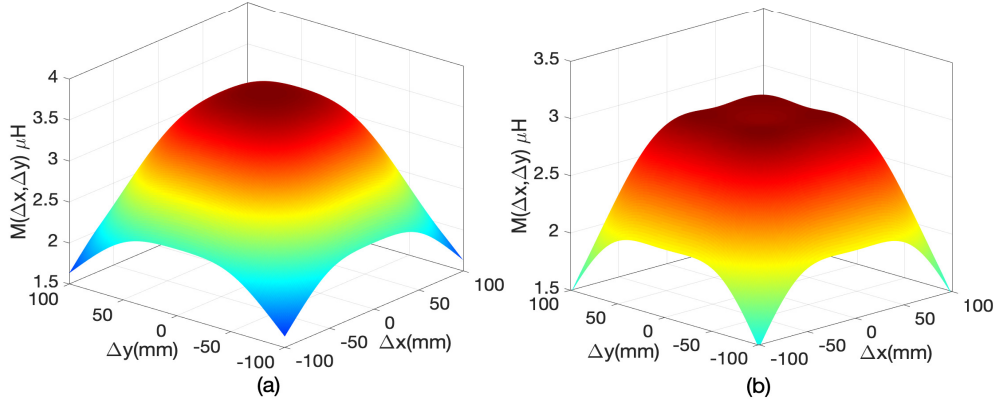


Figure 6.6: The 3D analytical results of $M(\Delta x, \Delta y)$ of (a) conventional planar Rx coil antenna, and (b) proposed Design-3 Rx coil antenna.

UF(M($\Delta x, \Delta y$)) is mere 4.84% with $M(0,0) = 3.51 \mu H$. This does not serve the purpose to mitigate lateral misalignment problem, and the design is designated as conventional planar Rx coil antenna. Whereas, at $\theta = 30^o$, the UF(M($\Delta x, \Delta y$)) is 32.49% which depicts significant improvement by minimally compromising the peak value $M(0,0) = 3.12 \mu H$; therefore, it is considered as optimal $\theta$. Additionally, at $\theta = 30^o$, the placement of Rx coil is practically viable in comparison with orthogonally positioned Rx coil antenna (i.e., $\theta = 90^o$) proposed in [105, 106, 107, 108]. Whereas, the misalignment tolerance and peak value of mutual inductance significantly decreases for $\theta > 30^o$, as the contribution of the magnetic field due to the z-component reduces. The 3D analytical results of mutual inductance, $M(\Delta x, \Delta y)$ for conventional and proposed Rx coil antennas are presented in in Figure. 6.6. The 3D $M(\Delta x, \Delta y)$ results signifies the misalignment tolerance is improved in the entire active region of the Rx-plane. The system is further experimentally validated

Table 6.1: Measured parameters of Design-3 Rx coil antenna

| Physical parameters of Tx coil Antenna | |
|---|---|
| $2a/\delta/N_t/h/f$ | 200mm/1mm/6/50mm/400kHz |
| **Physical parameters of Design-3 Rx coil Antenna** | |
| $2b/N_{r1}/N_{r2}/\theta$ | 100mm/6/6/30$^o$ |
| **Circuit parameters of Tx-Rx coil** | |
| $R_T/L_T/C_T/R_{R1}/R_{R2}$ | 1.29$\Omega$/22.915$\mu H$/6.9$nF$/0.84$\Omega$/0.88$\Omega$ |
| $L_{R1}/L_{R2}/C_{R1}/C_{R2}$ | 14.2$\mu H$/14.6$\mu H$/11.15$nF$/10.84$nF$ |
| $R_L/R_s$ | 10$\Omega$/0$\Omega$ |
| $M(0,0)$ @ $\theta = 0^0$ | 3.51$\mu H$ |
| $M(0,0)$ @ $\theta = 30^0$ | 3.12$\mu H$ |
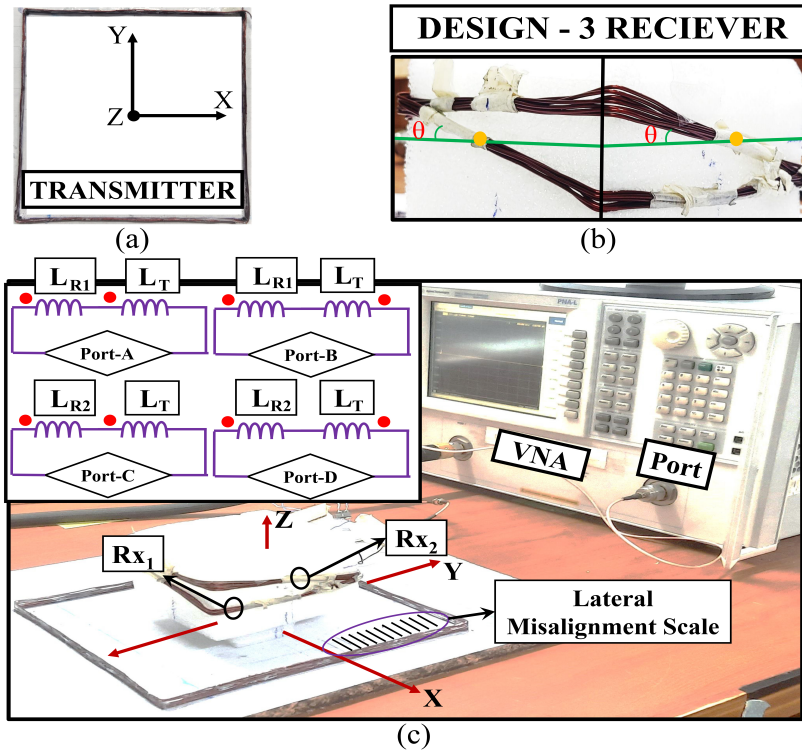


Figure 6.7: (a) Fabricated prototype of Tx coil antenna, (b) fabricated Design-3 Rx coil antenna, and (c) experimental setup to determine circuit parameters.

at $\theta = 30^o$ in the following section.

## 6.1.4   Experimental Setup and Results of Design-3 Rx coil Antenna

The proposed Design-3 Rx coil antenna and Tx coil are fabricated using 20 SWG single strand copper wire as shown in Figure. 6.7(a) and Figure. 6.7(b). Additionally, the experimental setup consisting of a PNA N5320C Agilent-made network analyzer to measure the Tx-Rx coil's circuit parameters is demonstrated in Figure. 6.7(c). The parameters such as $R_T$, $L_T$, $R_{R1}$, $R_{R2}$, $L_{R1}$, and $L_{R2}$ are measured directly. Whereas, exemplified below, by series aiding configuration (SAC) and series opposing configuration
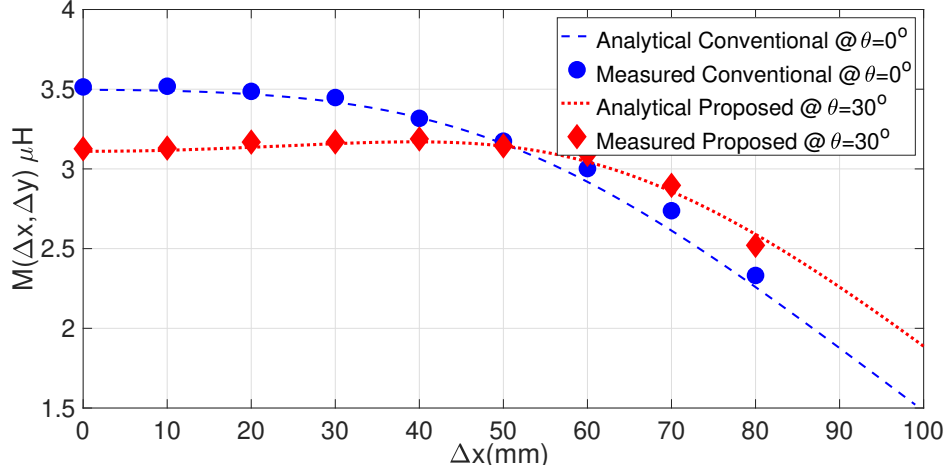
Figure 6.8: Performance results of $M(\Delta x, \Delta y)$ of proposed Design-3 and conventional planar Rx coil antennas.

(SOC), $M$ is measured indirectly.

- The Tx-Rx coils are connected in SAC and SOC as illustrated in the inset of Figure. 6.7(c). Subsequently, the effective inductance is evaluated individually for $Rx_1$ and $Rx_2$. For $Rx_1$, the SAC and SOC are measured by connecting Tx-$Rx_1$ coils as shown in port-A, and port-B of Figure. 6.7(c), thereby, computed as $L_{SAC1} = L_T + L_{R1} + 2M_{TR1}$ and $L_{SOC1} = L_T + L_{R1} - 2M_{TR1}$ using a network analyzer. Similarly, $L_{SAC2} = L_T + L_{R2} + 2M_{TR2}$ and $L_{SOC2} = L_T + L_{R2} - 2M_{TR2}$ are determined by connecting Tx-$Rx_2$ coil connections given in port-C, and port-D of Figure. 6.7(c).

- Further, the resultant mutual inductance $M_{TR1}$ in terms of $L_{SAC1}$ and $L_{SOC1}$ is determined as $M_{TR1} = \frac{L_{SAC1} - L_{SOC1}}{4}$.

- Similarly, the resultant mutual inductance $M_{TR2}$ in terms of $L_{SAC2}$ and $L_{SOC2}$ is determined as $M_{TR2} = \frac{L_{SAC2} - L_{SOC2}}{4}$.

- Thereby, the magnitude of total mutual inductance $M$ is determined by replacing $M_{TR1}$ and $M_{TR2}$ in (6.6).

- The procedure is repeated at every 10mm interval along $y = 0$ line for proposed and conventional Rx coil designs. The measured results plotted in Figure. 6.8 corroborate with the analytical results.

The dimensional parameters of Tx-Rx coils and measured circuit parameters using network analyzer are tabulated in Table 6.1. Additionally. using SAC and SOC, the mutual inductance between $Rx_1$ and $Rx_2$ is measured and found to be $0.2\mu H$, which is insignificant compared to the measured value of $M(0,0)$ given in Table 6.1. Therefore, the cross-coupling between Rx coils will have a negligible effect on Tx-Rx coil coupling.
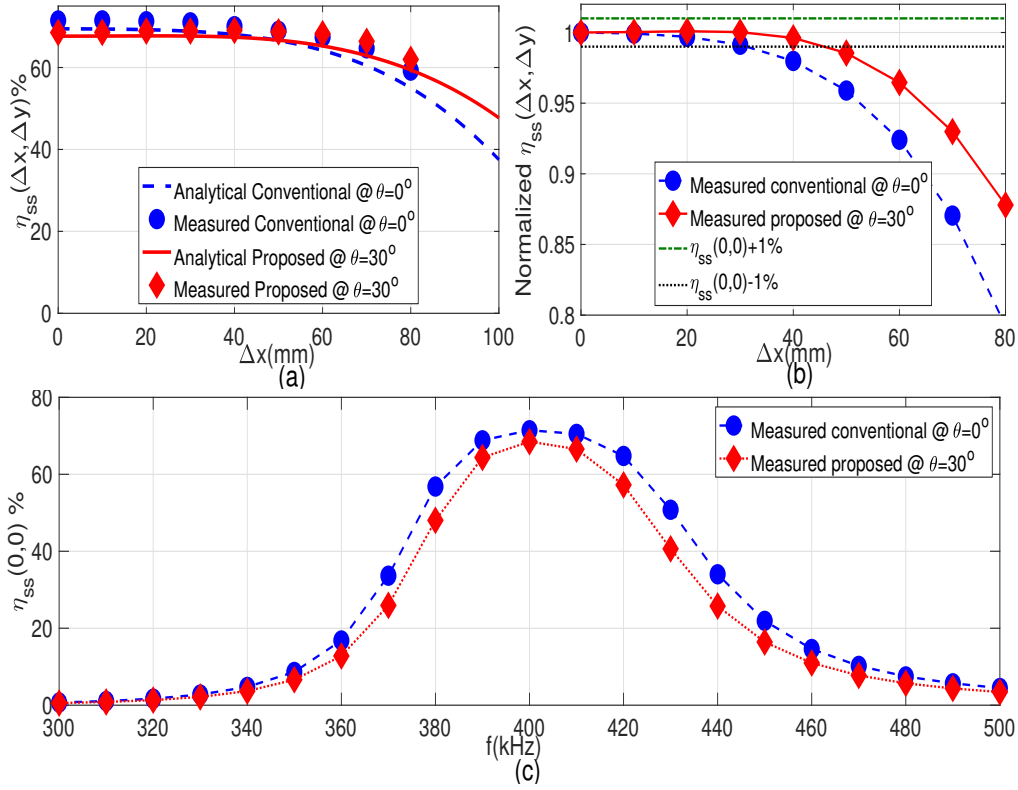
Figure 6.9: Performance results of (a) $\eta_{ss}$ versus misalignment tolerance $(\Delta x, \Delta y)$, (b) normalized $\eta_{ss}$ versus $(\Delta x, \Delta y)$, and (c) $\eta_{ss}$ versus operating frequency, $f$.

The measured parameters are utilized to determine the PTE, $\eta_{ss}(\Delta x, \Delta y)$ using (2.16). In general, the source resistance of realistic power supply is negligible, hence, considered as $(R_s \approx 0\Omega)$ [1]. However, at the load side, $R_L$ is selected as $10\Omega$ according to the drone application [104]. The experimental outcomes of $\eta_{ss}$ under misaligned Rx coil $(\Delta x, \Delta y)$ for proposed and conventional designs are mapped in Figure. 6.9(a). The UF($\eta_{ss}(\Delta x, \Delta y)$) for the proposed Design-3 Rx coil antenna has better visualization from normalized plots shown in Figure. 6.9(b) and is evaluated as 21.16%, whereas conventional design's UF($\eta_{ss}(\Delta x, \Delta y)$) is 9.61%. Thus it follows the UF($\eta_{ss}(\Delta x, \Delta y)$) for the proposed Rx coil antenna is improved effectively to 120.187% in comparison with conventional design. Additionally, under perfectly aligned Rx coil, the $\eta_{ss}(0,0)$ with distinct frequencies is measured and plotted in Figure. 6.9(c). Here, the $\eta_{ss}(\Delta x, \Delta y)$ is maximized at $f = 400$kHz, because the compensation capacitors are designed at $f$ to provide minimum impedance to Tx-Rx coils.

## 6.2 Summary

In this chapter, a new Design-3 Rx-coil antenna [i] is proposed, which has the ability to capture magnetic fields in all three dimensions {x, y, and z} and improve misalignment tolerance in the wireless power transfer (WPT) system. Additionally, the Tx coil is

Table 6.2: Qualitative comparison of the proposed Design-3 Rx coil antenna with the designs available in the literature.

| Ref | working Area | Rx harvests | flux control | Safety Guidelines | Misalignment dimension |
|---|---|---|---|---|---|
| [105] | Rx | $H_x$, $H_z$ | no | Followed | 1-D ($\Delta x$) |
| [108] | Rx | $H_x$, $H_z$ | no | Not followed | 1-D ($\Delta x$) |
| [106] | Rx | $H_x$, $H_z$ | no | - | 1-D ($\Delta x$) |
| [107] | Rx | $H_x$, $H_z$ | no | Followed | 1-D ($\Delta x$) |
| **Design-3** | **Rx** | $\boldsymbol{H_x, H_y, H_z}$ | **no** | **Followed** | **2-D** ($\Delta x, \Delta y$) |

Table 6.3: Quantitative comparison of the proposed Design-3 Rx coil antenna with the designs available in the literature.

| Ref | UF($M(\Delta x, \Delta y)$) | $\Delta x$ | $\Delta y$ |
|---|---|---|---|
| [105] | fluctuation | $\leq$ [-10, 10] mm | N.A |
| [108] | fluctuation | $\leq$ [-10, 10] mm | N.A |
| [106] | fluctuation | $\leq$ [-10, 10] mm | N.A |
| [107] | fluctuation | $\leq$ [-10, 10] mm | N.A |
| **Design-3** | **32.49%** | **[-57, 57] mm** | **[-57, 57] mm** |

optimized to meet the safety constraints set forth by the ICNIRP organization. Compared to previous studies on Rx coil antennas, the proposed design improves misalignment tolerance in two dimensions ($\Delta x$, $\Delta y$) instead of just one dimension ($\Delta x$) in previous works [105, 106, 107, 108]. Furthermore, the tilt angle of the proposed design is optimized to be $30^o$, which is more practical than the $90^o$ used in previous works [105, 107]. As a result, the proposed design is suitable for a wider range of applications.

The proposed Design-3 Rx coil antenna also achieves better performance than the conventional planar Rx coil antenna. The efficiency ($\eta_{ss}$) of the proposed design remains stable in the range of $\Delta x \in [-46, 46]$mm, which is an improvement over the range of $\Delta x \in [-31, 31]$mm for the conventional planar Rx coil antenna. The effective improvement over the conventional planar Rx coil antenna is 120.18%. However, the peak value of $\eta_{ss}(0, 0)$ of the proposed design is slightly lower than that of the conventional planar Rx coil antenna (67.65% vs. 69.43%).

Moreover, the mutual inductance ($M$) of the proposed design is significantly better than that of the conventional planar Rx coil antenna, with an improvement of 571.28%. The previous issues with optimizing the Tx coil antenna, such as complexity and cost, have been addressed in this chapter. Therefore, it is believed that the proposed Design-3 Rx coil antenna has potential for medium power drone-based WPT applications. Moreover, the qualitative and quantitative comparison of Design-3 Rx coil antenna is made with prior literary works and presented in Table 6.2 and Table 6.3. In final, the Design-3 acomplishes the objectives mentioned in EP-5 of SO-B with the significant improvements in various performance metrics over distinct literary works summarized in Table 6.2 and Table 6.3. Despite its many advantages, the Design-3 Rx coil antenna has a few disadvantages, such as its 3D geometrical configuration, which limits its applicability in some wireless charging

applications. Therefore, the author intends to develop a planar Rx coil antenna to capture vertical and horizontal magnetic field components in future work.

CHAPTER OUTCOMES

[0][i] **A. Bharadwaj**, V. K. Srivastava, A. Sharma and C. C. Reddy, "A Tilted-Orthogonal Receiver Coil Antenna to Improve Misalignment Tolerance in WPT Systems," in **IEEE Transactions on Antennas and Propagation**, vol. 70, no. 12, pp. 11434-11441, Dec. 2022, doi: 10.1109/TAP.2022.3209207.

# Chapter 7

# Conclusion and Future Works

In conclusion, this thesis provides a potential solution for mitigating the lateral misalignment problem in near-field wireless power transfer (WPT) systems. Furthermore, for better understanding of the achievements by various designs proposed in SO-B are summarized by comparing with previous literature works quatitatively in Table 7.1 and qualitatively in Table 7.2. In **Chapter 1**, potential design solutions to address misalignment issues in WPT systems are discussed. However, it was observed that the designs proposed in prior works lack a mathematical framework, which limits their potential to effectively address misalignment problems. As a contribution to the research community, this thesis developed a total of six different coil antenna designs in a systematic and evolutionary process using the mathematical background provided in **Chapter 2**. The most significant achievements of this thesis are outlined as follows:

## 7.0.1 Chapter-3

In **Chapter 3**, a novel S-parameter based measurement setup using S-parameters is presented. This proposed measurement framework enables researchers to estimate the efficiency of the WPT system, which is equivalent to that obtained when the transmitter coil is excited with high-frequency power inverters. Additionally, a new set of S-parameters ($S11$, $S12$, $S21$, and $S22$) for secondary-parallel compensation topology (S-P and P-P) is mathematically derived and experimentally verified for the very first time.

## 7.0.2 Chapter-4

In **Chapter 4**, single port Tx coil antennas such as Design-1A, Design-1B, and Design-1C are presented to mitigate the lateral misalignment problem in WPT systems. Moreover, during the evolution from Design-1A to Design-1C, the author has pioneered a mathematical framework for determining the optimal magnetic field distribution to enhance lateral misalignment tolerance. Consequently, the non-uniform magnetic field distribution has been identified as the optimal field distribution, which also helps to reduce the size of the Tx coil antenna. The proposed analytical techniques have been thoroughly validated through simulated and measurement results.

## 7.0.3 Chapter-5

In **Chapter 5**, multi-port Tx coil antennas, such as Design-2A and Design-2B, are presented to reduce the undesired leakage of magnetic flux outside the operating region

Table 7.1: Quantitative comparison of the proposed designs in SO-B with the designs available in the literature. ('-' means not given)

| Ref | Tx type | Tx size (in mm) | UF($V(\Delta x, \Delta y)$) | $P_{R_R}$ | $\eta_{ss}$ |
|---|---|---|---|---|---|
| [65] | Single-port | $200 \times 200$ | 4.84% | - | 83% |
| [1] | Single-port | $200 \times 200$ | 5.76% | 8.1W | 91% |
| [109] | Multi port | $195 \times 90$ | - | 4.5W | 50% |
| [79] | Multi port | $700 \times 700$ | 31.36% | 183.7W | 90.8% |
| Design-1A | Single port | $300 \times 100$ | 55.33% | - | -% |
| Design-1B | Single port | $200 \times 200$ | 14.44% | 7.66W | 74.7% |
| Design-1C n=2 | Single port | $179 \times 179$ | 22.65% | - | - |
| Design-1C n=3 | Single port | $276 \times 276$ | 45.41% | - | - |
| Design-2A | Single port | $276 \times 276$ | 45.41% | - | - |
| Design-2B | Multi port | $428 \times 428$ | 75.5% | 109.99W | 96.096% |

Table 7.2: Qualitative comparison of the proposed designs in SO-B designs available in the literature.

| Ref | Detection system | Circuit complexity | Cost Cost | Flux leakage | Design Design | Misalignmet Region |
|---|---|---|---|---|---|---|
| [65] | No | Low | Low | high | planar | $(\Delta x, \Delta y)$ |
| [1] | No | Low | Low | high | planar | $(\Delta x, \Delta y)$ |
| [109] | No | High | Medium | Low | Planar | $(\Delta x)$ |
| [79] | yes | Very High | High | Low | Planar | $(\Delta x, \Delta y)$ |
| Design-1A | No | Low | Low | High | 3D | $(\Delta x)$ |
| Design-1B | No | Low | Low | High | planar | $(\Delta x, \Delta y)$ |
| Design-1C n=2 | No | Low | Low | High | Planar | $(\Delta x, \Delta y)$ |
| Design-1C n=3 | No | Low | Low | Very High | Planar | $(\Delta x, \Delta y)$ |
| Design-2A | No | High | Medium | low | Planar | $(\Delta x, \Delta y)$ |
| Design-2B | yes | High | High | Low | Planar | $(\Delta x, \Delta y)$ |

of the Rx coil. However, this advantage is achieved by targeting the primary objective of mitigating the lateral misalignment problem. This reduction in leakage of magnetic flux is achieved using switching of sub-coils. To activate the switching circuit based on the Rx coil position, a rigorous simulation-based optimization process was undergone to design a novel detection system. The evolution from Design-2A to Design-2B resulted in the best possible misalignment tolerance, along with the miniaturization of the Tx charging pad.

### 7.0.4 Chapter-6

In **Chapter 6**, the author focuses on enhancing misalignment tolerance in WPT systems from the receiver coil side. To achieve this goal, an analytical parametric optimization process is carried out to develop a novel tilted Rx coil antenna. The proposed design ensures constant induced voltage, even under misalignment of the receiver coil, by

harnessing both vertical and lateral magnetic field components in the receiver coil antenna. Moreover, the proposed design is simple and cost-effective, eliminating the need for complexity at the transmitter coil.

Overall, this thesis work has made a significant contribution to the research community in the field of WPT systems by providing novel and effective solutions to address the lateral misalignment problem, thereby improving the performance of WPT systems. The proposed designs have been validated through rigorous simulations and experiments, and the novel measurement setup, switching circuit, and analytical techniques presented in this thesis work can be useful for future research in this field.

## 7.1   Future works

There is substantial potential in further developement in the field of near-field WPT system as follows:

### 7.1.1   Tx-Rx coil antennas

- In future works, an integration of a high-frequency inverter module and a rectifier module into the design of the Tx-Rx coil antenna can be investigated to develop a more compact and efficient WPT system.

- Exploration of various cost-effective composite materials can be done to design Tx-Rx coil antennas to enhance PTE.

- Examination of planar Rx coil antennas to capture both vertical and horizontal magnetic field distributions in the Rx coil region, aimed at mitigating lateral misalignment issues, can be a possible extension of this thesis work.

### 7.1.2   Electromagnetic Compatibality (EMC)

- A potential to design artificial materials such as metamaterials to reduce the complexity of switching circuits and detection systems at kHz frequencies can be an exciting area to investigate for developing efficient and cost-effictive near-field WPT system.

### 7.1.3   Realistic charging system

- The current literature lacks a comprehensive wireless charging system that integrates a detection system, switching circuits, safety constraints, and battery management system at high-frequency power signal typically at MHz's range. Hence, there is a scope to explore this gap in the development of a realistic system in future works.

# References

[1] Shengming Wang, Zhaoyang Hu, CanCan Rong, Conghui Lu, Junfeng Chen, and Minghai Liu. Planar multiple-antiparallel square transmitter for position-insensitive wireless power transfer. *IEEE Antennas and Wireless Propagation Letters*, 17(2): 188–192, 2018. doi: 10.1109/LAWP.2017.2779755.

[2] Hongchang Li, Jie Li, Kangping Wang, Wenjie Chen, and Xu Yang. A maximum efficiency point tracking control scheme for wireless power transfer systems using magnetic resonant coupling. *IEEE Transactions on Power Electronics*, 30(7): 3998–4008, 2015. doi: 10.1109/TPEL.2014.2349534.

[3] Xiao Zhu, Xing Zhao, Yong Li, Shunpan Liu, Huanyu Yang, Jihao Tian, Jiefeng Hu, Ruikun Mai, and Zhengyou He. High-efficiency wpt system for cc/cv charging based on double-half-bridge inverter topology with variable inductors. *IEEE Transactions on Power Electronics*, 37(2):2437–2448, 2022. doi: 10.1109/TPEL.2021.3107461.

[4] Hamed Tebianian, Younes Salami, Benjamin Jeyasurya, and John E. Quaicoe. A 13.56-mhz full-bridge class-d zvs inverter with dynamic dead-time control for wireless power transfer systems. *IEEE Transactions on Industrial Electronics*, 67 (2):1487–1497, 2020. doi: 10.1109/TIE.2018.2890505.

[5] Lixin Shi, J.C. Rodriguez, Miguel Jiménez Carrizosa, and Pedro Alou. Zvs tank optimization for class-d amplifiers in high frequency wpt applications. In *2021 IEEE Applied Power Electronics Conference and Exposition (APEC)*, pages 1593–1598, 2021. doi: 10.1109/APEC42165.2021.9487455.

[6] N.O. Sokal and A.D. Sokal. Class e-a new class of high-efficiency tuned single-ended switching power amplifiers. *IEEE Journal of Solid-State Circuits*, 10(3):168–176, 1975. doi: 10.1109/JSSC.1975.1050582.

[7] Samer Aldhaher, Patrick C. K. Luk, and James F. Whidborne. Wireless power transfer using class e inverter with saturable dc-feed inductor. In *2013 IEEE Energy Conversion Congress and Exposition*, pages 1902–1909, 2013. doi: 10.1109/ECCE. 2013.6646940.

[8] D. Shen, G. Du, W. Zeng, J. Li, and Z. Yang. Parameter design and analysis of class e inverter for magnetically coupled resonant wireless power transmission system. In *The 16th IET International Conference on AC and DC Power Transmission (ACDC 2020)*, volume 2020, pages 158–162, 2020. doi: 10.1049/icp.2020.0085.

[9] Dakshina Murthy-Bellur, Andrew Bauer, Walter Kerin, and Marian K. Kazimierczuk. Inverter using loosely coupled inductors for wireless power transfer.

In *2012 IEEE 55th International Midwest Symposium on Circuits and Systems (MWSCAS)*, pages 1164–1167, 2012. doi: 10.1109/MWSCAS.2012.6292232.

[10] S.D. Kee, I. Aoki, A. Hajimiri, and D. Rutledge. The class-e/f family of zvs switching amplifiers. *IEEE Transactions on Microwave Theory and Techniques*, 51(6):1677–1690, 2003. doi: 10.1109/TMTT.2003.812564.

[11] Samer Aldhaher, David C. Yates, and Paul D. Mitcheson. Design and development of a class ef$_2$ inverter and rectifier for multimegahertz wireless power transfer systems. *IEEE Transactions on Power Electronics*, 31(12):8138–8150, 2016. doi: 10.1109/TPEL.2016.2521060.

[12] Samer Aldhaher, George Kkelis, David C. Yates, and Paul D. Mitcheson. Class ef2 inverters for wireless power transfer applications. In *2015 IEEE Wireless Power Transfer Conference (WPTC)*, pages 1–4, 2015. doi: 10.1109/WPT.2015.7140141.

[13] Samer Aldhaher, David C. Yates, and Paul D. Mitcheson. Modeling and analysis of class ef and class e/f inverters with series-tuned resonant networks. *IEEE Transactions on Power Electronics*, 31(5):3415–3430, 2016. doi: 10.1109/TPEL.2015.2460997.

[14] Jun-Han Choi, Sung-Ku Yeo, Seho Park, Jeong-Seok Lee, and Gyu-Hyeong Cho. Resonant regulating rectifiers (3r) operating for 6.78 mhz resonant wireless power transfer (rwpt). *IEEE Journal of Solid-State Circuits*, 48(12):2989–3001, 2013. doi: 10.1109/JSSC.2013.2287592.

[15] Jun-Han Choi, Sung-Ku Yeo, Chang-Byong Park, Seho Park, Jeong-Seok Lee, and Gyu-Hyeong Cho. A resonant regulating rectifier (3r) operating at 6.78 mhz for a 6w wireless charger with 86In *2013 IEEE International Solid-State Circuits Conference Digest of Technical Papers*, pages 64–65, 2013. doi: 10.1109/ISSCC.2013.6487638.

[16] Xing Li, Chi-Ying Tsui, and Wing-Hung Ki. A 13.56 mhz wireless power transfer system with reconfigurable resonant regulating rectifier and wireless power control for implantable medical devices. *IEEE Journal of Solid-State Circuits*, 50(4): 978–989, 2015. doi: 10.1109/JSSC.2014.2387832.

[17] Kim Fung Edward Lee. A timing controlled ac-dc converter for biomedical implants. In *2010 IEEE International Solid-State Circuits Conference - (ISSCC)*, pages 128–129, 2010. doi: 10.1109/ISSCC.2010.5434021.

[18] Patrick C. K. Luk and Samer Aldhaher. Analysis and design of a class d rectifier for a class e driven wireless power transfer system. In *2014 IEEE Energy Conversion Congress and Exposition (ECCE)*, pages 851–857, 2014. doi: 10.1109/ECCE.2014.6953486.

[19] George Kkelis, David C. Yates, and Paul D. Mitcheson. Class-e half-wave zero dv/dt rectifiers for inductive power transfer. *IEEE Transactions on Power Electronics*, 32 (11):8322–8337, 2017. doi: 10.1109/TPEL.2016.2641260.

[20] Viktor Shevchenko, Oleksandr Husev, Ryszard Strzelecki, Bohdan Pakhaliuk, Nikolai Poliakov, and Natalia Strzelecka. Compensation topologies in ipt systems: Standards, requirements, classification, analysis, comparison and application. *IEEE Access*, 7:120559–120580, 2019. doi: 10.1109/ACCESS.2019.2937891.

[21] Jia Hou, Qianhong Chen, Xiaoyong Ren, Xinbo Ruan, Siu-Chung Wong, and Chi K. Tse. Precise characteristics analysis of series/series-parallel compensated contactless resonant converter. *IEEE Journal of Emerging and Selected Topics in Power Electronics*, 3(1):101–110, 2015. doi: 10.1109/JESTPE.2014.2320524.

[22] Yao Wang, Weiguo Liu, and Yigeng Huangfu. Design of wireless power transfer system with load-independent voltage/current output based on the double-sided clc compensation network. In *2019 IEEE Transportation Electrification Conference and Expo (ITEC)*, pages 1–5, 2019. doi: 10.1109/ITEC.2019.8790560.

[23] Lin Yang, Xiaoming Li, Sheng Liu, Ziwei Xu, and Changsong Cai. Analysis and design of an lccc/s-compensated wpt system with constant output characteristics for battery charging applications. *IEEE Journal of Emerging and Selected Topics in Power Electronics*, 9(1):1169–1180, 2021. doi: 10.1109/JESTPE.2020.2971583.

[24] Rui Yue, Chunfang Wang, Houji Li, and Yunrui Liu. Constant-voltage and constant-current output using p-clcl compensation circuit for single-switch inductive power transfer. *IEEE Transactions on Power Electronics*, 36(5):5181–5190, 2021. doi: 10.1109/TPEL.2020.3028128.

[25] Jing Zhou, Yuqing Gao, Chenxi Zhou, Jien Ma, Xiaoyan Huang, and Youtong Fang. Optimal power transfer with aluminum shielding for wireless power transfer systems. In *2017 20th International Conference on Electrical Machines and Systems (ICEMS)*, pages 1–4, 2017. doi: 10.1109/ICEMS.2017.8056143.

[26] Wan Peng and Zhizhang Chen. Enhanced planar wireless power transfer systems with ferrite material. In *2018 IEEE Wireless Power Transfer Conference (WPTC)*, pages 1–4, 2018. doi: 10.1109/WPT.2018.8639455.

[27] Woosol Lee and Yong-Kyu Yoon. Wireless power transfer systems using metamaterials: A review. *IEEE Access*, 8:147930–147947, 2020. doi: 10.1109/ACCESS.2020.3015176.

[28] Seongsoo Lee, Yeonje Cho, Seungtaek Jeong, Seokwoo Hong, Boogyo Sim, Hongseok Kim, and Joungho Kim. High efficiency wireless power transfer system using a two-stack hybrid metamaterial slab. In *2019 IEEE Wireless Power Transfer*

*Conference (WPTC)*, pages 616–619, 2019. doi: 10.1109/WPTC45513.2019. 9055525.

[29] Matthew J. Chabalko, Jordan Besnoff, and David S. Ricketts. Magnetic field enhancement in wireless power with metamaterials and magnetic resonant couplers. *IEEE Antennas and Wireless Propagation Letters*, 15:452–455, 2016. doi: 10.1109/ LAWP.2015.2452216.

[30] Junfeng Chen and Hui Tan. Investigation of wireless power transfer with 3d metamaterial for efficiency enhancement. In *2017 7th IEEE International Symposium on Microwave, Antenna, Propagation, and EMC Technologies (MAPE)*, pages 309–312, 2017. doi: 10.1109/MAPE.2017.8250863.

[31] Conghui Lu, Cancan Rong, Xiutao Huang, Zhaoyang Hu, Xiong Tao, Shengming Wang, Junfeng Chen, and Minghai Liu. Investigation of negative and near-zero permeability metamaterials for increased efficiency and reduced electromagnetic field leakage in a wireless power transfer system. *IEEE Transactions on Electromagnetic Compatibility*, 61(5):1438–1446, 2019. doi: 10.1109/TEMC.2018.2865520.

[32] Tarakeswar Shaw and Debasis Mitra. Wireless power transfer system based on magnetic dipole coupling with high permittivity metamaterials. *IEEE Antennas and Wireless Propagation Letters*, 18(9):1823–1827, 2019. doi: 10.1109/LAWP.2019. 2930769.

[33] Tarakeswar Shaw and Debasis Mitra. Wireless power transfer system based on magnetic dipole coupling with high permittivity metamaterials. *IEEE Antennas and Wireless Propagation Letters*, 18(9):1823–1827, 2019. doi: 10.1109/LAWP.2019. 2930769.

[34] Senlin Zhu, Chunyu Zhao, Zhenyu Huang, Yuxiang Zhang, and Xudong Luo. Enhancement of wireless power transmission based on side-positioned metamaterials. In *2018 IEEE PES Asia-Pacific Power and Energy Engineering Conference (APPEEC)*, pages 241–245, 2018. doi: 10.1109/APPEEC.2018.8566376.

[35] Jiseong Kim, Jonghoon Kim, Sunkyu Kong, Hongseok Kim, In-Soo Suh, Nam Pyo Suh, Dong-Ho Cho, Joungho Kim, and Seungyoung Ahn. Coil design and shielding methods for a magnetic resonant wireless power transfer system. *Proceedings of the IEEE*, 101(6):1332–1342, 2013. doi: 10.1109/JPROC.2013.2247551.

[36] Silvano Cruciani, Tommaso Campi, Francescaromana Maradei, and Mauro Feliziani. Active shielding design for wireless power transfer systems. *IEEE Transactions on Electromagnetic Compatibility*, 61(6):1953–1960, 2019. doi: 10.1109/TEMC.2019. 2942264.

[37] Theodoros Theodoulidis and Robert J. Ditchburn. Mutual impedance of cylindrical coils at an arbitrary position and orientation above a planar conductor. *IEEE*

*Transactions on Magnetics*, 43(8):3368–3370, 2007. doi: 10.1109/TMAG.2007. 894559.

[38] Jesús Acero, Claudio Carretero, Ignacio Lope, Rafael Alonso, Óscar Lucia, and José M. Burdio. Analysis of the mutual inductance of planar-lumped inductive power transfer systems. *IEEE Transactions on Industrial Electronics*, 60(1):410–420, 2013. doi: 10.1109/TIE.2011.2164772.

[39] David Gilabert-Palmer, Esteban Sanchis-Kilders, Vicente Esteve, Agustín Ferreres, Juan B. Ejea, Enrique Maset, José Jordn, and Enrique Dede. Measuring coupling coefficient of windings with dissimilar turns' number or tight coupling using resonance. *IEEE Transactions on Power Electronics*, 33(11):9790–9802, 2018. doi: 10.1109/TPEL.2018.2794621.

[40] Muhammad Ali and Hermawan Nugroho. Effective power amplifier of wireless power transfer system for consumer electronics. In *2016 IEEE International Conference on Power System Technology (POWERCON)*, pages 1–5, 2016. doi: 10.1109/POWERCON.2016.7754023.

[41] Minfan Fu, He Yin, Xinen Zhu, and Chengbin Ma. Analysis and tracking of optimal load in wireless power transfer systems. *IEEE Transactions on Power Electronics*, 30(7):3952–3963, 2015. doi: 10.1109/TPEL.2014.2347071.

[42] Mohammad Kamar Uddin, Gobbi Ramasamy, Saad Mekhilef, K. Ramar, and Yew-Choy Lau. A review on high frequency resonant inverter technologies for wireless power transfer using magnetic resonance coupling. In *2014 IEEE Conference on Energy Conversion (CENCON)*, pages 412–417, 2014. doi: 10.1109/CENCON. 2014.6967539.

[43] Dawei Li, Yang Zhou, Yongqiang Cui, Sijia Huang, and Dongqin Deng. A wireless power transmission system with load regulation for implantable devices. *IEEE Instrumentation  Measurement Magazine*, 23(4):68–76, 2020. doi: 10.1109/MIM. 2020.9126074.

[44] Daerhan Liu and Stavros V. Georgakopoulos. Cylindrical misalignment insensitive wireless power transfer systems. *IEEE Transactions on Power Electronics*, 33(11): 9331–9343, 2018. doi: 10.1109/TPEL.2018.2791350.

[45] R.A. Schill. General relation for the vector magnetic field of a circular current loop: a closer look. *IEEE Transactions on Magnetics*, 39(2):961–967, 2003. doi: 10.1109/TMAG.2003.808597.

[46] Zhichao Luo and Xuezhe Wei. Analysis of square and circular planar spiral coils in wireless power transfer system for electric vehicles. *IEEE Transactions on Industrial Electronics*, 65(1):331–341, 2018. doi: 10.1109/TIE.2017.2723867.

[47] Pingan Tan, Fu Yi, Chunxia Liu, and Yougui Guo. Modeling of mutual inductance for hexagonal coils with horizontal misalignment in wireless power transfer. In *2018 IEEE Energy Conversion Congress and Exposition (ECCE)*, pages 1981–1986, 2018. doi: 10.1109/ECCE.2018.8558464.

[48] Hadi Tavakkoli, Ebrahim Abbaspour-Sani, Amin Khalilzadegan, Ghader Rezazadeh, and Abdollah Khoei. Analytical study of mutual inductance of hexagonal and octagonal spiral planer coils. *Sensors and Actuators A: Physical*, 247:53–64, 2016.

[49] Shuai Ding, Wangqiang Niu, and Wei Gu. Lateral misalignment tolerant wireless power transfer with a tumbler mechanism. *IEEE Access*, 7:125091–125100, 2019. doi: 10.1109/ACCESS.2019.2936627.

[50] Zhen Zhang and Bowen Zhang. Angular-misalignment insensitive omnidirectional wireless power transfer. *IEEE Transactions on Industrial Electronics*, 67(4): 2755–2764, 2020. doi: 10.1109/TIE.2019.2908604.

[51] Taejun Lim and Yongshik Lee. Reconfigurable coil array for near-field beamforming to compensate for misalignment in wpt systems. *IEEE Transactions on Microwave Theory and Techniques*, 69(11):4711–4719, 2021. doi: 10.1109/TMTT.2021.3090066.

[52] Ivan Cortes and Won-jong Kim. Lateral position error reduction using misalignment-sensing coils in inductive power transfer systems. *IEEE/ASME Trans. Mechatronics*, 23(2):875–882, 2018.

[53] Y. Gao, C. Duan, A. A. Oliveira, A. Ginart, K. B. Farley, and Z. T. H. Tse. 3-d coil positioning based on magnetic sensing for wireless ev charging. *IEEE Trans. Transport. Electrific.*, 3(3):578–588, 2017. doi: 10.1109/TTE.2017.2696787.

[54] T. V. Jeshma and B. George. Mr sensor-based coil alignment sensing system for wirelessly charged evs. *IEEE Sensors J.*, 20(10):5588–5596, 2020. doi: 10.1109/ JSEN.2020.2969432.

[55] Kai Song, Guang Yang, Yu Guo, Yu Lan, Shuai Dong, Jinhai Jiang, and Chunbo Zhu. Design of dd coil with high misalignment tolerance and low emf emissions for wireless electric vehicle charging systems. *IEEE Transactions on Power Electronics*, 35(9):9034–9045, 2020. doi: 10.1109/TPEL.2020.2971967.

[56] Md Morshed Alam, Saad Mekhilef, Mehdi Seyedmahmoudian, and Ben Horan. Dynamic charging of electric vehicle with negligible power transfer fluctuation. *Energies*, 10(5):701, 2017.

[57] Aqueel Ahmad, Mohammad Saad Alam, and Ahmed A. S. Mohamed. Design and interoperability analysis of quadruple pad structure for electric vehicle wireless charging application. *IEEE Transactions on Transportation Electrification*, 5(4): 934–945, 2019. doi: 10.1109/TTE.2019.2929443.

[58] Abiezer Tejeda, Seho Kim, Fei Yang Lin, Grant A. Covic, and John T. Boys. A hybrid solenoid coupler for wireless charging applications. *IEEE Transactions on Power Electronics*, 34(6):5632–5645, 2019. doi: 10.1109/TPEL.2018.2867430.

[59] Z. Luo and X. Wei. Analysis of square and circular planar spiral coils in wireless power transfer system for electric vehicles. *IEEE Transactions on Industrial Electronics*, 65(1):331–341, 2018.

[60] p. tan, t. peng, X. Gao, and B. Zhang. Flexible combination and switching control for robust wireless power transfer system with hexagonal array coil. *IEEE Transactions on Power Electronics*, pages 1–1, 2020. doi: 10.1109/TPEL.2020.3018908.

[61] Y. Li, J. Zhao, Q. Yang, L. Liu, J. Ma, and X. Zhang. A novel coil with high misalignment tolerance for wireless power transfer. *IEEE Transactions on Magnetics*, 55(6):1–4, 2019. doi: 10.1109/TMAG.2019.2904086.

[62] X. Mou, D. T. Gladwin, R. Zhao, and H. Sun. Survey on magnetic resonant coupling wireless power transfer technology for electric vehicle charging. *IET Power Electronics*, 12(12):3005–3020, 2019. doi: 10.1049/iet-pel.2019.0529.

[63] C. M. Zierhofer and E. S. Hochmair. Geometric approach for coupling enhancement of magnetically coupled coils. *IEEE Transactions on Biomedical Engineering*, 43(7): 708–714, 1996. doi: 10.1109/10.503178.

[64] U. Jow and M. Ghovanloo. Design and optimization of printed spiral coils for efficient transcutaneous inductive power transmission. *IEEE Transactions on Biomedical Circuits and Systems*, 1(3):193–202, 2007. doi: 10.1109/TBCAS.2007.913130.

[65] Tae-Hyung Kim, Gi-Ho Yun, Woong Yong Lee, and Jong-Gwan Yook. Asymmetric coil structures for highly efficient wireless power transfer systems. *IEEE Transactions on Microwave Theory and Techniques*, 66(7):3443–3451, 2018.

[66] A. Sharma, I. J. G. Zuazola, A. Perallos, J. C. Batchelor, and A. Gupta. Fabricated non-uniformly distributed-turns coil. In *2014 IEEE Antennas and Propagation Society International Symposium (APSURSI)*, pages 1536–1537, 2014. doi: 10.1109/APS.2014.6905094.

[67] M. Grzeskowiak, A. Diet, M. Benamara, P. Poulichet, C. Conessa, S. Protat, M. Biancheri-Astier, F. de Oliveira Alves, Y. Le Bihan, and G. Lissorgues. Distributed diameter subcoil twisted loop antenna in nonradiative wpt. *IEEE Antennas and Wireless Propagation Letters*, 17(1):4–7, 2018. doi: 10.1109/LAWP.2017.2767020.

[68] Z. Liu, Z. Chen, C. Peng, J. Liang, P. Xiao, L. Bian, Y. Qiu, and G. Li. A misalignment resilient system for magnetically coupled resonant wireless power transfer. *IEEE Transactions on Antennas and Propagation*, pages 1–1, 2020. doi: 10.1109/TAP.2020.2996749.

[69] W. Lee, S. Park, J. Lee, and M. M. Tentzeris. Longitudinally misalignment-insensitive dual-band wireless power and data transfer systems for a position detection of fast-moving vehicles. *IEEE Transactions on Antennas and Propagation*, 67(8):5614–5622, 2019. doi: 10.1109/TAP.2019.2916697.

[70] Wang-Sang Lee, Han Lim Lee, Kyoung-Sub Oh, and Jong-Won Yu. Uniform magnetic field distribution of a spatially structured resonant coil for wireless power transfer. *Applied Physics Letters*, 100(21):214105, 2012.

[71] Joaquin J Casanova, Zhen Ning Low, Jenshan Lin, and Ryan Tseng. Transmitting coil achieving uniform magnetic field distribution for planar wireless power transfer system. In *2009 IEEE Radio and Wireless Symposium*, pages 530–533. IEEE, 2009.

[72] Chun Qiu, KT Chau, Chunhua Liu, Tze Wood Ching, and Zhen Zhang. Modular inductive power transmission system for high misalignment electric vehicle application. *Journal of Applied Physics*, 117(17):17B528, 2015.

[73] D. Yinliang, S. Yuanmao, and G. Yougang. Design of coil structure achieving uniform magnetic field distribution for wireless charging platform. In *2011 4th International Conference on Power Electronics Systems and Applications*, pages 1–5, 2011. doi: 10.1109/PESA.2011.5982959.

[74] Z. Zhang and K. T. Chau. Homogeneous wireless power transfer for move-and-charge. *IEEE Transactions on Power Electronics*, 30(11):6213–6220, 2015. doi: 10.1109/TPEL.2015.2414453.

[75] Y. Zhang, L. Wang, Y. Guo, and Y. Zhang. Optimisation of planar rectangular coil achieving uniform magnetic field distribution for ev wireless charging based on genetic algorithm. *IET Power Electronics*, 12(10):2706–2712, 2019. doi: 10.1049/iet-pel.2018.6202.

[76] Y. Yang, Xiaofei Kuang, Peng Yang, Yonghai Jing, Xiang Su, and Y. Cheng. Parallel connected transmitting coil for achieving uniform magnetic field distribution in wpt. In *2015 IEEE 16th International Conference on Communication Technology (ICCT)*, pages 529–532, 2015. doi: 10.1109/ICCT.2015.7399893.

[77] M. R. Basar, M. Y. Ahmad, J. Cho, and F. Ibrahim. Stable and high-efficiency wireless power transfer system for robotic capsule using a modified helmholtz coil. *IEEE Transactions on Industrial Electronics*, 64(2):1113–1122, 2017. doi: 10.1109/TIE.2016.2614268.

[78] Z. Bie, K. Song, C. Zhu, X. Huang, and Q. Zhang. A high magnetic field uniformity staggered-series square transmitting coil for wireless electric vehicle charging systems. In *2020 IEEE Transportation Electrification Conference Expo (ITEC)*, pages 831–834, 2020. doi: 10.1109/ITEC48692.2020.9161755.

[79] C. Cai, J. Wang, H. Nie, P. Zhang, Z. Lin, and Y. G. Zhou. Effective-configuration wpt systems for drones charging area extension featuring quasi-uniform magnetic coupling. *IEEE Transactions on Transportation Electrification*, 6(3):920–934, 2020. doi: 10.1109/TTE.2020.2995733.

[80] Martin Misakian. Equations for the magnetic field produced by one or more rectangular loops of wire in the same plane. *Journal of research of the National Institute of Standards and Technology*, 105(4):557, 2000.

[81] Matthew NO Sadiku and Shrikrishna V Kulkarni. *Principles of electromagnetics*, volume 2. oxford university Press New Delhi and Oxford, 2009.

[82] Ashwani Sharma, Ignacio J. Garcia Zuazola, Anshu Gupta, Asier Perallos, and John C. Batchelor. Non-uniformly distributed-turns coil antenna for enhanced h-field in hf-rfid. *IEEE Transactions on Antennas and Propagation*, 61(10):4900–4907, 2013. doi: 10.1109/TAP.2013.2275244.

[83] Jeff P. W. Chow, Nan Chen, Henry S. H. Chung, and Leanne L. H. Chan. Misalignment tolerable coil structure for biomedical applications with wireless power transfer. In *2013 35th Annual International Conference of the IEEE Engineering in Medicine and Biology Society (EMBC)*, pages 775–778, 2013. doi: 10.1109/EMBC. 2013.6609615.

[84] Jeff Po Wa Chow, Nan Chen, Henry Shu Hung Chung, and Leanne Lai Hang Chan. An investigation into the use of orthogonal winding in loosely coupled link for improving power transfer efficiency under coil misalignment. *IEEE Transactions on Power Electronics*, 30(10):5632–5649, 2015. doi: 10.1109/TPEL.2014.2374651.

[85] Qinghua Wang, Wenquan Che, Mauro Mongiardo, and Giuseppina Monti. Wireless power transfer system with high misalignment tolerance for bio-medical implants. *IEEE Transactions on Circuits and Systems II: Express Briefs*, 67(12):3023–3027, 2020. doi: 10.1109/TCSII.2020.2985056.

[86] Chang-Yeob Chu, Sungryul Huh, Semin Choi, Jong-Hyeok Park, Seungyoung Ahn, Sang-Gug Lee, and Ki-Bum Park. Wireless power transfer system design for electric vehicle charging considering a wide range of coupling coefficient variation depending on the coil misalignment. In *2021 24th International Conference on Electrical Machines and Systems (ICEMS)*, pages 732–737, 2021. doi: 10.23919/ICEMS52562. 2021.9634575.

[87] Fandan Zhao, Jinhai Jiang, Shumei Cui, Xingjian Zhou, Chunbo Zhu, and Ching Chuen Chan. Research on bipolar nonsalient pole transmitter for high-power ev dynamic wireless power transfer system. *IEEE Transactions on Power Electronics*, 37(2):2404–2412, 2022. doi: 10.1109/TPEL.2021.3105441.

[88] Hongjie Wang, Ujjwal Pratik, Aleksandar Jovicic, Nazmul Hasan, and Zeljko Pantic. Dynamic wireless charging of medium power and speed electric vehicles. *IEEE Transactions on Vehicular Technology*, 70(12):12552–12566, 2021. doi: 10.1109/TVT.2021.3122366.

[89] James C. Lin. Safety of wireless power transfer. *IEEE Access*, 9:125342–125347, 2021. doi: 10.1109/ACCESS.2021.3108966.

[90] Peiyue Wang, Yue Sun, Yuchen Feng, Tianxu Feng, Yuanshuang Fan, and Xiaofei Li. An improvement of snr for simultaneous wireless power and data transfer system with full-duplex communication mode. *IEEE Transactions on Power Electronics*, 37 (2):2413–2424, 2022. doi: 10.1109/TPEL.2021.3106903.

[91] Young-Joon Kim, Dohyuk Ha, William J. Chappell, and Pedro P. Irazoqui. Selective wireless power transfer for smart power distribution in a miniature-sized multiple-receiver system. *IEEE Transactions on Industrial Electronics*, 63(3): 1853–1862, 2016. doi: 10.1109/TIE.2015.2493142.

[92] Mahmoud Wagih, Abiodun Komolafe, and Bahareh Zaghari. Wearable wireless power transfer using direct-write dispenser printed flexible coils. In *2020 IEEE International Conference on Flexible and Printable Sensors and Systems (FLEPS)*, pages 1–4, 2020. doi: 10.1109/FLEPS49123.2020.9239595.

[93] Qinghua Wang, Wenquan Che, Mauro Mongiardo, and Giuseppina Monti. Wireless power transfer system with high misalignment tolerance for bio-medical implants. *IEEE Transactions on Circuits and Systems II: Express Briefs*, 67(12):3023–3027, 2020. doi: 10.1109/TCSII.2020.2985056.

[94] Guilin Sun, Badar Muneer, Ying Li, and Qi Zhu. Ultracompact implantable design with integrated wireless power transfer and rf transmission capabilities. *IEEE Transactions on Biomedical Circuits and Systems*, 12(2):281–291, 2018. doi: 10.1109/TBCAS.2017.2787649.

[95] Alexander Khripkov, Wonbin Hong, and Konstantin Pavlov. Integrated resonant structure for simultaneous wireless power transfer and data telemetry. *IEEE Antennas and Wireless Propagation Letters*, 11:1659–1662, 2012. doi: 10.1109/LAWP.2013.2238602.

[96] Uei-Ming Jow and Maysam Ghovanloo. Geometrical design of a scalable overlapping planar spiral coil array to generate a homogeneous magnetic field. *IEEE Transactions on Magnetics*, 49(6):2933–2945, 2013. doi: 10.1109/TMAG.2012.2235181.

[97] Qiang Feng and Bing-Zhao Li. Convolution and correlation theorems for the two-dimensional linear canonical transform and its applications. *IET Signal Processing*, 10(2):125–132, 2016.

[98] Ivan Cortes and Won-jong Kim. Lateral position error reduction using misalignment-sensing coils in inductive power transfer systems. *IEEE/ASME Transactions on Mechatronics*, 23(2):875–882, 2018. doi: 10.1109/TMECH.2018. 2801250.

[99] Ahmed N. Azad, Allon Echols, Vladimir A. Kulyukin, Regan Zane, and Zeljko Pantic. Analysis, optimization, and demonstration of a vehicular detection system intended for dynamic wireless charging applications. *IEEE Transactions on Transportation Electrification*, 5(1):147–161, 2019. doi: 10.1109/TTE.2018.2870339.

[100] Wei Ni, Iain B. Collings, Xin Wang, Ren Ping Liu, Alija Kajan, Mark Hedley, and Mehran Abolhasan. Radio alignment for inductive charging of electric vehicles. *IEEE Transactions on Industrial Informatics*, 11(2):427–440, 2015. doi: 10.1109/TII.2015. 2400925.

[101] Dimitris Baros, Nick Rigogiannis, Panagiotis Drougas, Dionisis Voglitsis, and Nick P. Papanikolaou. Transmitter side control of a wireless ev charger employing iot. *IEEE Access*, 8:227834–227846, 2020. doi: 10.1109/ACCESS.2020.3045803.

[102] Xuyang Liu, Chunhua Liu, Wei Han, and Philip W. T. Pong. Design and implementation of a multi-purpose tmr sensor matrix for wireless electric vehicle charging. *IEEE Sensors Journal*, 19(5):1683–1692, 2019. doi: 10.1109/JSEN.2018. 2883708.

[103] Prithvi Krishna Chittoor, Bharatiraja Chokkalingam, and Lucian Mihet-Popa. A review on uav wireless charging: Fundamentals, applications, charging techniques and standards. *IEEE Access*, 9:69235–69266, 2021. doi: 10.1109/ACCESS.2021. 3077041.

[104] Cancan Rong, Xiangrui He, Yitong Wu, Yongtao Qi, Ruohan Wang, Yunong Sun, and Minghai Liu. Optimization design of resonance coils with high misalignment tolerance for drone wireless charging based on genetic algorithm. *IEEE Transactions on Industry Applications*, 58(1):1242–1253, 2022. doi: 10.1109/TIA.2021.3057574.

[105] Jeff P. W. Chow, Nan Chen, Henry S. H. Chung, and Leanne L. H. Chan. Misalignment tolerable coil structure for biomedical applications with wireless power transfer. In *2013 35th Annual International Conference of the IEEE Engineering in Medicine and Biology Society (EMBC)*, pages 775–778, 2013. doi: 10.1109/EMBC. 2013.6609615.

[106] Xiaoyang Tian, K. T. Chau, Wei Liu, and Christopher H. T. Lee. Analysis of multi-coil omnidirectional energy harvester. *IEEE Transactions on Magnetics*, 57 (2):1–6, 2021. doi: 10.1109/TMAG.2020.3015732.

[107] Libo Qian, Kefang Qian, Yong Shi, Huakang Xia, Jian Wang, and Yinshui Xia. Tsv based orthogonal coils with high misalignment tolerance for inductive power

transfer in biomedical implants. *IEEE Transactions on Circuits and Systems II: Express Briefs*, 68(6):1832–1836, 2021. doi: 10.1109/TCSII.2020.3048040.

[108] Jeff Po Wa Chow, Nan Chen, Henry Shu Hung Chung, and Leanne Lai Hang Chan. An investigation into the use of orthogonal winding in loosely coupled link for improving power transfer efficiency under coil misalignment. *IEEE Transactions on Power Electronics*, 30(10):5632–5649, 2015. doi: 10.1109/TPEL.2014.2374651.

[109] Dibin Zhu, Neil J. Grabham, Lindsay Clare, Bernard H. Stark, and Steve P. Beeby. Inductive power transfer in e-textile applications: Reducing the effects of coil misalignment. In *2015 IEEE Wireless Power Transfer Conference (WPTC)*, pages 1–4, 2015. doi: 10.1109/WPT.2015.7140116.

# Appendix

**Vector Network Analyzer (VNA)**

The model number of VNA used for acquiring measurement data in this thesis work is N5320C. The operating procedure of N5320C network analyzer is detailed as follows:

- **Power ON the VNA**: Connect the power supply and turn on the VNA following the manufacturer's instructions. Allow the instrument to warm up if necessary.

- **Connect the cables**: Appropriate low loss coaxial cables and connectors to connect the input and output ports of the VNA's test ports. Ensure proper grounding and tight connections.

- **Calibrate the VNA**: Perform a calibration procedure to remove systematic errors introduced by the test setup. For this, a calibration kit model no: 85052D is explicitly employed. Here, in the calibration process the Short-Open-Load-Through (SOLT) are conected in sequence for two ports to ensure both cables are calibrated at 50Ω characteristic impedance.

- **Connect the device**: Connect the Device Under Test (DUT), here, it is Tx-Rx coils. Measure, the passive coil parameters (i.e., resistance, self-inductance, mutual inductance) by selecting smith chart formatting option in VNA menu bar.

- **Set up measurement parameters**: Select the desired measurement parameters. such as PTE between Tx-Rx coil. To get PTE, it is required to collect the measured data of S11, and S21 parameters of Tx-Rx coils. Therefore, using log magnitude format option from VNA's menubar, the S-parameters are fetched at desired operating frequency. Further, to eliminate the noise, trigger the averaging function from VNA's menu bar.

- **Repeat measurements or adjust setup**: If needed, repeat the measurements with different misalignment positions or adjust the test setup (e.g., change connectors, cables, or DUT configuration) to obtain additional data to complete the measurement process.

- **Power OFF the VNA**: After completing the measurements, power off the VNA as per the manufacturer's instructions.

# M. ANANTH BHARADWAJ

**Senior Research Fellow**
**Lab:304, Antenna and Microwave Research Laboratory,**
**Department of Electrical Engineering,**
**Indian Institute of Technology, Ropar,**
**Punjab, India-140001.**

## CONTACT

- ✉ 2018eez0023@iitrpr.ac.in
- ✉ bharadwajamr13@gmail.com
- ☎ +91 9381346908
- ⌂ Ananth bharadwaj
- in Ananth Bharadwaj
- ⚲ IIT Ropar, Punjab, India
- iD 0000-0001-7601-2903

- ⌂ Google Scholar
- ⌂ Research Gate
- ⌂ IEEE Xplorer

## RESEARCH SUPERVISOR

**Dr. Ashwani Sharma**
- ✉ ashwani.sharma@iitrpr.ac.in
- ⌂ AMR Lab IIT Ropar
- iD 0000-0002-5297-4232

**Prof. C.C Reddy**
- ✉ reddy@iitrpr.ac.in
- ⌂ HV Lab IIT Ropar
- iD 0000-0002-7576-6735

## SKILLS

*Software Tools*

**Matlab** ●●●●●
**Ie3D Simulator** ●●●●●
**LaTeX** ●●●●●
**LTspice** ●●●○○
**Ansys HFSS** ●●●○○
**PCB Editor** ●●●○○

*Hardware instruments*

**Network Analyzer** ●●●●●
**Signal Generator** ●●●●●
**Spectrum Analyzer** ●●●●●
**PCB Machine** ●●●●○

*Languages*

**English** ●●●●●
**Hindi** ●●●●○
**Telugu** ●●●●●
**Tamil** ●●○○○

## CURRENT STATUS

Pursuing final year Ph.D. in AMR Lab, IIT Ropar, and submitted my thesis on 20th April 2023. The thesis topic for the PhD program is 'Mitigation of Lateral Misalignment Problem in Wireless Power Transfer Applications.'

## WORK HISTORY

- Teaching Assistant       -       January, 2019 - Ongoing
    ⚲ Indian Institute of Technology, Ropar

- Assistant Professor       -       June, 2018 - December, 2018
    ⚲ Sree Vidyaniketan Engineering College, Tirupati

- Teaching Assistant       -       August, 2016- May, 2018
    ⚲ National Institute of Technology, Arunachal Pradesh

## EDUCATION

- Doctor of philosophy       -       Jan, 2019 - Ongoing
  Electrical Engineering       -       (C.G.P.A-8.79/10)
    ⚲ Indian Institute of Technology, Ropar.

- Master of Technology       -       August, 2016- May, 2018
  Electrical Engineering       -       (C.G.P.A-8.93/10)
    ⚲ National Institute of Technology, Arunachal Pradesh

- Bachelor of Engineering   -   August, 2011- May, 2015
  Electrical & Electronics    -    (C.G.P.A- 7.87/10)
    ⚲ Anna University, Chennai

## AWARDS

- Best paper award in IEEE 15th International Conference on Industrial and Information Systems (ICIIS), 2020 in Power, HV and Control system category.
- Best paper award in IEEE 15th International Conference on Industrial and Information Systems (ICIIS), 2020 in Signal processing and communication category.